GENERALIZED METHOD OF MOMENTS: A NOVEL DISCRETIZATION TECHNIQUE FOR INTEGRAL EQUATIONS

Ву

Naveen V. Nair

A DISSERTATION

Submitted to
Michigan State University
in partial fulfillment of the requirements
for the degree of

DOCTOR OF PHILOSOPHY

Electrical Engineering

2010

ABSTRACT

GENERALIZED METHOD OF MOMENTS: A NOVEL DISCRETIZATION TECHNIQUE FOR INTEGRAL EQUATIONS

$\mathbf{B}\mathbf{y}$

Naveen V. Nair

Integral equation formulations to solve electromagnetic scattering and radiation problems have existed for over a century. The method of moments (MoM) technique to solve these integral equations has been in active use for over 40 years and has become one of the cornerstones of electromagnetic analysis. It has been successfully employed in a wide variety of problems ranging from scattering and antenna analysis to electromagnetic compatibility analysis to photonics. In MoM, the unknown quantity (currents or fields) is represented using a set of basis functions. This representation, together with Galerkin testing, results in a set of equations that may then be solved to obtain the coefficients of expansion. The basis functions are typically constructed on a tessellation of the geometry and its choice is critical to the accuracy of the final solution. As a result, considerable energy has been expended in the design and construction of optimal basis functions. The most common of these functions in use today are the Rao-Wilton-Glisson (RWG) functions that have become the de-facto standard and have also spawned a set of higher order complete and singular variants. However, their near-ubiquitous popularity and success notwithstanding, they come with certain important limitations.

The chief among these is the intimate marriage between the underlying triangulation of the geometry and the basis function. While this coupling maintains continuity of the normal component of these functions across triangle boundaries and makes them very easy to implement, this also implies an inherent restriction on the kind of basis function spaces that can be employed. This thesis aims to address this issue and provides a novel framework for the discretization of integral equations that

demonstrates several significant advantages.

In this work, we will describe a new umbrella framework for the discretization of integral equations called the Generalized Method of Moments (GMM). We will show that within this framework it is possible to choose from a very wide variety of functions to form the basis space. While the choice of basis functions can be completely arbitrary, the thesis will describe in detail one particular scheme that utilizes a surface quasi-Helmholtz decomposition and provides a mechanism for the use of any available knowledge of the physics of the problem. The thesis will describe the theoretical framework required for the design of this scheme and develop error bounds for the approximation of the unknown quantities using the proposed basis functions. Following that, we will delve into the implementation of the GMM starting from commonly available triangular tessellations, carefully identifying and solving several key issues along the way.

The GMM, developed here, will be applied to a plethora of examples, validated against analytical solutions and compared against the standard RWG discretizations. It will further be shown that the use of the quasi-Helmholtz decomposition will result in a scheme that is well conditioned over a wide range of frequencies. We will then extend the GMM to both the analysis of scattering from dielectric bodies using the PMCHWT and Müller operators and to the analysis of transient scattering from conducting objects. Several results will be presented in either case that demonstrate the advantage of the proposed method.

DEDICATION

To my wife, my parents and my sister

ACKNOWLEDGMENT

This thesis would have been impossible without the unfaltering support and advice of Shanker Balasubramaniam, my primary advisor. His understanding and enthusiasm has helped me navigate many a tough corner during the last four years. He has taught me so much more than computational electromagnetics that it would be an injustice to even try to list it here. He has gone, and continues to go, far beyond the calls of duty as an advisor to be a friend, guide and reality check to me and his focus, energy and work ethic will be constant sources of inspiration throughout my life and career.

During the first three years of my graduate career I was supported and guided by my co-advisor Satish Udpa. The experience I gained under his tutelage will prove invaluable to me in the future. I have been indeed blessed with two excellent PhD advisors; either of whom any student would be lucky to get alone. I would also like to thank each member of my doctoral committee: Leo Kempel, Ed Rothwell and Jian Liang Qian for their support and guidance.

Several people have played key roles behind the curtain to make my graduate student life work. Chief among them is Linda Clifford, who has patiently proof-read many a document for my research and cooked many a meal for thanksgiving dinners throughout the seven years I have been in graduate school. I would also like to acknowledge Pauline Vandyke for all her support when I needed a teaching assistanship to push through a semester or when I needed to steal some coffee from the faculty kitchen.

I would like to acknowledge the support of my friends and lab mates: Vikram Melapudi, Andrew B., Andrew P., Ozgur Tuncer and Dan Dault for being excellent touchstones for my ideas over the past several years. In particular I would like to thank Andrew Pray for generating several of the results in the latter part of this thesis. A special thanks needs to go out to Vikram Melapudi and Mayur Mudigonda for their invaluable friendship over the years.

With more than two decades of schooling nearly behind me, I would like to thank my teachers over the years who have played a major part in making me who I am to-day: Poonam Lal, Nakku and Kusum Chandragupta, back in highschool, for teaching me how to learn; A. Venkatesh at the Indian Institute of Technology Madras for first getting me interested in heat transfer, and therefore, partial differential equations and finally, Krishnan Balasubramaniam for being the first advisor I ever had and instilling in me a deep rooted passion for rigor in reasearch.

I would like to thank my brother in law, Saju, for appearing in my family's life exactly around the time of my comprehensive and distracting my entire family enough to give me an extra year to finish this thesis.

And, finally my deepest gratitude goes out to my family: my wife Aneesha, my mother Sobhana, father Vijayakumaran and my sister Indu whose constant and unwavering support has helped me keep my sanity through my (long) tenure as a graduate student. It is to them that I dedicate this thesis.

TABLE OF CONTENTS

| | List | of Fig | gures | Х |
|---|-------------------------------------|---|--|--|
| 1 | Intr 1.1 1.2 1.3 1.4 | Differe Integra Basis | ion | 1 2 3 4 6 |
| 2 | Mat 2.1 2.2 2.3 2.4 | Maxwe Vector Integra | rell's Equations | 10 13 16 20 |
| 3 | Nur 3.1 3.2 | Metho | od of moments solution for integral equations | 23 23 25 |
| 4 | The 4.1 4.2 4.3 4.4 4.5 4.6 4.7 4.8 | Partiti Definit Design Error Benefi Impler Constr Comp | tion of Unity functions and Overlapping Patches tion of Basis Functions of the Vector Approximating Function Bounds for the Discrete Integral Operators its of the GMM framework mentation of the GMM. ruction of Overlapping Patches utation of Matrix Elements \mathbf{r} and \mathbf{r}' lie on the same triangle \mathbf{r} and \mathbf{r}' lie on triangles that share an edge \mathbf{r} and \mathbf{r}' are not in neighbouring triangles but are close $(\mathbf{r}-\mathbf{r}' \leq 0.15\lambda)$. \mathbf{r} and \mathbf{r}' are sufficiently separated from each other A transformation for the near singular integration of $\nabla g(R)\mathbf{j}(\mathbf{r}')$ for $\mathbf{r} \to \mathbf{r}'$ \mathbf{r} and \mathbf{r}' are not in neighbouring triangles but are close $(\mathbf{r}-\mathbf{r}' \leq 0.15\lambda)$. \mathbf{r} and \mathbf{r}' are not in neighbouring triangles but are close $(\mathbf{r}-\mathbf{r}' \leq 0.15\lambda)$. \mathbf{r} and \mathbf{r}' are sufficiently separated from each other | 30 33 35 42 46 51 52 56 60 60 60 61 61 |
| | 4.9 | 4.8.3 Numer | Integration with acceleration techniques | 62 62 |

| | 4.10 | Qualit | ty of Approximation | 62 |
|---|------|--------------|--|--------------|
| | | 4.10.1 | Approximation of Polynomial Functions | 63 |
| | | 4.10.2 | Approximation of sinusoidal functions | 64 |
| | | 4.10.3 | Approximation of non-smooth and near-singular functions | 64 |
| | 4.11 | Scatte | ering Results | 69 |
| | | 4.11.1 | Analytical Validation and p-convergence | 70 |
| | | 4.11.2 | Comparison with standard RWG | 71 |
| | | 4.11.3 | Comparison with measured data | 74 |
| | 4.12 | Flexib | oility of the GMM scheme | 78 |
| | | 4.12.1 | Mixing orders of basis functions | 78 |
| | | 4.12.2 | Mixing types of basis functions | 79 |
| | | 4.12.3 | Use of non-conformal meshes | 83 |
| | 4.13 | Condi | tion Number of the System | 83 |
| | 4.14 | Summ | nary | 91 |
| | | | | |
| 5 | | | on of the Generalized Method of Moments for Dielectri | |
| | | | | 93 |
| | 5.1 | | em Statement | 93 |
| | 5.2 | | Discretization of the PMCHWT and Müller Integral Equations | 97 |
| | ۲ ، | 5.2.1 | Müller Operator | 97 |
| | 5.3 | - | mentation Results | 98 |
| | | 5.3.1 | Validation of GMM PMCHWT and Müller Solvers | 99 |
| | | 5.3.2 | Salient features of the GMM scheme | 100 |
| | | | Mixtures of Basis functions | 105 |
| | | | Mixed Order Bases: | 105 |
| | | | Mixed Types of Bases: | 106 |
| | | | hp-adaptivity: | 108 |
| | | r o o | Non Conformal meshes | 111 |
| | | 5.3.3 | Low frequency stability and multiply connected scatterers | 111 |
| 6 | Ana | alvsis o | of transient scattering using the Generalized Method o | \mathbf{f} |
| | | ments | | |
| | 6.1 | The F | Ourier transform pair | 118 |
| | 6.2 | Time | Domain EFIE and MFIE | 119 |
| | 6.3 | The N | Marching on in Time (MOT) scheme | 122 |
| | 6.4 | Tempe | oral basis functions | 124 |
| | 6.5 | | for transient scattering | 126 |
| | 6.6 | Nume | rical Experiments | 129 |
| | | 6.6.1 | Validation | 129 |
| | | 6.6.2 | Low frequency stability | 130 |
| | | 6.6.3 | Mixtures of basis functions | 135 |
| | | 6.6.4 | Non conformal meshes | 138 |

| 7 | Con | clusion | ns and Future Work | 143 |
|---|----------------|----------|---|-----|
| | 7.1 | Future | Work | 145 |
| | | 7.1.1 | Mathematical proof for the well conditioned nature of the GMM | 145 |
| | | 7.1.2 | Generalized higher order patch construction | 146 |
| | | 7.1.3 | Further development of the transient GMM | 147 |
| | | 7.1.4 | Application to multi-scale geometries | 147 |
| | | 7.1.5 | Domain Decomposition | 148 |
| | | 7.1.6 | Application to other integral equations | 148 |
| | | | | |
| | \mathbf{Bib} | oliograp | phy | 150 |

LIST OF FIGURES

| 2.1 | General representation for a domain $D^+ = V$ with inner and outer boundaries | 17 |
|-----|--|----|
| 2.2 | General description of a scattering problem | 20 |
| 3.1 | A schematic showing the definition of the RWG basis functions on an edge shared by two triangles | 28 |
| 4.1 | Currents on a PEC cube showing the singular nature of the currents near the edges and the smooth currents towards the center. For interpretation of the references to color in this and all other figures, the reader is referred to the electronic version of this dissertation | 32 |
| 4.2 | Construction of GMM patches (Ω_i) shown as shaded region | 34 |
| 4.3 | Examples of linear PU functions in (a) one and (b) two dimensions . | 36 |
| 4.3 | Examples of linear PU functions in (a) one and (b) two dimensions . | 37 |
| 4.4 | Construction of scalar GMM basis functions. (a) the GMM approximation function and (b) the product of the approximation function and the partition of unity function | 38 |
| 4.5 | Vector GMM basis functions based on the quasi-surface Helmhotlz decomposition basis functions. (a) The quasi curl-free basis functions and (b) the quasi-divergence free basis functions. Both functions are of order $p=3$ | 44 |
| 4.6 | Construction of GMM patches (Ω_i) shown as shaded region. The patches are constructed as a set of triangles joined at a node | 52 |

| 4.7 | Construction of (a) GMM Patches (Ω_i) shown as shaded region and (b) Projection Planes (Γ_i) from standard triangulations. The patches are constructed as a set of triangles joined at a node | 55 |
|------|--|----|
| 4.8 | Basis functions defined on (a) the projection plane and (b) the true geometry (surface of a tessellated sphere). The figure (b) shows that there is no discontinuities introduced by the projection | 57 |
| 4.9 | Quality of approximation of (a) polynomial function and (b) sinusoidal functions | 64 |
| 4.10 | Quality of approximation of discontinuous function: (a) without using a partition of unity; and (b) with a partition of unity. | 66 |
| 4.11 | Comparison of approximation error with and without PU | 70 |
| 4.12 | Validation studies: Scattering from PEC spheres of different radii. Fig. (a) shows the RCS comparison and figure (b) shows the convergence of solutions with basis order p | 72 |
| 4.13 | Validation studies: scattering from (a) a PEC plate and an open cavity. Plot of bistatic RCS ($\phi=0$). Fig. (b) bistatic scattering RCS from a NASA thin almond and a PEC conesphere. The RCS is compared at $\phi=0$ for the almond and $\theta=\pi/2$ for the conesphere. Inset figures show the surface current on the almond and the conesphere | 75 |
| 4.14 | RCS comparison for a PEC box (0.7λ) . The figure compares RCS due to scattering of a $-\hat{\mathbf{x}}$ directed plane wave polarized along $-\hat{\mathbf{y}}$. The bistatic RCS is compared at $\phi=0$ against that obtained using an RWG discretization and against measured data | 77 |
| 4.15 | RCS comparison for regular GMM and mixed order GMM: (a) comparison of bistatic RCS ($\phi=0$) for a PEC box. Fig. (b) shows the comparison of bistatic RCS ($\phi=0$) for a PEC thin almond. In each case, the incident field is directed along $-\hat{\mathbf{z}}$ and polarized along $\hat{\mathbf{x}}$ and bistatic RCS is evaluated at $\phi=0$ | 80 |
| 4.16 | RCS obtained due to scattering of a $\hat{\mathbf{x}}$ polarized plane wave directed along $-\hat{\mathbf{z}}$ from a PEC box $(\lambda \times 0.5\lambda \times 0.5\lambda)$ directed along $\hat{\mathbf{x}}$ obtained using regular GMM and mixed basis GMM with polynomials and plane waves. | 82 |
| | | |

| 4.17 | Backscatter RCS comparison for scattering from a non conformally meshed PEC plate (shown in figure (a)) RCS obtained by using the GMM discretization on a non conformal mesh compared against that obtained by discretizing on a (standard) conformal mesh for a PEC plate | 84 |
|------|--|-----|
| 4.18 | EFIE Condition number comparisons for PEC sphere (0.2) , square plate $(1m)$ and cube $(1m)$ using GMM, RWG and loop star basis | 85 |
| 4.19 | EFIE Condition number comparisons for PEC sphere $(0.2m)$ and strip $(1m \times 0.2m)$ using higher order $(p=3)$ complete GMM and RWG basis. | 86 |
| 4.20 | EFIE Condition number comparisons for non-uniformly discretized square plate $(1m)$ and thin almond $(1:3:9)$ using GMM and RWG and loop star basis. The plate is discretized at average edge length ranging from 0.1λ to 0.025λ and the almond is discretized from 0.1λ to 0.02λ | 87 |
| 4.21 | Comparison of RCS (GMM vs. loop star) at $30MHz$, $30kHz$ and $3kHz$ for constant h for a Plate: side $1m$. The RCS is compared against that obtained using Loop Star basis functions. | 88 |
| 4.22 | Condition number vs. frequency for a PEC box: The figures show the condition numbers using the regular GMM basis set and using just the quasi-divergence free basis functions from the GMM basis set. In each case; the RCS is computed to good accuracy as shown inset | 90 |
| 4.23 | Bistatic RCS ($\phi = 0$) comparison for a dielectric toroid (outer radius $0.75\lambda_0$ and inner radius $0.5\lambda_0$, $\varepsilon_r = 4.0$). This result demonstrates the advantage of using an <i>local</i> quasi-surface Helmholtz decomposition basis function set. The inset shows direction and polarization of the incident field along with an image of the surface current density on the toroid | 91 |
| 5.1 | RCS obtained using GMM basis functions used to discretize the PM-CHWT amd Müller equations for the solution of scattering from (a) dielectric spheres (radii $0.1\lambda_0,0.3\lambda_0$ and $0.5\lambda_0$ and $\varepsilon_r = 4.0$) and (b) a cube (side λ_0 , $\varepsilon_r = 4.0$) due to plane wave incidence. The bistatic RCS (at $\phi = 0$) are compared against that obtained using an RWG discretization and analytical results (for spheres). | 101 |

| 5.3 RCS comparison of standard GMM vs. Mixed-order GMM (a) NASA almond discretized with GMM basis functions complete to order $p=4$ near edges and $p=1$ elsewhere. (b) Dielectric box using $p=1$ near |
|---|
| edges and $p=2$ in larger patches near center. The bistatic RCS is computed at $\phi=0$ and the incident field is polarized along $\hat{\mathbf{x}}$ and incident along $-\hat{\mathbf{z}}$ |
| 8.4 RCS comparison of standard GMM vs. Mixed-Basis GMM $(5.0\lambda_0 \times 2.0\lambda_0 \times 0.5\lambda_0)$. Electric field is incident along $-\hat{\mathbf{z}}$ and polarized along $\hat{\mathbf{x}}$. The bistatic RCS $(\phi=0)$ is compared for GMM using polynomial basis functions against GMM using polynomials mixed with plane wave basis functions |
| 5.5 RCS comparison for scattering from a dielectric arrow $(2.0\lambda_0 \times 3.0\lambda_0 \times \lambda_0)$. Electric field is incident along $-\hat{\mathbf{z}}$ and polarized along $\hat{\mathbf{x}}$. The bistatic RCS $(\phi = 0)$ is compared for four different combinations of h and polynomial order of basis function p |
| 5.6 RCS comparison for scattering from a non conformally meshed dielectric box. Bistatic RCS ($\phi = 0$) obtained by discretizing the Müller integral equation on a non conformal mesh (shown inset) compared against that obtained by discretizing on a (standard) conformal mesh for a thin dielectric ($\varepsilon_r = 4.0$) box $(2.0\lambda_0 \times 0.2\lambda_0 \times 0.5\lambda_0)$ |
| 5.7 Condition number comparisons. All objects are discretized at $0.1\lambda_m$ at $30MHz$ and the operating frequency is swept from $30MHz$ to $30Hz$ and condition number of the impedance matrix obtained on GMM discretization is compared against that obtained using a standard RWG discretization. (a) Sphere (radius $0.1m$, $\varepsilon_r = 4.0$) and (b) Cube (side $1m$ and $\varepsilon_r = 4.0$) |
| 5.9 Bistatic RCS ($\phi = 0$) comparison for a dielectric toroid (outer radius $0.75\lambda_0$ and inner radius $0.5\lambda_0$, $\varepsilon_r = 4.0$). Figure 5.9(a) shows direction and polarization of the incident field along with an image of the surface current density on the toroid. |

| 6.1 | General description of a scattering problem | 120 |
|-----|---|-----|
| 6.2 | Temporal basis functions for solution of the TDIE. (a) shows the Lagrange polynomial basis functions which are not band limited as opposed to (b) approximate prolate spheroidal functions that are band limited but require extrapolation to maintain causality | 126 |
| 6.3 | Backscatter RCS comparison for (a) two spheres of radii $0.2m$ and $0.5m$ and (b) a thin NASA almond $(0.3m \times 1.15m \times 3m)$ compared against RWG discretization. The inset figure shows snapshots of the magnitude of the current density on the almond | 131 |
| 6.4 | Backscatter RCS comparison for (a) a thin box of size $20m \times 1m \times 20m$ compared against RWG discretization and (b) a PEC cube of side $0.7m$ compared against both RWG and experimental result. The inset figures show snapshots of the magnitude of the current density on the scatterer | 133 |
| 6.5 | Backscatter RCS comparison for (a) thin box $(20m \times 1m \times 20m)$ and (b) a toroid (outer radius $0.75m$ and inner radius $0.5m$). The inset figures show a snapshot of the magnitude of the current density and direction of propagation and incidence. | 135 |
| 6.6 | Backscatter RCS comparison of standard GMM vs. Mixed-order GMM (a) Box using $p=1$ near edges and $p=2$ in larger patches near center (b) NASA almond discretized with GMM basis functions complete to order $p=2$ near edges and $p=1$ elsewhere and (c) dielectric box using $p=1$ near edges, $p=3$ near the center and $p=2$ in the transition region | 138 |
| 6.7 | Backscatter RCS comparison for scattering from a non conformally meshed PEC box. RCS obtained by using the GMM discretization on a non conformal mesh (shown inset) compared against that obtained by discretizing on a (standard) conformal mesh for a thin box | 142 |

Chapter 1

Introduction

The preface to a collection of seminal papers on computational electromagnetics, compiled in 1973, says "Computer electromagnetics is a relatively new and rapidly growing field" [1]. Today, almost four decades later, computational electromagnetics is a field that is still growing equally rapidly. The growth of computational electromagnetics has provided the community with simulation tools that solve a wide array of problems ranging from electrical to electronic to computer to optical. For most of the initial part of this growth, computational tools were largely used to complement, and not supplant, experiments. The design of most electromagnetics structures such as antennas, gratings etc. were reliant on the designers' intuitive understanding of the underlying physics. This, in turn, implied that non-intuitive designs were automatically precluded. However in the last two decades, computational techniques have grown by leaps and bounds in terms of speed and accuracy, and the simulation of complicated, realistic structures is well within reach. Today, therefore, computational techniques are a viable alternative to experiments in a wide variety of applications.

The idea of using computational techniques for the solution of partial differential equations historically comes from the field of fluid dynamics [2–5] where the most problems, even for reasonably "canonical" geometries, are analytically intractable ow-

ing to the inherent non linearity of the Navier Stokes equations. Maxwell's equations, by contrast, are linear and therefore, permit a wide class of analytical and asymptotic approaches. However, the solution of realistic electromagnetic problems on complex geometries and the rapid advancements in computing power strongly motivates the use of computational techniques. The spate of techniques that exist today in computational electromagnetics generally fall into two categories: differential equation based and integral equation based. In the next two sections, we will visit the salient features of both these methods.

1.1 Differential Equation Methods

Differential equation based methods [6–8] have the advantage of a simpler formulation since they directly discretize the PDE. As a result, they lend themselves easily to theoretical analysis viz-a-viz existence of solutions, stability and convergence and there is a plethora of work that has been devoted to these studies [7,9–17]. Differential equation based techniques also yield matrix systems that have $O(N_S)$ entries, where N_S is the number of degrees of freedom. The direct discretization of the PDE also implies, however, that boundary conditions need to be explicitly enforced in the numerical scheme. Extensive work has been done on the incorporation of boundary conditions including the radiation boundary condition [18] which has seen considerable mathematical work. Differential equation methods have seen an explosion in application specific research with the development of hierarchical basis functions [8, 19], discontinuous Galerkin methods [20] and vector generalized finite elements [21], and domain decomposition methods [22] among others.

1.2 Integral Equation Methods for Electromagnetics

Integral equation methods [23–30] offer more advantages than differential equation based methods for scattering problems primarily because the number of unknowns is reduced significantly, for surface scattering problems. This does come at the expense of a theoretically more involved formulation due to which these methods have eluded complete theoretical analysis for a very long time. While several recent efforts have been made to fully understand the theoretical nature of integral equations [31–37], several questions about the existence, uniqueness and convergence of solutions remain open. The second problem is the full matrix that needs to be solved as a result of the numerical discretization of the integral equation, which yields a matrix system of size $0(N_s^2)$; correspondingly leading to higher demands on computational complexity $O(N_s^3)$, and memory.

Recently however, the state of art of integral equation (IE) based methods has received a shot in the arm with the development of fast methods [38–40] which reduced the computational complexity and memory scaling from $\mathcal{O}(N_s^2)$ to $\mathcal{O}(N_s \log^{\alpha}(N_s))$, where $0 \le \alpha \le 2$. Steady advances in this technology (a woefully incomplete list being Refs. [38,39,41–47]) has made the analysis of radiation and scattering from electrically large structures possible; see [48] for a more comprehensive list of applications and recent advances. In a similar manner, the development of the plane wave time domain method (a time domain analogue of the fast multiple method) has enabled transient analysis of electrically large and complex geometries [49–58]. This method reduces the computational complexity from $\mathcal{O}(N_t N_s^2)$ to $\mathcal{O}(N_t N_s \log^{\alpha} N_s)$, where N_t is the number of temporal degrees of freedom.

While electromagnetic problems have been analysed using integral equations since 1897 when Poklington analysed wave propagation along wires, the most commonly used numerical technique for the "discretization" of integral equations is the method of moments (MoM), proposed for electromagnetics by Harrington [24]. This technique starts out by expanding the unknown quantity in a set of basis functions and testing the resulting integral equation using a space of testing functions. While it is possible to define "whole domain" basis functions for some canonical problems; most realistic problems are solved using a simplicial tessellation of the geometry. The basis functions are then defined local to each patch of this tessellation. It can be shown that the acuraccy of the integral equation scheme relies heavily on definition of the basis functions. As a result, there has been a significant amount of work that has gone into the design of appropriate basis functions. In the rest of this chapter, we will focus on the design of these basis functions as this is the main theme of the dissertation.

1.3 Basis Functions for Electromagnetic Integral Equations

Historically, the design of basis functions, and indeed the solution of the integral equation itself has been motivated by the design of the tessellation for the geometry. The first method utilized for the solution to scattering problems using integral equations was to model the surface with a wire mesh, called a wire-grid model. This method with its ease of implementation and ability to solve a rather large variety of scattering problems, remained popular in the community for almost two decades starting with [59]. However the method is inherently inaccurate in the model for the computation of near field quantities and input impedance. Furthermore, the method also suffered from ill conditioned matrices, numerical resonances [60] and other theoretical issues [61]. Surface patch modelling, developed as an alternative to wire-grid modelling was seen to preform better on all these grounds and therefore, much of the research gravitated towards developing basis functions for surface patch models.

The first set of surface patch models started with both planar [62] and non-planar quadrilaterals [63] for the magnetic field integral equations (MFIE). This was followed by planar rectangular patches for the electric field equations by [64]. Sinusoidal basis functions were then extended to surface patches from their wire-grid equivalents for the electric field integral equation (EFIE) [65]. This was followed by what was probably the first attempt to model surfaces using triangular patches [66]. While the approach in [66] modeled square plates, the authors astutely pointed out the ability of triangular patches to model arbitrary surfaces and their work was also one of the first to model the entire integral equation using an equivalent of the Galerkin scheme in use today. Planar triangular patches along with the MFIE and phase variation into the definition of the basis function for the MFIE was first introduced by [67,68]. In what was the first work that directly implemented surface patch models for arbitrary surfaces, the authors used non planar triangular patches to model the MFIE [69]. The subsequent development of a special set of basis functions for triangles by Rao and Glisson for arbitrary triangulations, analogous to roof-top functions for rectangular patches [70] was a critical contribution to the research. The authors in [70] followed up this work with what is arguably the most influential paper in the method of moments research where they developed the Rao-Wilton-Glisson (RWG) functions to model vector surface currents on non-planar triangulations of arbitrary surfaces [71]. These basis functions also support an important property called divergence conformance. This means that the divergence of the basis functions do not have any discontinuities across internal patch boundaries. It must be mentioned that a curl conforming equivalent of these basis functions were also independently introduced by Nedelec [72] et al. and implemented by Bossavit et al. [11], Barton et al. [14] and others and the divergence conforming functions were also independently introduced by Raviart and Thomas [73].

1.4 Higher order basis functions

While we will revisit the RWG functions in great detail elsewhere in this thesis, suffice it to say that it has become the de-facto standard for the method of moment analysis of electromagnetic integral equations. Several higher orders and singular variants have been proposed in literature [74,75] and the RWG method has become the corner stone for all frequency and time domain integral equation analysis over the past three decades. However, while higher order basis functions have been in use for a few years, the ability to include arbitrary functions in the basis space or to switch from one basis function to another is still limited. This is a direct consequence of the historically close relationship between the basis function and the underlying tessellation. Both the original RWG and its higher order/singular variants have been designed to satisfy continuity properties across internal boundaries of the tessellation. It is widely accepted that any basis function designed to model continuous quantities, must satisfy some constraints on continuity across patches. As a result, the incorporation of different classes of functions in the basis space is only possible within a framework that ensures continuity [76–78].

The ability to include arbitrary functions may be critical when some information is known about the physics of the problem, and it is desirable to include this behavior in the definition of the basis functions. For example, [79–81] incorporate Meixner series based functions in the basis space to model singular currents near edges. However, if the marriage with the tessellation could be removed, it would be possible to mix arbitrary classes of basis functions within the same geometric region. Unfortunately, all existing methods are specific to the underlying tessellation. Indeed, inclusion of a completely arbitrary basis function space might not even be possible within the framework of current basis function definitions.

Along these lines, a question has recently been posed whether the explicit enforce-

ment of continuity should be required [82,83]. Indeed [82] makes arguments that, in two dimensions, the use of a moderately high order complete basis function set eliminates the need for explicit enforcement of continuity conditions. Likewise, it has been demonstrated in two dimensions, that the continuity constraints can be replaced by a partition of unity function to maintain the h and p convergence [84].

The problems of enlarging functions spaces has been addressed in the finite element community. Melenk et al. [76] developed the scalar GFEM as an umbrella framework for a class of mesh-based and mesh-less methods that allowed for the inclusion of a larger class of basis functions. He demonstrated that the global errors were bounded by the local errors in approximation. The scheme was extended to vector finite elements for electromagnetics by Lu et al. [77]. The GFEM uses a product of a partition of unity function and a higher order approximation function to define basis functions on overlapping domains. However, extension of this method to integral equations is not trivial and will form the central focus of this thesis. In GFEM, overlapping patches are defined by combining canonical patches. However, unlike in the GFEM framework, the patches for surface integral equations need to conform to an arbitrary scatterer surface and can not be expected to map on to canonical geometries. This, in turn, makes the definition of vector basis functions on these non-canonical surfaces challenging. The structure of these patches may lead to functions that are piece-wise differentiable (for piecewise continuous patches). Therefore, computation of matrix elements involves evaluating singular and hyper singular integrals that need to be carefully handled. Furthermore, one needs to define vector basis functions on these surfaces to represent currents. This poses additional challenges.

In this dissertation, we will describe the design and implementation of a new umbrella framework for the discretization of integral equations called the Generalized Method of Moments. We will show that within this framework it is possible to choose from a very wide variety of functions to form the basis space. While the choice of basis functions can be completely arbitrary, the thesis will describe in detail one particular scheme that utilizes a surface quasi-Helmholtz decomposition and provides a mechanism for the use of any available knowledge of the physics of the problem. The thesis will describe the theoretical framework required for the design of this scheme and develop error bounds for the approximation of the unknown quantities using the proposed basis functions. Following that, we will delve into the implementation of the GMM starting from commonly available triangular tessellations, carefully identifying and solving several key issues along the way.

The GMM will be applied to a plethora of examples, validated against analytical solutions and compared against the standard RWG discretizations. It will further be shown that the use of the proposed basis functions will result in a scheme that is well conditioned over a wide range of frequencies. We will also provide a host of examples showcasing the advantages of the GMM scheme, including its ability to incorporate multiple types and orders of basis functions and its ability to handle non conformal meshes. We will then extend the GMM to both the analysis of scattering from dielectric bodies using the PMCHWT and Müller operators and to the analysis of transient scattering from conducting objects. Several results will be presented in both cases that demonstrate the advantage of the proposed method over traditional RWG based discretization.

The remainder of this thesis will be organized as follows. Chapter 2 will lay out the mathematical preliminaries required for the rest of this thesis. We will start from the Maxwell's equations and derive an integral formulation for the solution of electromagnetic scattering from surfaces. We will specialize the derivation to conducting structures in preparation for Chapter 3 where we describe the method of moments technique for the discretization of integral equations and describe the Rao Wilton Glisson basis functions that are most commonly in use today. In Chapter 4 we will describe the GMM in detail. This chapter will first describe the theoretical founda-

tions of this work and then proceed to discuss its implementation details. It will also present a variety of results to validate the technique and demonstrate its advantages. The following chapter will discuss the extension of the GMM to the analysis of scattering from dielectric bodies. The formulation will be discussed followed by specifics of the implementation and results. Chapter 6 will describe the GMM applied to the analysis of transient scattering. This chapter will start with the definition of the time domain integral equations and proceed to describe the standard temporal discretization techniques. This will be followed by the application details of the GMM to time domain integral equations and a gamut of results describing the advantages of the new technique. Finally Chapter 7 will provide a summary and describe possibilities for future work.

Chapter 2

Mathematical Preliminaries

In this chapter, we will present the mathematical preliminaries from which the rest of this thesis will follow. The equations and derivations presented herein can be found in a number of references including [29, 85, 86].

2.1 Maxwell's Equations

To lay the foundation for the integral equations for electromagnetics, we start from the Maxwell's equations in their point form. Consider a linear, isotropic, homogeneous region in space having relative permittivity ε_r and relative permeability μ_r . Electromagnetic fields $\mathcal{E}(\mathbf{r},t)$, $\mathcal{H}(\mathbf{r},t)$ and corresponding flux densities $\mathcal{D}(\mathbf{r},t)$ and $\mathcal{B}(\mathbf{r},t)$ in this region satisfy Maxwell's equations:

$$\nabla \times \mathcal{E}(\mathbf{r}, t) = -\frac{\partial \mathcal{B}(\mathbf{r}, t)}{\partial t} - \mathcal{M}(\mathbf{r}, t)$$
 (2.1a)

$$\nabla \times \mathcal{H}(\mathbf{r}, t) = \frac{\partial \mathcal{D}(\mathbf{r}, t)}{\partial t} + \mathcal{J}(\mathbf{r}, t)$$
 (2.1b)

$$\nabla \cdot \mathcal{D}(\mathbf{r}, t) = \varrho(\mathbf{r}, t) \tag{2.1c}$$

$$\nabla \cdot \mathcal{B}(\mathbf{r}, t) = \varrho_m(\mathbf{r}, t), \tag{2.1d}$$

where $\mathcal{J}(\mathbf{r},t)$ and $\varrho(\mathbf{r},t)$ are the electric current and charge density and $\mathcal{M}(\mathbf{r},t)$ and $\varrho_m(\mathbf{r},t)$ are their (fictitious) magnetic equivalents. Further, the current and charge satisfy the continuity equations given by

$$\nabla \cdot \mathcal{J}(\mathbf{r}, t) + \frac{\partial \varrho(\mathbf{r}, t)}{\partial t} = 0$$
 (2.2a)

$$\nabla \cdot \mathcal{M}(\mathbf{r}, t) + \frac{\partial \varrho_m(\mathbf{r}, t)}{\partial t} = 0$$
 (2.2b)

In addition, the constitutive relations

$$\mathcal{D}(\mathbf{r},t) = \varepsilon_0 \varepsilon_r(\mathbf{r},t) *_t \mathcal{E}(\mathbf{r},t)$$
(2.3a)

and

$$\mathcal{B}(\mathbf{r},t) = \mu_0 \mu_r(\mathbf{r},t) *_t \mathcal{H}(\mathbf{r},t), \tag{2.3b}$$

where $*_t$ indicates a convolution in time defined as $a(t) *_t b(t) = \int_0^\infty d\tau \ a(t-\tau)b(\tau)$, relate the flux densities to the corresponding fields. The assumptions of linearity allow for the application of the principle of superposition and thereby, allows for the application of the Fourier transform. Equivalently, if we assume that all the time dependent quantities are time harmonic of the form $\mathcal{A}(\mathbf{r},t) \doteq \mathcal{R}e\left[\mathbf{A}(\mathbf{r})e^{j\omega t}\right]$, where ω is the frequency in radians per second (and \mathcal{A} represents any of the vectors above), we obtain the familiar time harmonic form of equations (2.1a)-(2.1d) given by

$$\nabla \times \mathbf{E}(\mathbf{r}) = -j\omega\mu_0\mu_r(\mathbf{r})\mathbf{H} - \mathbf{M}(\mathbf{r})$$
 (2.4a)

$$\nabla \times \mathbf{H}(\mathbf{r}) = j\omega \varepsilon_0 \varepsilon_r(\mathbf{r}) \mathbf{E}(\mathbf{r}) + \mathbf{J}(\mathbf{r})$$
(2.4b)

$$\varepsilon_0 \nabla \cdot \varepsilon_r(\mathbf{r}) \mathbf{E}(\mathbf{r}) = \rho(\mathbf{r})$$
 (2.4c)

$$\mu_0 \nabla \cdot \mu_r(\mathbf{r}) \mathbf{H}(\mathbf{r}) = \rho_m(\mathbf{r}),$$
 (2.4d)

and the equations of continuity transform to

$$\nabla \cdot \mathbf{J}(\mathbf{r}) + j\omega \rho(\mathbf{r}) = 0 \tag{2.5a}$$

and

$$\nabla \cdot \mathbf{M}(\mathbf{r}) + j\omega \rho_m(\mathbf{r}) = 0. \tag{2.5b}$$

For simplicity, we have used the same symbols for ε_r and μ_r in frequency and time domain. At the interface between two media 1 and 2 with material parameters $\mu_{1(2)}$ and $\varepsilon_{1(2)}$, the fields satisfy the boundary conditions given by

$$\hat{\mathbf{n}}(\mathbf{r}) \times (\mathbf{E}_1(\mathbf{r}) - \mathbf{E}_2(\mathbf{r})) = -\mathbf{M}_S \tag{2.6a}$$

$$\hat{\mathbf{n}}(\mathbf{r}) \times (\mathbf{H}_1(\mathbf{r}) - \mathbf{H}_2(\mathbf{r})) = \mathbf{J}_S \tag{2.6b}$$

$$\hat{\mathbf{n}}(\mathbf{r}) \cdot (\varepsilon_1(\mathbf{r})\mathbf{E}_1(\mathbf{r}) - \varepsilon_2(\mathbf{r})\mathbf{E}_2(\mathbf{r})) = -\rho_s \tag{2.6c}$$

and

$$\hat{\mathbf{n}}(\mathbf{r}) \cdot (\mu_1(\mathbf{r})\mathbf{H}_1(\mathbf{r}) - \mu_2(\mathbf{r})\mathbf{H}_2(\mathbf{r})) = -\rho_{m,s}, \tag{2.6d}$$

where $\hat{\mathbf{n}}$ is the normal to the material boundary from medium 2 to 1.

To derive the vector wave equations for electric field, we take a curl of (2.4a) and substitute from (2.4b) to obtain

$$\nabla \times \left\{ \frac{1}{\mu(\mathbf{r})} \nabla \times \mathbf{E}(\mathbf{r}) \right\} - \omega^2 \varepsilon(\mathbf{r}) \mathbf{E}(\mathbf{r}) = -j\omega \mathbf{J}(\mathbf{r}) - \nabla \times \left\{ \frac{1}{\mu(\mathbf{r})} \mathbf{M}(\mathbf{r}) \right\}$$
(2.7)

where $\mu(\mathbf{r}) \doteq \mu_0 \mu_r(\mathbf{r})$ and $\varepsilon(\mathbf{r}) \doteq \varepsilon_0 \varepsilon_r(\mathbf{r})$. A similar equation can be derived for the magnetic field:

$$\nabla \times \left\{ \frac{1}{\varepsilon(\mathbf{r})} \nabla \times \mathbf{H}(\mathbf{r}) \right\} - \omega^2 \mu(\mathbf{r}) \mathbf{H}(\mathbf{r}) = -j\omega \mathbf{M}(\mathbf{r}) + \nabla \times \left\{ \frac{1}{\varepsilon(\mathbf{r})} \mathbf{J}(\mathbf{r}) \right\}. \tag{2.8}$$

An important simplification is obtained upon assuming that the material is homogeneous, which results in

$$\nabla \times \nabla \times \mathbf{E}(\mathbf{r}) - k^2(\mathbf{r})\mathbf{E}(\mathbf{r}) = -j\omega\mu\mathbf{J}(\mathbf{r}) - \nabla \times \mathbf{M}(\mathbf{r})$$
 (2.9)

where $k \doteq \omega^2 \varepsilon \mu$, and

$$\nabla \times \nabla \times \mathbf{H}(\mathbf{r}) - k^2 \mathbf{H}(\mathbf{r}) = -j\omega \varepsilon \mathbf{M}(\mathbf{r}) + \nabla \times \mathbf{J}(\mathbf{r}). \tag{2.10}$$

2.2 Vector and Scalar Potentials

While it is possible to solve the above equations to obtain the fields for a given source distribution, it is often easier to proceed by defining a set of auxiliary potentials. To this end, first consider Maxwell's equations in a medium free of magnetic sources $(\rho_m(\mathbf{r}) = 0 \text{ and } \mathbf{M}(\mathbf{r}) = 0)$. Since $\nabla \cdot \mathbf{B}(\mathbf{r}) = 0$ under this assumption, we can define the magnetic vector potential, $\mathbf{A}(\mathbf{r})$ such that $\mathbf{B}(\mathbf{r}) = \nabla \times \mathbf{A}(\mathbf{r})$. Combining this with (2.4a), we obtain the following equations

$$\mathbf{B}(\mathbf{r}) = \nabla \times \mathbf{A}(\mathbf{r}) \tag{2.11}$$

$$\nabla \times (\mathbf{E}(\mathbf{r}) + j\omega \mathbf{A}(\mathbf{r})) = 0. \tag{2.12}$$

Equation (2.12) implies that $\mathbf{E}(\mathbf{r} + j\omega\mathbf{A}(\mathbf{r}))$ can be written as a gradient of a scalar Φ_e , called the electric scalar potential, as

$$\mathbf{E}(\mathbf{r}) + j\omega \mathbf{A}(\mathbf{r}) = -\nabla \Phi_{e}(\mathbf{r}). \tag{2.13}$$

To obtain a unique solution for the field from these potentials, we need an additional constraint. One such constraint is the Lorentz gague, given by

$$\nabla \cdot \mathbf{A} + j\omega\mu\varepsilon\Phi_e = 0. \tag{2.14}$$

Substituting the definition of \mathbf{A} into (2.4b) and assuming, again, a homogeneous medium, we obtain

$$\frac{1}{\mu}\nabla \times \nabla \times \mathbf{A}(\mathbf{r}) = j\omega\varepsilon[-j\omega\mathbf{A}(\mathbf{r}) - \nabla\Phi_e(\mathbf{r})] + \mathbf{J}(\mathbf{r})$$
 (2.15a)

$$= j\omega\varepsilon[-j\omega\mathbf{A}(\mathbf{r}) + \frac{1}{j\omega\mu\varepsilon}\nabla\nabla\cdot\mathbf{A}(\mathbf{r})] + \mathbf{J}(\mathbf{r}) \qquad (2.15b)$$

$$= \omega^2 \varepsilon A(\mathbf{r}) + \frac{1}{\mu} \nabla \nabla \cdot \mathbf{A}(\mathbf{r}) + \mathbf{J}(\mathbf{r})$$
 (2.15c)

leading to

$$\nabla^2 \mathbf{A}(\mathbf{r}) + k^2 \mathbf{A}(\mathbf{r}) = -\mu \mathbf{J}(\mathbf{r}). \tag{2.15d}$$

Substitution of the Lorentz gauge directly into (2.13) will result in an equation for Φ_e as

$$\nabla^2 \Phi_e(\mathbf{r}) + k^2 \Phi_e(\mathbf{r}) = -\frac{\rho(\mathbf{r})}{\varepsilon}.$$
 (2.16)

Either by inspection, or by completing a similar derivation for a medium free of electric sources (but containing magnetic sources) result in the definition of the electric vector potential $\mathbf{F}(\mathbf{r})$ and the magnetic scalar potential $\Phi_m(\mathbf{r})$ and the following related equations.

$$\mathbf{D}(\mathbf{r}) = -\nabla \times \mathbf{F}(\mathbf{r}) \tag{2.17}$$

$$\mathbf{H}(\mathbf{r}) = -j\omega\varepsilon\mathbf{F}(\mathbf{r}) - \nabla\Phi_m(\mathbf{r}) \tag{2.18}$$

$$\nabla^2 \mathbf{F}(\mathbf{r}) + k^2 \mathbf{F}(\mathbf{r}) = -\varepsilon \mathbf{M}(\mathbf{r})$$
 (2.19)

$$\nabla^2 \Phi_m(\mathbf{r}) + k^2 \Phi_m(\mathbf{r}) = -\frac{\rho_m(\mathbf{r})}{\mu}$$
 (2.20)

By superposition, in a medium having both magnetic and electric sources, the field equations in terms of the potentials can be written as

$$\mathbf{E}(\mathbf{r}) = -j\omega\mathbf{A}(\mathbf{r}) - \nabla\Phi_{e}(\mathbf{r}) - \frac{1}{\varepsilon}\nabla \times \mathbf{F}(\mathbf{r})$$
 (2.21)

$$\mathbf{H}(\mathbf{r}) = \frac{1}{\mu} \nabla \times \mathbf{A}(\mathbf{r}) - j\omega \mathbf{F}(\mathbf{r}) - \nabla \Phi_m(\mathbf{r})$$
 (2.22)

In Cartesian coordinates, the splitting of the vector Laplacian into its components motivates the analysis of (2.15d) and (2.16) (or equivalently, (2.19) and (2.20)) using scalar wave equations of the form

$$(\nabla^2 + k^2)\psi(\mathbf{r}) = f(\mathbf{r}), \tag{2.23}$$

where ψ denotes each component of the field and f denotes the corresponding source component. As with any partial differential equation, obtaining a unique solution to the above equation requires boundary conditions.

For scattering problems, which will form the bulk of the problems that we deal with in this thesis, we solve the above equation subject to the Sommerfield radiation boundary condition. For scalar waves this condition is given by

$$\lim_{|r| \to \infty} |\mathbf{r}| \left(\frac{\partial \psi(\mathbf{r})}{\partial |\mathbf{r}|} + jk\psi(\mathbf{r}) \right) = 0.$$
 (2.24)

In order to solve the above partial differential equation, one can define a Green's function for the differential equation and its boundary condition, given by

$$g(|\mathbf{r}|) = \frac{e^{-jk|\mathbf{r}|}}{4\pi|\mathbf{r}|}.$$
 (2.25)

The solution to (2.23) is given by

$$\psi(\mathbf{r}) = g(|\mathbf{r}|) *_{S} f(|\mathbf{r}'|), \tag{2.26}$$

where $*_s$ denotes the spatial convolution defined by $a(\mathbf{r})*_s b(\mathbf{r}) \doteq \int_{\Omega} d\mathbf{r'} \ a(\mathbf{r} - \mathbf{r'})b(\mathbf{r'})$. Using the Green's function, the electric and magnetic potentials can be now written as

$$\mathbf{A}(\mathbf{r}) = \mu g(|\mathbf{r}|) *_{S} \mathbf{J}(\mathbf{r}), \tag{2.27}$$

$$\mathbf{F}(\mathbf{r}) = \varepsilon g(|\mathbf{r}|) *_{S} \mathbf{M}(\mathbf{r}), \tag{2.28}$$

$$\Phi_e(\mathbf{r}) = \frac{1}{\varepsilon} g(|\mathbf{r}|) *_S \rho_e, \tag{2.29}$$

$$\Phi_m(\mathbf{r}) = \frac{1}{\mu} g(|\mathbf{r}|) *_S \rho_m. \tag{2.30}$$

2.3 Integral Equation Representation of Solutions

The above preamble sets the stage for the derivation of the electric and magnetic field integral equations for the fields. We follow the derivation of [29], which in turn is derived from [87] and [88] but extended to non-smooth surfaces. We start with the vector Green's identity for any two vector functions $\mathbf{P}(\mathbf{r})$ and $\mathbf{Q}(\mathbf{r})$ with continuous first and second derivatives.

$$\int_{V} d\mathbf{r} \left(\mathbf{Q}(\mathbf{r}) \cdot \nabla \times \nabla \times \mathbf{P}(\mathbf{r}) - \mathbf{P}(\mathbf{r}) \cdot \nabla \times \nabla \times \mathbf{Q}(\mathbf{r}) \right)
= \int_{\partial V} d\mathbf{r} \ \hat{\mathbf{n}}(\mathbf{r}) \cdot \left(\mathbf{P}(\mathbf{r}) \times \nabla \times \mathbf{Q}(\mathbf{r}) - \mathbf{Q}(\mathbf{r}) \times \nabla \times \mathbf{P}(\mathbf{r}) \right).$$
(2.31)

Assume that the volume V is represented by D^+ and its inner boundary by Ω and the outer boundary by Ω_0 . Let the volume bounded by the inner boundary be D^- .

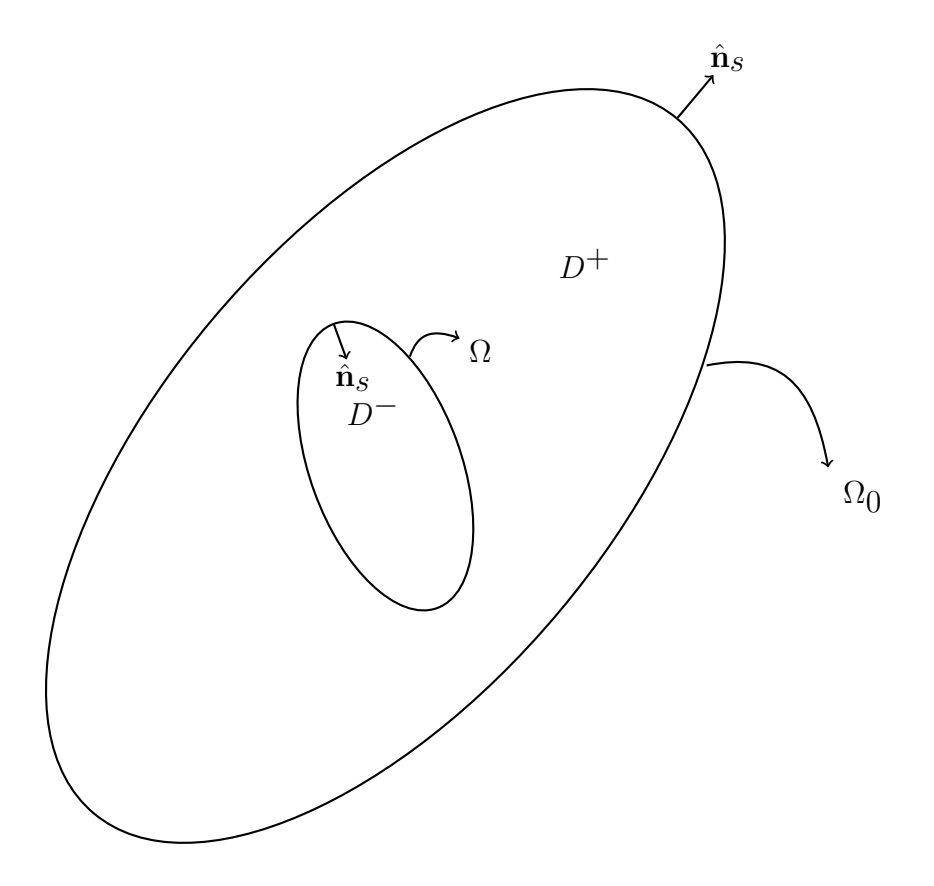


Figure 2.1: General representation for a domain $D^+ = V$ with inner and outer boundaries

Since $\mathbf{Q}(\mathbf{r})$ is arbitrary, we choose an arbitrary pilot vector $\hat{\mathbf{a}}$ and define

$$\mathbf{Q}(\mathbf{r}) \doteq \hat{\mathbf{a}}g(R) = \hat{\mathbf{a}}\frac{e^{-jkR}}{4\pi R},\tag{2.32}$$

where $R \doteq |\mathbf{r} - \mathbf{r'}|$ and \mathbf{r} and $\mathbf{r'}$ are the observation and source locations respectively. Further, choice of $\mathbf{P}(\mathbf{r}) \doteq \mathbf{E}(\mathbf{r})$ results, after some detailed vector manipulation [87] in

$$\int_{D^{+}} d\mathbf{r'} \left\{ j\omega\mu \mathbf{J}(\mathbf{r'})g(R) + \mathbf{M}(\mathbf{r'}) \times \nabla g(R) - \frac{\rho(\mathbf{r'})}{\varepsilon} \nabla g \right\} = (2.33)$$

$$\int_{\Omega + \Omega_{0}} d\mathbf{r'} \left\{ j\omega\mu \left[\hat{\mathbf{n}}(\mathbf{r'}) \times \mathbf{H}(\mathbf{r'}) \right] g(R) - (\hat{\mathbf{n}}(\mathbf{r'}) \times \mathbf{E}(\mathbf{r'}))g(R) - \left[\hat{\mathbf{n}}(\mathbf{r'}) \cdot \mathbf{E}(\mathbf{r'}) \right] \nabla g(R) \right\}$$
(2.34)

For simplicity we will assume at this point that the observation location \mathbf{r} does not lie on Ω_0 and that Ω is smooth. The case where these assumptions fail happen can be dealt with explicitly and the reader is referred to [29] for an excellent description. However, under this assumption, (2.34) reduces to

$$T\mathbf{E}(\mathbf{r}) = \int_{D^{+}} d\mathbf{r}' \qquad \left\{ j\omega\mu \mathbf{J}(\mathbf{r}')g(R) + \mathbf{M}(\mathbf{r}') \times \nabla' g(R) - \frac{\rho}{\varepsilon} \nabla' g(R) \right\}$$
$$- \int_{\Omega + \Omega_{0}} d\mathbf{r}' \qquad \left\{ j\omega\mu \left[\hat{\mathbf{n}}'(\mathbf{r}') \times \mathbf{H}(\mathbf{r}') \right] g(R) - \hat{\mathbf{n}}'(\mathbf{r}') \times \mathbf{E}(\mathbf{r}') \times \nabla' g(R) - \left[\hat{\mathbf{n}}'(\mathbf{r}') \cdot \mathbf{E}(\mathbf{r}') \right] \nabla' g(R) \right\}, \tag{2.35}$$

where primed coordinates relate to the quantities (and operations) defined on the source position $\mathbf{r'}$ and \mathbf{f} indicates that the integral is performed by excluding the principal value contribution from the singularity $\mathbf{r} = \mathbf{r'}$. T is a parameter such that $T \doteq 2$ if $\mathbf{r} \in \Omega$ and $T \doteq 1$ otherwise. By observation (and applying the duality of

Maxwell's equations) a similar equation for $\mathbf{H}(\mathbf{r})$ can be written as

$$T\mathbf{H}(\mathbf{r}) = \int_{D^{+}} d\mathbf{r'} \qquad \left\{ -j\omega\varepsilon\mathbf{M}(\mathbf{r'})g(R) + \mathbf{J}(\mathbf{r'}) \times \nabla'g(R) + \frac{\rho_{m}}{\mu}\nabla'g(R) \right\}$$

$$+ \int_{\Omega+\Omega_{0}} d\mathbf{r'} \qquad \left\{ j\omega\varepsilon[\hat{\mathbf{n}'}(\mathbf{r'}) \times \mathbf{E}(\mathbf{r'})]g(R) + \hat{\mathbf{n}'}(\mathbf{r'}) \times \mathbf{H}(\mathbf{r'}) \times \nabla'g(R) + \left[\hat{\mathbf{n}'}(\mathbf{r'}) \cdot \mathbf{H}(\mathbf{r'})\right] \nabla'g(R) \right\}. \tag{2.36}$$

Further, allowing Ω_0 to move out to ∞ , it can be seen that the integral over Ω_0 vanishes as a result of the radiation boundary conditions resulting in

$$T\mathbf{E}(\mathbf{r}) = \mathbf{E}^{i}(\mathbf{r}) + \int_{D^{+}} d\mathbf{r}' \quad \left\{ j\omega\mu \mathbf{J}(\mathbf{r}')g(R) + \mathbf{M}(\mathbf{r}') \times \nabla'g(R) - \frac{\rho}{\varepsilon} \nabla'g(R) \right\}$$
$$- \int_{\Omega} d\mathbf{r}' \quad \left\{ j\omega\mu [\hat{\mathbf{n}}'(\mathbf{r}') \times \mathbf{H}(\mathbf{r}')]g(R) - \hat{\mathbf{n}}'(\mathbf{r}') \times \mathbf{E}(\mathbf{r}') \times \nabla'g(R) - [\hat{\mathbf{n}}'(\mathbf{r}') \cdot \mathbf{E}(\mathbf{r}')]\nabla'g(R) \right\}, \tag{2.37a}$$

and

$$T\mathbf{H}(\mathbf{r}) = \mathbf{H}^{i}(\mathbf{r}) + \int_{D^{+}} d\mathbf{r'} \left\{ -j\omega\varepsilon\mathbf{M}(\mathbf{r'})g(R) + \mathbf{J}(\mathbf{r'}) \times \nabla'g(R) + \frac{\rho m}{\mu} \nabla'g(R) \right\}$$

$$+ \int_{\Omega} d\mathbf{r'} \left\{ j\omega\varepsilon[\hat{\mathbf{n'}}(\mathbf{r'}) \times \mathbf{E}(\mathbf{r'})]g(R) \right.$$

$$+ \hat{\mathbf{n'}}(\mathbf{r'}) \times \mathbf{H}(\mathbf{r'}) \times \nabla'g(R)$$

$$+ [\hat{\mathbf{n'}}(\mathbf{r'}) \cdot \mathbf{H}(\mathbf{r'})]\nabla'g(R) \right\},$$

$$(2.37b)$$

where we have denoted all the fields outside ∂V_0 by \mathbf{E}^i and \mathbf{H}^i and will call them the incident fields resulting from sources at or beyond infinity.

These equations are called, respectively, the electric and magnetic field integral equations (EFIE,MFIE). We will now specialize these equations to the first case that

will be studied in the next chapter. For the rest of the thesis beyond chapter 4, we will revisit this formulation and specialize it to other cases as necessary.

2.4 EFIE and MFIE for PEC structures

Consider a perfect electrically conducting body occupying a domain $D_- \subset \mathbb{R}^3$ in free space. Let Ω denote the bounding surface of D_- and let the outward pointing unit vector normal at any point \mathbf{r} on Ω be denoted by $\hat{\mathbf{n}}(\mathbf{r})$. Assume that a time harmonic field $\{\mathbf{E}^i(\mathbf{r}), \mathbf{H}^i(\mathbf{r})\}$ is incident on this body. This field induces currents on the surface Ω , that radiate scattered fields $\{\mathbf{E}^S(\mathbf{r}), \mathbf{H}^S(\mathbf{r})\}$. Thus, the total electric and magnetic fields in all of $D_+ = \mathbb{R}^3/D_-$, denoted by $\mathbf{E}(\mathbf{r})$ and $\mathbf{H}(\mathbf{r})$, can be decomposed into the incident and scattered fields by

$$\mathbf{E}(\mathbf{r}) : \mathbb{R}^3 \to \mathbb{C}^3 = \mathbf{E}^i(\mathbf{r}) + \mathbf{E}^s(\mathbf{r}) \tag{2.38a}$$

and

$$\mathbf{H}(\mathbf{r}): \mathbb{R}^3 \to \mathbb{C}^3 = \mathbf{H}^i(\mathbf{r}) + \mathbf{H}^s(\mathbf{r})$$
 (2.38b)

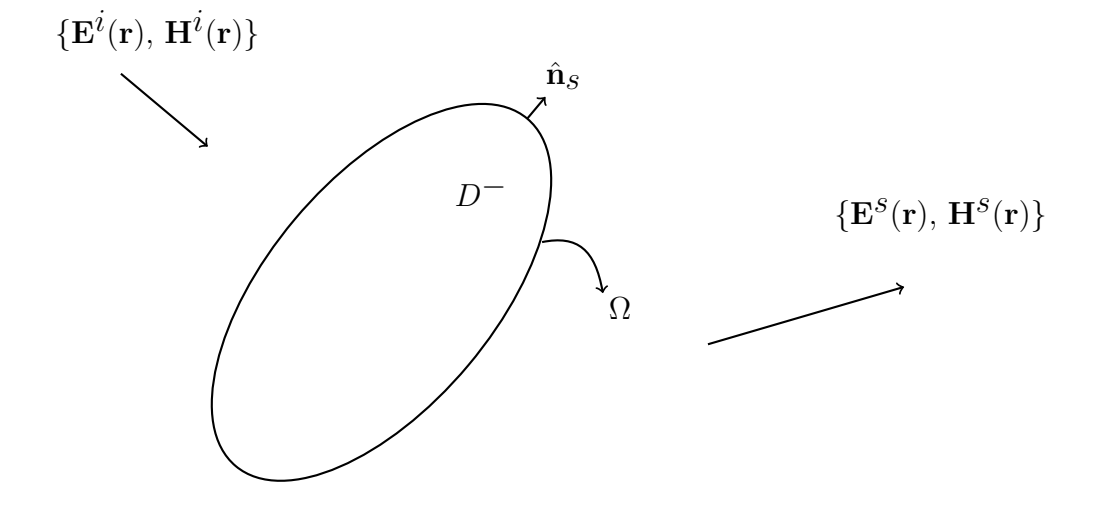


Figure 2.2: General description of a scattering problem

Since the domain D^- is a perfect electric conductor, further simplifications can be effected to the equations (2.37a) and (2.37b) above. We can specialize equations (2.6a) and (2.6d) and the equation of continuity to the case of $\mathbf{H}_- = \mathbf{E}_- = 0$ and $\mathbf{H}_+ = \mathbf{H}$, $\mathbf{E}_+ = \mathbf{E}$ where the subscript – and + denotes quantities in D_- and D_+ , respectively. We then, obtain for any \mathbf{r} on the surface Ω ,

$$\hat{\mathbf{n}}(\mathbf{r}) \times \mathbf{E}(\mathbf{r}) = 0, \tag{2.39a}$$

$$\hat{\mathbf{n}}(\mathbf{r}) \cdot \mathbf{H}(\mathbf{r}) = 0, \tag{2.39b}$$

$$\hat{\mathbf{n}}(\mathbf{r}) \times \mathbf{H}(\mathbf{r}) = \mathbf{J}(\mathbf{r}),\tag{2.39c}$$

$$\hat{\mathbf{n}}(\mathbf{r}) \cdot \mathbf{E}(\mathbf{r}) = \frac{j}{\omega \varepsilon} \nabla \cdot \mathbf{J}(\mathbf{r}),$$
 (2.39d)

where **J** is the surface current on Ω . Substituting into (2.37a) and (2.37b) and applying the boundary conditions on the tangential components of the fields, on the surface (Ω) to arrive at

$$\hat{\mathbf{n}}(\mathbf{r}) \times (\mathbf{E}^{i}(\mathbf{r}) + \mathbf{E}^{s}(\mathbf{r})) = 0 \bigg|_{\mathbf{r} \in \Omega}$$
 (2.40a)

and

$$\hat{\mathbf{n}}(\mathbf{r}) \times (\mathbf{H}^{i}(\mathbf{r}) + \mathbf{H}^{s}(\mathbf{r})) = 0 \bigg|_{\mathbf{r} \in \Omega},$$
 (2.40b)

gives us

$$\hat{\mathbf{n}}(\mathbf{r}) \times \mathbf{E}^{i}(\mathbf{r}) = \hat{\mathbf{n}}(\mathbf{r}) \times \int_{\Omega} d\mathbf{r}' \left(j\omega\mu \mathbf{J}(\mathbf{r}')g(R) + \left[\frac{j}{\omega\varepsilon} \nabla' \cdot \mathbf{J}(\mathbf{r}') \right] \nabla' g(R) \right), \quad (2.41a)$$

and

$$\mathbf{J}(\mathbf{r}) = T\hat{\mathbf{n}}(\mathbf{r}) \times \mathbf{H}^{i}(\mathbf{r}) + T \int_{\Omega} d\mathbf{r'} \ \mathbf{J}(\mathbf{r'}) \times \nabla' g(R). \tag{2.41b}$$

Further simplification using vector identities and the observations that $\nabla' g(R) =$

 $-\nabla g(R)$ and $\hat{\mathbf{n}} \cdot \mathbf{J} = 0$, along with setting T = 2 (since $\mathbf{r} \in \Omega$) will lead to

$$\hat{\mathbf{n}}(\mathbf{r}) \times \mathbf{E}^{i}(\mathbf{r})) = \hat{\mathbf{n}}(\mathbf{r}) \times \int_{\Omega} d\mathbf{r'} \left(j\omega\mu g(R) \mathbf{J}(\mathbf{r'}) + \frac{j}{\omega\varepsilon} \nabla \nabla g(R) \cdot \mathbf{J}(\mathbf{r'}) \right), \quad (2.42a)$$

and

$$\hat{\mathbf{n}}(\mathbf{r}) \times \mathbf{H}^{i}(\mathbf{r}) = \frac{\mathbf{J}(\mathbf{r})}{2} - \hat{\mathbf{n}}(\mathbf{r}) \times \int_{\Omega} d\mathbf{r'} \, \mathbf{J}(\mathbf{r'}) \times \nabla g(R).$$
 (2.42b)

which are the surface EFIE and MFIE for PEC bodies.

Chapter 3

Numerical Solution of Integral

Equations

The integral equations that were developed in chapter 2 are the so-called "surface" integral equations since the field quantities in all space are expressed in terms of their values (or the values of some equivalent quantities) on the surface of the scatterer. These integral equations cannot be analytically solved except for canonical scatterer geometries. This motivates the development of numerical solution techniques to these equations.

3.1 Method of moments solution for integral equations

The method of moments (MoM), developed for electromagnetic problems in the seminal work by Harrington [24] proposes an elegant technique for the solutions to integral equations. Consider an equation of the form

$$\mathbf{E}(\mathbf{r}) = \mathcal{L} \circ \{\mathbf{J}(\mathbf{r})\},\tag{3.1}$$

on a domain Ω , where \mathcal{L} represents either of the integral equations in (2.42a) or (2.42b). The MoM solution to this equation is sought in two steps. The first is to obtain a finite dimension approximation to the unknown $\mathbf{J}(\mathbf{r})$ using a set of basis functions $\mathbf{j}_i(\mathbf{r})$, namely

$$\mathbf{J}(\mathbf{r}) \approx \mathbf{J}_{N}(\mathbf{r}) \doteq \sum_{i=1}^{N} a_{i} \mathbf{j}_{i}(\mathbf{r}). \tag{3.2}$$

Using this, and recognizing the linearity of the integral operator, (3.1) can now be re-written as

$$\mathbf{E}(\mathbf{r}) = \sum_{i=1}^{N} a_i \mathcal{L} \circ \{ \mathbf{j}_i(\mathbf{r}) \}. \tag{3.3}$$

To complete the process of discretization of this equation, the equation is enforced using a set of testing functions $\{\mathbf{t}_j(\mathbf{r})\}_{j=1}^N$ to obtain

$$\int_{\Omega} d\mathbf{r} \ \mathbf{E}(\mathbf{r}) \mathbf{t}_{j}(\mathbf{r}) = \int_{\Omega} d\mathbf{r} \ \mathbf{t}_{j}(\mathbf{r}) \sum_{i} a_{i} \mathcal{L} \circ \{ \mathbf{j}_{i}(\mathbf{r}) \}. \tag{3.4}$$

This procedure transforms the integral equation into an equivalent matrix equation of the form

$$\underline{e} = \underline{\underline{Z}} \ \underline{a} \tag{3.5a}$$

where the elements of the RHS vector \underline{e} and "impedance matrix" $\underline{\underline{Z}}$ are given by

$$\underline{\underline{e}}_{j} = \int_{\Omega} d\mathbf{r} \ \mathbf{E}(\mathbf{r}) \mathbf{t}_{j}(\mathbf{r})$$

$$\underline{\underline{Z}}_{j,i} = \int_{\Omega} d\mathbf{r} \ \mathbf{t}_{j}(\mathbf{r}) \mathcal{L} \circ \{ \mathbf{j}_{i}(\mathbf{r}) \}$$
(3.5b)

and $\underline{a} = \{a_1, a_2, \dots\}$ is the vector of basis function coefficients. Significant work has gone into the proof of the validity of the method of moments, especially in the special case where the function spaces that $\{\mathbf{j}_i\}$ and $\{\mathbf{t}_j\}$ are identical (referred to as the

Ritz-Galerkin procedure) [12, 13]. While the issue of the choice of functions spaces for $\{\mathbf{j}_i\}$ and $\{\mathbf{t}_j\}$ are important, and indeed critical; we will defer that discussion to a later stage. At this point, we will assume that Ω is smooth enough and therefore, that $\{\mathbf{j}_i\}$ and $\{\mathbf{t}_j\}$ can be picked from the standard L^2 spaces.

3.2 Approximation errors

The method of moments procedure described above introduces errors in the solution of the integral equation. The primary source of error is the approximation of the function. This approximation error, ε_a is defined as follows.

Definition 1.

$$\varepsilon_a \doteq \mathbf{J} - \mathbf{J}_N = \mathbf{J} - \sum_{i=1}^N a_i \mathbf{j}_i(\mathbf{r})$$
(3.6)

Theorem 3.2.1. For any linear and bounded integral operator \mathcal{L} , \exists a constant C such that

$$\left| \int_{\Omega} d\mathbf{r} \ \mathbf{t}_{j}(\mathbf{r}) \mathcal{L} \circ \{ \mathbf{J}_{N}(\mathbf{r}) \} - \int_{\Omega} d\mathbf{r} \ \mathbf{t}_{j}(\mathbf{r}) \mathcal{L} \circ \{ \mathbf{J}(\mathbf{r}) \} \right| \le C \varepsilon_{a}$$
 (3.7)

Proof. By linearity of the integral operator, we have

$$\left| \int_{\Omega} d\mathbf{r} \ \mathbf{t}_{j}(\mathbf{r}) \mathcal{L} \circ \{ \mathbf{J}_{N}(\mathbf{r}) \} - \int_{\Omega} d\mathbf{r} \ \mathbf{t}_{j}(\mathbf{r}) \mathcal{L} \circ \{ \mathbf{J}(\mathbf{r}) \} \right| = \left| \int_{\Omega} d\mathbf{r} \ \mathbf{t}_{j}(\mathbf{r}) \mathcal{L} \circ \{ \mathbf{J}_{N}(\mathbf{r}) - \mathbf{J}(\mathbf{r}) \} \right|$$
(3.8)

Using Cauchy Schwartz inequality we have:

$$\left| \int_{\Omega} d\mathbf{r} \ \mathbf{t}_{j}(\mathbf{r}) \mathcal{L} \circ \{ \mathbf{J}_{N}(\mathbf{r}) - \mathbf{J}(\mathbf{r}) \} \right| = \| \mathbf{t}_{j}(\mathbf{r}) \|_{2} \| \mathcal{L} \circ \{ \mathbf{J}_{N}(\mathbf{r}) - \mathbf{J}(\mathbf{r}) \} \|_{2}.$$
(3.9a)

Since $\mathbf{t}_{j}(\mathbf{r}) \in L^{2}(\Omega)$, we have

$$\|\mathbf{t}_{j}(\mathbf{r})\|_{2} \le C_{2},\tag{3.9b}$$

and finally by the boundedness of the integral operator, we have

$$\|\mathcal{L} \circ \{\mathbf{J}_{N}(\mathbf{r}) - \mathbf{J}(\mathbf{r})\}\|_{2} \le C_{1} \|\mathbf{J}_{N}(\mathbf{r}) - \mathbf{J}(\mathbf{r})\|_{2}$$
(3.9c)

Combining the two results, we have,

$$\left| \int_{\Omega} d\mathbf{r} \ \mathbf{t}_{j}(\mathbf{r}) \mathcal{L} \circ \{ \mathbf{J}_{N}(\mathbf{r}) - \mathbf{J}(\mathbf{r}) \} \right| \leq C \| \left(\mathbf{J}_{N}(\mathbf{r}) - \mathbf{J}(\mathbf{r}) \right) \|_{2} = C \varepsilon_{a}.$$
 (3.9d)

The above result motivates the need for the accurate representation of the currents in terms of the basis functions. In the MoM community, there have been a wide variety of basis functions that were proposed for the solution of integral equations [59, 62, 63, 66, 69–71, 74]. While global basis functions can provide excellent approximation qualities on canonical geometries; for most practical problems, the best that can be hoped for, is a good local approximation to the currents. To this end, all basis function schemes typically start out by subdividing the geometry using a simplicial tessellation.

The ease and generality of triangular tessellations led to a basis function scheme called the Rao-Wilton-Glisson (RWG) basis functions [71] that have become the defacto standard for the MoM solution to integral equations in electromagnetics. The number of applications that use these functions today are innumerable. These functions have since been extended to the analysis of dielectric objects [89], layered media [90,91], transient scattering [92] and many other applications. Though the initial work was specific to first order basis functions, since then both higher order [74] and singular [81] variants that have been developed.

The RWG basis functions are designed on each interior edge of the underlying mesh. Fig. 3.1 shows two triangles sharing a common edge. On this edge, a basis

function is defined such that it vanishes everywhere on the surface except within the two triangles attached to the edge. Points inside each triangle is designated by a position vector ρ^{\pm} associated with the free vertex T_n^{\pm} . The vector basis function on these triangles can be defined as

$$\mathbf{f_n}(\mathbf{r}) = \begin{cases} \frac{l_n}{2A_n^+} \boldsymbol{\rho}_n^+ & \mathbf{r} \in T_n^+ \\ \frac{l_n}{2A_n^-} \boldsymbol{\rho}_n^- & \mathbf{r} \in T_n^- \\ \mathbf{0} & \text{otherwise} \end{cases}$$
(3.10)

where l_n is the length of the edge and A_n^{\pm} is the area of the triangle T_n^{\pm} . The basis function f_n satisfies the following useful properties.

- 1. The normal component of the basis function vanishes on all boundaries except the common boundary
- 2. The normal component of the basis function on the common edge is continuous and, for each interior basis function, cancels the corresponding contribution from the second triangle supported by the edge.
- 3. The surface divergence of the basis function is given by

$$\nabla \cdot_{s} \cdot \mathbf{f_{n}}(\mathbf{r}) = \begin{cases} \frac{l_{n}}{2A_{n}^{+}} & \mathbf{r} \in T_{n}^{+} \\ -\frac{l_{n}}{2A_{n}^{-}} & \mathbf{r} \in T_{n}^{-} \\ 0 & otherwise \end{cases}$$
(3.11)

The RWG basis functions have become the cornerstone for the method of moment analysis over the past three decades. However, their intimate relationship with the underlying tessellation, while providing some unique advantages, also has some im-

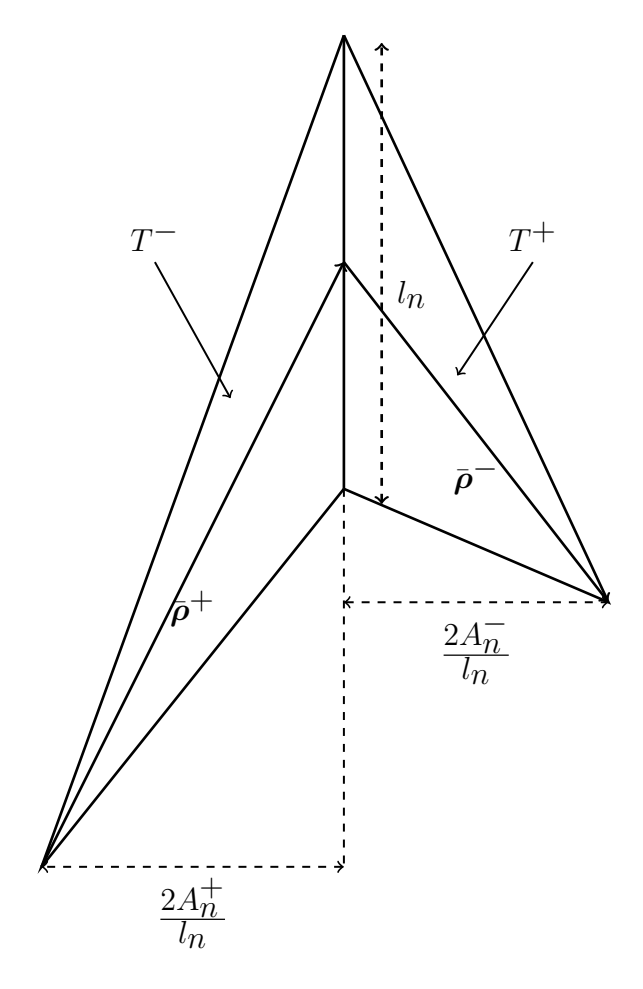


Figure 3.1: A schematic showing the definition of the RWG basis functions on an edge shared by two triangles $\frac{1}{2}$

portant drawbacks, the amelioration of which will be the central focus of this thesis.

Chapter 4

The Generalized Method of

Moments

The standard RWG-MoM scheme as described in chapter 3 utilizes a set of basis functions defined on a tessellation of the geometry. The RWG functions, as described in [71] were designed for a triangular tessellation of the geometry and the function spaces offer several advantages that are very useful in their implementation; (i) they are divergence conforming, (ii) the normal component vanishes on the interior edges of the geometry and (iii) the normal component is continuous across the edge. These basis functions have become the cornerstone of most MoM methods for electromagnetic integral equations. However, notwithstanding the significant advantages of both triangular tessellations themselves and RWG functions, the intimate relationship between the basis function and tessellation comes with some significant disadvantages.

The chief problem with having a basis function specification closely tied to the discretization of the geometry is that it severely limits the size of the function space from which basis functions can be chosen. It is worth mention that more than two decades after the introduction of the RWG functions there are very few higher order variants in active use today [19]. In fact all higher order and singular variations of

the RWG [74,81] are constructed by multiplying suitably chosen polynomials with first order RWG functions. This is a direct consequence of the construction of the RWG functions and implies that the close relationship between tessellation and basis functions is carried over to higher orders as well. Not only is the inclusion of arbitrary functions in the basis space is almost completely precluded by the construction of a basis function so tailored to the tessellation; even the use of mixed orders of basis functions requires careful consideration to maintain order continuity across interior boundaries [81]. This is especially critical in situations where some knowledge is available about the local behavior of the current.

Consider for illustration purposes, scattering from a PEC cube. Fig. 4.1 shows the distribution of currents when illuminated by an electric field, polarized along \hat{x} and incident along $-\hat{z}$. What is clear from the figure is that the currents are smooth on each face of the cube and the variations are limited to the edges. This would suggest the use of lower order basis functions or larger size patches on the faces of the cube which would serve to both reduce computational complexity and increase accuracy. However, this procedure of mixing basis functions is extremely non-trivial in the case of RWG basis functions.

While the simple case of a cube serves for illustration, this need for mixing basis functions becomes magnified in the case of realistic, multi-scale, problems. In existing basis function frameworks for MoM, it is difficult to mix different orders and impossible to mix different types of functions. Both these features deal with enlarging the possible functions that can be used for approximating the currents; a feature that would be beneficial in reducing the computational cost and increasing accuracy. For instance, in a geometrically complex object that is electrically large, the current behaves differently in different regions. Near regions of geometric complexity, it may be better to use either high density meshes with low order polynomials or vice-versa in areas of low geometric complexity. Near an edge singularity, one needs to capture the

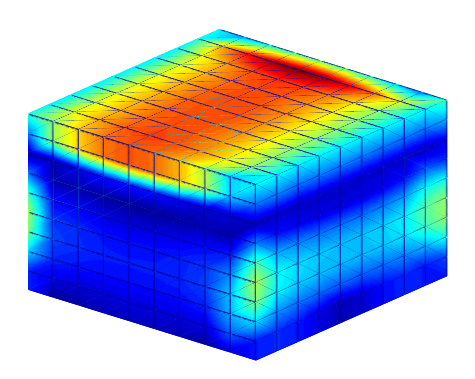


Figure 4.1: Currents on a PEC cube showing the singular nature of the currents near the edges and the smooth currents towards the center. For interpretation of the references to color in this and all other figures, the reader is referred to the electronic version of this dissertation.

singular behavior of the fields. In smooth regions, the phase of the current may be better captured using plane-wave type functions. The ability to mix approximation spaces become important when it is necessary to capture fields with high fidelity.

Next, given the complexity of creating a tessellation for complex objects, this task is typically partitioned to multiple sub-domains. More often than not, this results in meshes that are non-conformal. The ability to include these class of meshes with minimal effort is valuable to the accurate analysis of scattering from such geometries and is another feature missing in the state-of-art of the basis functions today.

Finally, in many realistic geometries, often the smallest geometrical feature dictates the tessellation and thereby the basis function space that is used to discretize the equation. This in turn leads to the "low-frequency problem" where the resulting matrix equation is very badly conditioned. There have been several attempts to solve this problem in literature where either special basis functions, called loop and star functions, are constructed specifically for low frequency problems using linear combinations of RWG functions [93, 94], or a different, well conditioned, integral equation is derived using mathematical properties of the Calderon operator [31, 95]. However

both the above approaches are very involved. The former approach of designing loop and star functions require scaling the basis functions depending on the frequency and will not work for truly multi-scale problems, where a large range of discretization scales (ranging from $10^{-5}\lambda$ to $10^{-1}\lambda$) are involved. Further the loop-star scheme cannot be used for multiply connected domains [96]. The latter approach is applicable to multi-scale problems but involve the careful construction of intermediary function spaces to handle the Calderón projector [97].

These shortcomings of the traditional RWG based discretization technique is the chief motivation for the development of the Generalized Method of Moments. In the remainder of this chapter, we will describe a mechanism for the construction of an "umbrella" framework that allows for the inclusion of a wide variety of basis functions. This framework will allow us to decouple the discretization of the geometry from the definition of the basis function. Starting from this decoupling we will describe a scheme that allows the easy mixing of various classes of functions in the basis space. The scheme described herein will allow for the trivial transition from one order of basis function to another. We will further describe a choice of basis functions that alleviates the ill-conditioning problem at low frequencies.

In order to remove the usually close knit relationship between the basis functions and the tessellation of the geometry, the GMM methodology follows a sequence of steps in the design of basis functions for the solution of (2.42a) and (2.42b). In the rest of this chapter, we will discuss each of these steps in detail.

4.1 Partition of Unity functions and Overlapping Patches

The GMM procedure starts by replacing the regular tessellation of the geometry with a set of overlapping patches as shown in Fig. 4.2. These patches provide for a

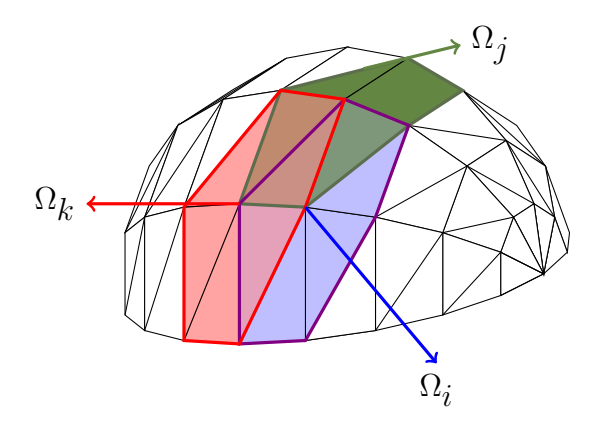


Figure 4.2: Construction of GMM patches (Ω_i) shown as shaded region.

mechanism of modelling the surface of the geometry but at the same time, via the nature of their overlap, allow for the mixing of different types of functions.

Definition 2. Open Cover Let $\Omega \in \mathbb{R}^3$ be an open set. Define an open cover of the domain Ω , $\{\Omega_i\}$ such that $\bigcup_i \Omega_i = \Omega$ that satisfies a point-wise overlap condition

$$\exists M \in \mathbb{N} \ni \forall \mathbf{r} \in \Omega \ card \{i | \mathbf{r} \in \Omega_i\} \leq M$$

Once these patches are defined, we require a scheme to provide for the smooth transition from one basis function to the next. This is effected through the use of a partition of unity function. Mathematically, we provide the following definition.

Definition 3. Partition of Unity

Let $\{\psi_i\}$ be a Lipschitz partition of unity subordinate to the cover $\{\Omega_i\}$ satisfying the following conditions:

- (i) $supp(\psi_i) \subset \Omega_i$ for all i;
- (ii) $\sum_{i} \psi_{i} \equiv 1$ on Ω ;
- (iii) $||\psi_i||_{L^{\infty}(\mathbb{R}^3)} \leq C_{\infty}$; and

$$(iv) ||\nabla \psi_i||_{L^{\infty}(\mathbb{R}^3)} \le C_d = \frac{C_{\nabla}}{diam(\Omega_i)}.$$

Here C_{∞} and C_{∇} are two constants. Then $\{\psi_i\}$ is called an $(M, C_{\infty}, C_{\nabla})$ partition of unity subordinate to $\{\Omega_i\}$. The partition of unity is said to be of degree k if $\psi_i \in \mathcal{C}^k(\mathbb{R}^d)$. The covering sets Ω_i are called patches and they take the place of the tessellation typically used in standard MoM.

Thus in the GMM framework, the standard tessellation is replaced by (i) a set of overlapping patches that cover the domain Ω and (ii) a partition of unity subordinate to this cover. Once this is achieved, we can define basis functions on these partitions of unity and corresponding Galerkin testing yields a linear system of equations.

This concept of overlapping domains and corresponding PU functions is shown in Fig. 4.3a. Generalization to higher dimensions can be effected using tensor products as shown in Fig. 4.3b. Higher order extensions of these functions can be trivially defined [98]. Thus, by definition, the PU functions and overlapping domains ensures continuity across patch boundaries.

Once these patches and the partition of unity is defined, basis functions are defined on these patches as a product of the partition of unity and an approximation function in each patch. Due to the fact that the continuity is enforced using the partition of unity, the approximation function can be chosen completely arbitrarily.

4.2 Definition of Basis Functions

Vector basis functions in each patch Ω_i are defined as a product of the PU function $\psi_i(\mathbf{r})$ and an appropriate approximation function of order m, $\boldsymbol{\nu}_i^m(\mathbf{r})$. For a GMM discretization, the approximation \mathbf{J}_N to the current \mathbf{J} can then be written as

Definition 4. GMM Basis Functions and Approximation Spaces

$$\mathbf{J} \approx \mathbf{J}_N = \sum_{i=1}^N \mathbf{j}_i \doteq \sum_{i=1}^N \sum_m a_{i,m} \psi_i \boldsymbol{\nu}_i^m. \tag{4.1}$$

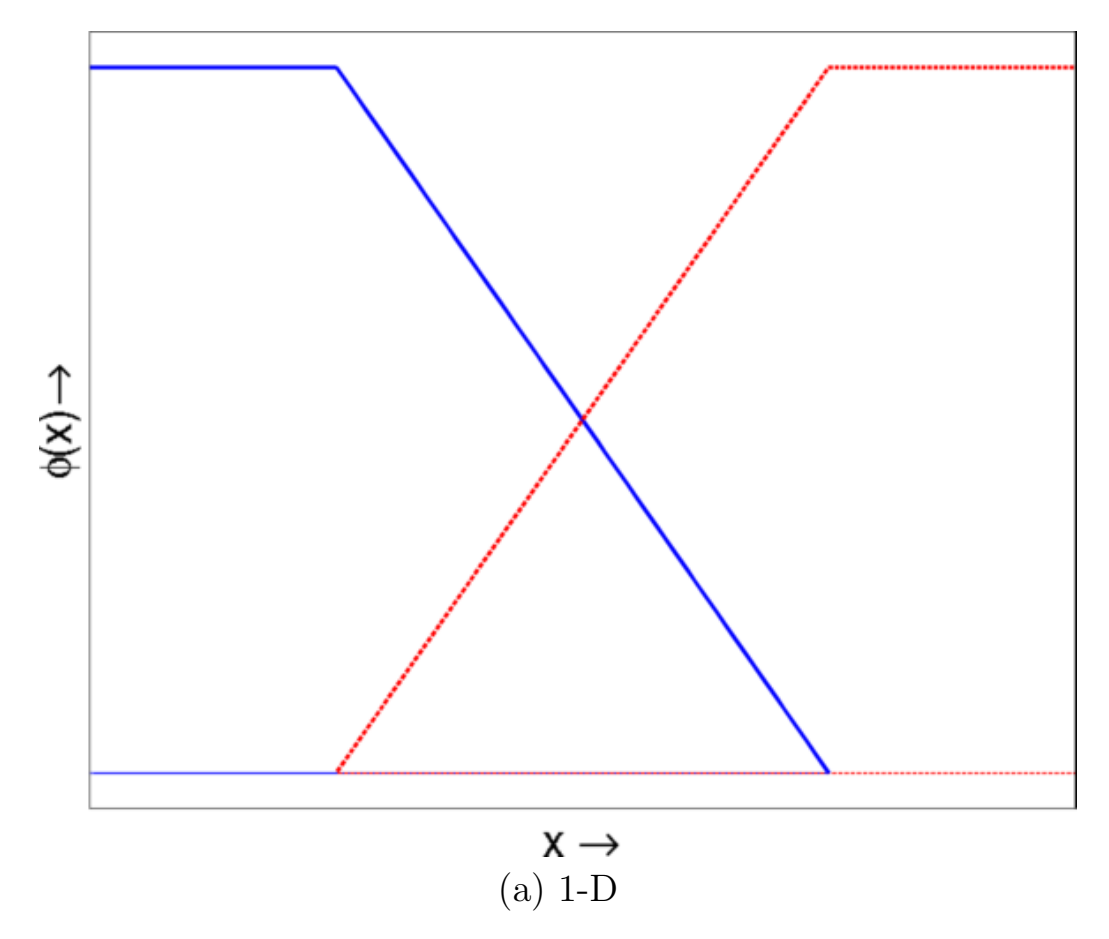


Figure 4.3: Examples of linear PU functions in (a) one and (b) two dimensions

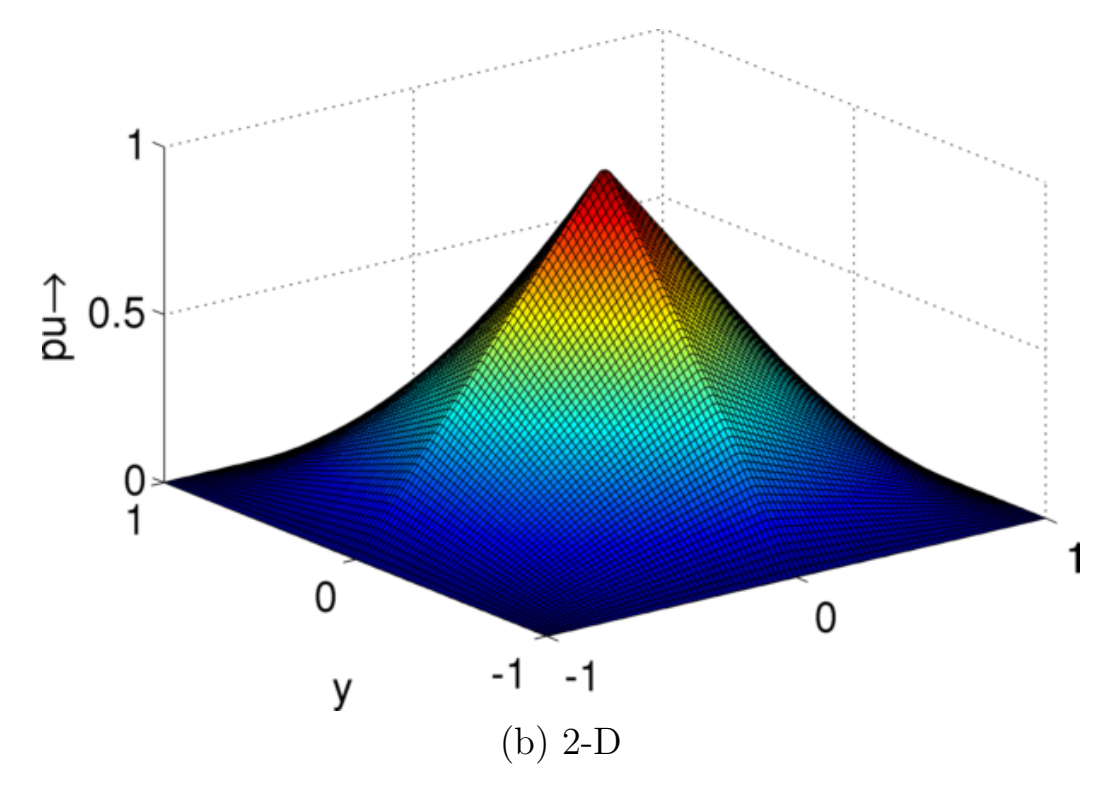


Figure 4.3 Continued: Examples of linear PU functions in (a) one and (b) two dimensions

Then the local approximating space in each patch Ω_i is given by

$$\mathbf{V}_{i} = span_{m} \left\{ \psi_{i} \boldsymbol{\nu}_{i}^{m} \right\}. \tag{4.2}$$

Note that within each patch Ω_i , there is no restriction on the set of functions $\boldsymbol{\nu}_i^m$. This set can be any mix of functions such as simple higher order complete polynomials, functions that best approximate the local physics, etc. The construction of a scalar basis function using a product of a two-dimensional linear PU function (shown in Fig. 4.3b) and a tensor product of higher order polynomials (in Fig. 4.4a) is shown in Fig. 4.4. For ease of presentation, the summation over m will be implicitly assumed and the corresponding indices will be dropped in the rest of this work.

With this definition of the basis function, we can now state an important theorem about the approximation errors introduced by the GMM scheme.

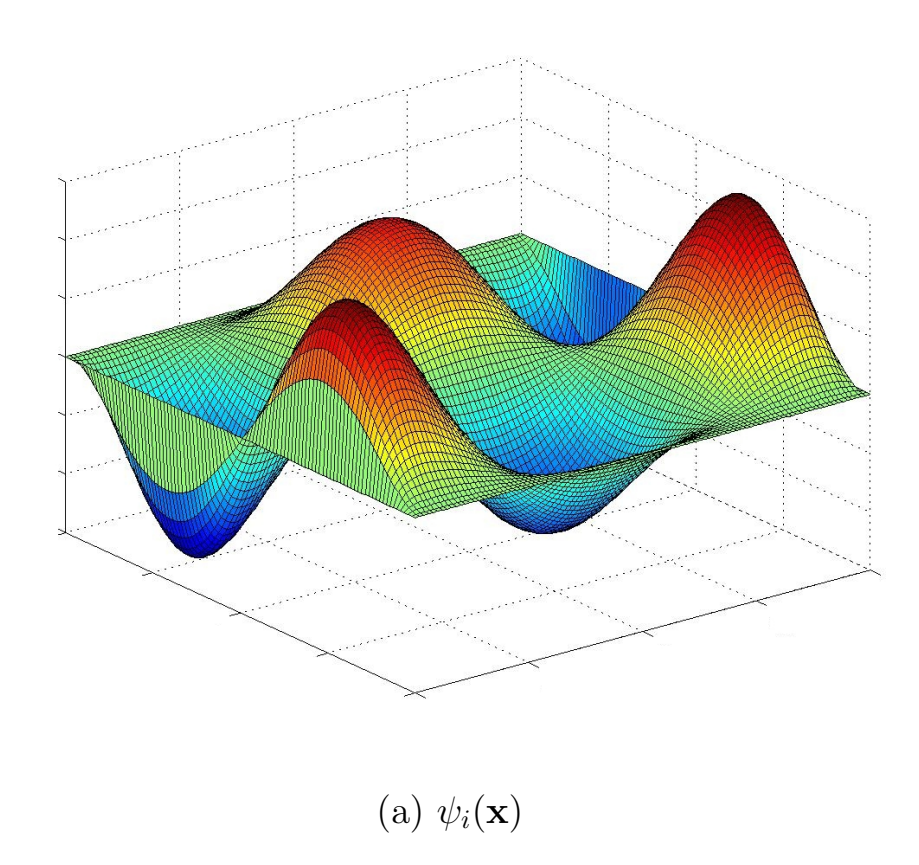
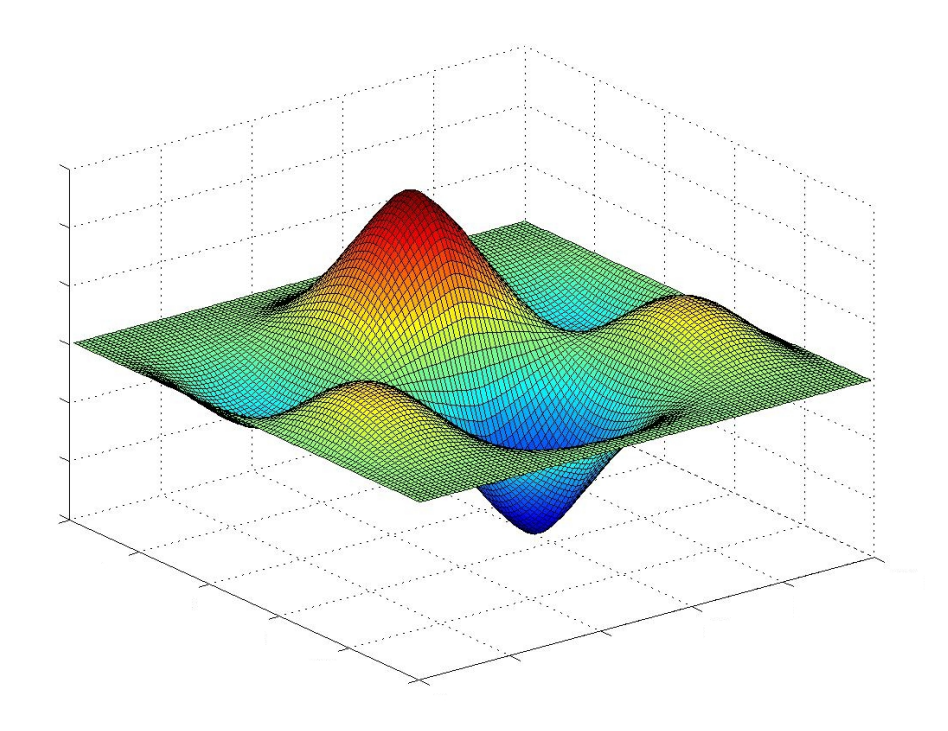


Figure 4.4: Construction of scalar GMM basis functions. (a) the GMM approximation function and (b) the product of the approximation function and the partition of unity function.



(b)
$$j_i(\mathbf{x}) = \phi_i(\mathbf{x})\psi_i(\mathbf{x})$$

Figure 4.4 Continued: Construction of scalar GMM basis functions. (a) the GMM approximation function and (b) the product of the approximation function and the partition of unity function.

Theorem 4.2.1. For the quantities, M, C_{∞} and C_{∇} as defined above, let $\mathbf{J} \in H^{1/2}(\Omega)$ [37] be a function to be approximated. Assume that on each patch $\Omega_i \cap \Omega$, \mathbf{J} can be approximated by a function $\mathbf{j}_i \in \mathbf{V}_i$ such that

$$\begin{aligned} \max_{i} \left\{ \left\| \mathbf{J} - \mathbf{j}_{i} \right\|_{L^{2}(\Omega_{i} \cap \Omega)} \right\} &\leq \varepsilon_{1} \\ \max_{i} \left\{ \left\| \nabla \cdot \left\{ \mathbf{J} - \mathbf{j}_{i} \right\} \right\|_{L^{2}(\Omega_{i} \cap \Omega)} \right\} &\leq \varepsilon_{2} \\ \max_{i} \left\{ \left\| \nabla \times \left\{ \mathbf{J} - \mathbf{j}_{i} \right\} \right\|_{L^{2}(\Omega_{i} \cap \Omega)} \right\} &\leq \varepsilon_{3} \end{aligned}$$

then the following holds for \mathbf{J}_N as defined in (4.1).

$$\|\mathbf{J} - \mathbf{J}_N\|_{L^2(\Omega)} \le \sqrt{M} C_{\infty} \varepsilon_1 \tag{4.3}$$

$$\|\nabla \cdot (\mathbf{J} - \mathbf{J}_N)\|_{L^2(\Omega)} \leq \sqrt{2M} \left((C_d \varepsilon_1)^2 + (C_\infty \varepsilon_2)^2 \right)^{1/2} \tag{4.4}$$

$$\|\nabla \times (\mathbf{J} - \mathbf{J}_N)\|_{L^2(\Omega)} \leq \sqrt{2M} \left((C_d \varepsilon_1)^2 + (C_\infty \varepsilon_3)^2 \right)^{1/2} \tag{4.5}$$

Proof. The proof is presented here for (4.4) and (4.5) and that for (4.3) follows trivially. Using the basis function definition in equation (4.1), it can be shown that

$$\nabla \times \{\mathbf{J} - \mathbf{J}_{N}\} = \nabla \times \{\mathbf{J} - \sum_{i} \psi_{i} \boldsymbol{\nu}_{i}\}$$

$$= \nabla \times \{\sum_{i} \psi_{i} (\mathbf{J} - \boldsymbol{\nu}_{i})\}$$

$$= \sum_{i} (\nabla \times \{\psi_{i} (\mathbf{J} - \boldsymbol{\nu}_{i})\})$$

$$= \sum_{i} (\nabla \psi_{i} \times \{\mathbf{J} - \boldsymbol{\nu}_{i}\} + \psi_{i} \nabla \times \{\mathbf{J} - \boldsymbol{\nu}_{i}\})$$
(4.6)

where the summation over the order m is assumed. To prove (4.4), note that the identity in equation (4.6) holds identically for the divergence operator as well. Given

equation (4.6) above, it can be easily verified that

$$\|\nabla \times \{\mathbf{J} - \mathbf{J}_{N}\}\|_{L^{2}(\Omega)}^{2} = \|\sum_{i} (\nabla \psi_{i} \times \{\mathbf{J} - \boldsymbol{\nu}_{i}\})\|_{L^{2}(\Omega)}^{2}$$

$$+ \psi_{i} \nabla \times \{\mathbf{J} - \boldsymbol{\nu}_{i}\})\|_{L^{2}(\Omega)}^{2}$$

$$\leq 2\|\sum_{i} (\nabla \psi_{i} \times \{\mathbf{J} - \boldsymbol{\nu}_{i}\})\|_{L^{2}(\Omega)}^{2}$$

$$+ 2\|\sum_{i} (\psi_{i} \nabla \times \{\mathbf{J} - \boldsymbol{\nu}_{i}\})\|_{L^{2}(\Omega)}^{2}$$

$$\leq 2\|\sum_{i} (\nabla \psi_{i} \times \{\mathbf{J} - \boldsymbol{\nu}_{i}\})\|_{L^{2}(\Omega_{i} \cap \Omega)}^{2}$$

$$+ 2\|\sum_{i} (\psi_{i} \nabla \times \{\mathbf{J} - \boldsymbol{\nu}_{i}\})\|_{L^{2}(\Omega_{i} \cap \Omega)}^{2}$$

$$\leq 2M^{2}C_{d}^{2}\|\{\mathbf{J} - \boldsymbol{\nu}_{i}\}\|_{L^{2}(\Omega_{i} \cap \Omega)}^{2}$$

$$+ 2M^{2}C_{\infty}^{2}\|\nabla \times \{\mathbf{J} - \boldsymbol{\nu}_{i}\}\|_{L^{2}(\Omega_{i} \cap \Omega)}^{2}$$

$$\leq 2M^{2}\left[(C_{d}\varepsilon_{1})^{2} + (C_{\infty}\varepsilon_{3})^{2}\right]$$

$$(4.7)$$

Theorem 4.2.1 essentially states that the total error in the approximation to the current is bounded above by the local error in the approximation. This result is powerful in the sense that it allows for a direct way to control the approximation error, by careful choice of approximation function.

As is evident from the above discussion, the GMM provides a framework to include different approximation functions without explicitly requiring continuity constraints. The order of the PU function determines the order of continuity between patches [99]. Thus, the global approximation inherits the smoothness of the PU function. An advantage offered by the GMM framework is the freedom of choice in the approximation function. By disassociating the definition of the approximation function from the underlying tessellation, GMM allows for the mixing of multiple types and orders of

functions. While the approximation function can be chosen practically arbitrarily, we describe a mechanism to choose functions that are suited to approximating surface vector functions.

4.3 Design of the Vector Approximating Function

To define appropriate approximation functions $\boldsymbol{\nu}_i^m$ for the vector bases, we start with a surface Helmholtz decomposition of the current. For any vector field $\mathbf{J}(\mathbf{r})$ defined on the surface Ω , there exists two scalars fields $\phi(\mathbf{r})$ and $\zeta(\mathbf{r})$ such that

$$\mathbf{J}(\mathbf{r}) = \nabla_S \phi(\mathbf{r}) + \nabla_S \times \hat{\mathbf{n}}(\mathbf{r}) \zeta(\mathbf{r}). \tag{4.8}$$

Assume that we have an approximation $\boldsymbol{\nu}_i^m$ to the local behavior of the current $\mathbf{J}(\mathbf{r})$ on patch i.

Definition 5. Assume the knowledge of a local approximation, ν_i to ${\bf J}$ such that on patch i

•
$$\max_{i} \left\{ \left\| \boldsymbol{\nu}_{i} - \mathbf{J} \right\|_{L^{2}(\Omega \cup \Omega_{i})} \right\} \leq \varepsilon_{1}$$

•
$$\max_{i} \left\{ \left\| \nabla_{s} \cdot \boldsymbol{\nu}_{i} - \nabla_{s} \cdot \mathbf{J} \right\|_{L^{2}(\Omega \cup \Omega_{i})} \right\} \leq \varepsilon_{2}$$

•
$$\max_{i} \left\{ \left\| \nabla_{s} \times \boldsymbol{\nu}_{i} - \nabla_{s} \times \mathbf{J} \right\|_{L^{2}(\Omega \cup \Omega_{i})} \right\} \leq \varepsilon_{3}$$

Then, define two scalar functions $\phi_i(\mathbf{r})$ and $\zeta_i(\mathbf{r})$ such that

$$\boldsymbol{\nu}_{i}^{m,c} = \nabla_{s} \phi_{i}^{m}(\mathbf{r})$$

$$\boldsymbol{\nu}_{i}^{m,d} = \hat{\mathbf{n}}_{i}(\mathbf{r}) \times \nabla_{s} \zeta_{i}^{m}(\mathbf{r})$$
(4.9)

and consistent with (4.1) define the approximation to the current as

$$\mathbf{J}_{N} = \sum_{i=1}^{N} \sum_{q=\{c,d\}} \sum_{m} a_{i,q,m} \psi_{i} \boldsymbol{\nu}_{i}^{m,q}. \tag{4.10}$$

Again, we allow for summation over order for each approximation function m.

Given the Definition 5 above and the definition of M, C_{∞} and C_d in Definitions (2) and (3), the following result is a direct consequence of Theorem (4.2.1)

Result 4.3.1. For the local errors defined in (5) above the global errors in the approximation are bounded as follows

•
$$\|\mathbf{J} - \mathbf{J}_N\|_{L^2(\Omega)} \le \sqrt{M} C_{\infty} \varepsilon_1$$

•
$$\|\nabla \cdot (\mathbf{J} - \mathbf{J}_N)\|_{L^2(\Omega)} \le \sqrt{2M} \left((C_d \varepsilon_1)^2 + (C_\infty \varepsilon_2)^2 \right)^{1/2}$$

•
$$\|\nabla \times (\mathbf{J} - \mathbf{J}_N)\|_{L^2(\Omega)} \le \sqrt{2M} \left((C_d \varepsilon_1)^2 + (C_\infty \varepsilon_3)^2 \right)^{1/2}$$

Fig. 4.5a and 4.5b show the basis functions constructed using third order Legendre polynomials for $\phi_i^m(\mathbf{r})$ and $\zeta_i^m(\mathbf{r})$. These are obtained by multiplying the curl-free and divergence-free components of the approximation functions with the corresponding PU function for the patch. Note, however, that the local approximation is only quasi-curl and divergence free.

It is evident from the above exposition that there is no restriction on the functions ϕ_i^m and ζ_i^m . Indeed, if the local asymptotic behavior is known it can be readily incorporated into the approximation function space. Specifically, assuming that the local behavior of current $(\mathbf{j}(\mathbf{r}) \approx \boldsymbol{\nu}_i(\mathbf{r}))$ supports at least one derivative, a possible way to compute the functions $\phi_i(\mathbf{r})$ and $\zeta_i(\mathbf{r})$ is given by the following lemma.

Lemma 4.3.1. Consider a vector function $\boldsymbol{\nu}_i(\mathbf{r})$ defined on Ω_i . Let ϕ_i and ζ_i be

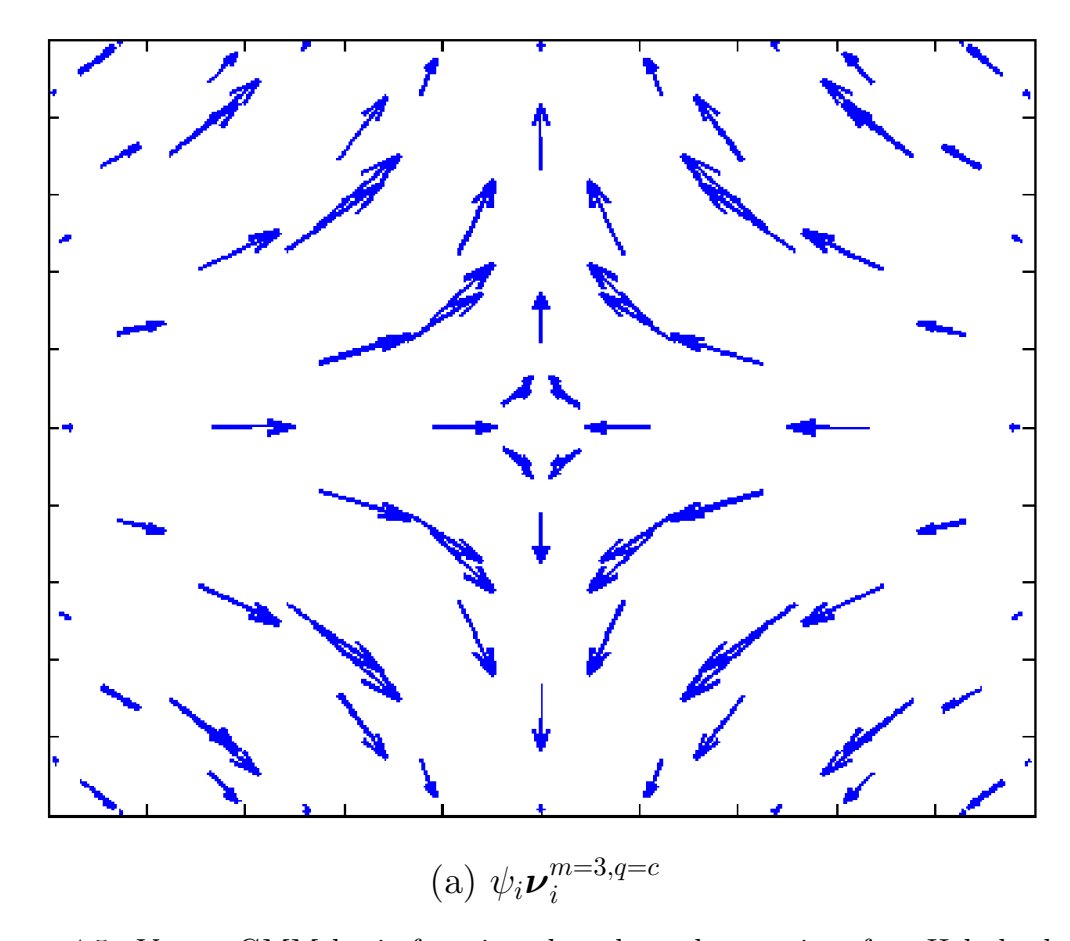


Figure 4.5: Vector GMM basis functions based on the quasi-surface Helmhotlz decomposition basis functions. (a) The quasi curl-free basis functions and (b) the quasi-divergence free basis functions. Both functions are of order p=3.

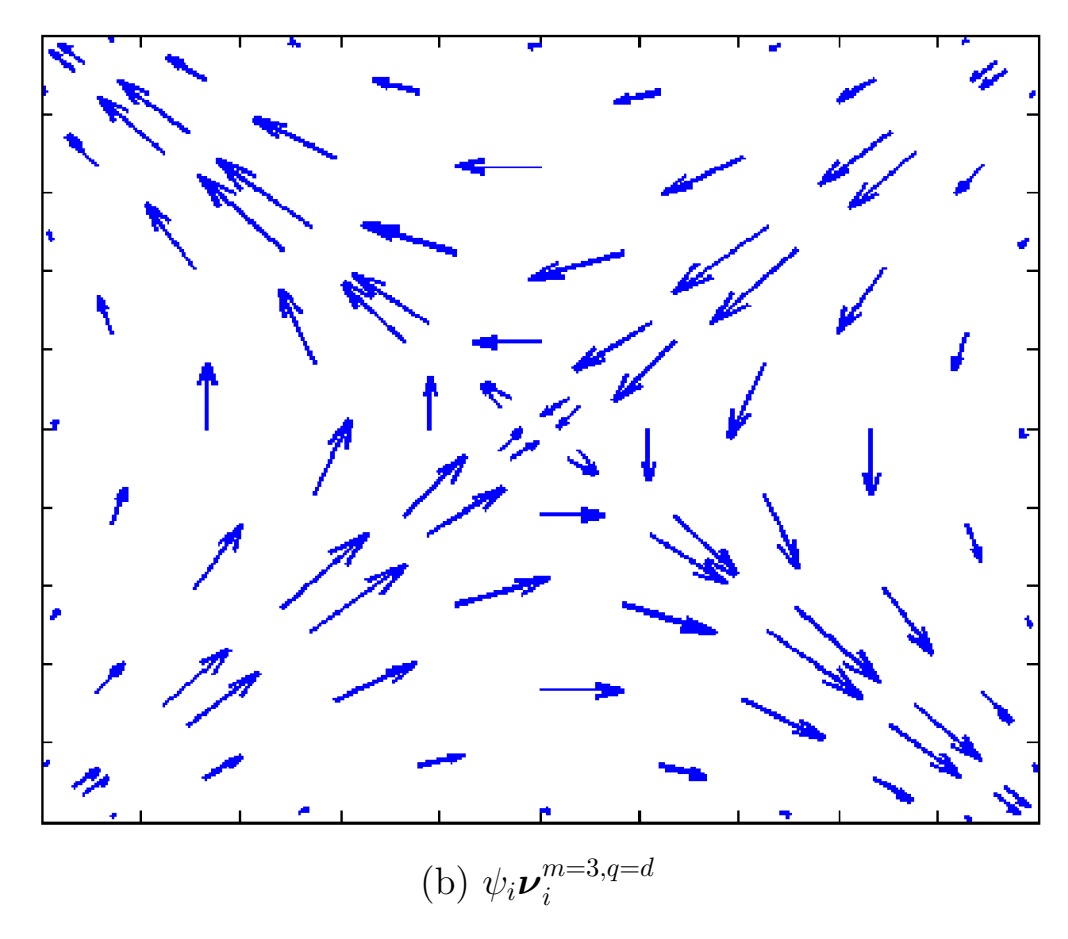


Figure 4.5 Continued: Vector GMM basis functions based on the quasi-surface Helmhotlz decomposition basis functions. (a) The quasi curl-free basis functions and (b) the quasi-divergence free basis functions. Both functions are of order p=3.

solutions to

$$\nabla^2 \phi_i(\mathbf{r}) = \nabla \cdot \boldsymbol{\nu}_i(\mathbf{r}) \tag{4.11}$$

$$\nabla^2 \zeta_i(\mathbf{r}) = \hat{\mathbf{n}}(\mathbf{r}) \cdot \nabla \times \boldsymbol{\nu}_i(\mathbf{r})$$
 (4.12)

then

$$\nu_i = \nabla_S \phi_i(\mathbf{r}) + \nabla_S \times \left[\hat{\mathbf{n}}_i(\mathbf{r}) \zeta_i(\mathbf{r}) \right]. \tag{4.13}$$

Scharstein [100] provides the proof of the above result along with some detailed insight into the physical implications of equations (4.11) and (4.12). We have previously shown for a class of surfaces, that once appropriate approximation and basis functions are defined the error propagated through the discretized integral operator is bounded above by the local error in approximation [101]. This section provides a mechanism to choose an approximation that minimizes this error using all available knowledge of the local behavior of the function. In the next section, we will examine the effect of this approximation error on propagation through the integral equation.

4.4 Error Bounds for the Discrete Integral Operators

For completeness, we state the following standard theorem from integral operator theory. The proof can be obtained from [28].

Theorem 4.4.1. Any integral operator with a weakly singular kernel is compact and therefore bounded.

From this theorem and the definition of the EFIE and MFIE operators in (2.42a) and (2.42b), the following lemma immediately follows.

Lemma 4.4.2. The MFIE operator defined by

$$\hat{\mathbf{n}}(\mathbf{r}) \times \mathbf{H}^{s}(\mathbf{r}) = \mathcal{K} \circ \{\mathbf{J}(\mathbf{r})\} \doteq \frac{1}{4\pi} \hat{\mathbf{n}}(\mathbf{r}) \times \int_{\Omega} d\mathbf{r'} \nabla g(R) \times \mathbf{J}(\mathbf{r'})$$
 (4.14)

where $g(R) = \frac{\exp{-j\kappa R}}{R}$ and $R \doteq |\mathbf{r} - \mathbf{r'}|$, is bounded. The EFIE operator, as defined by

$$\mathbf{E}^{S}(\mathbf{r}) = \mathcal{T} \circ \{\mathbf{J}(\mathbf{r})\} \doteq -\frac{jk\eta_{0}}{4\pi} \int_{\Omega} d\mathbf{r}' g(R) \mathbf{J}(\mathbf{r}') - \frac{j\eta_{0}}{4\pi k} \int_{\Omega} d\mathbf{r}' \nabla \nabla g(R) \cdot \mathbf{J}(\mathbf{r}') \quad (4.15)$$

is not necessarily bounded.

In what follows, we will consider the MFIE and EFIE in sequence. The following theorem holds directly for the MFIE.

Theorem 4.4.3. For any linear and bounded operator $\mathcal{K}: H^{1/2}_{div}(\Omega) \to H^{1/2}_{div}(\Omega)$ with kernel $\mathcal{G}_M(\mathbf{r}, \mathbf{r'}) := \hat{\mathbf{n}}(\mathbf{r}) \times \nabla g(R)$ and functions $\mathbf{J}, \mathbf{J}_N \in H^{1/2}_{div}(\Omega)$ and $\mathbf{t} \in H^{1/2}_{div}(\Omega)$ \exists a constant C_M such that

$$\left| \int_{\Omega} \left(\mathcal{K} \circ \{ \mathbf{J}_{N}(\mathbf{r'}) \} \right) \mathbf{t}_{i}(\mathbf{r}) d\mathbf{r} - \int_{\Omega} \left(\mathcal{K} \circ \{ \mathbf{J}(\mathbf{r'}) \} \right) \mathbf{t}(\mathbf{r}) d\mathbf{r} \right| \leq C_{M} \| \mathbf{J} - \mathbf{J}_{N} \|_{2}$$
(4.16)

Proof. The proof for the above follows from the Cauchy Schwartz inequality and the observation that $||u||_{(1/2),div} \leq ||u||_2 \, \forall u \in H_{div}^{1/2}$.

$$\left| \int_{\Omega} \left(\int_{\Omega} \mathcal{G}_{M}(\mathbf{r}, \mathbf{r'}) \times \mathbf{J}_{N}(\mathbf{r'}) d\mathbf{r'} \right) \mathbf{t}(\mathbf{r}) d\mathbf{r} - \int_{\Omega} \left(\int_{\Omega} \mathcal{G}_{M}(\mathbf{r}, \mathbf{r'}) \times \mathbf{J}(\mathbf{r'}) d\mathbf{r'} \right) \mathbf{t}(\mathbf{r}) d\mathbf{r} \right|$$

$$= \left| \int_{\Omega} \left(\int_{\Omega} \mathcal{G}_{M}(\mathbf{r}, \mathbf{r'}) \times \left(\mathbf{J}_{N}(\mathbf{r'}) - \mathbf{J}(\mathbf{r'}) \right) d\mathbf{r'} \right) \mathbf{t}(\mathbf{r}) d\mathbf{r} \right|$$
(4.17)

Applying Cauchy Schwartz inequality we obtain

$$\left| \int_{\Omega} \left(\int_{\Omega} \mathcal{G}_{M}(\mathbf{r}, \mathbf{r'}) \times \left(\mathbf{J}_{N}(\mathbf{r'}) - \mathbf{J}(\mathbf{r'}) \right) d\mathbf{r'} \right) \mathbf{t}(\mathbf{r}) d\mathbf{r} \right|$$

$$\leq \left\| \int_{\Omega} \mathcal{G}_{M}(\mathbf{r}, \mathbf{r'}) \times \left(\mathbf{J}_{N}(\mathbf{r'}) - \mathbf{J}(\mathbf{r'}) \right) d\mathbf{r'} \right\|_{2} \int_{\Omega} \|\mathbf{t}(\mathbf{r})\|_{2} d\mathbf{r}$$

$$(4.18)$$

Since, $\mathbf{t}(\mathbf{r}) \in H_{div}^{1/2}(\Omega)$ we have that

$$\int_{\Omega} \|\mathbf{t}(\mathbf{r})\|_2 \, dx \le C < \infty \tag{4.19}$$

Further we have from the definition of boundedness, that

$$\left\| \int_{\Omega} \mathcal{G}_{M}(\mathbf{r}, \mathbf{r'}) \times \left(\mathbf{J}_{N}(\mathbf{r'}) - \mathbf{J}(\mathbf{r'}) \right) d\mathbf{r'} \right\|_{2} \le C_{1} \left\| \left(\mathbf{J}_{N}(\mathbf{r'}) - \mathbf{J}(\mathbf{r'}) \right) \right\|_{2}$$
(4.20)

Combining equations (4.19) and (4.20) we have that

$$\left| \int_{\Omega} \left(\int_{\Omega} \mathcal{K} \circ \left\{ \mathbf{J}_{n}(\mathbf{r}') - \mathbf{J}(\mathbf{r}') \right) d\mathbf{r}' \right\} \mathbf{t}(\mathbf{r}) d\mathbf{r} \right| \le C_{M} \left\| \left(\mathbf{J}_{N} - \mathbf{J} \right) \right\|_{2}$$
(4.21)

where
$$C_M := CC_1$$
.

These theorems demonstrate that, in each patch, the error in approximation bounds the error propagated through the integral operator. Note that the theorems hold only for compact operators. It is not directly applicable to unbounded operators such as the EFIE. However, this can be overcome by casting the EFIE solution in a Galerkin testing framework. First, the bilinear form of the EFIE as follows

Definition 6. For the EFIE operator, \mathcal{T} given by

$$\mathcal{T} \circ \{\mathbf{J}(\mathbf{r})\} \doteq -\frac{jk\eta_0}{4\pi} \int_{\Omega} d\mathbf{r'} g(R) \mathbf{J}(\mathbf{r'}) + \frac{j\eta_0}{4\pi k} \int_{\Omega} d\mathbf{r'} \nabla g(R) \nabla_S' \cdot \mathbf{J}(\mathbf{r'})$$

Let \mathcal{B}_E be the bilinear form defined by

$$\mathcal{B}_E(\mathbf{J}, \mathbf{t}) = \langle \mathbf{t}, \mathcal{T} \circ \{\mathbf{J}\} \rangle$$
 (4.22)

Assuming that the domain Ω is smooth enough to permit the local basis functions to support at least one derivative, it can be shown that

$$\mathcal{B}_{E}(\mathbf{J}, \mathbf{t}) = \int_{\Omega} \mathcal{T} \circ \{\mathbf{J}(\mathbf{r})\} \cdot \mathbf{t}(\mathbf{r}) d(\mathbf{r})$$

$$= -\frac{jk\eta_{0}}{4\pi} \int_{\Omega} d\mathbf{r} \ \mathbf{t}(\mathbf{r}) \cdot \int_{\Omega} d\mathbf{r}' g(R) \mathbf{J}(\mathbf{r}') + \frac{j\eta_{0}}{4\pi k} \int_{\Omega} d\mathbf{r} \ \mathbf{t}(\mathbf{r}) \cdot \int_{\Omega} d\mathbf{r}' \nabla g(R) \nabla_{s}' \cdot \mathbf{J}(\mathbf{r}')$$

$$= -\frac{jk\eta_{0}}{4\pi} \int_{\Omega} \int_{\Omega} \mathbf{t}(\mathbf{r}) \cdot g(R) \mathbf{J}(\mathbf{r}') d\mathbf{r}' d\mathbf{r} - \frac{j\eta_{0}}{4\pi k} \int_{\Omega} \int_{\Omega} \nabla \cdot \mathbf{t}(\mathbf{r}) g(R) \nabla_{s} \cdot \mathbf{J}(\mathbf{r}') d\mathbf{r}' d\mathbf{r}$$

$$(4.23)$$

Definition 7. The above equations give the following splitting of the Galerkin tested EFIE operator

$$\langle \mathbf{t}, \mathcal{T} \circ \{ \mathbf{J} \} \rangle \stackrel{:}{=} \langle \mathbf{t}, \mathcal{T}_{c} \circ \{ \mathbf{J} \} \rangle + \langle t_{c}, \mathcal{T}_{q} \circ \{ J_{c} \} \rangle$$

$$\stackrel{:}{=} -\frac{ik\eta_{0}}{4\pi} \langle \mathbf{t}, G_{k}(\mathbf{r}, \mathbf{r'}) \circ \{ \mathbf{J} \} \rangle - \frac{i\eta_{0}}{4\pi k} \langle \nabla \cdot \mathbf{t}, G_{k}(\mathbf{r}, \mathbf{r'}) \circ \nabla (4\mathbf{J}2\mathbf{A}) \rangle$$

It can be shown, using Theorem 4.4.1, that the operators $\mathcal{T}_c(\mathbf{r}, \mathbf{r'})$ and $\mathcal{T}_q(\mathbf{r}, \mathbf{r'})$ with kernel $G_k(\mathbf{r}, \mathbf{r'}) \doteq g(R)$ are compact and therefore, bounded. Therefore, Theorem 4.4.3 is directly applicable to the first term in equation (4.24). Further a scalar specialization of 4.4.3 can be applied to the second term in equation (4.24)

Theorem 4.4.4. For any linear and bounded operator $\mathcal{T}_q: H^{1/2}(\Omega) \to H^{1/2}(\Omega)$ with kernel g(R) and (scalar) functions $J, J_N \in H^{1/2}(\Omega)$ and $t \in H^{1/2}(\Omega)$ \exists a

constant C_E such that

$$\left| \int_{\Omega} \left(\mathcal{T}_{q} \circ \{J_{N}(\mathbf{r}')\} \right) t_{i}(\mathbf{r}) d\mathbf{r} - \int_{\Omega} \left(\mathcal{T}_{q} \circ \{J(\mathbf{r}')\} \right) t(\mathbf{r}) d\mathbf{r} \right| \leq C_{E} \left\| \mathbf{j} - \mathbf{j}_{N} \right\|_{2}$$
(4.25)

Combining Theorems 4.2.1 and 4.4.3 (or equivalently, 4.4.4), we have the following results for both the EFIE and the MFIE.

Result 4.4.1. For local approximating functions \mathbf{J}_N that are at least C^1 (locally), the approximation error on each patch bounds the error propagated through the integral equation. If we assume the existence of a convergent inverse for the discretized equation, then the error in the solution will also be bounded by this error.

The local continuity assumption used in the result above is not restrictive since all it implies is that the domain needs to be partitioned such that each patch does not contain local singularities. In practice, this can be easily achieved by matching patch boundaries with any geometric singularities. One can then define functions $\mathbf{J}_N \in H_{div}^{1/2}$ as a set of functions that are piece-wise C^1 . Thus, finally the above result along with the observation that if $\mathbf{J}, \mathbf{J}_N \in H_{div}^{1/2}$, then $\|\mathbf{J} - \mathbf{J}_N\|_2 \leq C < \infty$ makes it possible to obtain L_2 bounded errors by choosing basis functions from the trace space. The above theorems provide the foundation for the development of the GMM and can be extended to any space of functions as long as the partition of unity framework is maintained. This freedom of choice is the inherent advantage of the GMM scheme as opposed to the standard MoM scheme where the basis functions are tightly coupled to the discretization. For example, it can be shown that the scalar higher order polynomial functions can be easily cast in this framework and error bounds can be derived.

4.5 Benefits of the GMM framework

The GMM method described in the previous subsections comprises of two components; (i) defining overlapping domains and partitions of unity on these domains and (ii) defining approximations functions in the partitions of unity. The definition of basis functions provides a mathematically rigorous framework for designing local approximation spaces. From an intuitive perspective, we have always used the PU functions whenever the basis function space has comprised of pulses or hat functions for the analysis of scalar problems. Likewise, basis functions that are commonly used in the computational electromagnetics community (eg. Rao-Wilton-Glisson [71], Buffa-Christiansen [102], characteristic basis [103] or Graglia-Wilton-Peterson [74]) can all be interpreted as a product of a partition of unity function and higher order approximating functions (with the correct definition of the PU domain). In most cases, the PU function is implicitly assumed and is typically a pulse function. When it is a pulse function, one has to worry about means to achieve conformal behavior between neighboring elements. As in GFEM [99], the use of basis functions that explicitly comprise of a product of an overlapping partition of unity and approximating functions removes the need for such boundary treatment between different sub domains, and dramatically increases the number of functions that can be used for approximation. For instance, one can use a third order approximation in a domain next to one where a first order is being used, without explicitly enforcing any condition. Or for that matter, mixture of polynomial and non-polynomial basis functions. Use of the these definitions of basis will be demonstrated in the Section 4.9. In the next Section, we present specifics of the implementation of the general GMM scheme for arbitrary 3D scatterers.

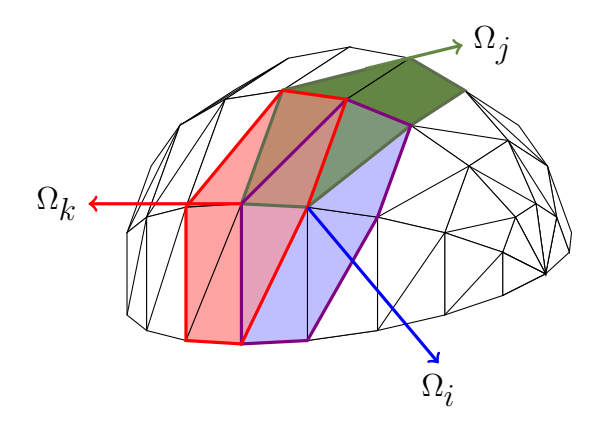


Figure 4.6: Construction of GMM patches (Ω_i) shown as shaded region. The patches are constructed as a set of triangles joined at a node.

4.6 Implementation of the GMM

The first need is to define the domain of support of each of these basis functions. This is done by partitioning the domain Ω into subdomains/patches Ω_i that overlap and completely cover the domain. This construction of overlapping patches is illustrated in Fig. 4.6. Formally, $\bigcup_i^{N_{pat}} \Omega_i = \Omega$, where N_{pat} is the number of patches/subdomains. Note, that at this point, a patch can be defined either within a meshless or a meshed framework. The key requirement is that one have a surface description for each patch Ω_i . At this time, for a wide range of problems such a description is most easily available as a surface tessellation. As a result, the rest of the development will focus on developing the GMM scheme and basis functions within a meshed framework. Parenthetically, we do observe that extending this to a meshless framework is not very difficult. As, objects are typically represented using a triangulation of their surfaces, that shall be our starting point.

4.7 Construction of Overlapping Patches

To define a set of overlapping patches starting from a triangular mesh, we designate each node as the "center" of a patch, defined as the union of all triangles that share the node.

Definition 8. Overlapping Patches

Consider a set of nodes $\mathcal{N}_L = \sum_{i=1}^L \{\mathcal{N}_i\}$ and a corresponding triangulation $\Delta_N = \sum_{n=1}^N \{\Delta_n\}$ of a domain Ω . Let $\{\mathcal{N}_{n_{j=1}-3}\}$ be the set of nodes associated with triangle Δ_n . For each node \mathcal{N}_i , denote a corresponding patch Ω_i defined by a set of triangles; $\Omega_i = \{\Delta_n : \Delta_n \in \Delta_N, \mathcal{N}_i \in \mathcal{N}_{n_j}\}$. The GMM covering is defined as the set of these (overlapping) patches $\{\Omega_i\}$. The overlap between any two patches Ω_p and Ω_q is another set of triangles $\Delta_{p,q} \doteq \Omega_p \cap \Omega_q$

This definition of GMM patches from a union of polygonal shapes can also be seamlessly translated to higher order geometries defined on triangulations described in [74]. In the remainder of this section, Δ_n will be used to represent both flat and equivalent higher order triangulations of the surface. The above patch design also allows for integration on the triangles described by the original tessellations and therefore, allows the use of available integration rules.

The next step is a consistent definition for basis functions on these patches. Note that these patches are no longer coplanar and do not correspond to any canonical geometry (unlike triangles, quads, etc.). This necessitates the careful definition of functions on Ω_i so as to maintain continuity. To this end, we first state the following lemma for continuous portions of the surface.

Lemma 4.7.1. Consider a patch Ω_i . Let the surface $\Omega \cap \Omega_i$ be at least $C^1(\mathbb{R}^3)$ smooth. Let the location of \mathcal{N}_i be denoted by \mathbf{r}_i . Let the surface normal at any point $\mathbf{r} \subset \{\Omega \cap \Omega_i\}$ be denoted by $\hat{\mathbf{n}}(\mathbf{r})$ (consistent with the previous definitions). Then by the definition of continuous surfaces, we have $\forall \delta_i \geq 0 \exists \mathcal{B}_{i,\varepsilon} \in \mathbb{R}^3$ such that $\forall \mathbf{r} \in \{\mathcal{B}_{i,\varepsilon} \cap \Omega_i\} \|\mathbf{n}(\mathbf{r}) - \mathbf{n}(\mathbf{r}_i)\|_2 \leq \delta_i$ where $\mathcal{B}_{i,\varepsilon}$ is a ball of radius ε centered at \mathcal{N}_i

With this preamble, we can now define a patch normal and projection plane for

each patch.

Definition 9. Patch Normal and Projection Plane

Consider a patch Ω_i composed of m triangles $\Omega_i = \bigcup_{k=1}^m \{\Delta_k\}$. Define an average normal for the patch, $\hat{\mathbf{n}}_i$ as $\hat{\mathbf{n}}_{i,\varepsilon} = 1/m \sum_{k=1}^m \hat{\mathbf{n}}(\mathbf{r}_k)$, where \mathbf{r}_m are points chosen on each of the triangles that make the patch such that $\mathbf{r}_m \subset \Omega_i \cap \Delta_k$ and $\|\mathbf{r}_k - \mathbf{r}_i\|_2 \leq \varepsilon$. The projection plane for patch Ω_i , \mathcal{P}_i is defined as the plane passing through \mathbf{r}_i and normal to $\hat{\mathbf{n}}_i$.

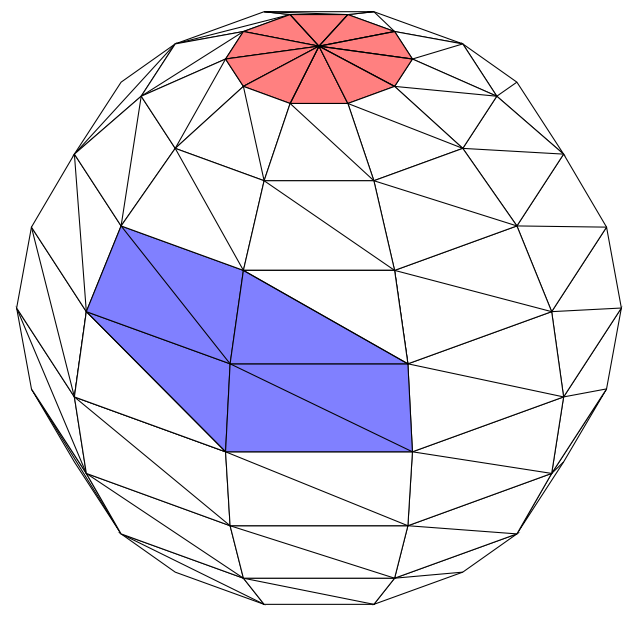
For purposes of illustration, Fig. 4.7 shows the construction of one patch and its corresponding projection plane. Observe that the patch normal $\hat{\mathbf{n}}_i$ coincides with the true surface normal at \mathbf{r}_i if the triangulations are smooth (and necessarily higher order), if not, the differences between the patch normal $\hat{\mathbf{n}}_i$ and the normals of the individual member triangles provide an intuitive measure of the "sharp-ness" of the surface at \mathbf{r}_i . This information can be used as a criteria for the design of approximation functions. If the surface is discontinuous, it is partitioned into areas that are piecewise continuous and then the above procedure is applied to each portion.

Once the normal and the projection planes are defined for each patch, the basis functions are defined on the projection of the entire patch on the plane using a local coordinate system on the projection plane.

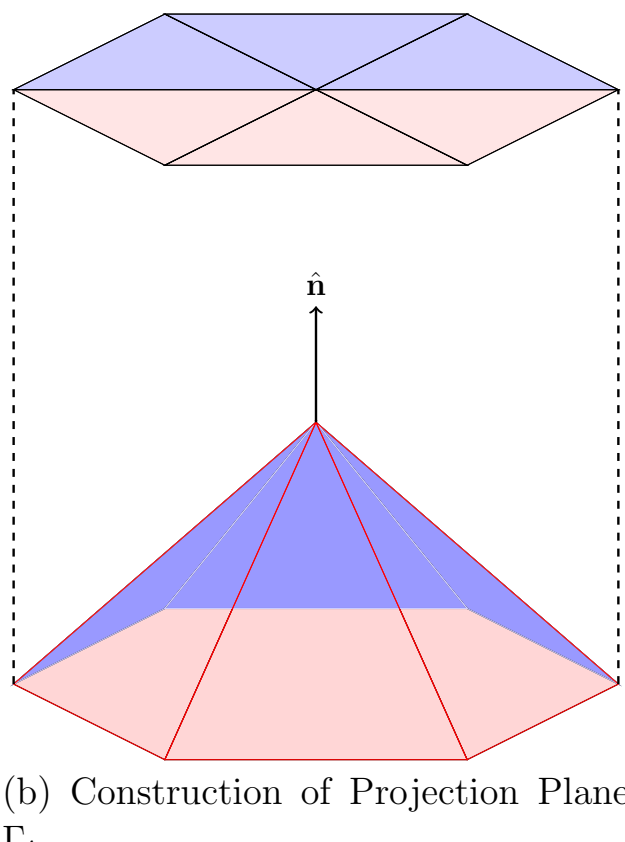
Definition 10. Local Coordinate System

Let Γ_i be the projection of a patch Ω_i on \mathcal{P}_i . For the rest of the discussion, primed coordinates denote the projection of the corresponding global coordinate on \mathcal{P}_i (note that, by construction, $\mathbf{r}_i = \mathbf{r}_i'$). Two local projection vectors are generated for each patch $\hat{\mathbf{u}}_{p,i}(\mathbf{r}')$ and $\hat{\mathbf{v}}_{p,i}(\mathbf{r}')$ as $\hat{\mathbf{u}}_p \doteq \mathbf{u}_p/\|\mathbf{u}_p\|_2$ where $\mathbf{u}_p = \mathbf{r}' - \mathbf{r}_i'$ such that $\|\mathbf{u}_p\|_2 \geq \|\mathbf{r}' - \mathbf{r}_i'\|_2 \ \forall \mathbf{r} \in \Gamma_i$ and $\hat{\mathbf{v}}_p = \hat{\mathbf{n}}_i \times \hat{\mathbf{u}}_p$.

With this preamble, it is now possible to define a mapping from regular x, y, z coordinate space into the u, v coordinate space defined on the projection Γ_i as follows:



(a) Definition of GMM Patch Ω_i



(b) Construction of Projection Plane Γ_i

Figure 4.7: Construction of (a) GMM Patches (Ω_i) shown as shaded region and (b) Projection Planes (Γ_i) from standard triangulations. The patches are constructed as a set of triangles joined at a node.

- $\forall \mathbf{r} \in \Omega_i \; \exists \; \mathbf{r'} \in \Gamma_i$,
- define $u = \mathbf{r'} \cdot \hat{\mathbf{u}}_p$ and $v = \mathbf{r'} \cdot \hat{\mathbf{v}}_p$, and
- then the local coordinates **u** and **v** are given by $u\hat{\mathbf{u}}_p$ and $v\hat{\mathbf{v}}_p$.

Approximation and basis functions are now constructed by defining functions on the corresponding planar coordinates. One consequence of the choice of the coordinate system is that the projection coordinates span an area that *contains*, but is not limited to, Γ_i . This is possible as functions defined on these patches are eventually multiplied by a PU function that goes to zero at patch boundaries.

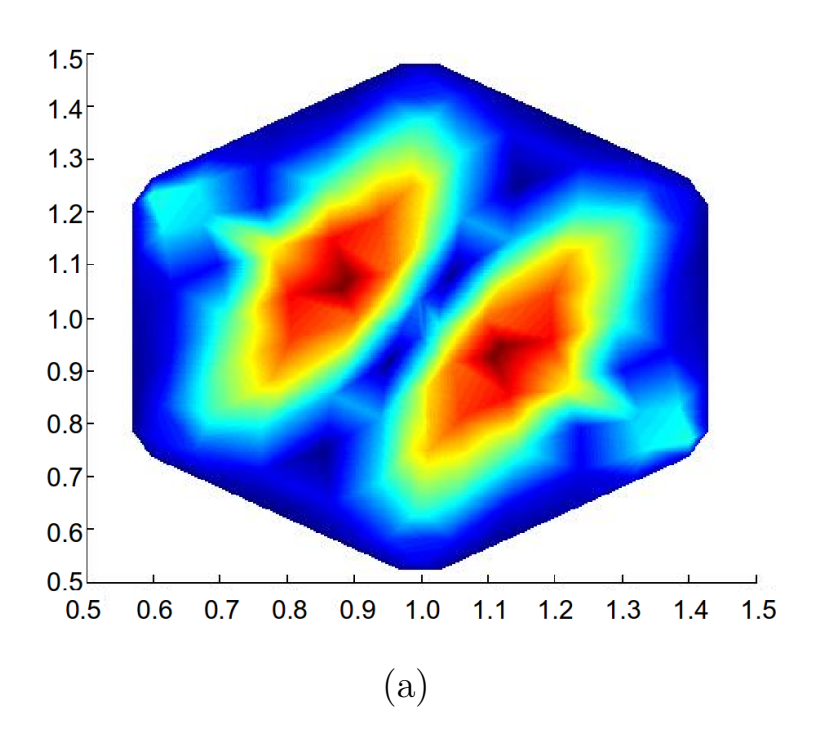
Given the definitions above, it is important to ensure that functions that are continuous in the projection domain are so in the real space as well. The following theorem (stated without proof) prescribes the necessary conditions.

Theorem 4.7.2. Given a surface description $\Omega_i(\mathbf{r})$ that is at least $C^1(\mathbb{R}^3)$ smooth, consider any function $F(u(\mathbf{r}), v(\mathbf{r}))$ defined on the projection Γ_i . Then, if $F \in C^m(\Gamma_i)$ then $F \in C^m(\Omega_i)$ for any m.

The proof follows from the definition of partial derivatives. While a corresponding result does not hold for piecewise continuous triangulations, we have observed, in practice, that it is possible to construct functions that are continuous across the interior edges of the patch. This fact is shown in Fig. 4.8 where a set of polynomial functions are defined on a flat projection plane, in Fig 4.8a, and then transformed to a non-flat, piecewise linear, triangulation in Fig. 4.8b. It is apparent from the figures that there are no discontinuities introduced due to the projection.

4.8 Computation of Matrix Elements

Next, the discrete versions of the EFIE and the MFIE are constructed using Galerkin testing. From the definition of the discretized EFIE and the MFIE in the previous



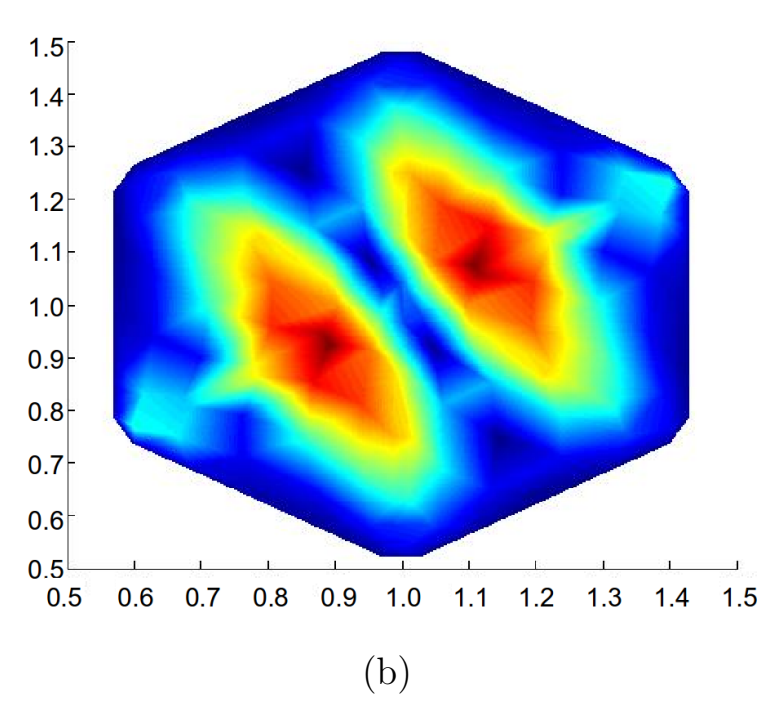


Figure 4.8: Basis functions defined on (a) the projection plane and (b) the true geometry (surface of a tessellated sphere). The figure (b) shows that there is no discontinuities introduced by the projection.

chapter, it can be verified that the computation of the matrix elements involves the evaluation of the following three types of integrals; viz.

$$I_{1} = \int_{\Omega_{i}} d\mathbf{r} \tilde{\mathbf{f}}_{i}^{n}(\mathbf{r}) \cdot \int_{\Omega_{j}} d\mathbf{r}' g_{q}(R) \mathbf{f}_{j}^{k}(\mathbf{r}')$$
(4.26a)

$$I_2 = \int_{\Omega_i} d\mathbf{r} \tilde{\mathbf{f}}_i^n(\mathbf{r}) \cdot \int_{\Omega_j} d\mathbf{r}' \nabla g_q(R) \times \mathbf{f}_j^k(\mathbf{r}')$$
 (4.26b)

$$I_{3} = \int_{\Omega_{i}} d\mathbf{r} \tilde{\mathbf{f}}_{i}^{n}(\mathbf{r}) \cdot \int_{\Omega_{j}} d\mathbf{r'} \nabla \nabla g_{q}(R) \cdot \mathbf{f}_{j}^{k}(\mathbf{r'})$$
(4.26c)

where $\tilde{\mathbf{f}}_i^n(br)$ can stand for either $\mathbf{f}_i^n(\mathbf{r})$ or $\hat{\mathbf{n}}(\mathbf{r}) \times \mathbf{f}_i^n(\mathbf{r})$. There is extensive literature on evaluating both the singular and hypersingular integral that occur in Eqns. (4.26a) and (4.26b) [104–106]. The methods that we have used follow those presented in these papers. In what follows, we shall deal with terms of the form (4.26c). The evaluation of (4.26c) is more involved. Assume that $\Omega_{i(j)}$ is the union of a set of triangles denoted by $\cup \Delta_{i(j)}$. Then (4.26c) can be rewritten in either of the following two forms:

$$\int_{\Omega_i} d\mathbf{r} \ \mathbf{t}(\mathbf{r}) \cdot \int_{\Omega_j} d\mathbf{r'} \ \nabla \nabla g_q(R) \cdot \mathbf{j}(\mathbf{r'}) =$$

$$\int_{\cup \Delta_i} d\mathbf{r} \ \mathbf{t}(\mathbf{r}) \cdot \int_{\cup \Delta_j} d\mathbf{r'} \ \nabla \nabla g_q(R) \cdot \mathbf{j}(\mathbf{r'})$$

$$= -\int_{\cup \Delta_{i}} d\mathbf{r} \, \nabla_{s} \cdot \mathbf{t}(\mathbf{r}) \int_{\cup \Delta_{j}} d\mathbf{r'} \, \nabla_{s} g_{q}(R) \cdot \mathbf{j}(\mathbf{r'})$$

$$+ \int_{\cup \partial \Delta_{i}} d\mathbf{r} \, \hat{\mathbf{m}}_{i}(\mathbf{r}) \cdot \mathbf{t}(\mathbf{r}) \int_{\cup \Delta_{j}} d\mathbf{r'} \, \nabla_{s} g_{q}(R) \cdot \mathbf{j}(\mathbf{r'})$$
(4.27a)

$$= -\int_{\cup \Delta_{i}} d\mathbf{r} \, \nabla_{s} \cdot \mathbf{t}(\mathbf{r}) \int_{\cup \Delta_{j}} d\mathbf{r}' \, g_{q}(R) \nabla_{s}' \cdot \mathbf{j}(\mathbf{r}')$$

$$+ \int_{\cup \partial \Delta_{i}} d\mathbf{r} \, \hat{\mathbf{m}}_{i}(\mathbf{r}) \cdot \mathbf{t}(\mathbf{r}) \int_{\cup \Delta_{j}} d\mathbf{r}' \, g_{q}(R) \nabla_{s}' \cdot \mathbf{j}(\mathbf{r}') \qquad (4.27b)$$

$$- \int_{\cup \partial \Delta_{i}} d\mathbf{r} \, \hat{\mathbf{m}}_{i}(\mathbf{r}) \cdot \mathbf{t}(\mathbf{r}) \int_{\cup \partial' \Delta_{j}} d\mathbf{r}' \, g_{q}(R) \hat{\mathbf{m}}_{j}(\mathbf{r}') \cdot \mathbf{j}(\mathbf{r}')$$

$$+ \int_{\cup \Delta_{i}} d\mathbf{r} \, \nabla_{s} \cdot \mathbf{t}(\mathbf{r}) \int_{\cup \partial' \Delta_{j}} d\mathbf{r}' \, g_{q}(R) \hat{\mathbf{m}}_{j}(\mathbf{r}') \cdot \mathbf{j}(\mathbf{r}')$$

where $\hat{\mathbf{m}}_i$ and $\hat{\mathbf{m}}_j$ are the unit normals to each boundary $\partial \Delta_i$ and $\partial' \Delta_j$ of Δ_i and Δ_j , respectively. The divergence operator $(\nabla^{(')})$ can be reduced to the corresponding surface divergence operator $(\nabla_s^{(')})$ because $\mathbf{j}(\mathbf{r})(\mathbf{t}(\mathbf{r}))$ are surface functions. In typical RWG settings, the normals $\hat{\mathbf{m}}_i = -\hat{\mathbf{m}}_j$ and so, very conveniently, the last three terms in (4.27b) drop out. This leaves an integrable singularity using the above mentioned techniques for the magnetic vector potential.

However, in GMM the set of triangles forming a patch are not co-planar. This means that the normal $\mathbf{m}_{i(j)}$ is not continuous within a patch and so, we need to compute all the terms on the right-hand side of the expansion in (4.27b). On the outer boundary of the patch though, the integral will vanish as a result of the PU function and thus only interior triangle edges need to be considered. (4.27a) involves integrals that are an order of singularity higher than (4.27b). However, as $\mathbf{r} \to \mathbf{r}'$ (gq is singular), (4.27b) can no longer be used since (1/R) is not integrable on a line when $\mathbf{r} \to \mathbf{r}'$. As a result, in the GMM implementation, this is handled depending on the location of \mathbf{r} and \mathbf{r}' .

r and r' lie on the same triangle

In this case, we employ a singularity subtraction technique which takes into account the measure provided by both the source and testing integral, in order to mollify the second order singularity. This technique was first proposed by [107] and computes the double integrals in (4.27a) together rather than first computing the source and then the testing integral as is usually done in practice.

r and r' lie on triangles that share an edge

In this case, the integral is not singular but the $1/R^3$ term needs to be handled carefully. This case is evaluated using (4.27a). The first term in the expansion can be computed for near singular (but non-singular) terms using a slight modification of the method described in [104] to integrate terms of the type $\frac{1}{R^2}$.

r and r' are not in neighbouring triangles but are close ($|\mathbf{r} - \mathbf{r'}| \le 0.15\lambda$)

Here we use (4.27b) to evaluate the integral since the line-line singularity is no longer a concern.

r and r' are sufficiently separated from each other

In this case, the (now) regular integral can be evaluated using either of the two expressions in (4.27a) or (4.27b), using standard numerical quadrature.

A transformation for the near singular integration of $\nabla g(R)\mathbf{j}(\mathbf{r'})$ for $\mathbf{r} \to \mathbf{r'}$ Consider the evaluation of the following integral for $\mathbf{r} \to \mathbf{r'}$ but $\mathbf{r} \neq \mathbf{r'}$:

$$\int_{\Delta}' d\mathbf{r'} \nabla g(R) \mathbf{j}(\mathbf{r'}) \tag{4.28}$$

We modify the steps outlined in [104] for the evaluation of

$$\int_{\Delta}' d\mathbf{r'} g(R) \mathbf{j}(\mathbf{r'}) \tag{4.29}$$

In [104], the authors split the triangle into three parts around the projection of \mathbf{r} on to the tangent plane and use a geometric transformation to transform the integral to the following form

$$\sum_{i=1}^{3} \int_{0}^{h_{i}} dy_{i} \int_{x_{i}(y_{i})} dx_{i} \mathbf{j}(\mathbf{r}'(x_{i}, y_{i})) e^{ikR} \frac{1}{\sqrt{(x_{i}^{2} + y_{i}^{2} + z^{2})}}$$
(4.30)

where z is the height of the \mathbf{r} above the equivalent tangent plane of the triangle Δ' , h_i and x_i are the height and the base length of each sub triangle. [104] further uses an \sinh^{-1} transformation to transfer the singularity of $1 \sqrt{x^2 + y^2 + z^2}$ from the integrand to the limits of the integral. It can be shown that a similar transfer of singularity can be achieved for $1 |\mathbf{r} - \mathbf{r}'|^2 = 1 x_i^2 + y_i^2 + z^2$ using a \tan^{-1} transformation. The rest of the steps remain identical.

4.8.1 r and r' are not in neighbouring triangles but are close $(|{\bf r}-{\bf r}'| \leq 0.15 \lambda)$

Here we use (4.27b) to evaluate the integral due to the (now) better behaved nature of the singularity.

4.8.2 r and r' are sufficiently separated from each other

In this case, the singularity is no longer a concern and the integral can be evaluated using either of the two expressions above.

4.8.3 Integration with acceleration techniques

At this point, we simply note that once the basis functions are defined and the appropriate integration rules chosen, integration with the wideband fast multipole method (FMM) is straightforward [38, 48, 108].

4.9 Numerical Experiments

Next, via a series of numerical experiments, we will demonstrate that the GMM discretization framework proposed here (i) provides excellent approximation of the unknown currents and its derivatives and (ii) accurate results for scattering from several topologically different objects, (iii) demonstrate the viability of this method to accurately analyze scattering from objects using a mixture of basis functions, (iv) demonstrate analysis from objects meshed with non-conformal meshes and (v) low frequency stability the choice of basis. Where necessary, results have been obtained using a GMM code augmented by FMM.

4.10 Quality of Approximation

The first goal is to test whether multiple functions can be seamlessly mixed together within the GMM approximation space. This will be verified by a series of numerical experiments described next. It is assumed that the current in a domain Ω satisfies some prescribed functional dependence, say $\mathbf{J}(\mathbf{r}) = \mathbf{f}(\mathbf{r})$. The coefficients of these basis functions

$$\mathbf{J}_{N}(\mathbf{r}) = \sum_{i} a_{i} \mathbf{j}_{i}(\mathbf{r}) = \sum_{i=1}^{N} \sum_{q=d,c} \sum_{m} a_{i,m} \psi_{i} \boldsymbol{\nu}_{i,q}^{m}(\mathbf{r})$$
(4.31)

are computed by solving a discrete system

$$\bar{\bar{\mathbf{Z}}}\bar{a} = \bar{\mathbf{b}} \tag{4.32}$$

where $\mathbf{Z}_{i,j} = \langle \mathbf{j}_i, \mathbf{j}_j \rangle$ and $\mathbf{b}_i = \langle \mathbf{j}_i, \mathbf{J} \rangle$ The approximation error defined as

$$\varepsilon(\mathbf{r}) = \frac{\left| \mathbf{f}(\mathbf{r}) - \sum_{i=1}^{N} a_i \mathbf{j}_i \right|}{\left| \mathbf{f}(\mathbf{r}) \right|}$$
(4.33)

is computed by oversampling the currents on the geometry. Similar errors are computed for both the curl and the divergence of the current using the coefficients $\{a_i\}$.

For each test described next, the approximation was computed on a square domain of side 1.0m using overlapping patches, each of size h = 0.2m. Fig. 4.9a-4.9b show the convergence of the maximum approximation error with approximation order p for each of the tests.

4.10.1 Approximation of Polynomial Functions

It was earlier argued that the GMM scheme permits the mixing basis functions of various types. For this to be effective, it is important that the higher order functions do not corrupt the approximation of smooth functions. Fig. 4.9a shows the convergence of the approximation error for two functions (i) a constant $\mathbf{f}(\mathbf{r}) = \hat{\mathbf{x}}$ and (ii) a polynomial $\mathbf{f}(\mathbf{r}) = \hat{\mathbf{x}}y^3 + \hat{\mathbf{y}}x^3$. As expected, the error is consistently less than 10^{-12} for the constant function. Similarly, it is very interesting to note here that once the order of the approximation reaches the order of the polynomial function (p = 3), the error in the GMM scheme drops to machine precision.

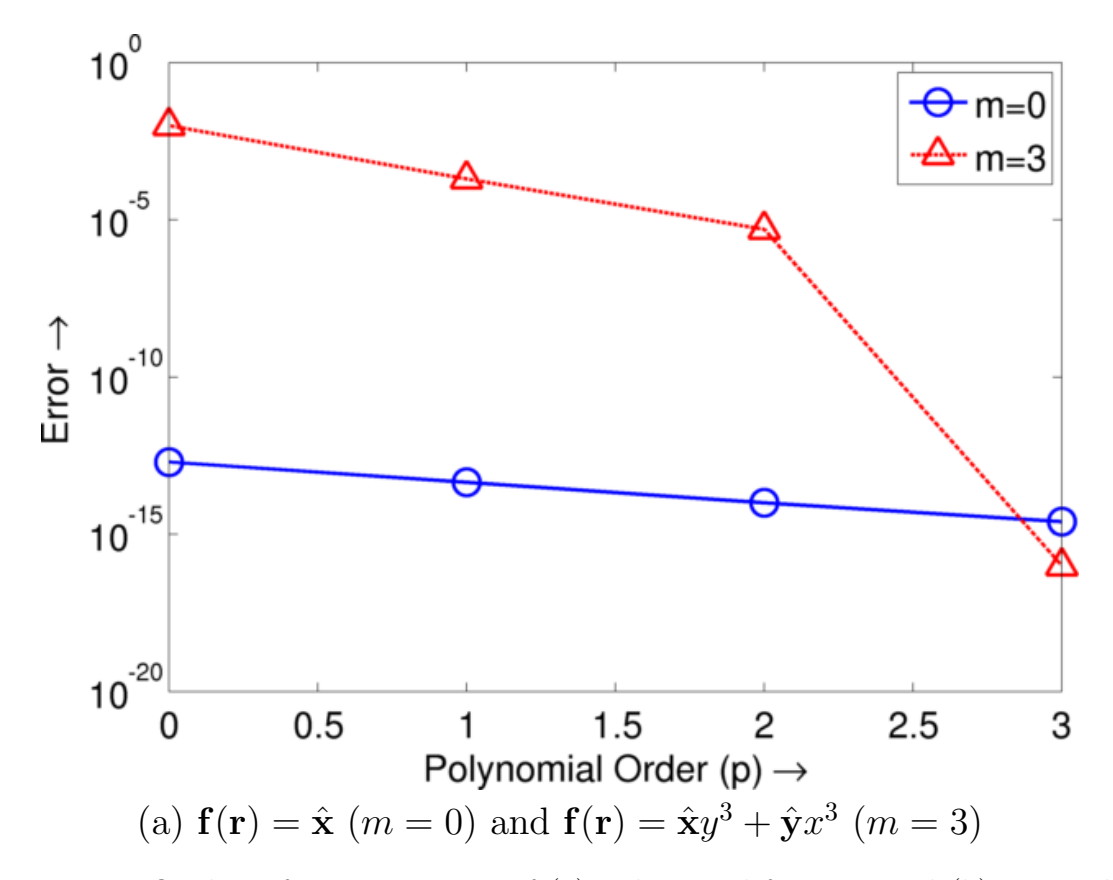


Figure 4.9: Quality of approximation of (a) polynomial function and (b) sinusoidal functions.

4.10.2 Approximation of sinusoidal functions

Fig. 4.9b shows the convergence graphs for $\mathbf{f}(\mathbf{r}) = \hat{\mathbf{x}} \sin(x) \sin(y)$ and $\mathbf{f}(\mathbf{r}) = \hat{\mathbf{x}} \exp(-\mathbf{j}\mathbf{k} \cdot \mathbf{r})$. The figures show the convergence curve for both the approximation in the current and its curl and divergence. As seen in the figures, the error in both $\nabla \cdot \mathbf{J}$ and $\nabla \times \mathbf{J}$ is the same and of order (p-1), as expected.

4.10.3 Approximation of non-smooth and near-singular functions

The true power of the partition of unity comes into play when the functions are discontinuous across the patch boundaries. To demonstrate this, consider a function that is first order discontinuous on a line that does not coincide with the patch

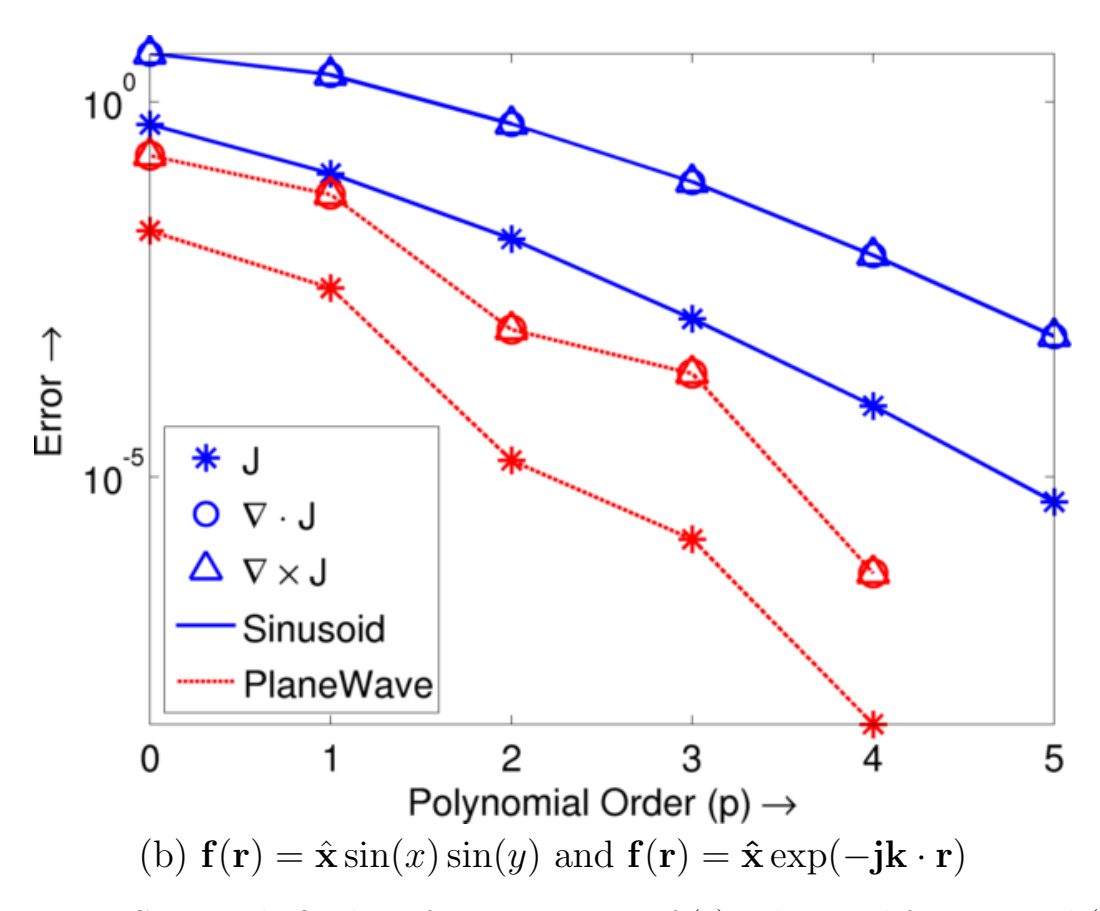


Figure 4.9 Continued: Quality of approximation of (a) polynomial function and (b) sinusoidal functions.

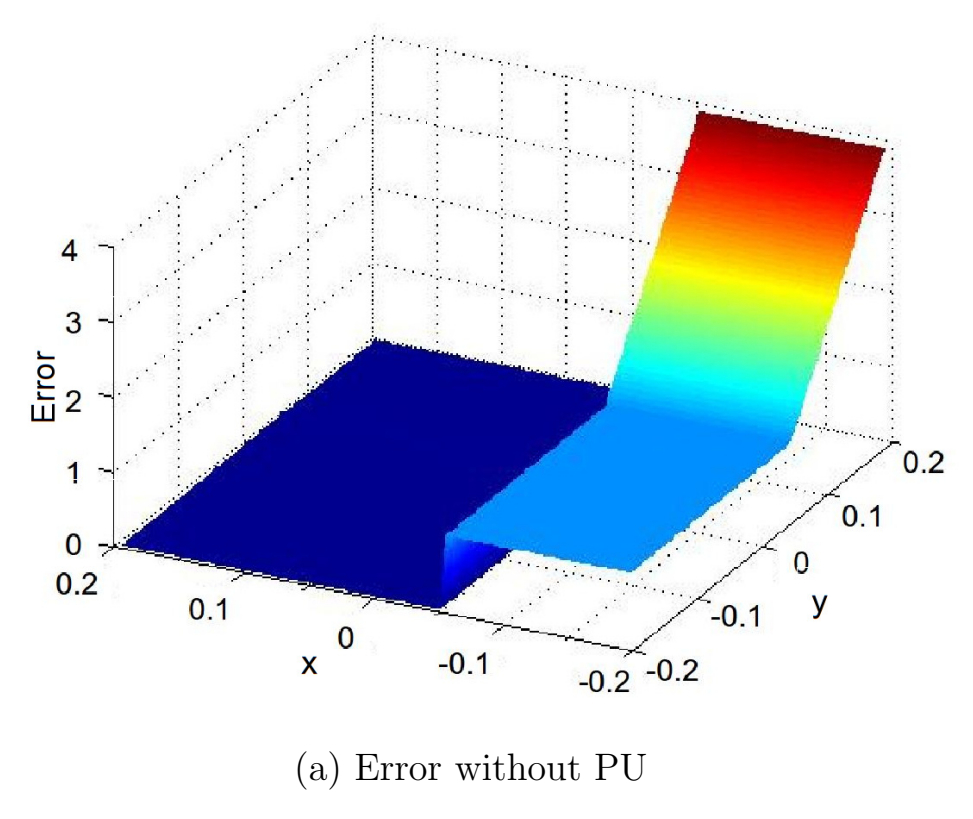


Figure 4.10: Quality of approximation of discontinuous function: (a) without using a partition of unity; and (b) with a partition of unity.

boundary described by

$$\mathbf{f}(\mathbf{r}) = \begin{cases} \hat{x} & \forall \ x \le x_0 \\ \hat{x}x/x_0 & \forall \ x \ge x_0 \end{cases}$$
 (4.34)

Fig. 4.10a shows the approximation error obtained by using two separate functions in each patch without overlapping patches or a partition of unity. As can be clearly seen, the error in the function propagates through the patch because the discontinuity does not coincide with the patch boundary. Fig. 4.10b on the other hand, shows the same function approximated by overlapping patches and a partition of unity. As the figures clearly show, the error is significantly better in the GMM basis function framework.

Next, we examine the efficacy of using a GMM framework in approximating cur-

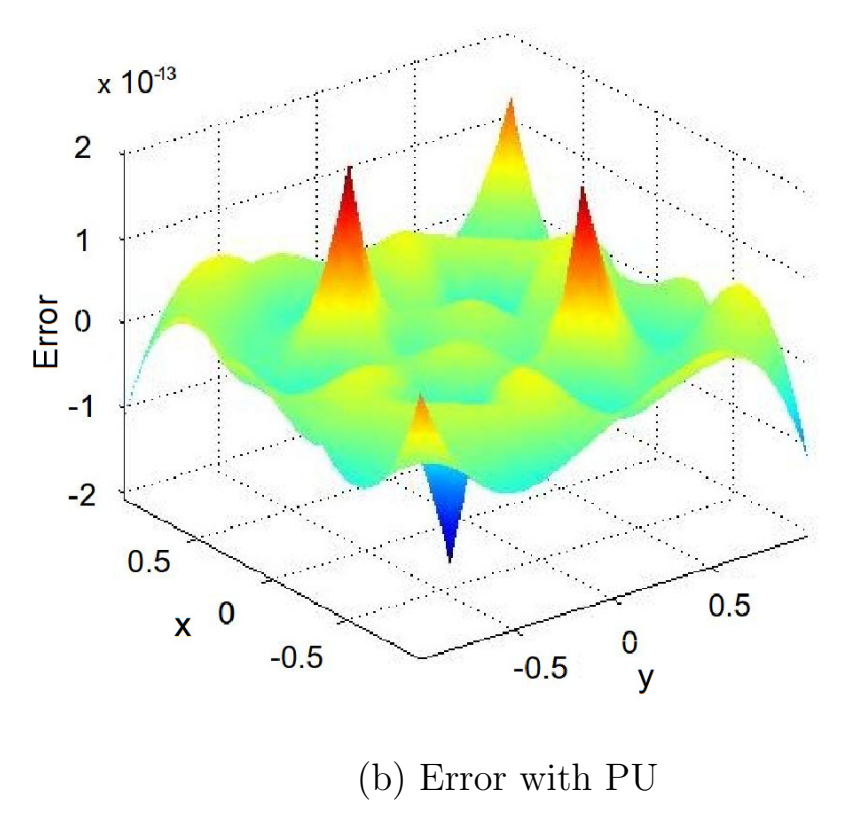


Figure 4.10 Continued: Quality of approximation of discontinuous function: (a) without using a PU and (b) with a PU.

rents near a one dimensional edge upto a distance 1m from the tip; see [79,80] and references therein for details of some of the basis functions in current use. Fig. 4.11 demonstrates the error convergence as a function of the number of unknowns for three different types of basis functions that are detailed next. Typically, the current perpendicular to the edge is modeled using leading order terms from a Meixner series expansion (as $1/\sqrt{d}$ where d is the distance from the edge). In [79], this dependence is incorporated by changing the basis function in the patch near the edge. Specifically, in [79] the domain is partitioned into segments of size h; in the patch nearest the edge, the basis function is chosen to be the leading term of the Meixner series, and in all other patches it is either a pulse or a hat function. In figure 4.11, we examine the error convergence, as a function of the number of unknowns, for the approximation to the current near a one dimensional edge. Fig. 4.11 shows three error curves, the first is obtained using the basis functions in [79]. In this case, the basis function in the first patch is $1/\sqrt{d}$ where d is the distance from the edge/tip. Starting from the second patch onwards hat functions are used as basis. This result establishes a baseline for comparison of convergence. The second curve is obtained using basis functions that are a combination both singular functions and higher order polynomials. Specifically, patches comprise of two adjacent segments. On patches that lie within a perpendicular distance of 0.1m of the edge, it is assumed that basis functions are a superposition of singular functions of the form $1/\sqrt{d}$ where d is the distance from the origin and polynomials that are complete to order p = 2. As is evident from fig. 4.11, this class of basis functions provides better approximating properties. The third curve in fig. 4.11 demonstrates the convergence obtained by using a partition of unity function. As before, patches are defined to comprise of two adjacent segments. For all patches whose perpendicular distance is less than 0.1mfrom the edge, basis functions comprise of a linear combination of singular functions $(1/\sqrt{d})$ and polynomials complete to p=1, both of which multiplied by a linear PU function. For all patches that are further from this point, the basis function is a product of a linear PU function and a polynomial of order p = 1. The use of a lower order polynomial ensures that the order of the basis function is p = 2. As is evident, the approximation provided by this scheme is considerably better than the previous case. In large part, this result is due to better continuity properties offered by the PU function; proofs for convergence of approximation to scalar and vector functions have been provided in [76,77].

As can be seen from all the examples presented in this Section, for a series of discretizations, the PU-based approximation consistently performs well. To a large extent, this is a consequence of the GMM framework which decouples the traditional link between tessellation and the basis function definition. In other words, it is possible to define dramatically different basis functions in the same patch (or adjacent patches) without worrying about auxiliary conditions to maintain continuity. Continuity of these functions is provided by the partition of unity function. As a result, the quality of approximation is better. In the next Section, we further explore the capabilities of this representation by applying it to compute electromagnetic scattering

4.11 Scattering Results

In this section, we compare the radar cross-section from a variety of PEC objects. Unless otherwise noted, in all examples that follow, the incident field is assumed to be $\hat{\mathbf{x}}$ polarized and propagating along the $-\hat{\mathbf{z}}$ direction. The object is discretized using a triangulation such that the average edge length is 0.1λ and GMM patches are constructed using the scheme outlined in this paper. Since the GMM patches are of arbitrary shape, we define the side of the smallest enclosing cube for each GMM patch as an equivalent "edge length" (h). In the following examples, h varies

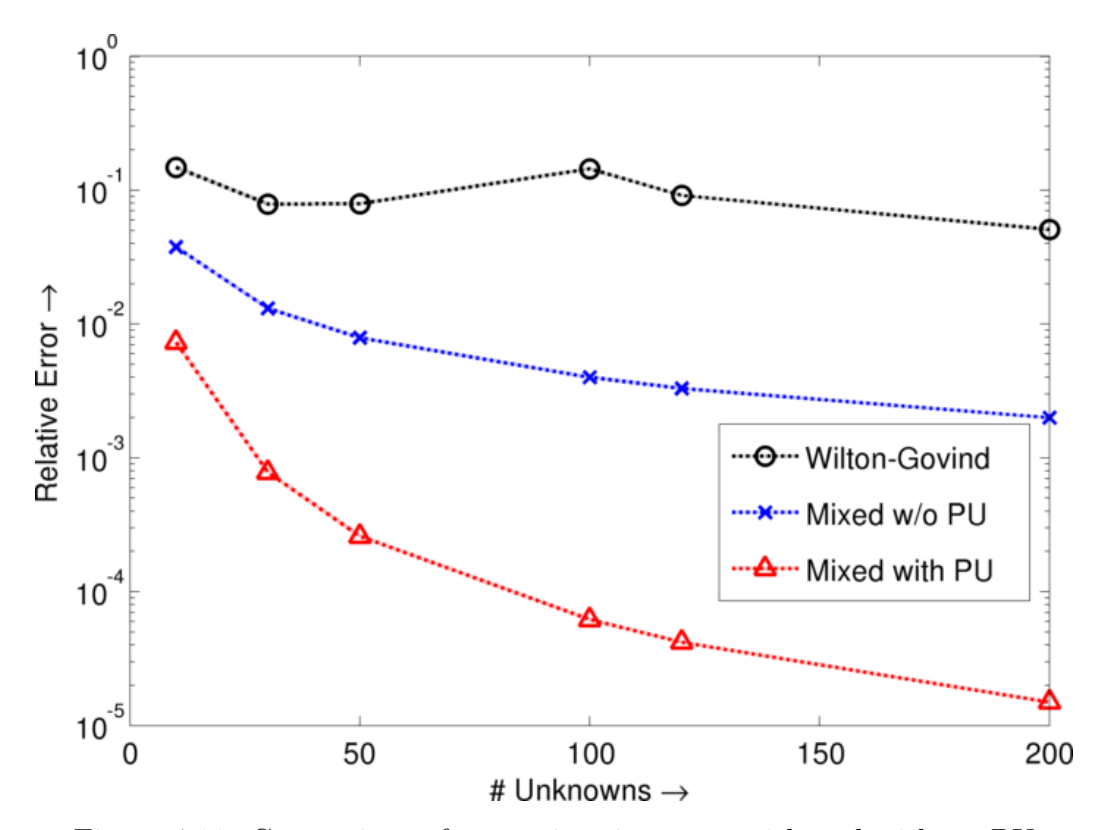


Figure 4.11: Comparison of approximation error with and without PU.

from 0.1λ to 0.4λ , where λ is the wavelength of the incident field. Unless specified otherwise, the GMM approximation functions, ϕ_i^m and ζ_i^m , were constructed using Legendre polynomial functions complete to order p. Finally, note that the underlying triangulation used is the same for both GMM and RWG or its higher order variant. In what follows, we have used the notation "higher order RWG" to denote basis functions develop by Graglia, Wilton and Peterson [74].

4.11.1 Analytical Validation and p-convergence

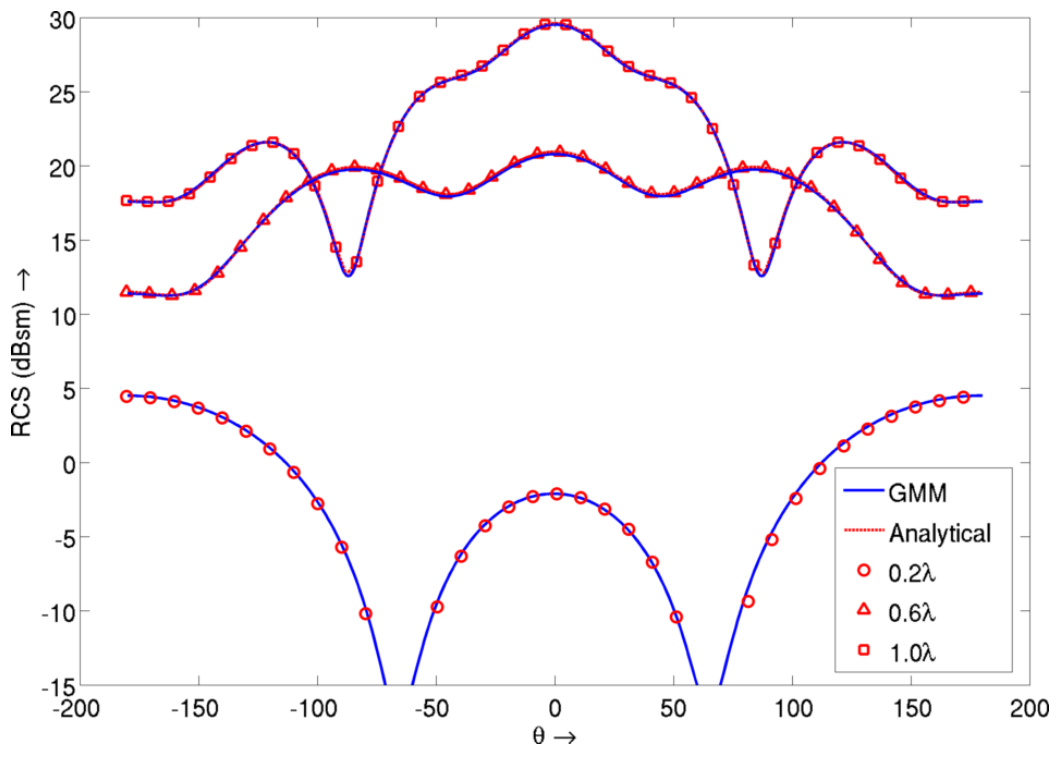
Fig. 4.12a compares the RCS of a PEC sphere obtained using GMM against analytical solutions evaluated using a Mie-series representation. The number of GMM unknowns (N_{GMM}) used is 200, 776 and 3080 for spheres of radii 0.2λ , 0.6λ and 1.0λ respectively. As is evident, the agreement between the two is excellent. Fig. 4.12b compares the convergence of the error as a function of the polynomial order of the basis function

used, for both the GMM and higher order RWG [74]. The comparison is performed for backscattered data obtained from two scatterers (i) a sphere of diameter 1.0λ and (ii) a NASA almond that fits in a box of dimensions $0.4\lambda \times 1.15\lambda \times 3\lambda$. The number of unknowns for the sphere is as follows: $N_{GMM} = 964$, 2604 and 5208 for p = 1, 2, 3, respectively. The number of higher order RWG unknowns are $N_{RWG} = 4230$, 9072, 15552 at p=1, 2 and 3, respectively. For the almond, $N_{GMM}=948, 4656$ and 7560 at $p=2,\,3$ and 4, respectively and $N_{RWG}=3800,\,7980$ and 13680 at $p=2,\,3$ and 4, respectively. In all cases, the incident field was $\hat{\mathbf{x}}$ polarized and incident along $\hat{\mathbf{z}}$. The axis of the almond was oriented along $\hat{\mathbf{x}}$. The convergence is evaluated for the error between the numerical and analytical solution for the sphere and for the relative error between successive steps in the case of the almond. In each case, the approximation functions used for GMM were p-order complete polynomials in each of the local projection co-ordinate spaces. Correspondingly the basis functions used for higher order RWG were of the type suggested in [74] and are complete to order p. The exponential nature of the convergence is clearly evident from the figure. It is interesting to note that the convergence rate for the GMM scheme seems consistently better than that for RWG for both the geometries.

4.11.2 Comparison with standard RWG

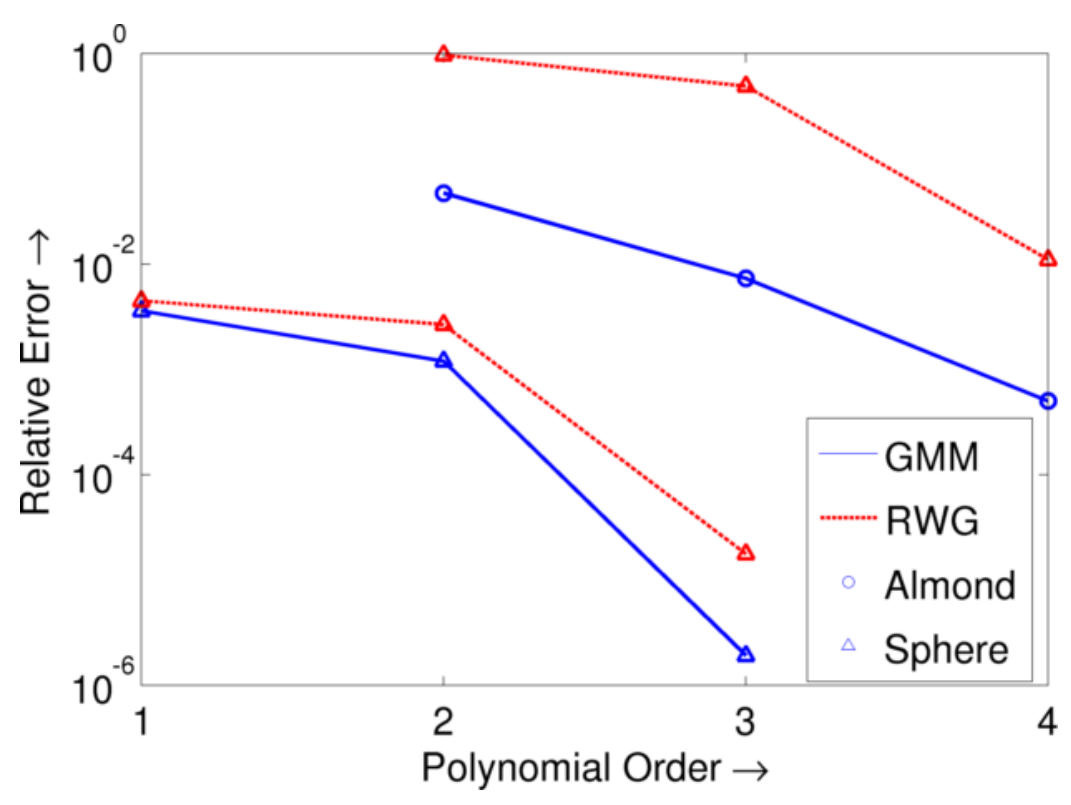
In this section, the RCS obtained due to scattering from a variety of geometries is computed using the GMM basis functions and compared against that obtained using RWG basis functions. In all cases, first order complete polynomials were used to construct basis functions for the GMM. Similarly first order RWG functions were used for the RWG scheme.

Fig. 4.13a shows the RCS from a square PEC plate of side λ discretized using 248 effective GMM unknowns (N_{GMM}) and 228 RWG unknowns (N_{RWG}) ; and an open cavity of dimensions $\lambda \times \lambda \times \lambda$ $(N_{GMM}=402, N_{RWG}=1746)$. The incident field



(a) Comparison with analytical solution for PEC sphere of various radii

Figure 4.12: Validation studies: Scattering from PEC spheres of different radii. Fig. (a) shows the RCS comparison and figure (b) shows the convergence of solutions with basis order p.



(b) Convergence with polynomial order (Sphere and NASA Almond)

Figure 4.12 Continued: Validation studies: Scattering from PEC spheres of different radii. Fig. (a) shows the RCS comparison and figure (b) shows the convergence of solutions with basis order p.

is $\hat{\mathbf{x}}$ polarized and propagates along $\hat{\mathbf{z}}$. The RCS is computed by an EFIE formulation discretized using both the GMM and a standard RWG. It is evident that the GMM result agrees very well with the standard RWG formulation.

Fig. 4.13b compares the RCS obtained due to scattering from a sphere of radius $1.0\lambda~(N_{GMM}=1736,~N_{RWG}=4320)$, an EMC benchmark cone-sphere of height 2.6λ and radius $0.5\lambda~(N_{GMM}=1792,~N_{RWG}=1656)$ and a NASA almond that fits in a box of dimensions $0.4\lambda\times1.15\lambda\times3\lambda~(1:3:9)~(N_{GMM}=1528,~N_{RWG}=2800)$. The cone-sphere and the almond are both oriented with their long axis along $\hat{\mathbf{x}}$. In each case, the incident field is $\hat{\mathbf{x}}$ polarized and propagates along the $\hat{\mathbf{z}}$ direction. Both the GMM and the MoM results are computed using a CFIE. While the sphere and cone-sphere results are obtained using polynomials of order p=1, the almond results are obtained for both p=1 and p=2. As is evident from the figures, the agreement between the GMM and MoM is excellent.

4.11.3 Comparison with measured data

Finally, we consider scattering from a PEC cube of side 0.7λ . The cube was discretized using $N_{GMM}=320$ and $N_{RWG}=1500$ unknowns. Measured data has been reported for scattering from this structure in [109]. Again, electric field polarized along $\hat{\mathbf{x}}$ is assumed in the $\hat{\mathbf{z}}$ direction. Fig. 4.14 shows the comparison of RCS obtained by GMM and RWG against that obtained from experimental measurement. Again, there is excellent agreement between all three RCS data sets. These numerical experiments demonstrate the ability of the GMM technique to accurately use first and higher order polynomial basis functions to compute scattering cross-sections from a wide variety of geometries.

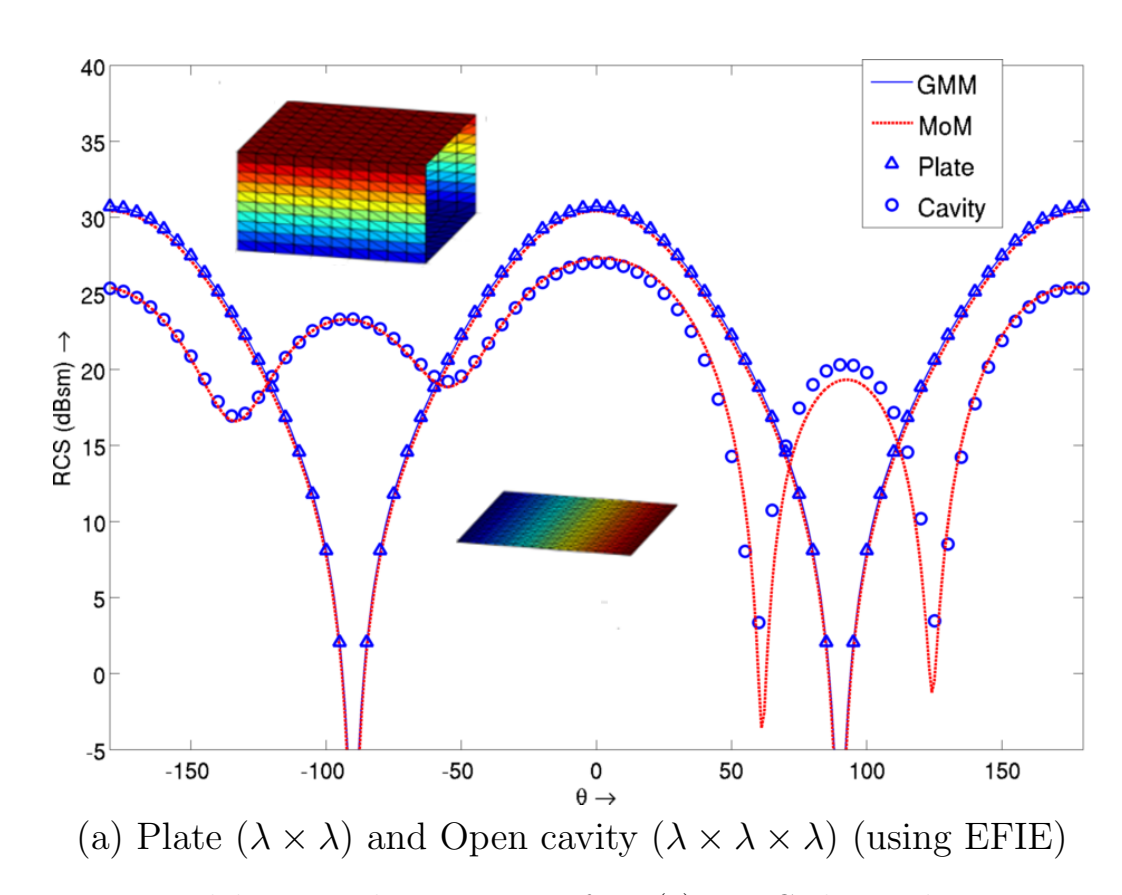
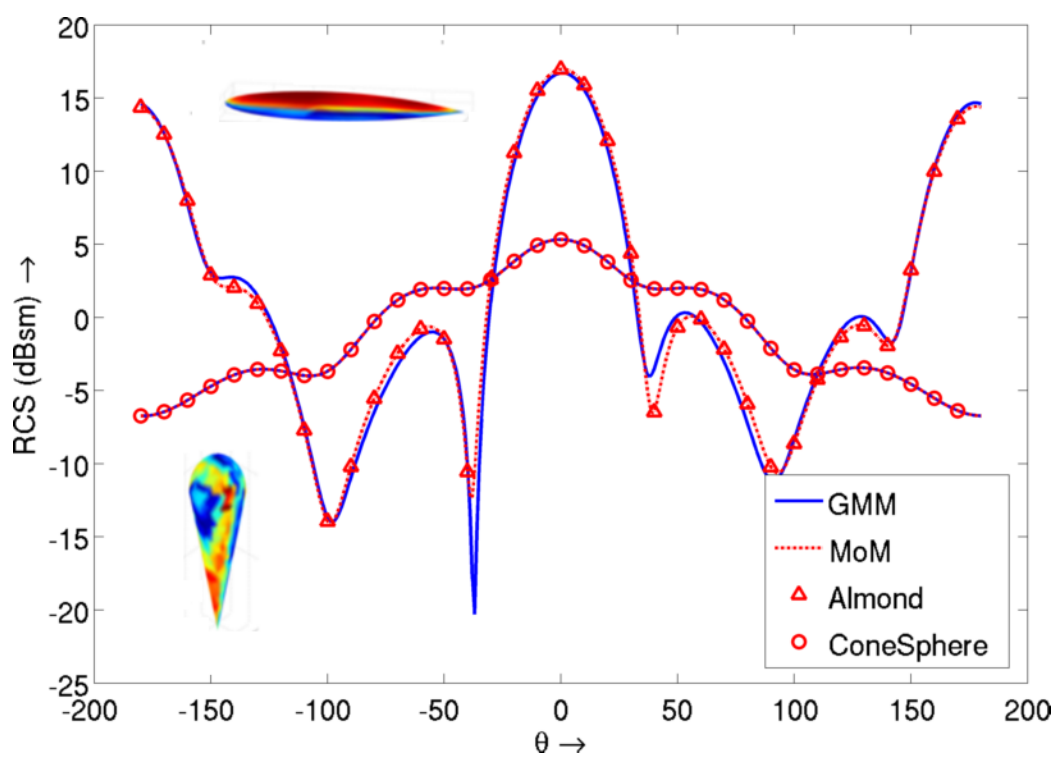


Figure 4.13: Validation studies: scattering from (a) a PEC plate and an open cavity. Plot of bistatic RCS ($\phi=0$). Fig. (b) bistatic scattering RCS from a NASA thin almond and a PEC conesphere. The RCS is compared at $\phi=0$ for the almond and $\theta=\pi/2$ for the conesphere. Inset figures show the surface current on the almond and the conesphere.



(b) Sphere (λ), Conesphere ($2.6\lambda \times 0.5\lambda$) and NASA Almond (1:3:9) (using CFIE)

Figure 4.13 Continued: Validation studies: scattering from (a) a PEC plate and an open cavity. Plot of bistatic RCS ($\phi = 0$). Fig. (b) bistatic scattering RCS from a NASA thin almond and a PEC conesphere. The RCS is compared at $\phi = 0$ for the almond and $\theta = \pi/2$ for the conesphere. Inset figures show the surface current on the almond and the conesphere.

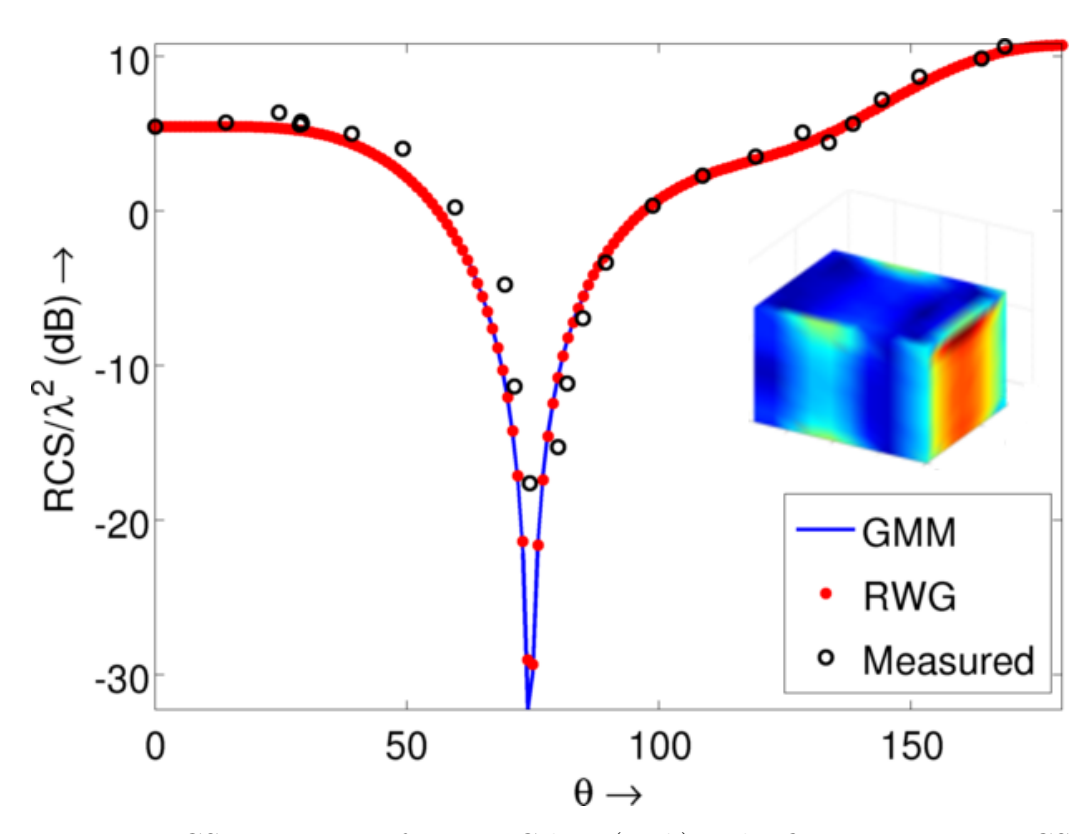


Figure 4.14: RCS comparison for a PEC box (0.7λ) . The figure compares RCS due to scattering of a $-\hat{\mathbf{x}}$ directed plane wave polarized along $-\hat{\mathbf{y}}$. The bistatic RCS is compared at $\phi=0$ against that obtained using an RWG discretization and against measured data.

4.12 Flexibility of the GMM scheme

The results presented thus far demonstrate the approximation quality of GMM basis functions, the convergence characteristics and applicability to calculating scattered fields from a variety of topologically different objects. In addition, the GMM scheme also provides the flexibility to mix different types of orders and types of basis functions, and use non-conformal meshes with minimal change to the overall computational structure. The examples presented in this section demonstrate these advantages. In all cases analyzed in this section, the incident field is polarized along the \hat{x} direction and the field is incident along the $-\hat{z}$ direction.

4.12.1 Mixing orders of basis functions

First, consider a PEC box of dimensions $\lambda \times 4\lambda \times \lambda$ that is oriented along the hatx direction. This box is meshed at 0.1λ everywhere to obtain an initial triangulation. GMM patches and basis functions complete to order p=1 are constructed to obtain the RCS due to illumination by a \hat{z} directed incident electric field polarized along \hat{E}_x . Next, the same geometry is discretized using an edge length 0.25λ for $0.75\lambda \leq \mathbf{x} \leq 2.25\lambda$ and of edge length 0.1λ elsewhere. Basis functions of order p=2 are used in the larger patches while basis functions of order p=1 are used in the small patches. RCS computed using this configuration is then compared against that obtained earlier using a denser (almost) uniform discretization in figure 4.15a. As is evident, the agreement is excellent. While the agreement between the two RCS data sets demonstrates the ability of the technique to mix different orders of basis functions, the ease with which this mixing can be effected within the GMM scheme is equally important. In our implementation, types and orders of basis functions to be used in a patch are specified by an input flag. This level of flexibility in choice of basis functions is unique to the GMM scheme.

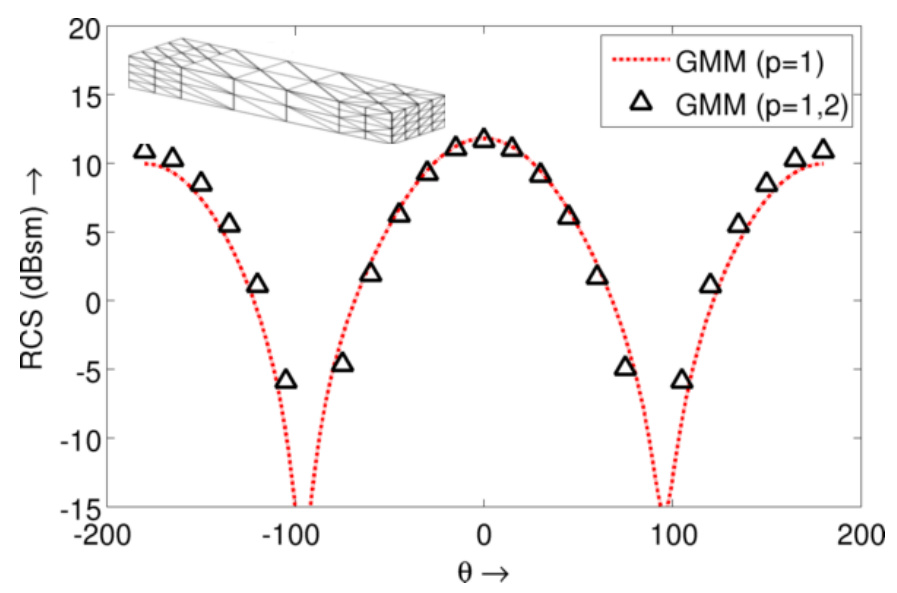
Fig. 4.15b demonstrates two RCS obtained due to scattering from a PEC almond that fits in a box of size $0.3\lambda \times \lambda \times 3.2\lambda$. The first RCS is obtained using basis functions of order p=1 everywhere and then second is obtained using basis functions of order p=2 in all patches within 0.2λ of the tip and p=1 everywhere else. Again, the agreement of between the two RCS data is excellent and demonstrates the ability of the GMM technique to mix different basis functions.

Finally, figure 4.15c shows RCS due to scattering from a PEC box of size $3\lambda \times 6\lambda \times 3\lambda$; meshed at three levels of discretization as shown in the inset figure. The discretizations are at $0.1\lambda, 0.2\lambda and 0.25\lambda$. The RCS is computed using polynomials of orders p=1,2,3 in each discretization range. This RCS is compared against one obtained using RWG basis functions on a uniform discretization of 0.1λ ; and as can be seen from the figure, both results agree very well with each other.

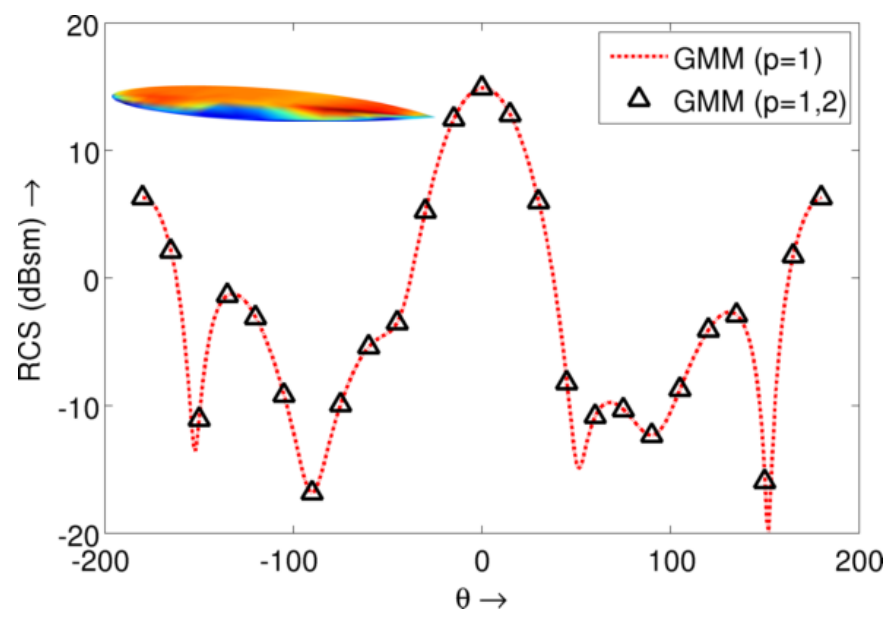
4.12.2 Mixing types of basis functions

The GMM scheme not only permits mixture of different orders of polynomial basis functions, but enables mixtures of different types of basis functions. As was mentioned earlier, the surface Helmholtz decomposition based system using scalar polynomial functions is only one possible way to define basis functions. In the following example, we demonstrate that these functions can be effortlessly combined with functions of the form $\hat{c}e^{i\mathbf{k}\cdot\mathbf{r}}$ where \hat{c} is a pilot vector and \mathbf{k} is the propagation vector.

Consider scattering from a PEC box of size $\lambda \times 0.5\lambda \times 0.5\lambda$. Three sets of RCS data are compared in figure 4.16. One is obtained using GMM based polynomial basis functions of order p=1 everywhere. The other two use a combination of polynomials of order p=1 and plane-wave basis as described next. The plane wave basis functions used are defined as follows: $\boldsymbol{\nu}_i^m$ for patch Ω_i is defined as $\boldsymbol{\nu}_i^{m,1} = \hat{u}e^{i\mathbf{k}m\cdot(\mathbf{r}-\mathbf{r}_i)}$ and $\boldsymbol{\nu}_i^{m,2} = \hat{v}e^{i\mathbf{k}m\cdot(\mathbf{r}-\mathbf{r}_i)}$ where \hat{u} and \hat{v} are the local coordinate vectors, \mathbf{r}_i is the center of patch i, and \mathbf{k}_m is defined as $(\mathbf{k}\cdot\hat{u})\cos(m\pi/(M+1))\hat{u} + (\mathbf{k}\cdot\hat{v})\cos(m\pi/(M+1))\hat{u}$

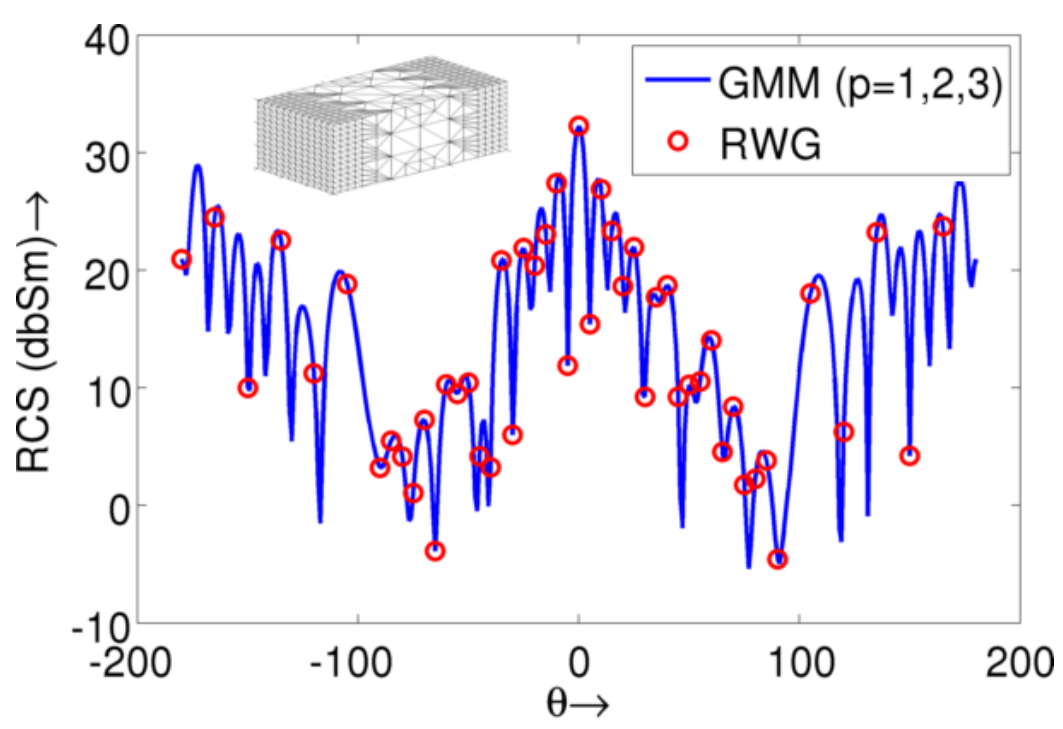


(a) PEC box $(\lambda \times 4\lambda \times \lambda)$: GMM mixed order $(p = \{1, 2\})$ vs. standard GMM p = 1.



(b) NASA Almond (1:3:9): GMM mixed order $(p = \{1, 2\})$ vs. standard GMM p = 1.

Figure 4.15: RCS comparison for regular GMM and mixed order GMM: (a) comparison of bistatic RCS ($\phi = 0$) for a PEC box. Fig. (b) shows the comparison of bistatic RCS ($\phi = 0$) for a PEC thin almond. In each case, the incident field is directed along $-\hat{\mathbf{z}}$ and polarized along $\hat{\mathbf{x}}$ and bistatic RCS is evaluated at $\phi = 0$.



(c) PEC Box $3\lambda \times 6\lambda \times 3\lambda$ GMM mixed order $(p=\{1,2,3\})$ vs. RWG p=1.

Figure 4.15 Continued: RCS comparison for regular GMM and mixed order GMM: Fig. (c)comparison of bistatic RCS ($\phi = 0$) for a PEC box using three different orders of basis functions. The incident field is directed along $-\hat{\mathbf{z}}$ and polarized along $\hat{\mathbf{x}}$ and bistatic RCS is evaluated at $\phi = 0$.

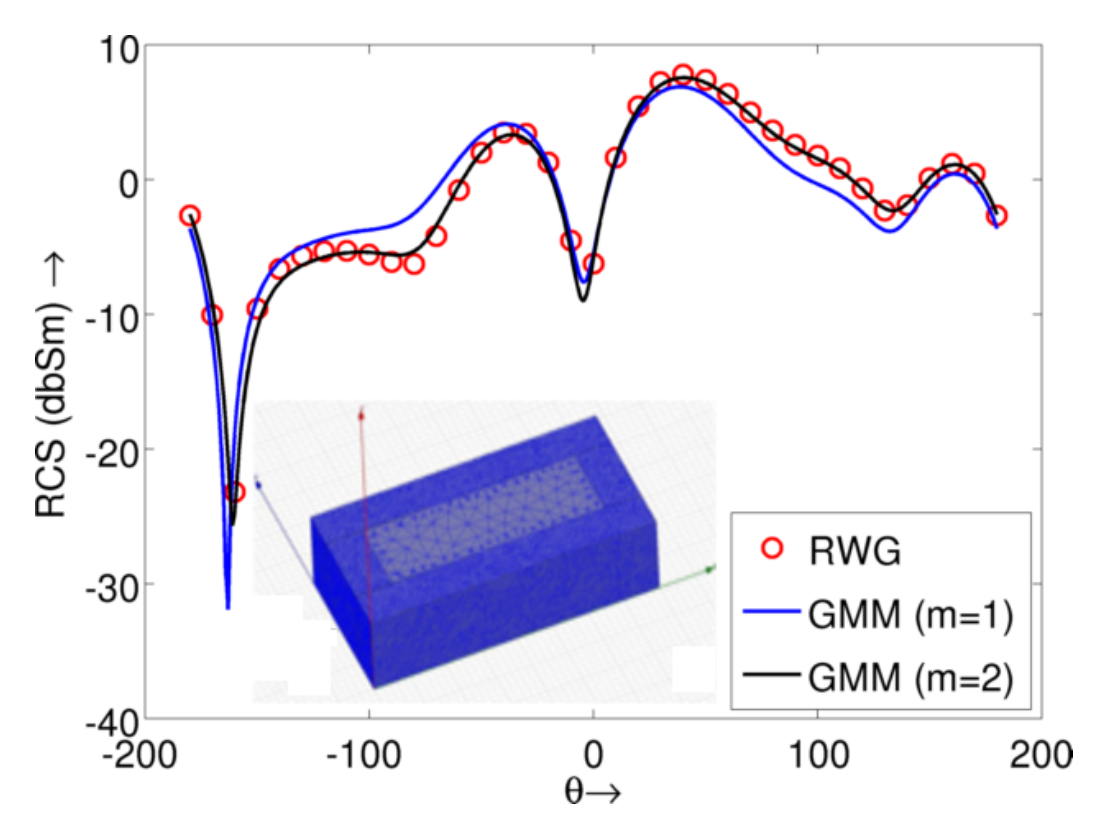


Figure 4.16: RCS obtained due to scattering of a $\hat{\mathbf{x}}$ polarized plane wave directed along $-\hat{\mathbf{z}}$ from a PEC box $(\lambda \times 0.5\lambda \times 0.5\lambda)$ directed along $\hat{\mathbf{x}}$ obtained using regular GMM and mixed basis GMM with polynomials and plane waves.

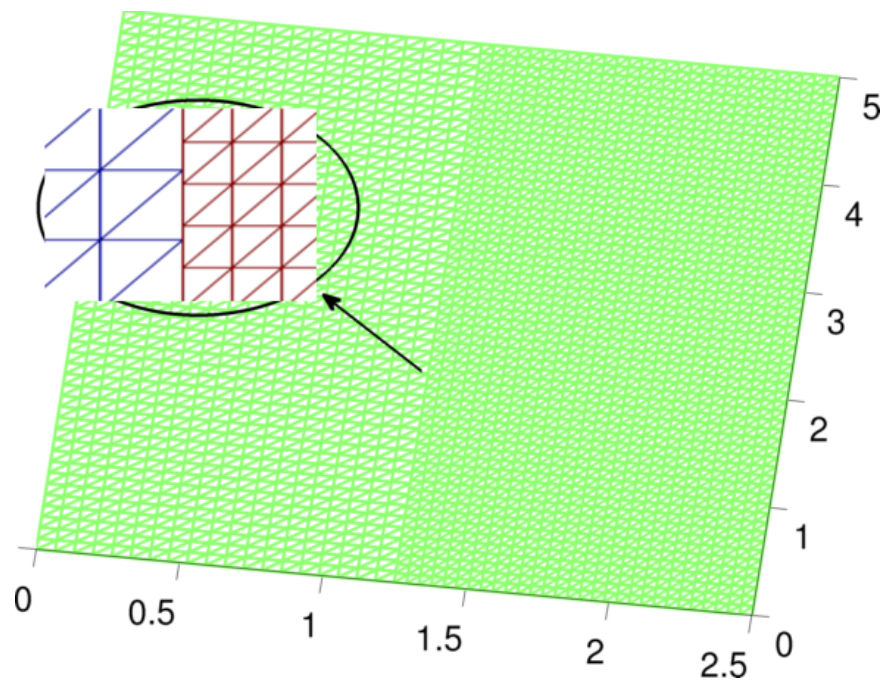
1)) $\hat{v} \forall m \in \{0...M\}$. The three cases that are compared are as follows: (i) only polynomials, (ii) plane waves (M=1) in all patches for $0.4\lambda \leq \hat{\mathbf{x}} \leq 0.6\lambda$ and polynomials elsewhere and finally (iii) using plane waves (M=2) in patches $0.4\lambda \leq \hat{\mathbf{x}} \leq 0.6\lambda$ and polynomials elsewhere. A plane wave electric field polarized along $\hat{\mathbf{x}} - \hat{\mathbf{y}}$ is assumed incident along $\hat{\mathbf{x}} + \hat{\mathbf{y}}$ and the RCS is observed for all θ at $\phi = 0$. It is observed that as the number of plane wave is increased, the RCS obtained rapidly approaches that obtained using purely polynomials. This example illustrates that idea that not only can one used non-polynomial basis functions with ease within the GMM scheme but also use a combination of polynomial and non-polynomial basis functions.

4.12.3 Use of non-conformal meshes

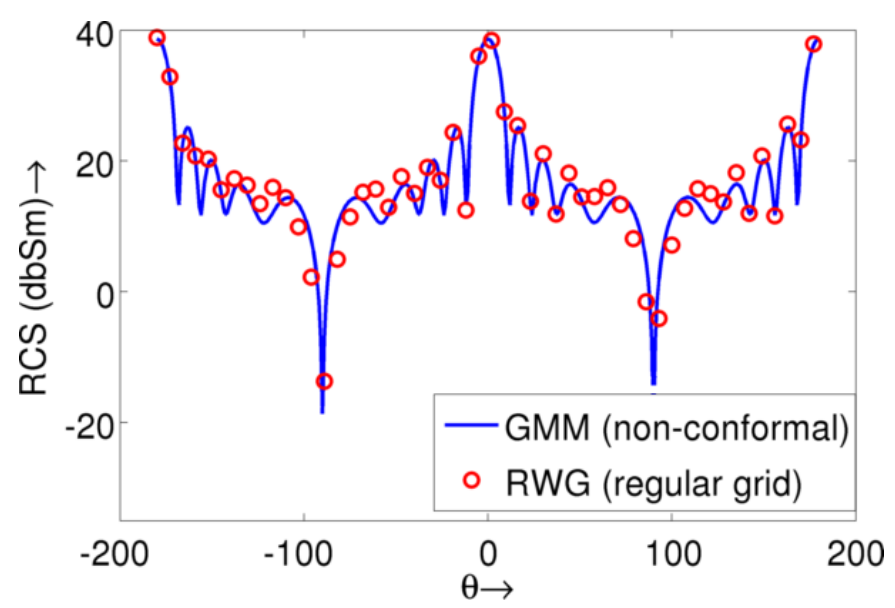
Finally, another advantage of the GMM arises from the initial motivation to separate the basis function definition from the tessellation of the geometry. Since, unlike the RWG, the GMM is not reliant on the tessellation; the GMM can be used with non-conformal meshes. It is common in practice to have different vendors mesh different areas of a geometry and this results in sets of meshes that need to be explicitly "stitched together" at the boundaries. There has been a considerable interest in the design of techniques that can handle non-conformal meshes [110]. However, a consequence of the design of the GMM scheme is that it can implicitly handle these kinds of meshes without any change to the framework or the implementation. Here we present one example illustrating this ability. Fig. 4.17a shows a $\lambda \times \lambda$ plate that is discretized at two slightly different scales; one at 0.1λ and the other at 0.15λ . These two halves are put together and a GMM covering is defined on this "non-conformal" tessellation. Fig. 4.17b shows the RCS obtained using the GMM scheme compared with the RCS obtained using a regular RWG discretization using a conformal meshing at 0.1λ of this plate.

4.13 Condition Number of the System

One of the consequences of using GMM is that the resultant discrete system appears to have a constant condition number over a wide range of frequencies. We have examined the condition number of the system over a wide range of frequencies for a variety of geometries. In each case, we use a constant mesh size that corresponds to an average edge length of 0.1λ at the highest frequency. This is used to construct the GMM patches (h varies from about 0.1λ to 0.4λ). The frequency is continuously reduced from 300MHz to 3Hz. The condition numbers of the impedance matrix obtained using regular RWG, GMM and loop-star basis functions are compared.



(a) PEC plate $(\lambda \times \lambda)$ discretized using two non-conformal meshes



(b) RCS comparison with standard RWG (on conformal mesh)

Figure 4.17: Backscatter RCS comparison for scattering from a non conformally meshed PEC plate (shown in figure (a)) RCS obtained by using the GMM discretization on a non conformal mesh compared against that obtained by discretizing on a (standard) conformal mesh for a PEC plate.

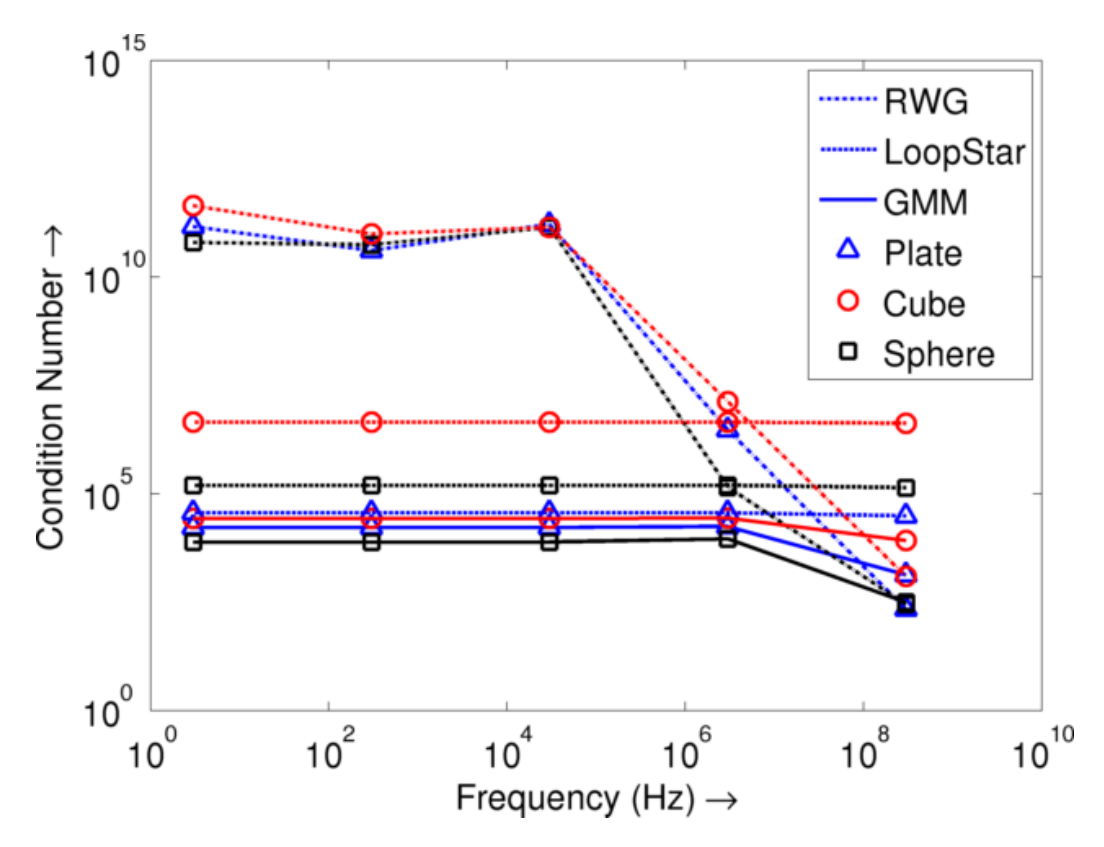


Figure 4.18: EFIE Condition number comparisons for PEC sphere (0.2), square plate (1m) and cube(1m) using GMM, RWG and loop star basis.

Fig. 4.18 shows the condition numbers for three geometries (i) PEC plate (size $1m \times 1m$, $N_{GMM} = 248$, $N_{RWG} = 228$) (ii) PEC cube (side 1m, $N_{GMM} = 320$, $N_{RWG} = 1500$) and a sphere (0.2m diameter, $N_{GMM} = 384$, $N_{MoM} = 480$). As expected, the regular MoM discretization is ill-conditioned at low frequencies. The loop-star scheme and the GMM scheme results in discrete systems with a constant condition number across a range of frequencies. It is evident from the figures that the condition number of the GMM scheme stays constant and is always less than or equal to the condition number of the loop-star scheme.

The above results demonstrated condition number for discretization using linear basis functions. Fig. 4.19 shows the condition numbers obtained on discretizing using higher order basis functions for a 0.2m diameter PEC sphere and PEC strip of dimensions $1m \times 0.2m$. The approximation functions used are third order complete

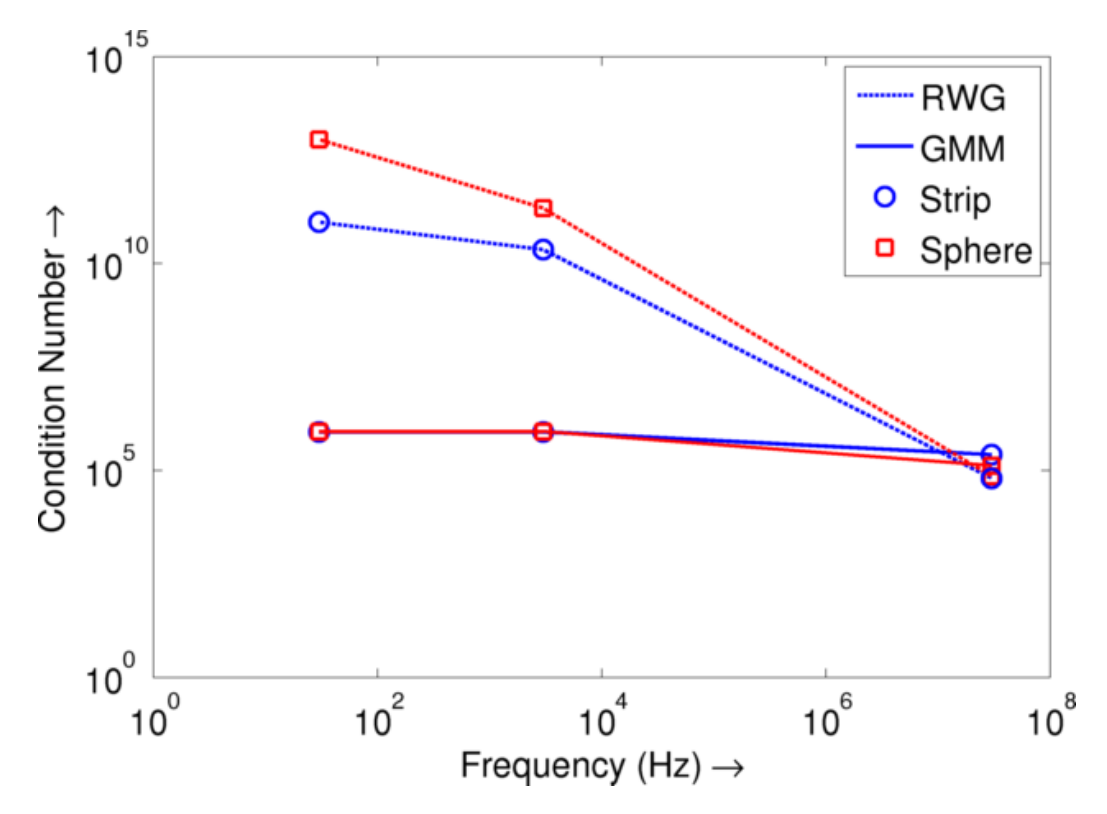


Figure 4.19: EFIE Condition number comparisons for PEC sphere (0.2m) and strip $(1m \times 0.2m)$ using higher order (p=3) complete GMM and RWG basis.

and the condition numbers are compared against those obtained using a higher order RWG scheme using higher order RWG basis functions of the same order. Again, it is evident that the RWG condition number increases exponentially with frequency, whereas the GMM condition number remains constant.

The purpose of a low frequency stable system is the ability to handle meshes involving a large range of discretization sizes. To test the efficacy of the GMM scheme on such structures, we compare the GMM scheme with a standard RWG scheme on two geometries using multi-scale discretizations. Fig. 4.20 shows the variation of the condition number with frequency of the impedance matrix generated for a square PEC plate (side 1m) and a thin almond of aspect ratio 1:3:9, both discretized non-uniformly. The ratio of the largest to smallest edge length used is 1:4 for the plate and 1:10 for the almond. The condition number is compared with both an RWG and

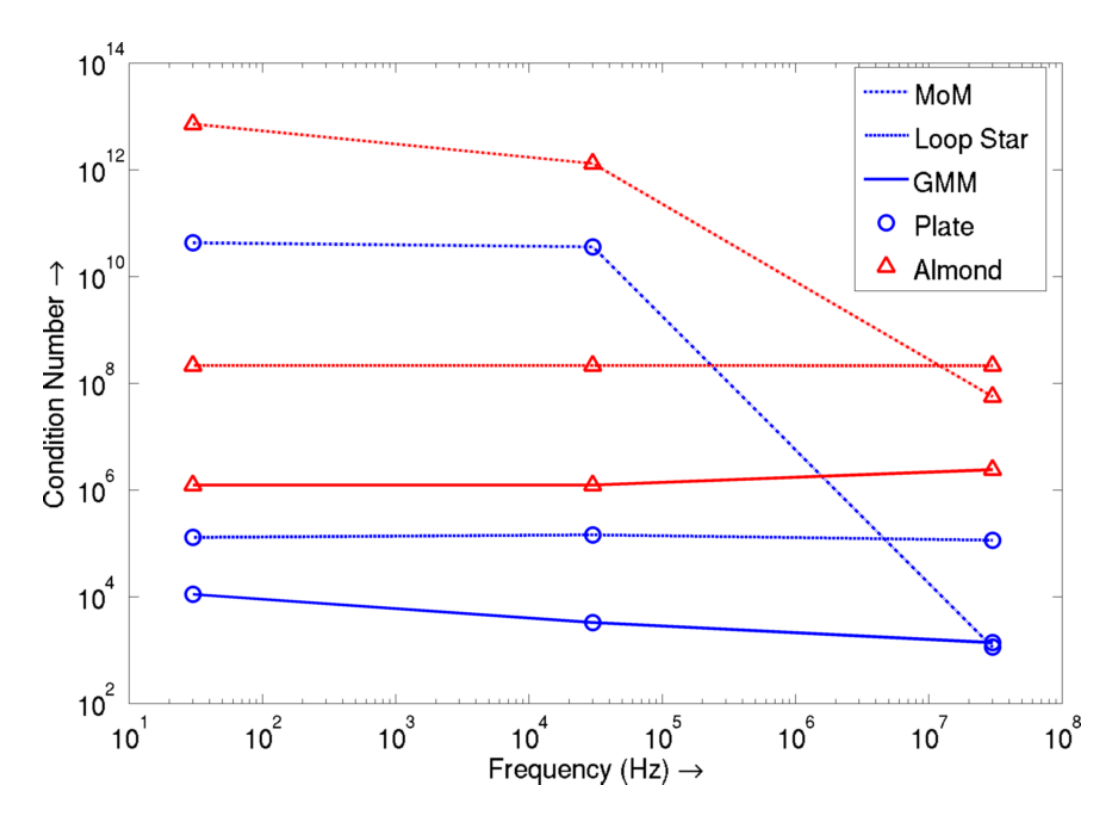


Figure 4.20: EFIE Condition number comparisons for non-uniformly discretized square plate (1m) and thin almond(1:3:9) using GMM and RWG and loop star basis. The plate is discretized at average edge length ranging from 0.1λ to 0.025λ and the almond is discretized from 0.1λ to 0.02λ .

a loop star scheme as the frequency is reduced. As can be clearly seen the condition number of the MoM scheme grows exponentially whereas the GMM condition number varies very slowly with frequency.

Finally, Fig. 4.21 shows the RCS for a square PEC plate (of side 1m) obtained using the GMM and loop star basis functions. The figure shows the RCS at three different frequencies (30MHz, 30kHz and 3kHz). The excellent agreement at all three frequencies demonstrate the low frequency accuracy of the proposed GMM scheme.

The variety of examples presented above demonstrate the ability of the GMM scheme coupled with the quasi-helmholtz basis functions to construct a well conditioned discretization scheme for the EFIE at low frequencies. While the full rationale

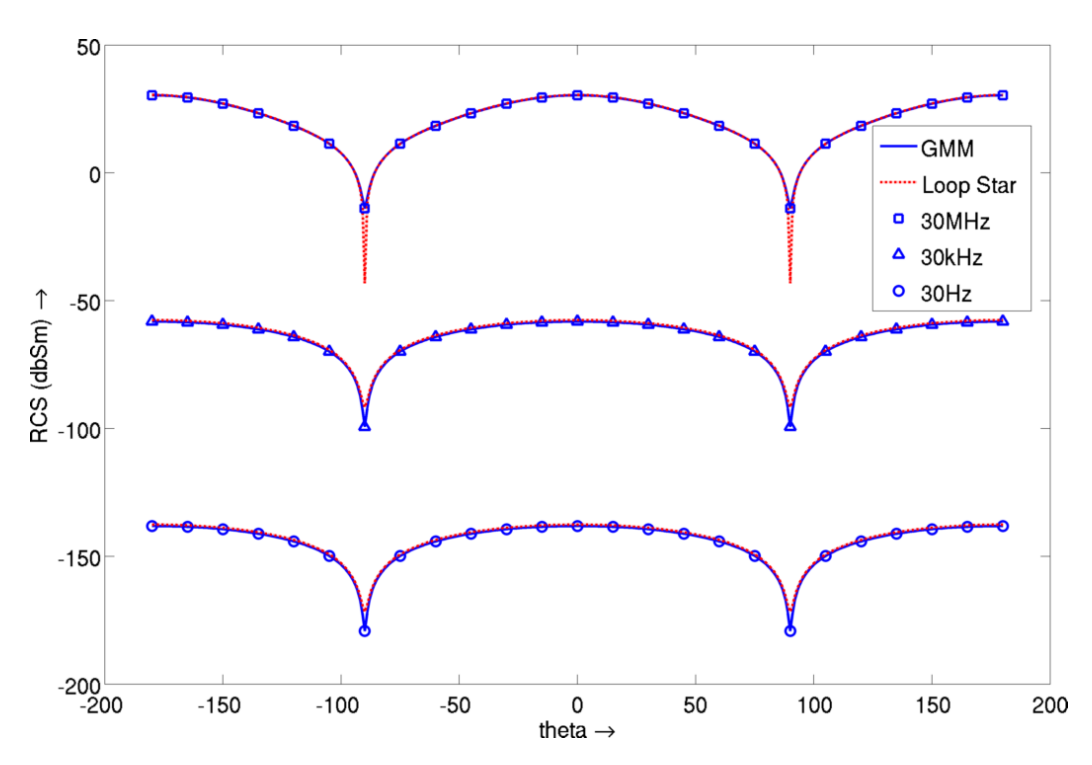


Figure 4.21: Comparison of RCS (GMM vs. loop star) at 30MHz, 30kHz and 3kHz for constant h for a Plate: side 1m. The RCS is compared against that obtained using Loop Star basis functions.

for this behavior is still under investigation; the quasi-Helmtholtz nature of the basis functions is expected to be the major contributing factor to the well conditioned nature of the scheme. As an illustration of this idea; in figure 4.22 we study condition numbers for a PEC box of sides $0.5m \times 0.5m \times 0.1m$ where we use just one of the two types of basis functions in each patch (we use the quasi-divergence free basis function). The RCS obtained by using just the quasi-divergence free basis function is compared against the RCS obtained using the complete GMM basis set, to ensure that the currents are represented adequately. The comparison of RCS is shown inset in the figure.

The condition numbers don't seem to maintain the near-constant nature that is seen when the complete basis set is used. This points, indirectly, to the importance of the role played by the quasi-Helmholtz nature of the basis functions. However, it should be pointed out that the GMM framework is crucial to the implementation of a locally quasi-Helmholtz basis function set and therefore; is critical to the well conditioned nature of the discretized integral equation.

Another key feature of the quasi-surface Helmholtz decomposition implemented in the GMM framework is that the decomposition is local to each patch. As a result, this technique is directly applicable to multiply connected domains; as opposed to the loop star system [93] which uses a global Helmholtz decomposition. A problem with a global Helmholtz decomposition can be viewed as a result of the Hodge decompositions of the surface fields. This means that the loop start technique is not applicable to multiply connected domains. In contrast, the GMM scheme is directly applicable to multiply connected domains such as a toroid.

To illustrate this, figure 4.23 below compares the scattering from a toroidal scatterer computed using the GMM discretization compared to that obtained using a standard RWG discretization. The incident field direction and polarization is shown inset in the figure. The excellent comparison of the RCS demonstrates the ability

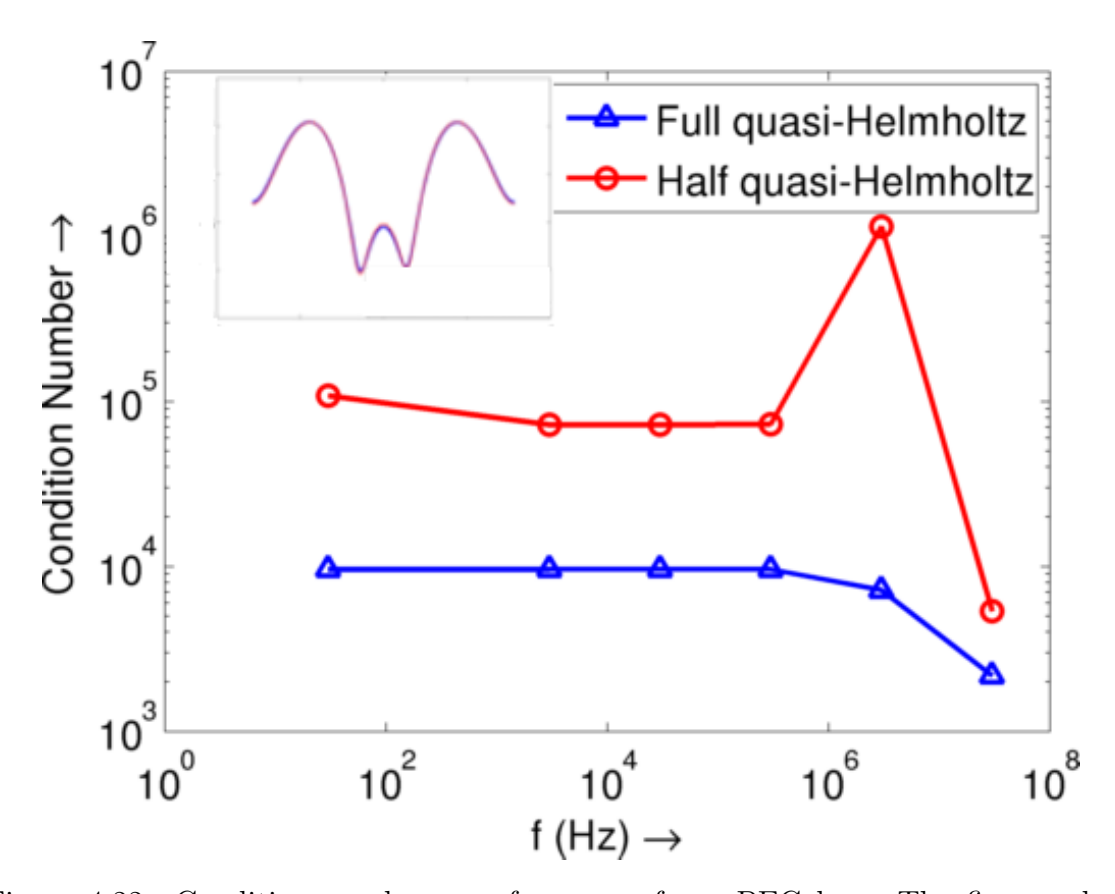


Figure 4.22: Condition number vs. frequency for a PEC box: The figures show the condition numbers using the regular GMM basis set and using just the quasi-divergence free basis functions from the GMM basis set. In each case; the RCS is computed to good accuracy as shown inset.

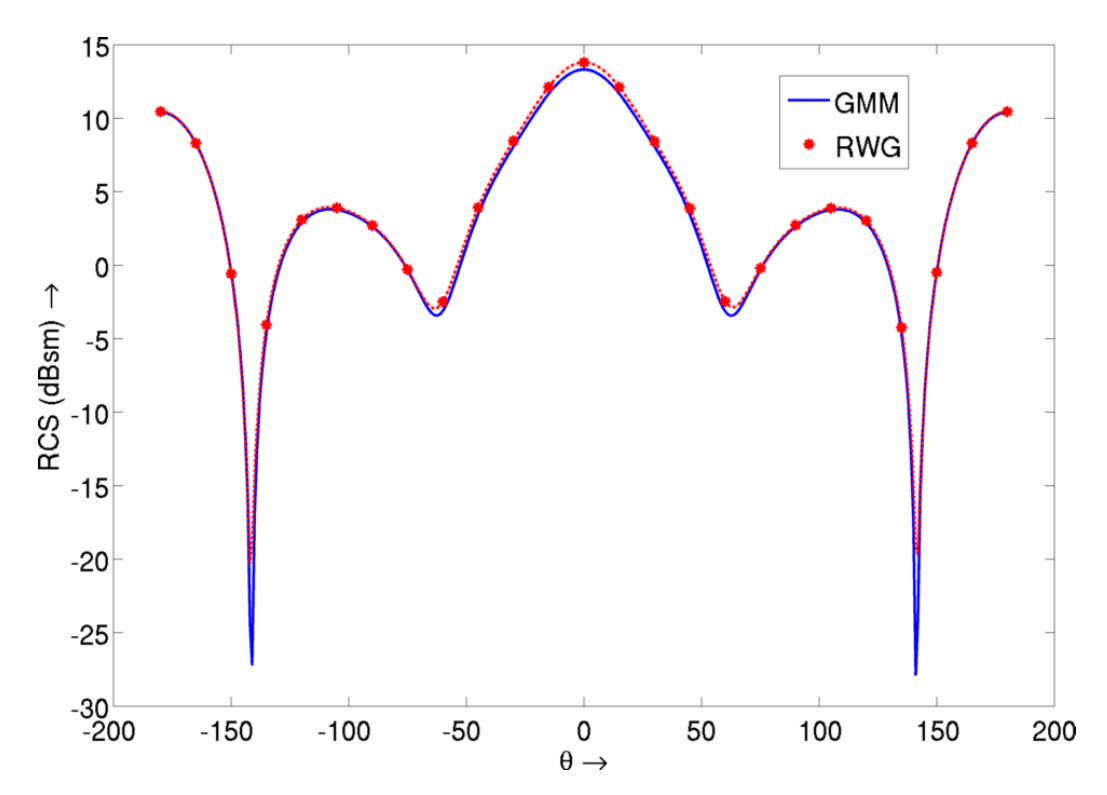


Figure 4.23: Bistatic RCS ($\phi = 0$) comparison for a dielectric toroid (outer radius $0.75\lambda_0$ and inner radius $0.5\lambda_0$, $\varepsilon_r = 4.0$). This result demonstrates the advantage of using an *local* quasi-surface Helmholtz decomposition basis function set. The inset shows direction and polarization of the incident field along with an image of the surface current density on the toroid.

of the GMM framework using the quasi-surface Helmholtz basis functions to handle multiply connected domains.

4.14 Summary

In this work we have presented a framework for the discretization of electromagnetic integral equations that (i) provides considerable freedom over the choice of basis functions and (ii) eliminates the traditional coupling of the basis function and the discretization. Consequently, this provides a general structure wherein different basis functions can be seamlessly integrated to best approximate the currents locally. More importantly, it implies that it is not necessary to have basis functions that satisfy

specific continuity requirements. As this is a departure from standard basis functions defined on tessellations, we have devised a methodology to use existing meshes to define basis functions and their domains of support. Results presented demonstrate the excellent approximation properties of the method as well as far field RCS data from three dimensional objects. Several results have been presented to showcase several of the advantages of the GMM scheme. The results show that the scheme is low frequency stable, can handle mixture of types and orders of basis functions and that the mechanism is able to handle non conformal meshes.

In the next two chapters; we will extend the GMM discretization scheme to the solution of scattering from dielectric bodies and to the analysis of transient scattering respectively.

Chapter 5

Application of the Generalized Method of Moments for Dielectric Bodies

So far, we have restricted our study to scattering from bodies that are perfectly conducting. We will now show how the GMM technique can be extended to the analysis of penetrable scatterers. We will start from the general integral equations developed in chapter 2. We restate the problem and equations slightly differently here, in a form that allows us to specialize to penetrable bodies.

5.1 Problem Statement

Consider a penetrable body that occupies a domain D and is bounded by a surface Ω . Let D_+ and D_- denote regions that are exterior and interior to Ω ; henceforth, the subscript $q = \pm$ will be used to denote all quantities associated with these regions. If no subscript is used, then it is assumed that the quantity is associated with region D_+ . Let the surface Ω be sufficiently smooth so that it is possible to define a unique normal $\hat{\mathbf{n}}_{\pm}(\mathbf{r})$ that points into regions D_{\pm} , respectively. It follows that $\hat{\mathbf{n}}_{+}(\mathbf{r}) = -\hat{\mathbf{n}}_{-}(\mathbf{r}) = \hat{\mathbf{n}}(\mathbf{r}) \ \forall \mathbf{r} \in \Omega$. Further, assume that the object is homogeneous, has permittivity and permeability $\{\varepsilon_{-}, \mu_{-}\}$, respectively, and resides in an unbounded homogeneous background with constitutive parameters $\{\varepsilon_{+}, \mu_{+}\}$. Sources residing within D_q produce incident electromagnetic fields $\{\mathbf{E}_q^i(\mathbf{r}), \mathbf{H}_q^i(\mathbf{r})\}$, and the interaction of these field with Ω produces scattered field $\{\mathbf{E}_q^s(\mathbf{r}), \mathbf{H}_q^s(\mathbf{r})\}$. The total fields in any region, $\{\mathbf{E}_q^{tot}(\mathbf{r}), \mathbf{H}_q^{tot}(\mathbf{r})\}$, comprise of the incident and scattered fields

$$\begin{aligned} \mathbf{E}_q^{tot}(\mathbf{r}) &= \mathbf{E}_q^i(\mathbf{r}) + \mathbf{E}_q^s(\mathbf{r}) \\ \mathbf{H}_q^{tot}(\mathbf{r}) &= \mathbf{H}_q^i(\mathbf{r}) + \mathbf{H}_q^s(\mathbf{r}) \end{aligned} \tag{5.1}$$

The scattered fields within region D_q are produced by equivalent sources that reside on the surface Ω and are defined as

$$\mathbf{M}_{q}(\mathbf{r}) = -\hat{\mathbf{n}}_{q} \times \mathbf{E}_{q}^{tot}(\mathbf{r})$$

$$\mathbf{J}_{q}(\mathbf{r}) = \hat{\mathbf{n}}_{q} \times \mathbf{H}_{q}^{tot}(\mathbf{r})$$
(5.2)

From these definition and the continuity of the tangential components of the fields, it follows that $\mathbf{J}_{+}(\mathbf{r}) = -\mathbf{J}_{-}(\mathbf{r})$ and $\mathbf{M}_{+}(\mathbf{r}) = -\mathbf{M}_{-}(\mathbf{r})$. These currents can be used to define magnetic and electric vector potentials

$$\mathbf{A}_{q}(\mathbf{r}) = \mu_{q} \int_{\Omega} d\mathbf{r}' g_{q}(R) \mathbf{J}_{q}(\mathbf{r}')$$
 (5.3a)

$$\mathbf{F}_{q}(\mathbf{r}) = \varepsilon_{q} \int_{\Omega} d\mathbf{r}' g_{q}(R) \mathbf{M}_{q}(\mathbf{r}')$$
 (5.3b)

where κ_q is the wavenumber in region q, $R = |\mathbf{R}| = |\mathbf{r} - \mathbf{r'}|$, and $g_q(R) = \frac{\exp[-j\kappa_q R]}{4\pi R}$ is homogeneous Green's function with parameters equal to that of region q. These

potentials can in turn be related to the scattered fields via

$$\mathbf{E}_{q}^{s}(\mathbf{r})\left\{\mathbf{J}_{q},\mathbf{M}_{q}\right\} = -j\omega\left(\mathcal{I} + \frac{1}{\kappa_{q}^{2}}\nabla\nabla\right)\cdot\mathbf{A}_{q}(\mathbf{r}) - \frac{1}{\varepsilon_{q}}\nabla\times\mathbf{F}_{q}(\mathbf{r})$$
(5.4a)

$$\mathbf{H}_{q}^{s}(\mathbf{r})\left\{\mathbf{J}_{q}, \mathbf{M}_{q}\right\} = \frac{1}{\mu_{q}} \nabla \times \mathbf{A}_{q}(\mathbf{r}) - j\omega \left(\mathcal{I} + \frac{1}{\kappa_{q}^{2}} \nabla \nabla\right) \cdot \mathbf{F}(\mathbf{r})$$
 (5.4b)

In these equations, \mathcal{I} is used to denote the idempotent. It is well known that knowledge of the equivalent currents is sufficient to express the total fields everywhere via (5.1) and (5.4). Given four equations (two in each region) that can be formulated using these currents, different combinations of these have been developed to solve for the two currents [23]. Of these, the most often used sets are the PMCHWT [26] and the Müller equations [23,111]. The former is a Fredholm first kind integral equation, whereas the second is a Fredholm second kind equation. In what follows, we will present a succinct derivation of both these equations for completeness.

The PMCHWT set of equations is derived by imposing the continuity of each field across Ω . That is, imposing $\hat{\mathbf{n}}(\mathbf{r}) \times \mathbf{E}_{+}^{tot}(br) = \hat{\mathbf{n}}(\mathbf{r}) \times \mathbf{E}_{-}^{tot}(\mathbf{r})$ and $\hat{\mathbf{n}}(\mathbf{r}) \times \mathbf{H}_{+}^{tot}(br) = \hat{\mathbf{n}}(\mathbf{r}) \times \mathbf{H}_{-}^{tot}(\mathbf{r})$ results in

$$\hat{\mathbf{n}}(\mathbf{r}) \times \left[\mathbf{E}_{+}^{inc}(\mathbf{r}) - \mathbf{E}_{-}^{inc}(\mathbf{r}) \right] = \hat{\mathbf{n}}(\mathbf{r}) \times \left[\mathbf{E}_{-}^{s}(\mathbf{r}) \left\{ \mathbf{J}_{-}, \mathbf{M}_{-} \right\} - \mathbf{E}_{+}^{s}(\mathbf{r}) \left\{ \mathbf{J}_{+}, \mathbf{M}_{+} \right\} \right]
= -\hat{\mathbf{n}}(\mathbf{r}) \times \left[\mathbf{E}_{-}^{s}(\mathbf{r}) \left\{ \mathbf{J}_{+}, \mathbf{M}_{+} \right\} + \mathbf{E}_{+}^{s}(\mathbf{r}) \left\{ \mathbf{J}_{+}, \mathbf{M}_{+} \right\} \right]
= -\hat{\mathbf{n}}(\mathbf{r}) \times \left[\mathbf{E}_{-}^{s}(\mathbf{r}) + \mathbf{E}_{+}^{s}(\mathbf{r}) \right] \left\{ \mathbf{J}_{+}, \mathbf{M}_{+} \right\}$$
(5.5a)

$$\hat{\mathbf{n}}(\mathbf{r}) \times \left[\mathbf{H}_{+}^{inc}(\mathbf{r}) - \mathbf{H}_{-}^{inc}(\mathbf{r}) \right] = \hat{\mathbf{n}}(\mathbf{r}) \times \left[\mathbf{H}_{-}^{s}(\mathbf{r}) \left\{ \mathbf{J}_{-}, \mathbf{M}_{-} \right\} - \mathbf{H}_{+}^{s}(\mathbf{r}) \left\{ \mathbf{J}_{+}, \mathbf{M}_{+} \right\} \right]
= -\hat{\mathbf{n}}(\mathbf{r}) \times \left[\mathbf{H}_{-}^{s}(\mathbf{r}) \left\{ \mathbf{J}_{+}, \mathbf{M}_{+} \right\} + \mathbf{H}_{+}^{s}(\mathbf{r}) \left\{ \mathbf{J}_{+}, \mathbf{M}_{+} \right\} \right]
= -\hat{\mathbf{n}}(\mathbf{r}) \times \left[\mathbf{H}_{-}^{s}(\mathbf{r}) + \mathbf{H}_{+}^{s}(\mathbf{r}) \right] \left\{ \mathbf{J}_{+}, \mathbf{M}_{+} \right\}$$
(5.5b)

On the other hand, the Müller equations are obtained using a linear combination of the currents in the two regions and the total fields. In other words, a linear combination of the magnetic currents in the two regions together with the total fields yields

$$-\hat{\mathbf{n}}(\mathbf{r}) \times \left[\mathbf{E}_{+}^{inc}(\mathbf{r}_{+}) + \alpha \mathbf{E}_{-}^{inc}(\mathbf{r}_{-}) \right]$$

$$= (1 + \alpha)\mathbf{M}_{+} + \hat{\mathbf{n}}(\mathbf{r}) \times \left[\mathbf{E}_{+}^{s}(\mathbf{r}_{+}) \left\{ \mathbf{J}_{+}, \mathbf{M}_{+} \right\} + \alpha \mathbf{E}_{-}^{s}(\mathbf{r}_{-}) \left\{ \mathbf{J}_{-}, \mathbf{M}_{-} \right\} \right]$$

$$= (1 + \alpha)\mathbf{M}_{+} + \hat{\mathbf{n}}(\mathbf{r}) \times \left[\mathbf{E}_{+}^{s}(\mathbf{r}_{+}) - \alpha \mathbf{E}_{-}^{s}(\mathbf{r}_{-}) \right] \left\{ \mathbf{J}_{+}, \mathbf{M}_{+} \right\}$$

$$(5.6a)$$

Similar operations on the electric current yields

$$-\hat{\mathbf{n}}(\mathbf{r}) \times \left[\mathbf{H}_{+}^{inc}(\mathbf{r}_{+}) + \beta \mathbf{H}_{-}^{inc}(\mathbf{r}_{-}) \right]$$

$$= -(1+\beta)\mathbf{J}_{+} + \hat{\mathbf{n}}(\mathbf{r}) \times \left[\mathbf{H}_{+}^{s}(\mathbf{r}_{+}) \left\{ \mathbf{J}_{+}, \mathbf{M}_{+} \right\} + \beta \mathbf{H}_{-}^{s}(\mathbf{r}_{-}) \left\{ \mathbf{J}_{-}, \mathbf{M}_{-} \right\} \right]$$

$$= -(1+\beta)\mathbf{J}_{+} + \hat{\mathbf{n}}(\mathbf{r}) \times \left[\mathbf{H}_{+}^{s}(\mathbf{r}_{+}) - \beta \mathbf{H}_{-}^{s}(\mathbf{r}_{-}) \right] \left\{ \mathbf{J}_{+}, \mathbf{M}_{+} \right\}$$

$$(5.6b)$$

where \mathbf{r}_{+} and \mathbf{r}_{-} denote points that are just above and just below \mathbf{r} for all $\mathbf{r} \in \Omega$. In these equation, α and β are constants. In our implementation, we use $\alpha = \varepsilon_{-}/\varepsilon_{+}$ and $\beta = \mu_{-}/\mu_{+}$ as suggested by Müller. To solve these equations numerically, one typically represents the currents in terms of spatial basis functions. That is, $\mathbf{J}_{+}(\mathbf{r}) = \sum_{i=1}^{N_{S}} J_{i}\mathbf{f}_{i}(\mathbf{r})$ and $\mathbf{M}_{-} = \sum_{i=1}^{N_{S}} M_{i}\mathbf{f}_{i}(\mathbf{r})$, where J_{i} , M_{i} are unknown coefficients, $\mathbf{f}_{i}(\mathbf{r})$ are basis functions, and N_{S} is the total number of spatial degrees of freedom for a current. Using Galerkin testing with the same space of basis functions yields a matrix equation that may then be solved for the unknown coefficients. Traditionally, RWG-basis functions have been used to represent the spatial variation of the currents and the fields [89, 112].

5.2 GMM Discretization of the PMCHWT and Müller Integral Equations

The PMCHWT formulation involves the discretization of the $\mathcal{L}_{\pm}|_t$ and the $\mathcal{K}_{\pm}|_t$ operators (where $|_t$ denotes the tangential component of the functional). While the former can be discretized in a manner identical to that done for conducting bodies in chapter 4, the \mathcal{K}_{\pm} operator needs to be handled slightly differently. For self triangles, the integral in the PEC MFIE can be computed for flat patches as as just the principal value component due to the fact that $\hat{\mathbf{n}} \times \mathbf{j}_i(\mathbf{r}) \times \nabla g_{\pm}(R) = 0$, when $\mathbf{r} \neq \mathbf{r}'$. However for the PMCHWT, the tangential component of $\mathbf{j}_i(\mathbf{r}) \times \nabla g_{\pm}(R)$ is 0.

5.2.1 Müller Operator

The discretization of the Müller operator involves the computation of the following bilinear forms.

$$<\mathbf{t}_{j}, \hat{\mathbf{n}} \times \mathcal{L}_{\pm} \circ \mathbf{j}_{i} > \doteq \mathbf{t}_{j} \cdot \hat{\mathbf{n}} \times \mathcal{L}_{\pm} \cdot \mathbf{j}_{i} = \hat{\mathbf{n}} \times \mathbf{t}_{j} \cdot \mathcal{L}_{\pm} \cdot \mathbf{j}_{i}$$
 (5.7a)

and

$$\mathbf{t}_{j} \cdot \hat{\mathbf{n}} \times \mathcal{K}_{\pm} \cdot \mathbf{j}_{i} \tag{5.7b}$$

As shown in equations (5.7a) and (5.7b), the bilinear form arising from the \mathcal{K} operator is identical to the case of the PEC in chapter 4 and that arising from the \mathcal{L} operator can be effected by testing the operator using $\hat{\mathbf{n}} \times \mathbf{t}_j$ (as opposed to \mathbf{t}_j . Thus the only modification required to implement the GMM is the evaluation of $\hat{\mathbf{n}} \times \mathbf{j}_i$ and $\nabla \cdot \hat{\mathbf{n}} \times \mathbf{j}_i$. To perform these operations, we revisit our basis functions described in chapter 4. The basis function set is formed of two functions given by

$$\mathbf{j}_{id}^{m}(\mathbf{r}) \doteq \psi_i \nabla_S \phi_i^{m}(\mathbf{r}) \tag{5.8a}$$

and

$$\mathbf{j}_{i,c}^{m}(\mathbf{r}) \doteq \psi_i \hat{\mathbf{n}} \times \nabla_S \zeta_i^{m}(\mathbf{r}). \tag{5.8b}$$

To compute $\hat{\mathbf{n}} \times$ these basis functions, if we assume that $\phi_i^m(\mathbf{r})$ is chosen to be the same as $\zeta_i^m(\mathbf{r})$, we observe that $\hat{\mathbf{n}} \times \mathbf{j}_{i,d} = \mathbf{j}_{i,c}$. From an algorithmic view point, this means that if we have a subroutine that computes $\mathbf{j}_{i,c}$, we can recycle that to compute $\hat{\mathbf{n}} \times \mathbf{j}_{i,d}$. Also, $\hat{\mathbf{n}} \times \mathbf{j}_{i,c}$ requires the computation of $\hat{\mathbf{n}} \times \psi_i \hat{\mathbf{n}} \times \nabla_s \cdot = -\psi_i \nabla_s \cdot$ which is algorithmically identical to the computation of $\mathbf{j}_{i,d}^m$. Thus the changes required to implement the GMM for dielectric bodies can be trivially effected using the same code as used for the PEC case.

5.3 Implementation Results

Next, we will present a series of results that serve to demonstrate several features of the GMM framework. We begin by presenting results that validate the application of the GMM framework to the solve both the PMCHWT and Müller equations. Here, the data obtained is compared either against analytical data or those obtained using RWG basis functions. Following this set, we will present results that (i) demonstrate hp-convergence, (ii) show well conditioned behavior for the PMCHWT formulation, (iii) demonstrate ability to handle non-conformal meshes with relative ease, (iv) ability to easily mix different order/types of basis function within a single simulation, and finally (v) ability to handle multiply connected domains. In all the cases considered herein, we will compare bistatic radar scattering cross-section data. It will be assumed that the scatterer geometry is discretized using triangular patches whose average edge length is approximately a tenth of the wavelength in the medium (or $0.1\lambda_-$). Further, unless otherwise specified, the same mesh is used to obtain results for both GMM and RWG basis functions. Also, λ_0 will be used to denote the wavelength of the incident field in free space.

5.3.1 Validation of GMM PMCHWT and Müller Solvers

Next, we validate GMM based PMCHWT and Müller integral equation solvers. Unless otherwise mentioned, the permittivity and permeability of the dielectric object is assumed to be $\varepsilon_{-} \doteq \varepsilon_{r}\varepsilon_{0} = 4.0\varepsilon_{0}$ and $\mu_{-} = \mu_{0}$, where ε_{0} and μ_{0} are the permittivity and permeability of free-space, respectively. Further, it is assumed that all objects considered herein are immersed in free-space, i.e., $\varepsilon_{+} = \varepsilon_{0}$ and $\mu_{+} = \mu_{0}$. In each case, the object under study is discretized using triangular patches of an average edge length $0.1\lambda_{-}$. GMM patches and basis functions are constructed starting from this triangulation. The RCS obtained is compared against analytical data (for spheres) or against a traditional RWG scheme constructed on the original tessellation.

First, Figure 5.1a compares the RCS data for three dielectric spheres obtained using the GMM and RWG based codes, as well as that obtained using Mie series [26]. The radii of the spheres are $0.1\lambda_0$, $0.3\lambda_0$ and $0.5\lambda_0$ respectively. The incident field is polarized along $\hat{\mathbf{x}}$ and propagates along $-\hat{\mathbf{z}}$. The GMM discretization for the spheres result in $N_{GMM} = \{400,776,9416\}$ total (**J** and **M**) unknowns, respectively. The order of basis function p is chosen to be one. The number of unknowns when using RWG basis are $N_{RWG} = \{596,1152,12004\}$, respectively. The bistatic RCS (at $\phi = 0$) obtained from the GMM, RWG based solvers for PMCHWT and Müller equations are compared in Figures 5.1a against analytical data. As is evident, the three sets of data agree very well with each other, demonstrating that the low order GMM performs as well RWG.

Next, we consider an $\hat{\mathbf{x}}$ polarized plane wave, traveling in the $-\hat{\mathbf{z}}$ direction that is incident on a dielectric cube of side length λ_0 , where λ_0 is the wavelength in free space. The object was discretized using triangular patches, and the corresponding number of the GMM and RWG unknowns for this mesh are $N_{GMM}=2404$ and $N_{RWG}=3600$. The GMM discretization is applied to both the PMCHWT and the

Müller equations. As is evident from the RCS data at the $\phi = 0$ plane shown in Figure 5.1b, the two sets of results agree very well with each other.

Next, we consider scattering of a plane wave from two non-canonical geometries—a NASA almond and a conesphere. The NASA almond fits in a box of dimension $0.4\lambda_0\times 1.15\lambda_0\times 3\lambda_0$. The incident field is polarized along $\hat{\mathbf{x}}$ direction, and propagates along the $-\hat{\mathbf{z}}$ direction. The number of GMM and RWG basis are $N_{GMM}=3056$ and $N_{RGW}=5600$, respectively. Figure 5.2a compares the RCS data obtained in the $\phi=0$ plane using PMCHWT and Müller integral equations that are solved using GMM and RWG basis functions. It is evident the agreement between the four RCS data is excellent.

Finally, Figure 5.2b the compares the RCS data obtained for a dielectric cone sphere of maximum radius $0.5\lambda_0$ and cone height $2.6\lambda_0$. As before, data is obtained using both PMCHWT and Müller integral equations, using both GMM and RWG basis functions. In this test, the incident field is polarized along $-\hat{\mathbf{y}}$, propagates along $\hat{\mathbf{x}}$ and bistatic RCS is observed at $\theta = \pi/2$. The number of total unknowns is $N_{GMM} = 2900$ and $N_{RWG} = 3312$ respectively. As can be seen in each of the above cases, the agreement between the RCS is excellent. All these results provide a measure of confidence on the GMM

5.3.2 Salient features of the GMM scheme

Thus far, we have demonstrated that GMM based discretization of both the PM-CHWT and Müller equation produces accurate results. In what follows, we shall present data that highlight some of the features of is approach, and contrast it with what can be done using RWG basis functions.

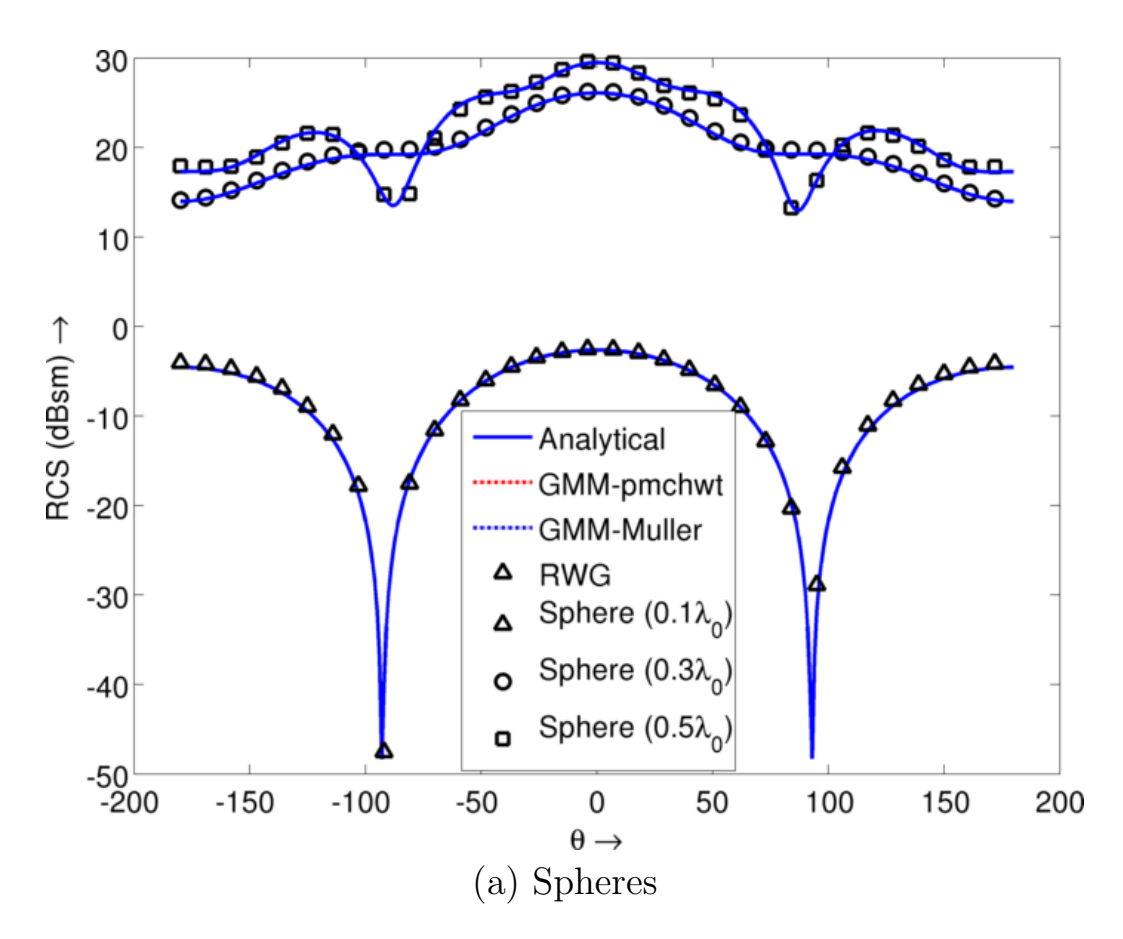


Figure 5.1: RCS obtained using GMM basis functions used to discretize the PM-CHWT amd Müller equations for the solution of scattering from (a) dielectric spheres (radii $0.1\lambda_0, 0.3\lambda_0$ and $0.5\lambda_0$ and $\varepsilon_r = 4.0$) and (b) a cube (side λ_0 , $\varepsilon_r = 4.0$) due to plane wave incidence. The bistatic RCS (at $\phi = 0$) are compared against that obtained using an RWG discretization and analytical results (for spheres).

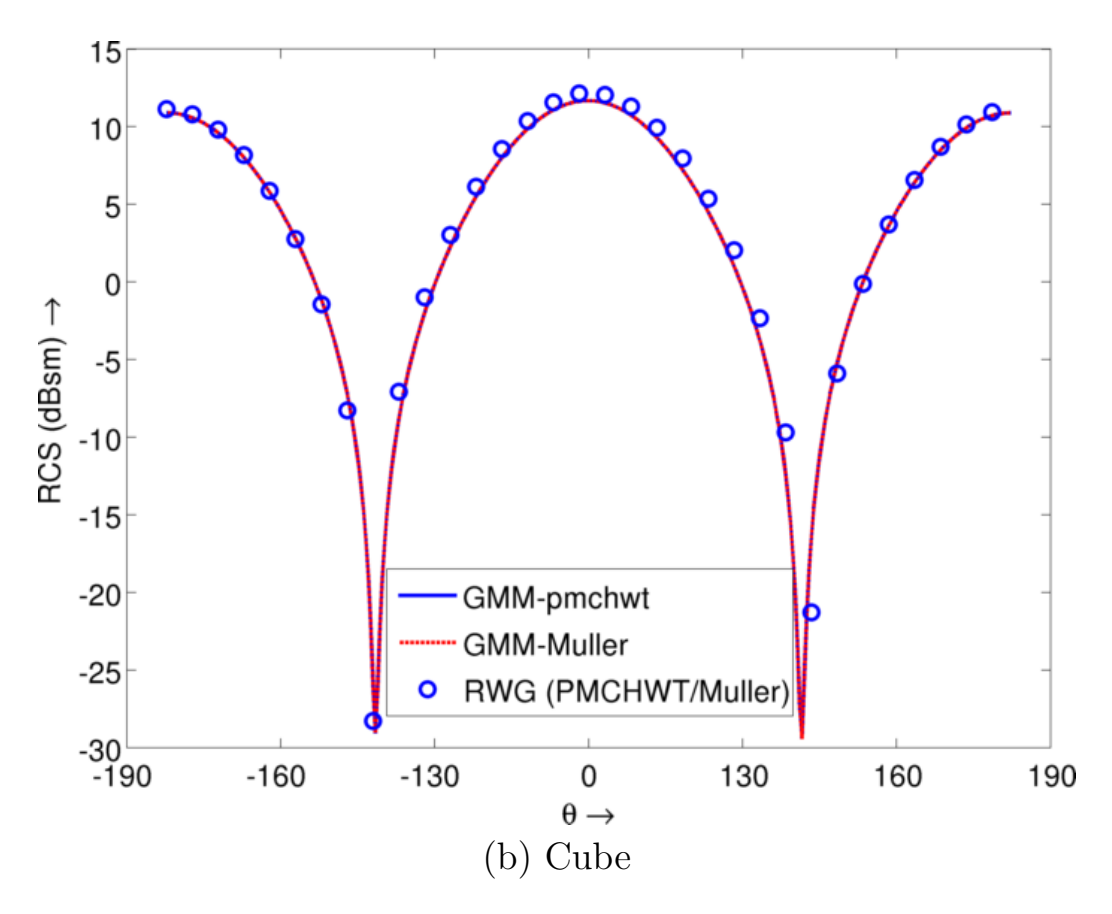


Figure 5.1 Continued: RCS obtained using GMM basis functions used to discretize the PMCHWT amd Müller equations for the solution of scattering from (a) dielectric spheres (radii $0.1\lambda_0, 0.3\lambda_0$ and $0.5\lambda_0$ and $\varepsilon_r = 4.0$) and (b) a cube (side $\lambda_0, \varepsilon_r = 4.0$) due to plane wave incidence. The bistatic RCS (at $\phi = 0$) are compared against that obtained using an RWG discretization and analytical results (for spheres).

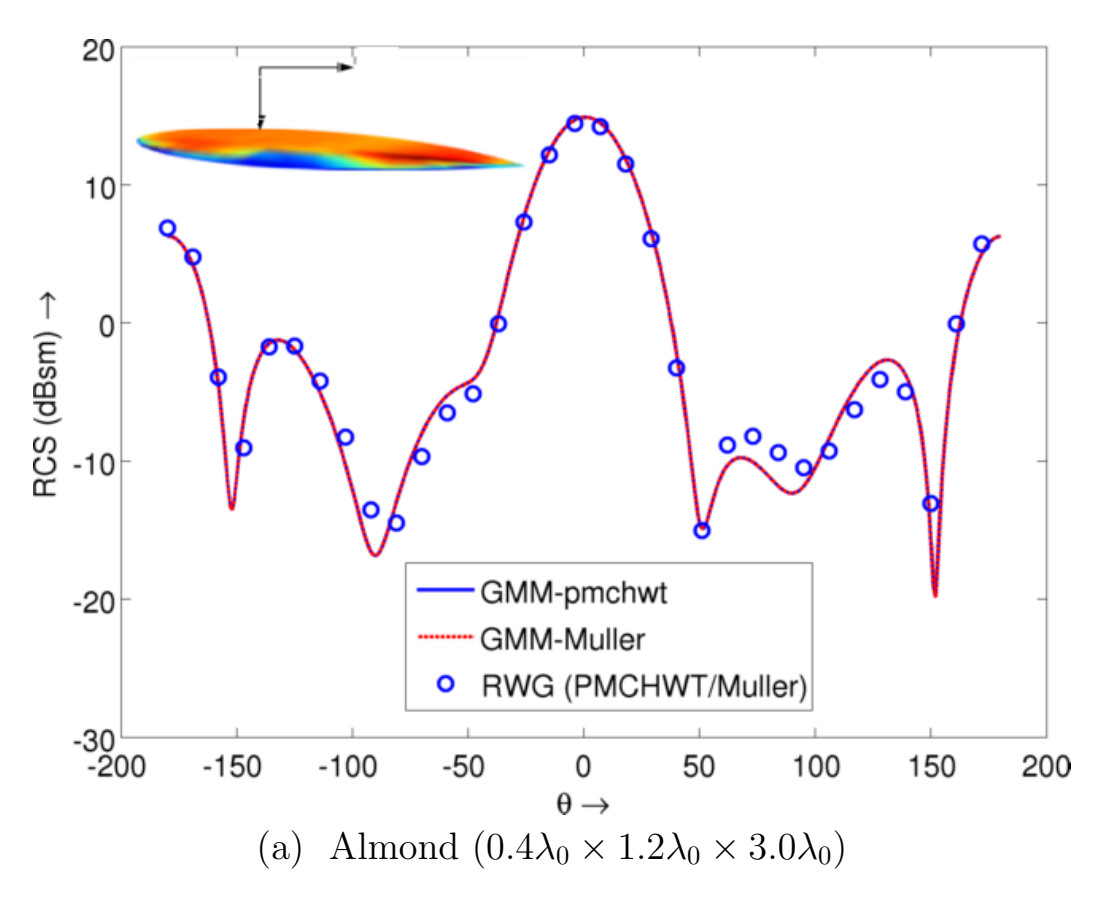


Figure 5.2: RCS obtained using GMM basis functions due to scattering from (a) NASA thin almond of $\varepsilon_r = 4.0$ that fits in a box of size $0.4\lambda_0 \times 1.2\lambda_0 \times 3.0\lambda_0$ due to a plane wave incident along $-\hat{\mathbf{z}}$ and polarized along $\hat{\mathbf{x}}$ and (b) a cone-sphere of radius $0.5\lambda_0$, cone height $2.6\lambda_0$ and $\varepsilon_r = 4.0$, due to a plane wave polarized along $-\hat{\mathbf{y}}$ and incident along $\hat{\mathbf{x}}$. Bistatic RCS is computed at $\phi = 0$ for the almond and at $\theta = \pi/2$ for the conesphere and used to validate the GMM scheme against RWG.

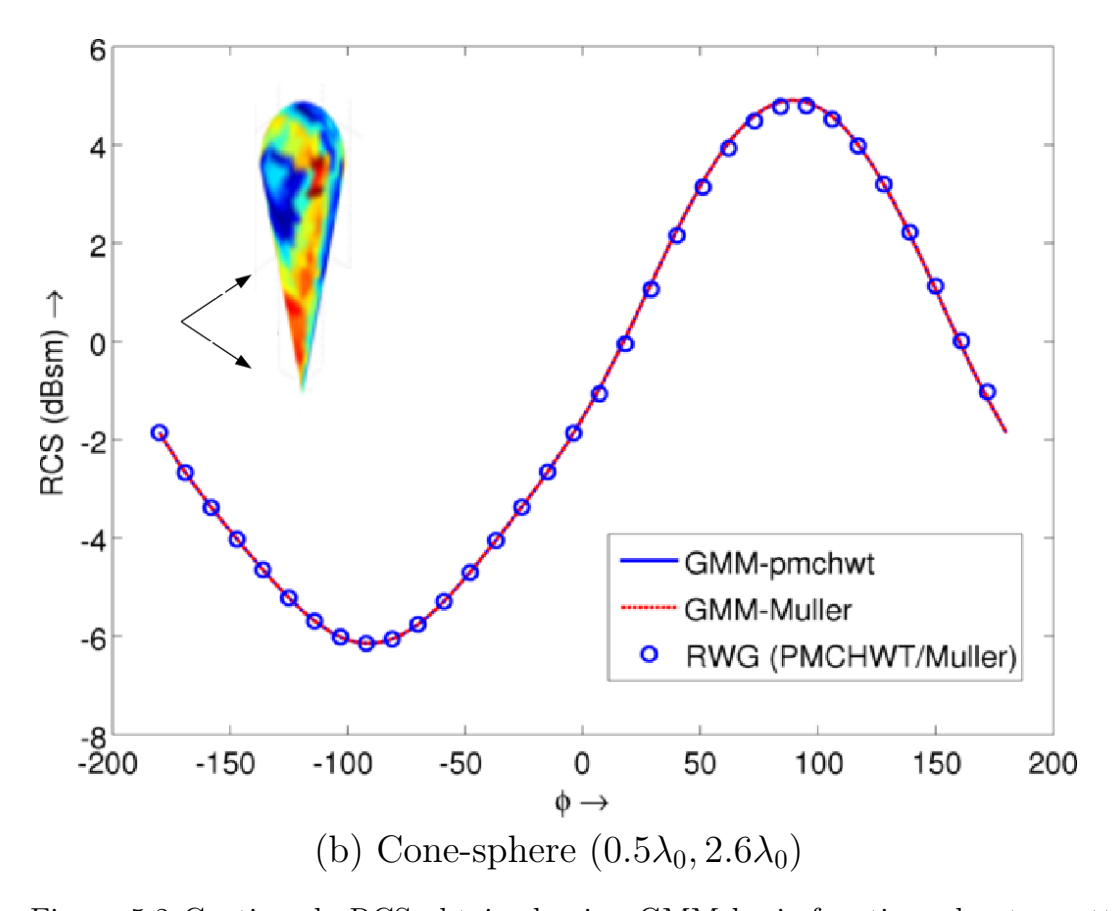


Figure 5.2 Continued: RCS obtained using GMM basis functions due to scattering from (a) NASA thin almond of $\varepsilon_r = 4.0$ that fits in a box of size $0.4\lambda_0 \times 1.2\lambda_0 \times 3.0\lambda_0$ due to a plane wave incident along $-\hat{\mathbf{z}}$ and polarized along $\hat{\mathbf{x}}$ and (b) a cone-sphere of radius $0.5\lambda_0$, cone height $2.6\lambda_0$ and $\varepsilon_r = 4.0$, due to a plane wave polarized along $-\hat{\mathbf{y}}$ and incident along $\hat{\mathbf{x}}$. Bistatic RCS is computed at $\phi = 0$ for the almond and at $\theta = \pi/2$ for the conesphere and used to validate the GMM scheme against RWG.

Mixtures of Basis functions

As was alluded to earlier, the GMM framework permits mixtures of basis functions within the simulation domain. This implies that one can use a set of basis function in a sub-domain and use an entirely different set in neighboring sub-domains without invoking any special condition regarding continuity of different orders. This is possible as patches overlap with each other and continuity is built into the basis functions. This property is extremely useful when analyzing complex structures where h-, p- or hp-adaptivity is required or if known asymptotic solutions are to be built into the approximation space. In what follows, we shall explore these features of the GMM framework. Note, it should be emphasized that the use of different basis functions with different patches is as simple as choosing a flag associated with a node in the input file that describes geometry. This is so as each node is associated with a patch and this flag can describe the function that is to be used in the patch.

Mixed Order Bases: The first class of numerical tests will be carried out using mixtures of basis functions of different orders. Figure 5.3 compares the RCS obtained due to scattering from the almond and box using two different orders of GMM basis functions. In both cases, the incident wave is $\hat{\mathbf{x}}$ polarized and travels in the $-\hat{\mathbf{z}}$ direction. The relative permittivity of both scatterers is $\varepsilon_r = 4$, and the RCS data is obtained in the $\phi = 0$ plane.

Figure 5.3a compares the RCS data for an almond obtained using p = 1 everywhere on the scatterer with that obtained using p = 1 or p = 2 in different regions. Specifically, basis functions on all patches that fall within $0.2\lambda_{-}$ of the tip were of order p = 2 and all others were of order p = 1. As is evident from Figure 5.3a, the two sets of data agree very well with each other.

Next, Figure 5.3b compares the RCS data obtained for scattering from a thin dielectric box of size $0.2\lambda_0 \times 0.2\lambda_0 \times 4\lambda_0$ with varying h and p with a reference

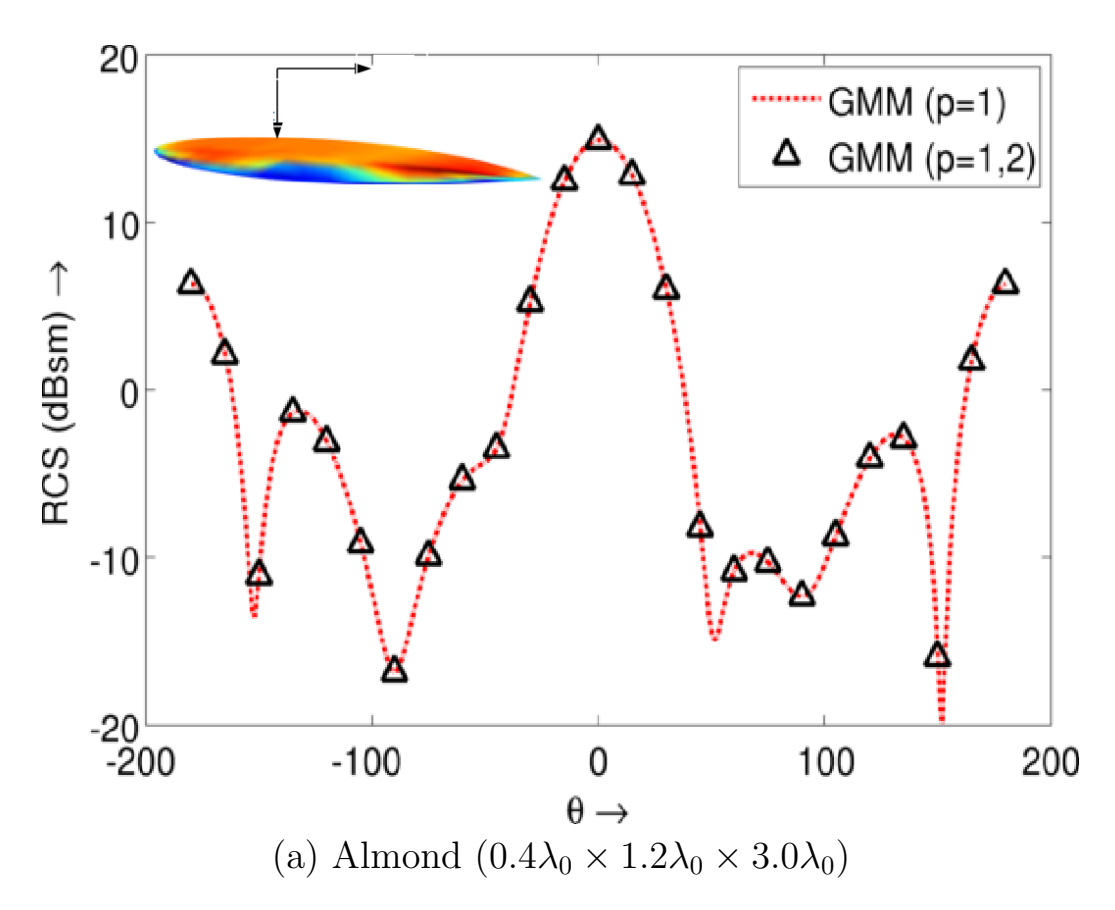


Figure 5.3: RCS comparison of standard GMM vs. Mixed-order GMM (a) NASA almond discretized with GMM basis functions complete to order p=4 near edges and p=1 elsewhere. (b) Dielectric box using p=1 near edges and p=2 in larger patches near center. The bistatic RCS is computed at $\phi=0$ and the incident field is polarized along $\hat{\mathbf{x}}$ and incident along $-\hat{\mathbf{z}}$.

data, obtained using GMM basis functions in a dense mesh with $N_{GMM}=1552$ unknowns, and p=1. As illustrated in the inset, the box was discretized using the following rule: $h=0.1\lambda_-$ within $h=0.25\lambda_-$ of any edge and $0.2\lambda_-$ elsewhere. For patches with $h=0.1\lambda_-$ the order of basis function was p=1, and for $h=0.25\lambda_-$ the order was p=2. This resulted in a system with $N_{GMM}=440$ unknowns. As is evident from Figure 5.3b that the two sets of results agree very well with each other.

Mixed Types of Bases: The next example demonstrates the use of a mixture of types of basis functions. Figure 5.4 compares the RCS obtained from a dielectric box of dimensions $5.0\lambda_0 \times 2.0\lambda_0 \times 0.5\lambda_0$ and $\varepsilon_r = 2.0$. This box is first meshed

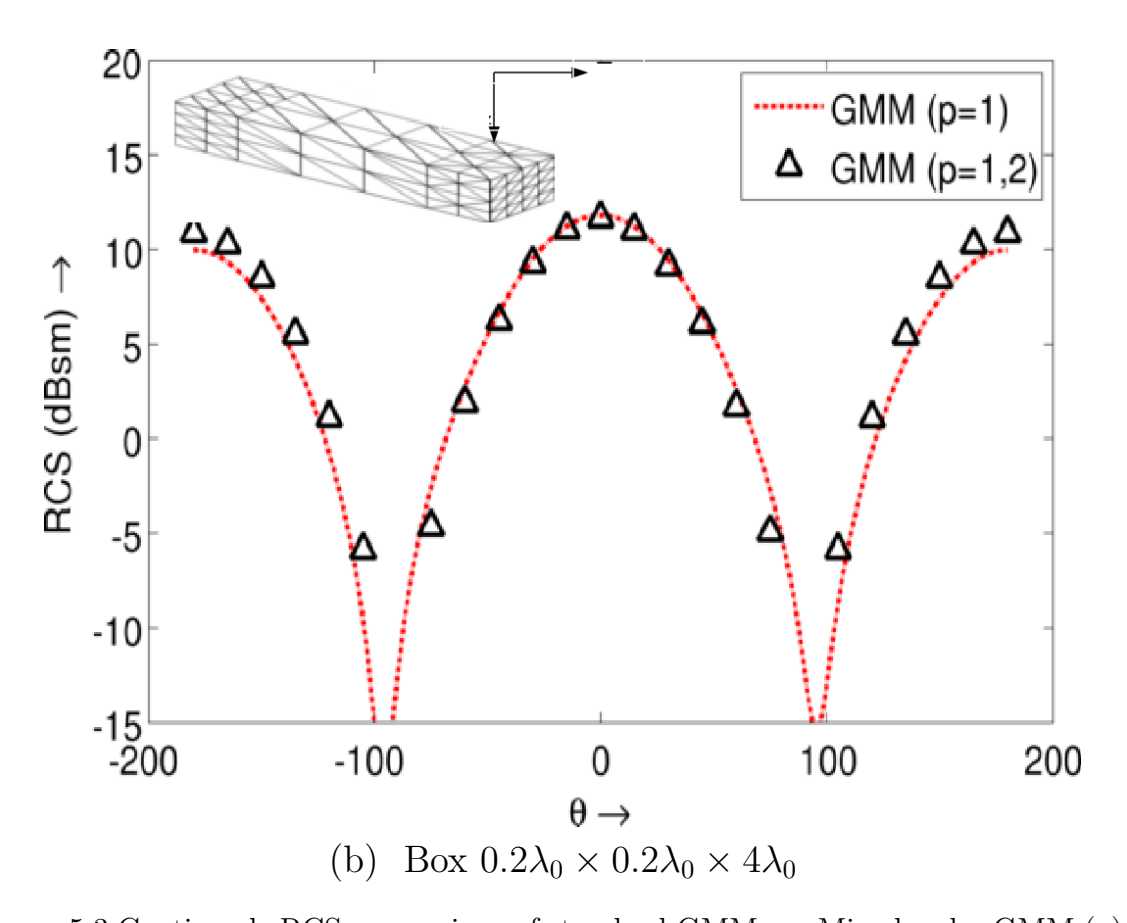


Figure 5.3 Continued: RCS comparison of standard GMM vs. Mixed-order GMM (a) NASA almond discretized with GMM basis functions complete to order p=4 near edges and p=1 elsewhere. (b) Dielectric box using p=1 near edges and p=2 in larger patches near center. The bistatic RCS is computed at $\phi=0$ and the incident field is polarized along $\hat{\mathbf{x}}$ and incident along $-\hat{\mathbf{z}}$.

uniformly using a triangulation of average edge length $0.1\lambda_-$. GMM basis functions are constructed on this tessellation and the RCS is computed by solving the Müller integral equation; using $N_{GMM}=21680$ unknowns. The box is then re-meshed using two sets of elements, of average edge length $0.1\lambda_-$ near the edges and $1.0\lambda_-$ at the center; as shown in the inset figure. GMM basis functions are constructed using polynomials as approximation functions in the smaller patches, using the quasisurface Helmholtz technique described in Section 4.3 and plane wave approximation functions of the form $\boldsymbol{\nu}_i^m(\mathbf{r}) \doteq \hat{\mathbf{u}}\cos(\theta^m)\exp{-j\omega\sqrt{\mu_-\varepsilon_-}\cos(\theta^m)}\hat{\mathbf{k}}\cdot(\mathbf{r}-\mathbf{r}_i)$; where $\hat{\mathbf{u}}$ is a pilot vector along the surface of the patch, $\hat{\mathbf{k}}$ is the incident field direction, \mathbf{r}_i is the patch center and θ^m is an order parameter between 0 and 2π ; in the larger patches. These functions are used to discretize the Müller equations with $N_{GMM}=12350$ unknowns; and the RCS's are compared.

The RCS obtained using the regular GMM and the mixed order GMM is demonstrated in Figure 5.4. It is evident from the figure that the RCS agrees very well. This demonstrates the efficacy of the GMM scheme in mixing different types of basis functions; a capability that is not available in any of the basis function frameworks currently in use for the discretization of electromagnetic integral equations.

hp-adaptivity: In this section, we utilize the flexibility of the GMM framework to study the hp- convergence of the RCS due to scattering from a dielectric arrow. The arrow has dimensions $2.0\lambda_0 \times 3.0\lambda_0 \times \lambda_0$ and $\varepsilon_r = 2.0$. RCS data is obtained for the arrow discretized at $\lambda_-/40$ to provide a baseline for comparison. The RCS data is then computed using the GMM basis functions constructed on this tessellation with $N_{GMM} = 64,048$ unknowns. The incident field is polarized along $-\hat{\mathbf{z}}$ and incident along $\hat{\mathbf{x}}$. This RCS is then compared against the following different discretizations in Figure 5.5. First, the arrow is meshed using elements with an average edge-length of $\lambda_-/10$ and approximation functions complete to order p=1 are used everywhere

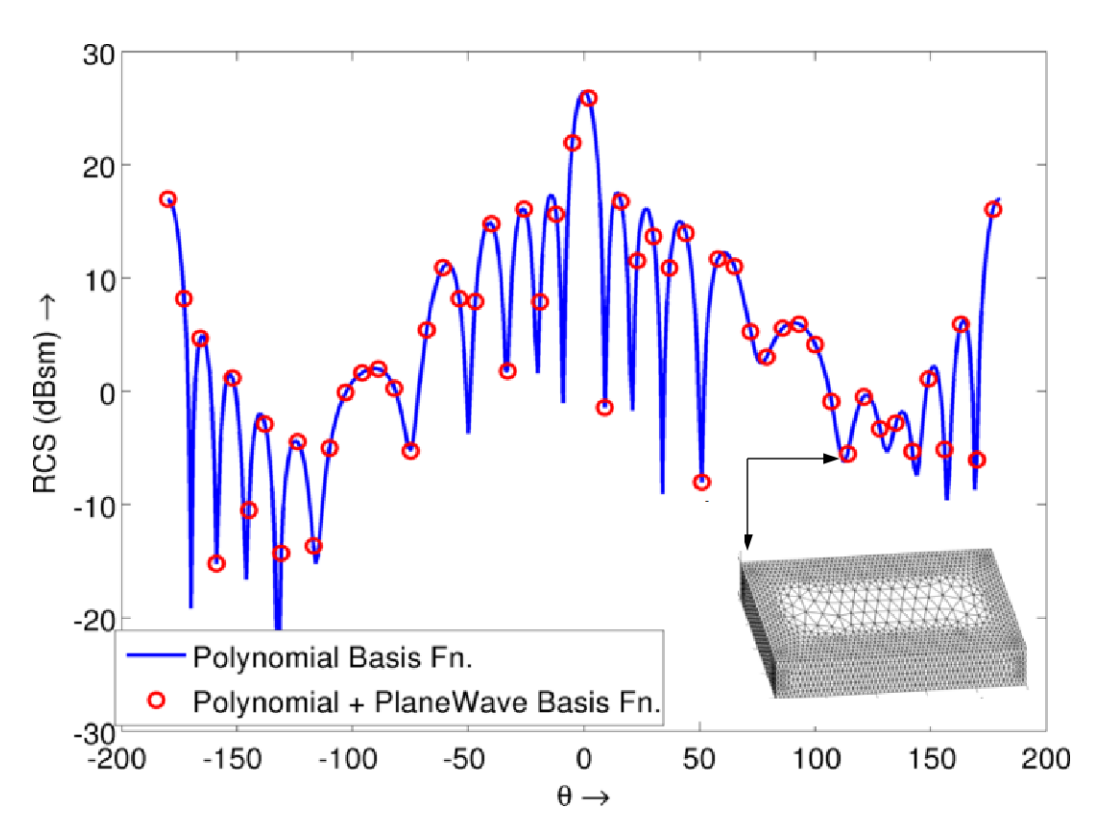


Figure 5.4: RCS comparison of standard GMM vs. Mixed-Basis GMM (5.0 $\lambda_0 \times 2.0\lambda_0 \times 0.5\lambda_0$). Electric field is incident along $-\hat{\mathbf{z}}$ and polarized along $\hat{\mathbf{x}}$. The bistatic RCS ($\phi=0$) is compared for GMM using polynomial basis functions against GMM using polynomials mixed with plane wave basis functions.

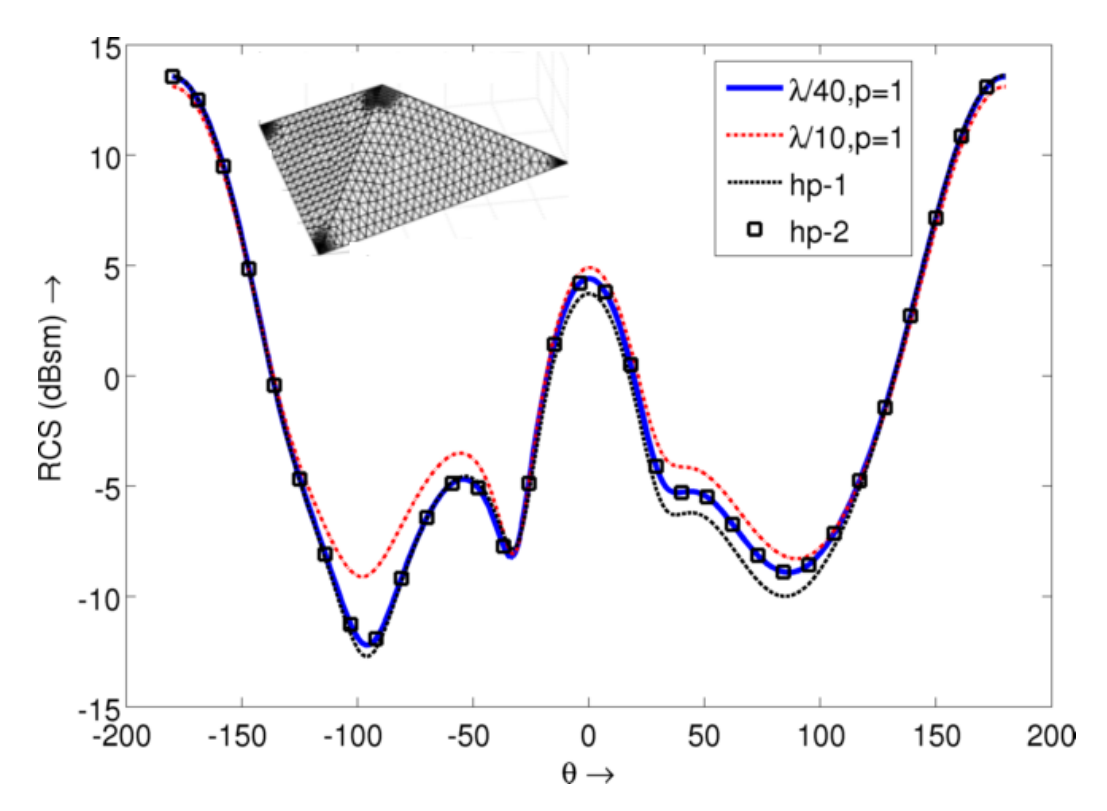


Figure 5.5: RCS comparison for scattering from a dielectric arrow $(2.0\lambda_0 \times 3.0\lambda_0 \times \lambda_0)$. Electric field is incident along $-\hat{\mathbf{z}}$ and polarized along $\hat{\mathbf{x}}$. The bistatic RCS $(\phi = 0)$ is compared for four different combinations of h and polynomial order of basis function p.

 $(N_{GMM}=8960)$. In the second test, the mesh is refined to an average edge length of $\lambda_-/20$ near the tips and basis functions of order p=1 are applied near the tip and basis functions of order p=2 everywhere. This case is shown as hp-1 $(N_{GMM}=12,048)$ in Figure 5.5. Finally, the mesh is refined further, in two levels, with $\lambda_-/20$ at the tip, $\lambda_-/10$ in the smooth areas and $\lambda_-/15$ in the transition region. In this case, basis functions of order p=1 are used in the patches of size $\lambda_-/10$ and p=2 everywhere else. This case is shown as hp-2 $(N_{GMM}=22,860)$. As can be seen the RCS demonstrates the hp-convergence of the method.

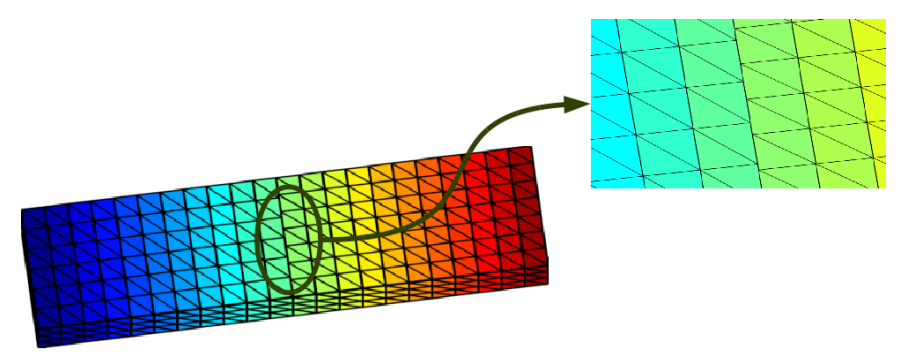
Non Conformal meshes

One advantage of disassociating the definition of the basis function from the underlying tessellation of the geometry is that it allows for the use of non conformal meshes. It is common, in the case of practical geometries, to have different vendors mesh different parts of a geometry. This results in sets of meshes that need to be explicitly "stitched together" at the boundaries. This motivates the design of techniques that can handle non-conformal meshes [110]. However, a consequence of the design of the GMM scheme is that it can implicitly handle these kinds of meshes without any change to the framework or the implementation.

Here, we present one example illustrating this ability. We consider scattering from a dielectric box ($\varepsilon_T = 4.0$) of dimensions $2.0\lambda_0 \times 0.2\lambda_0 \times 0.5\lambda_0$. Two halves of the box are meshed at slightly different discretization rates to obtain a non conformal mesh. The coarser mesh is $0.125\lambda_-$ while the finer is $0.1\lambda_-$. The RCS is computed due to scattering of a $\hat{\mathbf{x}}$ polarized plane wave incident along $\hat{\mathbf{z}}$ and is observed along $\phi = 0$. The RCS obtained due to scattering from a discretization constructed on this non conformal mesh is compared against that is obtained by constructing a fully conformal mesh on the geometry. The number of unknowns is $N_{GMM} = 5600$ for the non conformal mesh and $N_{GMM} = 6004$ for the conformal mesh. The agreement of the RCS data, shown in Figure 5.6, demonstrates the ability of the GMM scheme to seamlessly handle non conformal meshes.

5.3.3 Low frequency stability and multiply connected scatterers

It is well known that the condition number of the discrete integral equation is intimately related to the discretization size. A rule of thumb for linear basis functions is that the characteristic dimension h vary approximately as $\lambda_{min}/10$. This means



(a) Non conformal mesh for a box

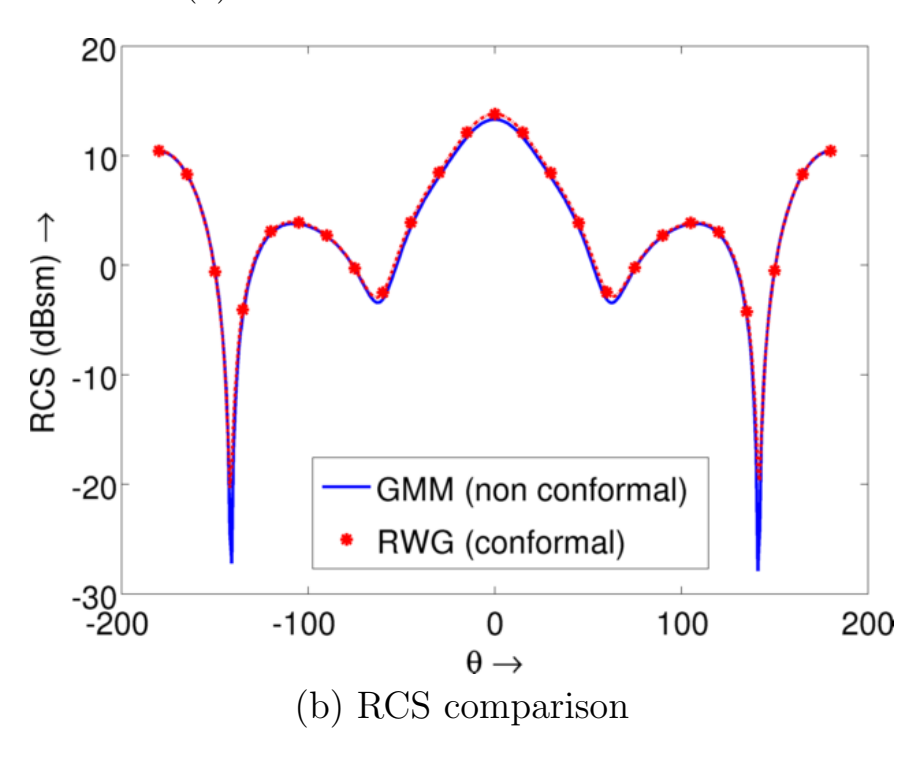


Figure 5.6: RCS comparison for scattering from a non conformally meshed dielectric box. Bistatic RCS ($\phi=0$) obtained by discretizing the Müller integral equation on a non conformal mesh (shown inset) compared against that obtained by discretizing on a (standard) conformal mesh for a thin dielectric ($\varepsilon_r=4.0$) box $(2.0\lambda_0\times0.2\lambda_0\times0.5\lambda_0)$

that the size of discretization is governed by both the frequency and the dielectric constant. Further, the size of discretization is often governed by the need to accurately capture geometric features and, as a result, may be quite small. Next, the two equations that are used in this paper, the PMCHWT and the Müller fall under the category of Fredholm first and second kind, respectively. It can be proven that the eigenvalue of the former spread further apart as the frequency becomes higher, with the smallest accumulating around zero and the largest tending to infinity. In contrast, the eigenvalues of the Müller cluster around a non-zero value [113]. As a result, discrete system that arise from the PMCHWT tend to be ill-conditioned when the wavelength is large compared to the feature size. In other words, they suffer from low-frequency breakdown. The common remedy to solve this problem has been the development of loop-star or loop-tree basis functions, that separate the basis functions into an solenoidal and non-solenoidal components [93]. This decomposition confers low-frequency stability to the discrete PMCHWT equations, however, unless these decompositions are augmented, it is not possible to use them for analysis of multiply connected objects. As the GMM basis functions are neither purely solenoidal nor non-solenoidal, and the basis functions are purely local to a patch. They have been shown excellent approximation properties of the function, its divergence and curl. In what follows, we will demonstrate that they yield well conditioned systems that can be used for analysis of multiply connected objects.

We compare the condition number of systems resulting from the discretization of PMCHWT equations using GMM and RWG basis for three different scatterers; (i) a sphere of radius 0.1m, (ii) a cube of side 1m and (iii) a thin NASA almond that fits in a box of size $0.4m \times 1.15m \times 3m$. The relative permittivity of each body is $\varepsilon_r = 4.0$. Figure 5.8 demonstrates the condition number of the impedance matrix obtained using the GMM basis functions and using RWG functions over a range of frequencies, starting from 30Hz to 30MHz. In each case, the object is discretized at $0.1\lambda_-$ at

the highest operating frequency. The number of GMM and RWG unknowns are $N_{GMM} = \{400, 2404, 3056\}$ and $N_{RWG} = \{596, 7200, 5600\}$ for the sphere, cube and almond, respectively. As is immediately apparent from Figure 5.8, the condition number of systems discretized using RWG basis grows exponentially as the frequency decreases whereas those discretized using GMM are relatively constant in across a six decade change in frequency.

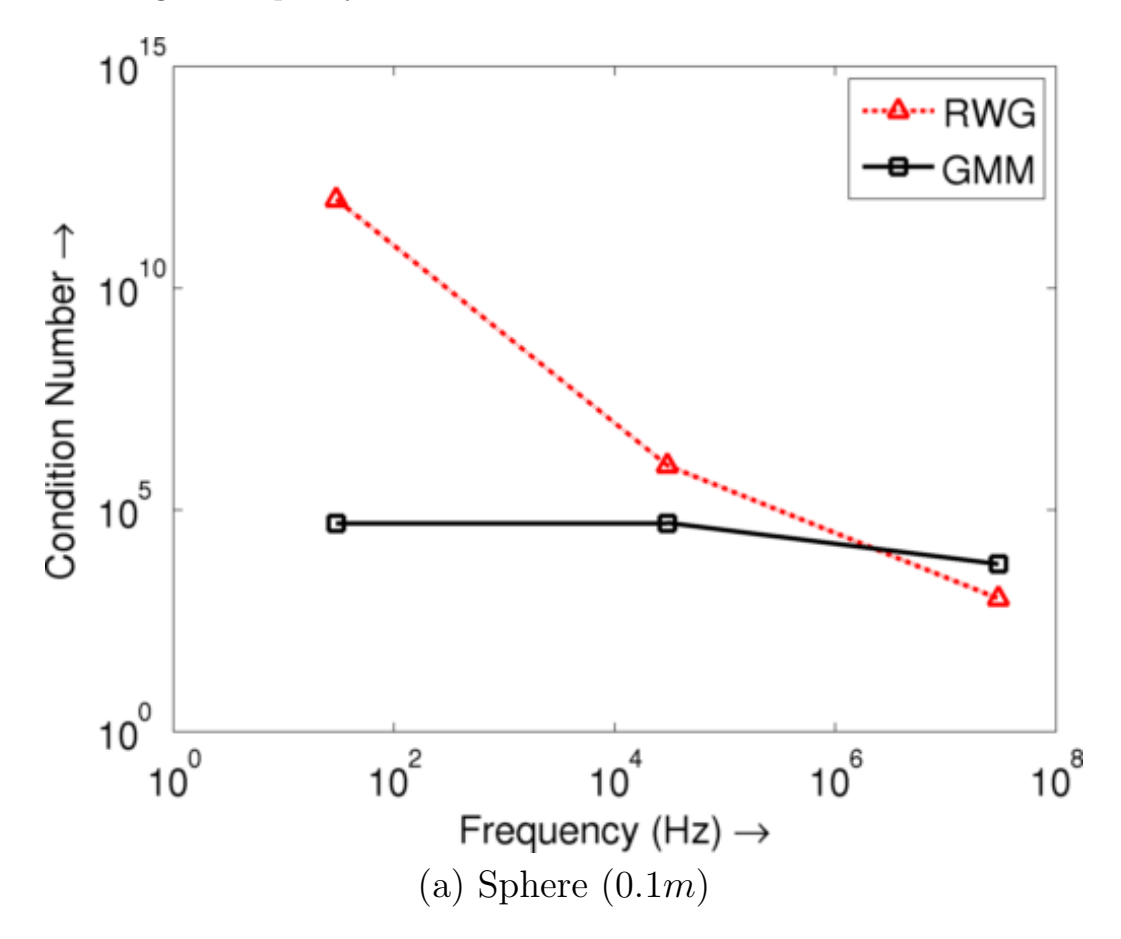


Figure 5.7: Condition number comparisons. All objects are discretized at $0.1\lambda_m$ at 30MHz and the operating frequency is swept from 30MHz to 30Hz and condition number of the impedance matrix obtained on GMM discretization is compared against that obtained using a standard RWG discretization. (a) Sphere (radius 0.1m, $\varepsilon_T = 4.0$) and (b) Cube (side 1m and $\varepsilon_T = 4.0$).

Next, we illustrate that these basis functions can be used to analyze scattering from multiply connected objects unlike loop-star or loop-tree functions [96]. Figure 5.9 below compares the scattering from a toroidal scatterer of outer radius $0.75\lambda_0$,

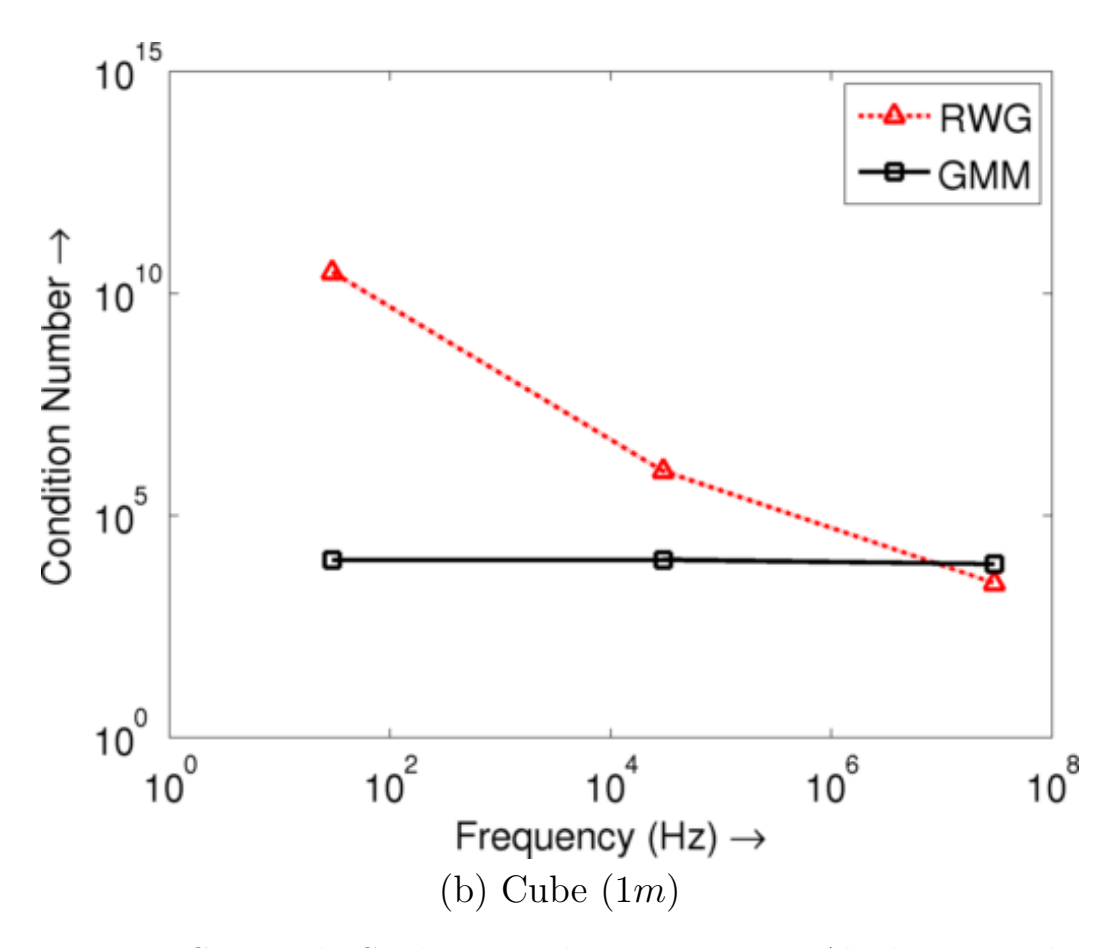


Figure 5.7 Continued: Condition number comparisons. All objects are discretized at $0.1\lambda_m$ at 30MHz and the operating frequency is swept from 30MHz to 30Hz and condition number of the impedance matrix obtained on GMM discretization is compared against that obtained using a standard RWG discretization. (a) Sphere (radius 0.1m, $\varepsilon_r = 4.0$) and (b) Cube (side 1m and $\varepsilon_r = 4.0$).

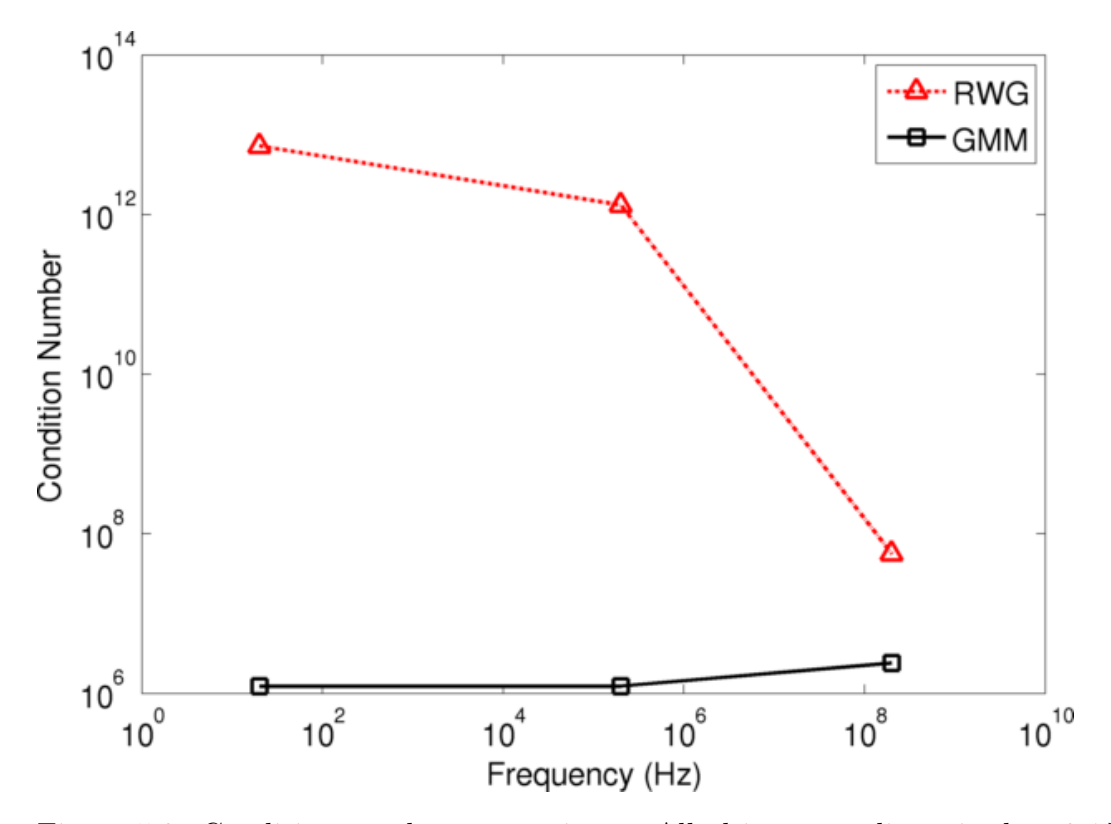
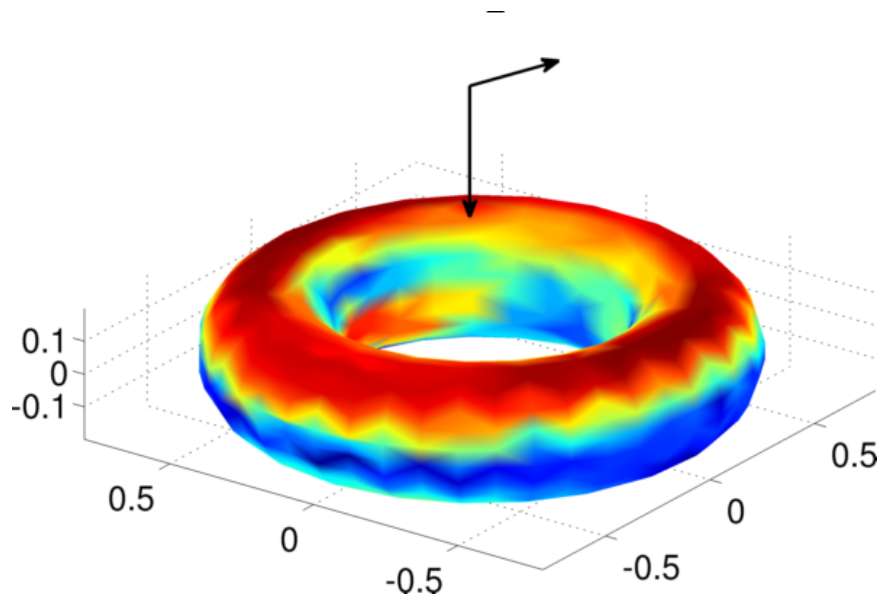
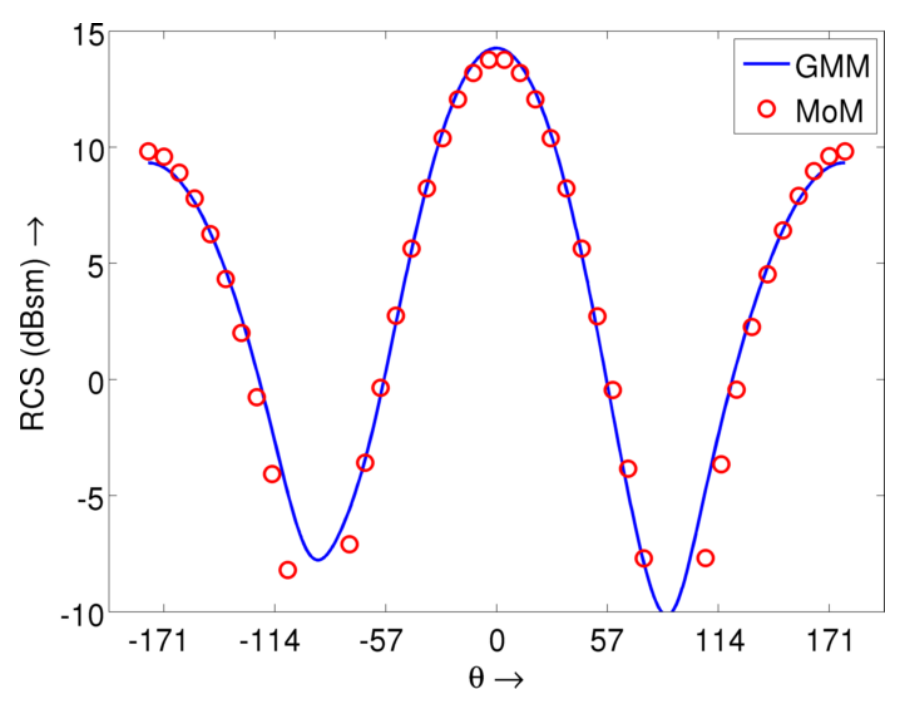


Figure 5.8: Condition number comparisons. All objects are discretized at $0.1\lambda_m$ at 30MHz and the operating frequency is swept from 30MHz to 30Hz and condition number of the impedance matrix obtained on GMM discretization is compared against that obtained using a standard RWG discretization. (c) NASA thin almost (side $0.4m \times 1.2m \times 3.0m$ and $\varepsilon_r = 4.0$)

inner radius $0.5\lambda_0$ and of relative permittivity 4.0 computed using the GMM discretization of the Müller equation $(N_{GMM}=3406)$ compared to that obtained using a standard RWG discretization $(N_{RWG}=7800)$. The incident field direction $(-\hat{\mathbf{z}})$ and polarization $(\hat{\mathbf{x}})$ is shown inset in the figure. The excellent comparison of the RCS demonstrates the ability of the GMM framework using the quasi-surface Helmholtz basis functions to handle multiply connected domains.



(a) Surface current on dielectric toroid



(b) RCS comparison for dieletric toroid

Figure 5.9: Bistatic RCS ($\phi = 0$) comparison for a dielectric toroid (outer radius $0.75\lambda_0$ and inner radius $0.5\lambda_0$, $\varepsilon_r = 4.0$). Figure 5.9(a) shows direction and polarization of the incident field along with an image of the surface current density on the toroid.

Chapter 6

Analysis of transient scattering using the Generalized Method of Moments

In this chapter, we extend the GMM technique to the solution of transient scattering from perfectly conducting bodies. We will proceed by deriving the time domain EFIE and MFIE. While these equations can be derived from first principles, in this work we will restrict to a simpler derivation starting from the frequency domain equations using the Fourier transforms.

6.1 The Fourier transform pair

The temporal Fourier transform pair that we will use for the derivation of the TD-EFIE and TD-MFIE are given by

$$\mathbf{F}(\mathbf{r},\omega) \doteq \mathfrak{F}\{\mathcal{F}(\mathbf{r},t)\} = \int_{-\infty}^{\infty} dt \ \mathcal{F}(\mathbf{r},t)e^{-j\omega t}$$
 (6.1a)

and

$$\mathcal{F}(\mathbf{r},t) = \mathfrak{F}^{-1}\{\mathbf{F}(\mathbf{r},\omega)\} \doteq \frac{1}{2\pi} \int_{-\infty}^{\infty} dt \ \mathbf{F}(\mathbf{r},\omega) e^{j\omega t}. \tag{6.1b}$$

We will freely use the following identities without proof:

$$\mathfrak{F}\left\{\frac{\partial}{\partial t}\mathcal{F}(\mathbf{r},t)\right\} = j\omega\mathbf{F}(\mathbf{r},\omega),\tag{6.2a}$$

$$\mathfrak{F}\left\{\delta(t-\tau)\right\} = e^{-j\omega\tau},\tag{6.2b}$$

which directly lead to

$$\mathfrak{F}^{-1}\left\{\frac{e^{-jkR}}{4\pi R}\right\} = \mathfrak{F}^{-1}\left\{\frac{e^{-j\omega R/c}}{4\pi R}\right\} = \frac{\delta(t - \frac{R}{c})}{4\pi R} \tag{6.2c}$$

and

$$\mathfrak{F}^{-1}\left\{\mathbf{F}(\mathbf{r},\omega)\mathbf{G}(\mathbf{r},\omega)\right\} = \mathcal{F}(\mathbf{r},t) *_{t} \mathcal{G}(\mathbf{r},t), \tag{6.2d}$$

where $*_t$ denotes convolution in time defined as

$$\mathcal{F}(\mathbf{r},t) *_{t} G(\mathbf{r},t) = \int_{-\infty}^{\infty} d\tau \mathcal{F}(\mathbf{r},\tau) G(\mathbf{r},t-\tau). \tag{6.2e}$$

6.2 Time Domain EFIE and MFIE

For the sake of completeness, we restate our scattering problem in a transient framework here. Consider a perfectly electric conducting body occupying a domain $D_{-} \subset \mathbb{R}^3$ in free space (μ_0, ε_0) . Let Ω denote the bounding surface of D_{-} and let the outward pointing unit vector normal at any point \mathbf{r} on Ω be denoted by $\hat{\mathbf{n}}(\mathbf{r})$. Assume that a field $\{\mathcal{E}^i(\mathbf{r},t), \mathcal{H}^i(\mathbf{r},t)\}$ is incident on this body. This field induces currents, $\mathcal{J}(\mathbf{r},t)$, on the surface Ω , that radiate scattered fields $\{\mathcal{E}^s(\mathbf{r},t), \mathcal{H}^s(\mathbf{r},t)\}$. Thus, the total electric and magnetic fields in all of $D_{+} = \mathbb{R}^3/D_{-}$, denoted by $\mathcal{E}(\mathbf{r},t)$ and

 $\mathcal{H}(\mathbf{r},t)$, can be decomposed into the incident and scattered fields by

$$\mathcal{E}(\mathbf{r},t): \mathbb{R}^3 \times \mathbb{R}^+ \to \mathbb{R}^3 = \mathcal{E}^i(\mathbf{r},t) + \mathcal{E}^s(\mathbf{r},t)$$
 (6.3a)

and

$$\mathcal{H}(\mathbf{r},t): \mathbb{R}^3 \times \mathbb{R}^+ \to \mathbb{R}^3 = \mathcal{H}^i(\mathbf{r},t) + \mathcal{H}^s(\mathbf{r},t).$$
 (6.3b)

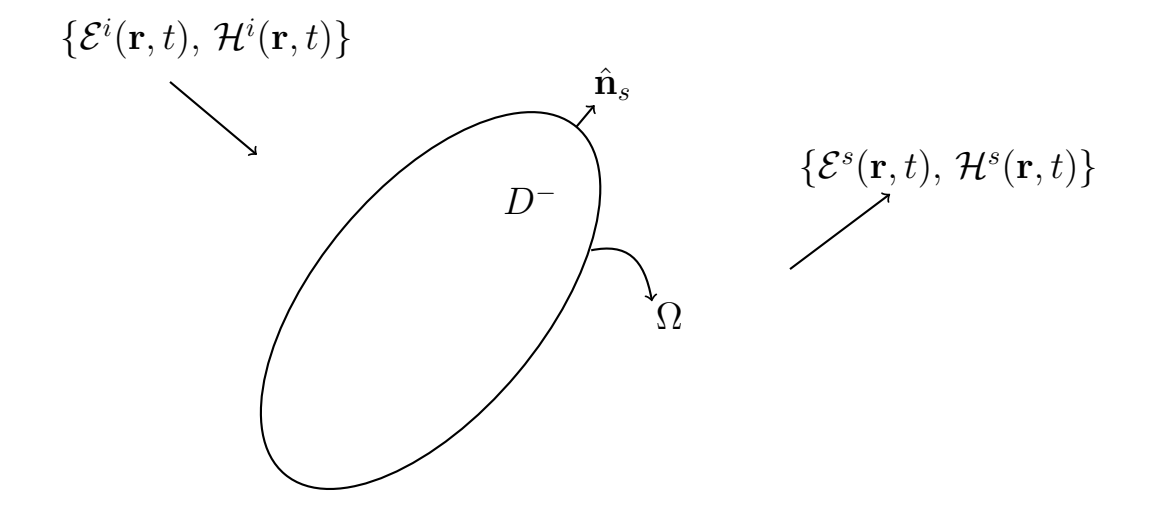


Figure 6.1: General description of a scattering problem

Applying the Fourier transform to equations (2.11) and (2.12), we obtain their time domain equivalents as

$$\mathcal{H}^{S}(\mathbf{r},t) = \frac{1}{\mu_{0}} \nabla \times \mathcal{A}(\mathbf{r},t)$$
 (6.4a)

and

$$\mathcal{E}^{S}(\mathbf{r},t) + \partial_{t}\mathcal{A}(\mathbf{r},t) = -\nabla\phi_{e}(\mathbf{r},t)$$
(6.4b)

Coupling (6.4a) and (6.4b) with the Lorentz gauge given by

$$\nabla \cdot \mathcal{A}(\mathbf{r}, t) + \mu_0 \varepsilon_0 \frac{\partial \phi_e(\mathbf{r}, t)}{\partial t} = 0$$
 (6.5)

, we obtain

$$\mathcal{E}^{S}(\mathbf{r},t) = -\partial_{t}\mathcal{A}(\mathbf{r},t) + \frac{1}{\mu_{0}\varepsilon_{0}} \int_{-\infty}^{t} du \, \nabla\nabla \cdot \mathcal{A}(\mathbf{r},u). \tag{6.6}$$

This provides us a relationship between the magnetic vector potential and the fields. The magnetic vector potential can be related to the induced current $\mathcal{J}(\mathbf{r},t)$ by the Fourier transform of equation (2.27) as

$$\mathcal{A}(\mathbf{r},t) = \mu_0 \int_{\Omega} d\mathbf{r}' \mathcal{J}(\mathbf{r}',t) *_t \frac{\delta(t-\tau)}{4\pi R}.$$
 (6.7)

where $\tau = t - R/c$ and $R = |\mathbf{R}| = |\mathbf{r} - \mathbf{r'}|$ and using (6.7) in (6.6) and (6.4a). We assume that all the integrals contain finite energy and that we can switch the order of integration to obtain the following equations for the scattered fields generated by $\mathcal{J}(\mathbf{r},t)$:

$$\mathcal{E}^{S}(\mathbf{r},t) = -\mu_{0} \partial_{t} \int_{\Omega} d\mathbf{r}' \, \frac{\mathcal{J}(\mathbf{r}',\tau)}{4\pi R} + \frac{1}{\varepsilon_{0}} \int_{\Omega} d\mathbf{r}' \, \nabla \nabla \cdot \int_{-\infty}^{\tau} dt \, \frac{\mathcal{J}(\mathbf{r}',t)}{4\pi R}$$
(6.8a)

and

$$\mathcal{H}^{S}(\mathbf{r},t) = \nabla \times \int_{\Omega} d\mathbf{r}' \frac{\mathcal{J}(\mathbf{r}',\tau)}{4\pi R}.$$
 (6.8b)

Equation (6.8b) can be, after some manipulation, reduced to

$$\mathcal{H}^{S}(\mathbf{r},t) = \frac{1}{4\pi} \int_{\Omega} d\mathbf{r'} \left[\frac{1}{cR} \partial_{t} \mathcal{J}(\mathbf{r'},\tau) + \frac{1}{R^{2}} \mathcal{J}(\mathbf{r'},\tau) \right] \times \mathbf{R}.$$
 (6.8c)

Applying the PEC boundary conditions from chapter 2 and proceeding very similar to the derivation of the frequency domain EFIE and MFIE, we obtain the time domain versions of the EFIE and the MFIE as

$$\hat{\mathbf{n}} \times \hat{\mathbf{n}} \times \mathcal{E}^{i}(\mathbf{r}, t) = \hat{\mathbf{n}} \times \hat{\mathbf{n}} \times \left\{ \frac{\mu_{0}}{4\pi} \partial_{t} \int_{\Omega} d\mathbf{r'} \ \mathcal{J}(\mathbf{r'}, \tau) - \frac{1}{4\pi\varepsilon_{0}} \int_{\Omega} d\mathbf{r'} \ \nabla \nabla \cdot \int_{-\infty}^{\tau} dt \ \mathcal{J}(\mathbf{r'}, t) \right\}$$
(6.9a)

and

$$\hat{\mathbf{n}} \times \mathcal{H}^{i}(\mathbf{r}, t) = -\hat{\mathbf{n}} \times \left\{ \frac{1}{4\pi} \int_{\Omega} d\mathbf{r'} \left[\frac{1}{cR} \partial_{t} \mathcal{J}(\mathbf{r'}, \tau) + \frac{1}{R^{2}} \mathcal{J}(\mathbf{r'}, \tau) \right] \times \mathbf{R} \right\}$$
(6.9b)

Finally, to avoid the integration involved in (6.9a), we use the time derivative of these equations to obtain the time domain EFIE (TD-EFIE) the time domain MFIE (TD-MFIE) as

$$\hat{\mathbf{n}} \times \hat{\mathbf{n}} \times \partial_t \mathcal{E}^i(\mathbf{r}, t) = \hat{\mathbf{n}} \times \hat{\mathbf{n}} \times \left\{ \frac{\mu_0}{4\pi} \int_{\Omega} d\mathbf{r'} \ \partial_t^2 \mathcal{J}(\mathbf{r'}, \tau) - \frac{1}{4\pi\varepsilon_0} \int_{\Omega} d\mathbf{r'} \ \nabla \nabla \cdot \mathcal{J}(\mathbf{r'}, \tau) \right\}$$
(6.10a)

and

$$\hat{\mathbf{n}} \times \partial_t \mathcal{H}^i(\mathbf{r}, t) = -\hat{\mathbf{n}} \times \left\{ \frac{1}{4\pi} \int_{\Omega} d\mathbf{r'} \left[\frac{1}{cR} \partial_t^2 \mathcal{J}(\mathbf{r'}, \tau) + \frac{1}{R^2} \partial_t \mathcal{J}(\mathbf{r'}, \tau) \right] \times \mathbf{R} \right\}$$
(6.10b)

The standard marching on in time (MOT) [92,114–116] solution to the above system of equations expands the unknown current in a set of spatio-temporal basis functions as $\mathbf{J}(\mathbf{r},t) = \sum_{n=1}^{N_s} \sum_{j=1}^{N_t} I_{n,j} \mathbf{j}_n(\mathbf{r}) T_j(t)$. The spatial basis functions $\mathbf{j}_n(\mathbf{r})$ typically chosen are RWG functions. However, the temporal basis functions $T_j(t)$ need to be carefully chosen. In the next section, we will visit this topic in some detail.

6.3 The Marching on in Time (MOT) scheme

To solve the TD-EFIE and TD-MFIE above, we will proceed similar to the frequency domain case. The spatio-temporal current $\mathcal{J}(\mathbf{r},t)$ is discretized using a set of basis functions that are assumed to be a product of N_s spatial vector basis functions (eventually the GMM basis functions) and N_t scalar shifted temporal functions (of

the form $T_j(t) \doteq T(t - j\delta t)$, that partition the time into segments of size Δt .

$$\mathcal{J}(\mathbf{r},t) \approx \sum_{i=1}^{N_S} \sum_{j=1}^{N_t} I_{j,n} T(t-j\Delta t) \mathbf{j}_n(\mathbf{r}). \tag{6.11}$$

Substituting (6.11) into the TD-EFIE/TD-MFIE and performing point testing ($\delta(t - i\Delta t)$) in time and Galerkin testing ($\mathbf{j}_m(\mathbf{r})$) in space results in a set of N_t , order- N_s matrix equations of the form

$$\sum_{j=1}^{N_t} \underline{Z_{i-j}} \, \underline{I_j} = \underline{V_i},\tag{6.12}$$

where

$$\underline{I_j} = \left[I_{j,n} \right], \tag{6.13a}$$

$$\underline{V_i} = \begin{cases}
\int_{\Omega} d\mathbf{r} \left[\hat{\mathbf{n}} \times \hat{\mathbf{n}} \times \partial_t \mathcal{E}^i(\mathbf{r}, i\Delta t) \right] \cdot \mathbf{j}_m(\mathbf{r}) \\
\int_{\Omega} d\mathbf{r} \left[\hat{\mathbf{n}} \times \partial_t \mathcal{H}^i(\mathbf{r}, i\Delta t) \right] \cdot \mathbf{j}_m(\mathbf{r})
\end{cases} (6.13b)$$

and

$$\underline{Z_{i-j}} = \begin{cases}
\int_{\Omega} d\mathbf{r} \, \mathbf{j}_{n}(\mathbf{r}) \cdot \left[\hat{\mathbf{n}} \times \hat{\mathbf{n}} \times \left\{ \frac{\mu_{0}}{4\pi} \int_{\Omega} d\mathbf{r'} \, \mathbf{j}_{n}(\mathbf{r'}) \partial_{t}^{2} T((i-j)\Delta t) - \frac{1}{4\pi\varepsilon_{0}} \int_{\Omega} d\mathbf{r'} \, \nabla \nabla \cdot \mathbf{j}_{n}(\mathbf{r'}) T((i-j)\Delta n) \right\} \right] \\
- \int_{\Omega} d\mathbf{r} \, \mathbf{j}_{n}(\mathbf{r}) \cdot \hat{\mathbf{n}} \times \left\{ \frac{1}{4\pi} \int_{\Omega} d\mathbf{r'} \, \left[\frac{1}{cR} \mathbf{j}_{n}(\mathbf{r'}) \partial_{t}^{2} T((i-j)\Delta t) + \frac{1}{R^{2}} \mathbf{j}_{n}(\mathbf{r'}) \partial_{t} T((i-j)\Delta t) \right] \times \mathbf{R} \right\}
\end{cases} (6.13c)$$

The most critical observation about the (6.13c) is that, if the temporal basis functions have finite support, that is $\exists k, l \rightarrow T(t) = 0 \ \forall t \leq -(l+1)\Delta t, t \geq (k+1)\Delta t$, then if R_{max} is the maximum spatial extent of the scatterer $(R_{max} \approx \text{diam}(\Omega))$, we

have that

$$\underline{\underline{Z_{i-j}}} = 0 \ \forall \ (i-j) < -l \text{ and } (i-j) > k + \frac{R_{max}}{c\Delta t}. \tag{6.14}$$

Further, if we assume that the temporal basis functions are causal, that is $T(\tau) = 0 \forall \tau \leq -\Delta t$, we have that $\underline{Z_{i-j}} = 0 \forall i < j-1$. This is called the "marching criterion", in that if this criterion is satisfied, the matrix equation (6.12) can be re-written as a marching scheme, given by

$$\underline{\underline{Z_0}I_i} = \underline{V_i} - \sum_{j=i-k_m}^{i-1} \underline{Z_{i-j}}\underline{I_j}$$
 (6.15a)

where k_m is given by

$$k_m = \frac{R_{\text{max}}}{c\Delta t} + k \tag{6.15b}$$

This naturally leads to a marching solution of the TDIE whereby the unknowns solved for in (a finite number of) prior time steps leads to the solution at the current time step.

6.4 Temporal basis functions

Given the marching scheme above, it is desirable to choose basis functions $T_j(t)$ that (i) have short temporal support, (ii) do not look forward in time, and (iii) provide good interpolation properties.

The most commonly used function in the literature are piecewise continuous functions of order p given by

$$T(t) = f_l(t)g_{p-l}(t) \text{ for } -\Delta t + l\Delta t \leq t \leq l\Delta t \text{ ; } l = 0\dots p \tag{6.16a}$$

where

$$f_l(t) = \begin{cases} 1 & l = 0\\ \prod_{i=1}^k \frac{t - i\Delta t}{-i\Delta t} & l \neq 0 \end{cases}$$

$$(6.16b)$$

and

$$g_{p-l}(t) = \prod_{i=1}^{p-l} \frac{t + i\Delta t}{i\Delta t}$$
 (6.16c)

Clearly, these functions satisfy (i)-(iii) and have been in active use for a very long time [52,92,114]. A plot of these functions are shown in figure 6.2a below. Another temporal basis function that has been used is the Approximate Prolate Spheroidal Wave Function (APSWF) given by

$$T(t) = \frac{\sin(s\omega_0 t)}{s\omega_0 t} \frac{\sin\left[a\sqrt{\left(\frac{t}{N\Delta t}\right)^2 - 1}\right]}{\sinh(a)\sqrt{\left(\frac{t}{N\Delta t}\right)^2 - 1}}$$
(6.17)

where ω_0 is the highest end of the frequency band of interest, s is an oversampling factor, $N \in \mathbb{Z}$ is the APSWF width parameter and $a = \pi N(s-1)/s$. These functions, shown in figure 6.2b can be shown to be band limited (to $\omega_{max} = (2s-1)\omega_0$), but are non causal, (the function value at a time instant depends on future values of time) [117]. This problem of the APSWF is solved by an extrapolation procedure that maps the forward part of the function using a least-squares approach, albeit at the expense of band-limitedness [116]. Either of these two approaches has an interesting consequence. Upon examination of equation (6.13c), it is clear that the solution of either TDIE requires the computation of at least one derivative of the temporal basis function. However, it can be shown that neither the Lagrange polynomials or the extrapolated APSWF functions used support more than one derivative. This has been reported to result in inaccuracies in the solution and instabilities in the marching

scheme. Some recent efforts to solve this effort attempt to use separable polynomial approximations to the Green's function to construct solutions [118, 119].

6.5 GMM for transient scattering

Traditionally the spatial basis functions used for the discretization of the TDIE are the RWG functions. These functions have been carried over to time domain integral equations (TDIE) from their frequency domain counterparts and have been shown to be highly effective in a variety of problems. However, the drawbacks that are suffered by the RWG functions in frequency domain are prevalent in the analysis of TDIE

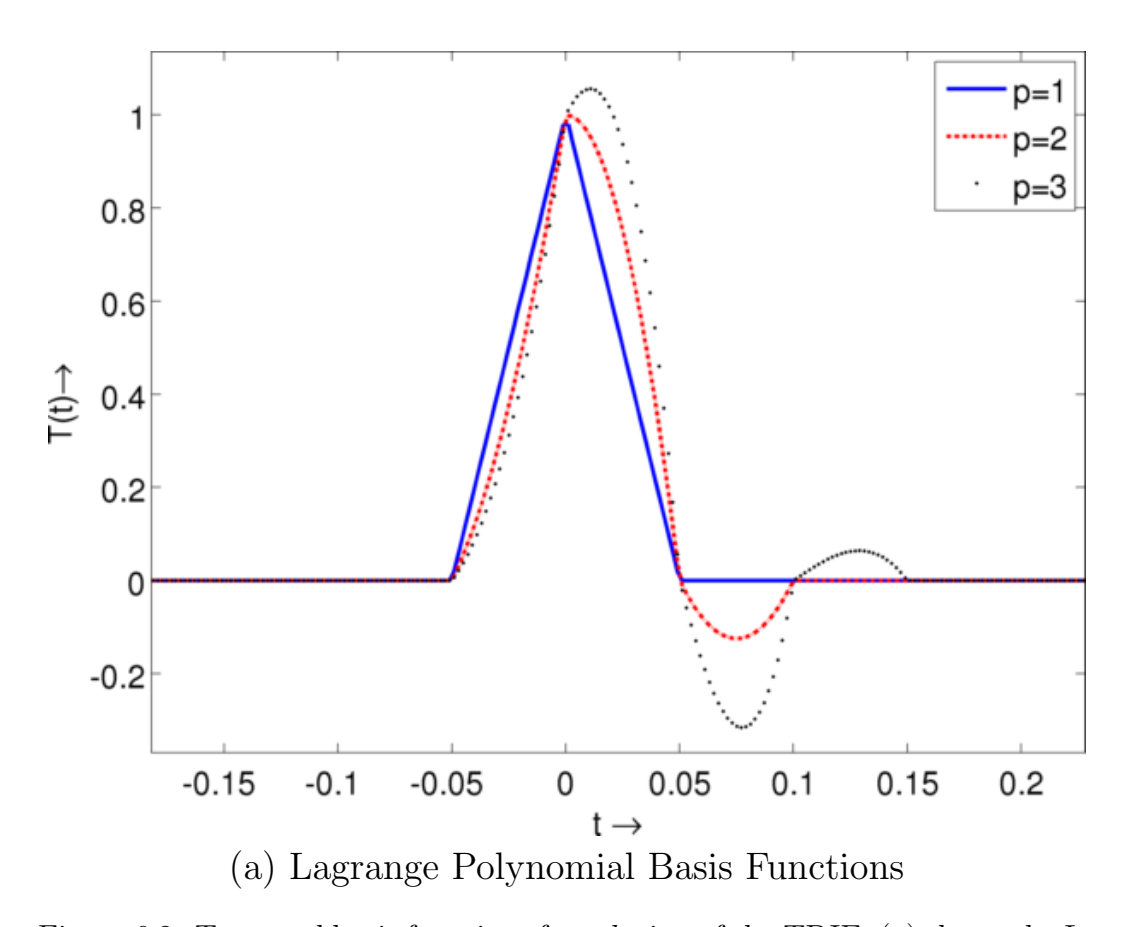


Figure 6.2: Temporal basis functions for solution of the TDIE. (a) shows the Lagrange polynomial basis functions which are not band limited as opposed to (b) approximate prolate spheroidal functions that are band limited but require extrapolation to maintain causality.

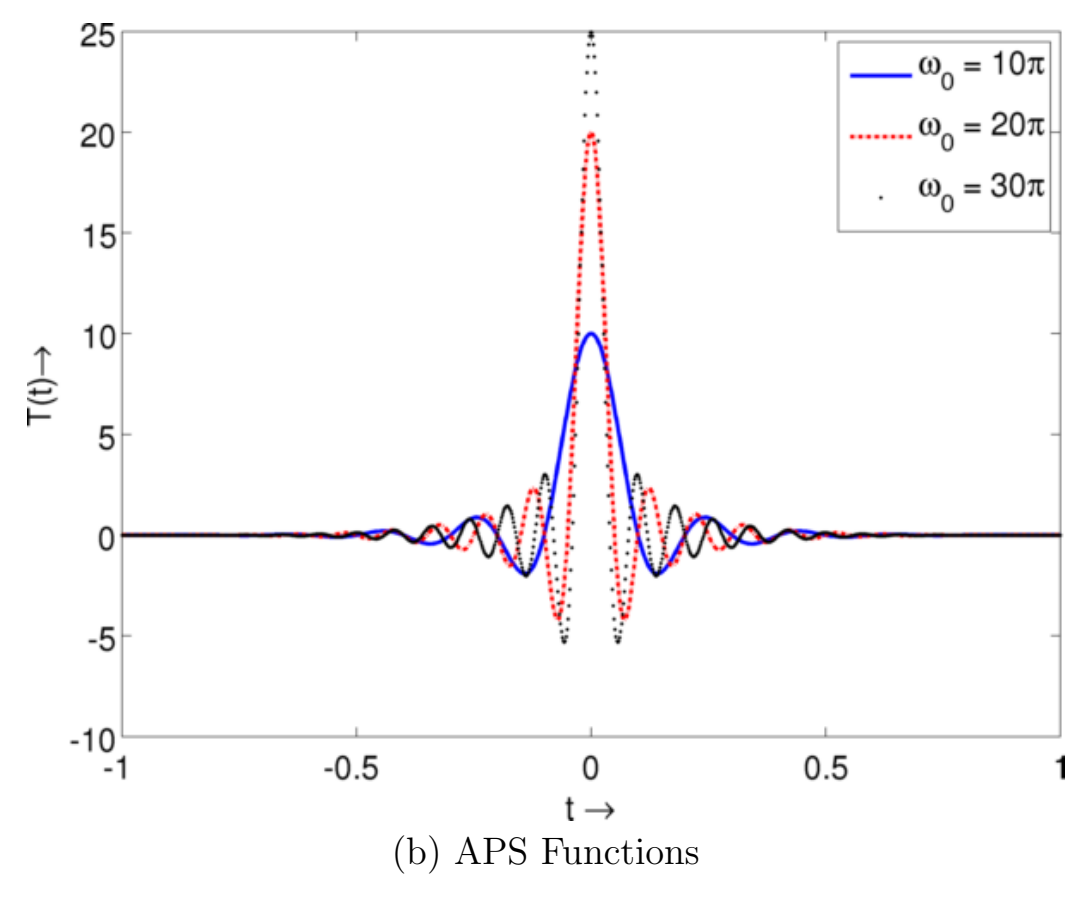


Figure 6.2 Continued: Temporal basis functions for solution of the TDIE. (a) shows the Lagrange polynomial basis functions which are not band limited as opposed to (b) approximate prolate spheroidal functions that are band limited but require extrapolation to maintain causality.

as well. While the close marriage between the basis function construction and the tessellation helps to satisfies continuity constraints across the interior edges of the tessellation, this nature of construction is inherently restrictive. As has been discussed before, even the use of mixed orders of polynomial basis functions is significantly involved and usually requires the careful design of patches and "transition" areas. In the frequency domain, the GMM was designed as an umbrella framework to include arbitrary functions in the basis space. We also demonstrated that the basis functions proposed result in a matrix system with stable condition numbers to very low frequencies. Here we extend the GMM scheme to the discretization of the TD-MFIE. We will describe a scheme for the extension of the GMM to time domain using products of GMM functions (for spatial basis functions) and interpolatory polynomials (for temporal basis functions). In the remainder of this chapter, we will first show that these basis functions provide accurate scattering results over a wide variety of geometries. Further, we will demonstrate several of the advantages of the GMM scheme including (i) its ability to arbitrarily mix basis functions across the geometry: using different basis functions in different areas of the tessellation can be trivially achieved under the GMM framework by simply changing an input flag. We will present results that show that the low frequency nature of the GMM discretized TD-MFIE is much more stable than the standard RWG-TD-MFIE.

The actual implementation of the GMM to the MOT scheme described above is straightforward. We retain the Lagrange polynomial interpolation in time and the point matching temporal testing scheme. The spatial basis functions can be replaced with the GMM functions exactly as done in the frequency domain case. The spatial integrals are now evaluated with a "Green's kernel" of 1/R as opposed to the oscillatory Green's kernel used for the frequency domain implementation.

6.6 Numerical Experiments

This section will illustrate a variety of numerical experiments that illustrate the validity and utility of the GMM discretization scheme. We will assume that the incident electric field is a Gaussian modulated plane wave of the form $\mathbf{E}^i(\mathbf{r},t) = \hat{\mathbf{p}}cos(2\pi f_0\tau)\exp\left[-(\tau-t_p)^2/2\sigma^2\right]$, where $\sigma=6/2\pi f_{bw}$ and $\tau=t-\hat{\mathbf{k}}\cdot\mathbf{r}/c$. $\hat{\mathbf{p}}$ and $\hat{\mathbf{k}}$ denote the polarization and the direction of propagation of the plane wave respectively. The center frequency f_0 and bandwidth f_{bw} describe the frequency characteristics of the signal. Examination of the incident field shows that the energy content is almost -160dB down at f_0+f_ω in comparison to the energy at f_0 . The scattered far field is computed from this signal and its Fourier transform is computed. The backscatter RCS is then extracted as the ratio of the frequency spectrum of the far field to that of the incident field. This allows us to evaluate the GMM discretization of the TD-MFIE against both other time domain methods (such as RWG-MOT) and frequency domain methods (by comparing RCS). The GMM basis functions are constructed starting from a triangular spatial discretization with an average edgelength of $0.1\lambda_m$, where λ_m is the lowest wavelength in the frequency bandwidth.

6.6.1 Validation

First we validate the GMM discretization scheme against both experiments and against the traditional RWG discretization. In this section, we will provide a plethora of results comparing the GMM-discretized TDIE compared with the standard RWG based TDIE. Figure 6.3a shows the backscatter RCS obtained from two PEC spheres, of radii 0.2m and 1.0m. The GMM discretizations result in $N_{GMM}=388$ and $N_{GMM}=200$ unknowns respectively. The RCS is compared to the that obtained from an MOT solver using RWG basis functions, resulting in $N_{RWG}=576$ and $N_{RWG}=192$ unknowns respectively. The center frequency $f_0=30MHz$ and band-

width is $f_{bw} = 15 MHz$. As is clear from the figures, there is excellent match between the backscatter RCS results.

Figure 6.3b compares the backscatter RCS for a NASA almond that fits in a box of dimensions $0.3m \times 1.15m \times 3m$. The direction of propagation $\hat{\mathbf{k}} = -\hat{\mathbf{z}}$ and the polarization $\hat{\mathbf{p}} = \hat{\mathbf{x}}$ of the incident wave is shown inset in the figure, along with a time-snapshot of the surface current. Again $f_0 = 1e8$ and the bandwidth extends to a low frequency end of 100Hz. The large bandwidth allows for the examination of the low frequency behavior of the GMM scheme. The number of unknowns are $N_{GMM} = 1528$ and $N_{RWG} = 1656$ respectively. The agreement between the RCS shown provides further confidence in the GMM discretization scheme.

Next, figure 6.4a compares the backscatter RCS obtained from a thin PEC box of size $20m \times 1m \times 20m$ using the GMM discretization $N_{GMM} = 1780$ to that using standard RWG $N_{RWG} = 2640$. The incident electric field is polarized along $\hat{\mathbf{y}}$ and incident along $\hat{\mathbf{x}}$, on the thin edge of the box. The center frequency of the incident field $f_0 = 15MHz$ and extends at the low frequency end to 100Hz. The agreement of the RCS in figure 6.4a further validates the GMM scheme. Finally, in figure 6.4b the backscatter RCS obtained from a PEC cube of side 0.7m, as a function of the incident wavelength, is compared against that obtained using both the RWG basis functions and experimental data reported in [109]. The direction of propagation $\hat{\mathbf{k}} = -\hat{\mathbf{y}}$ and polarization $\hat{\mathbf{p}} = \hat{\mathbf{x}}$ of the incident field is again reported inset in the figure along with a snapshot of the magnitude of surface current on the cube. Again, the agreement of the RCS to experiment and the RWG scheme validates the GMM scheme for the discretization of time domain integral equations.

6.6.2 Low frequency stability

The well conditioned nature of the GMM scheme at low frequencies is expected to result in low frequency stability in time. As a first step to investigating this property,

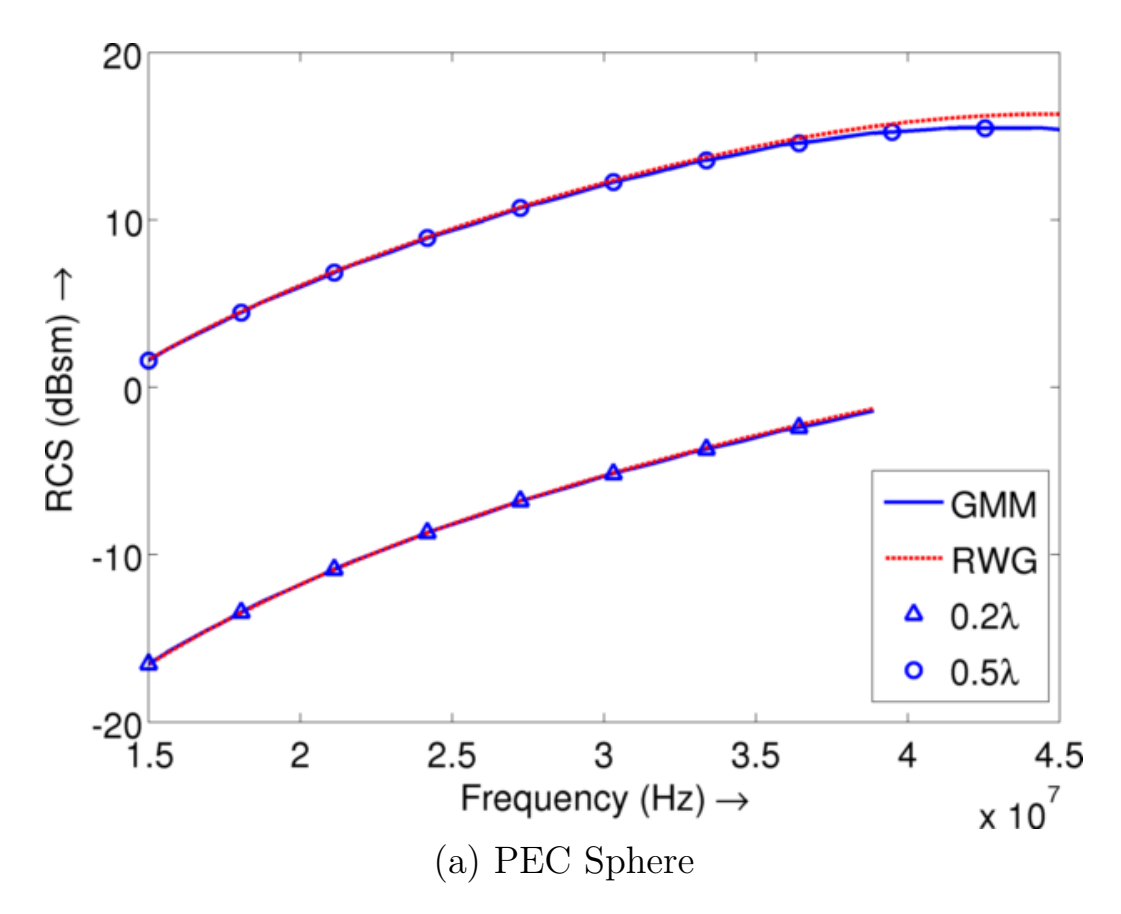


Figure 6.3: Backscatter RCS comparison for (a) two spheres of radii 0.2m and 0.5m and (b) a thin NASA almond $(0.3m \times 1.15m \times 3m)$ compared against RWG discretization. The inset figure shows snapshots of the magnitude of the current density on the almond.

we observe the backscatter RCS of the GMM scheme for very wideband incident fields. The same scattering problem is solved using both the GMM and RWG discretizations and the RCS observed in both cases is compared to a frequency domain scheme (using RWG basis functions) at a number of frequency points all the way down to the end of the frequency band of the input signal. Figure 6.5a compares the backscatter RCS for the thin box considered above $(20m \times 1m \times 20m, N_{GMM} = 1780, N_{RWG} = 2640)$. The incident field direction, polarization, center frequency and bandwidth are the same as the example in figure 6.4a above. As is clear from the figure, the RCS computed using the GMM discretization agrees with the frequency domain RCS down to very low frequencies. However, the RCS computed using the RWG scheme departs

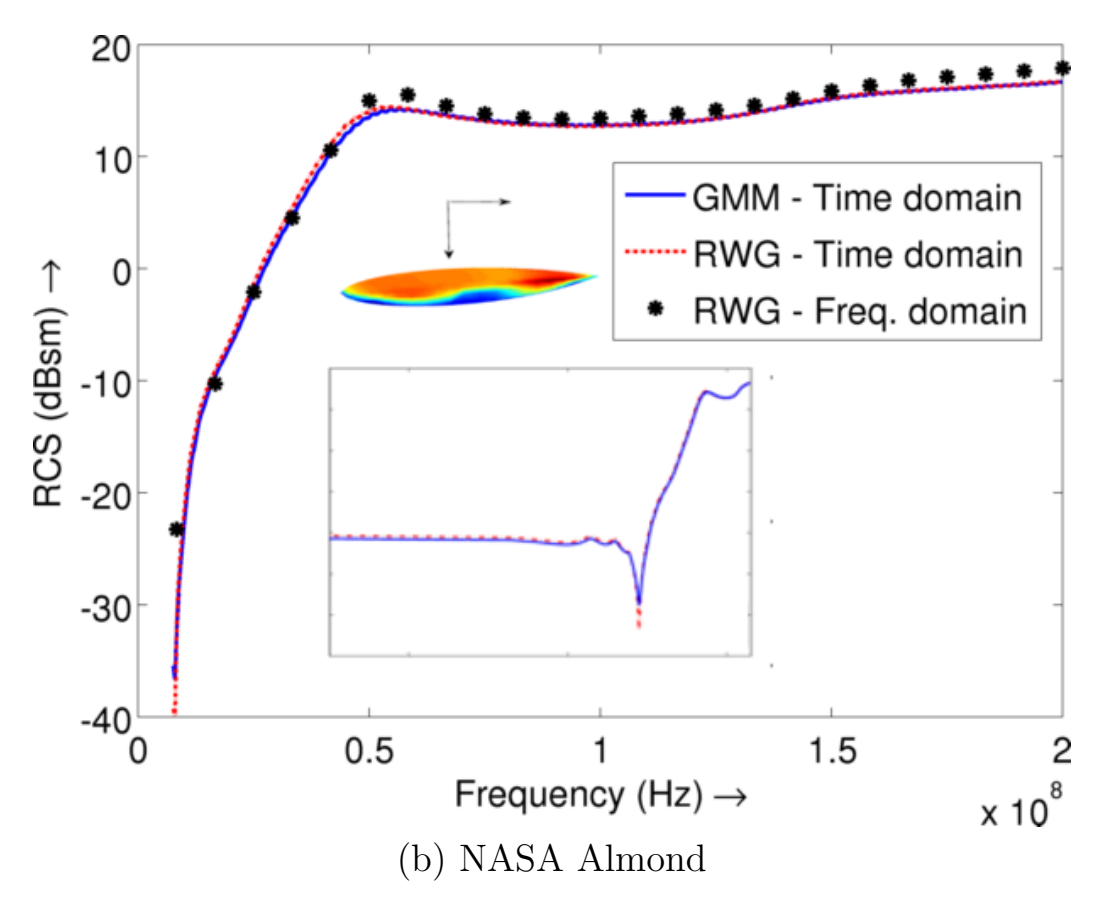


Figure 6.3 Continued: Backscatter RCS comparison for (a) two spheres of radii 0.2m and 0.5m and (b) a thin NASA almond $(0.3m \times 1.15m \times 3m)$ compared against RWG discretization. The inset figure shows snapshots of the magnitude of the current density on the almond.

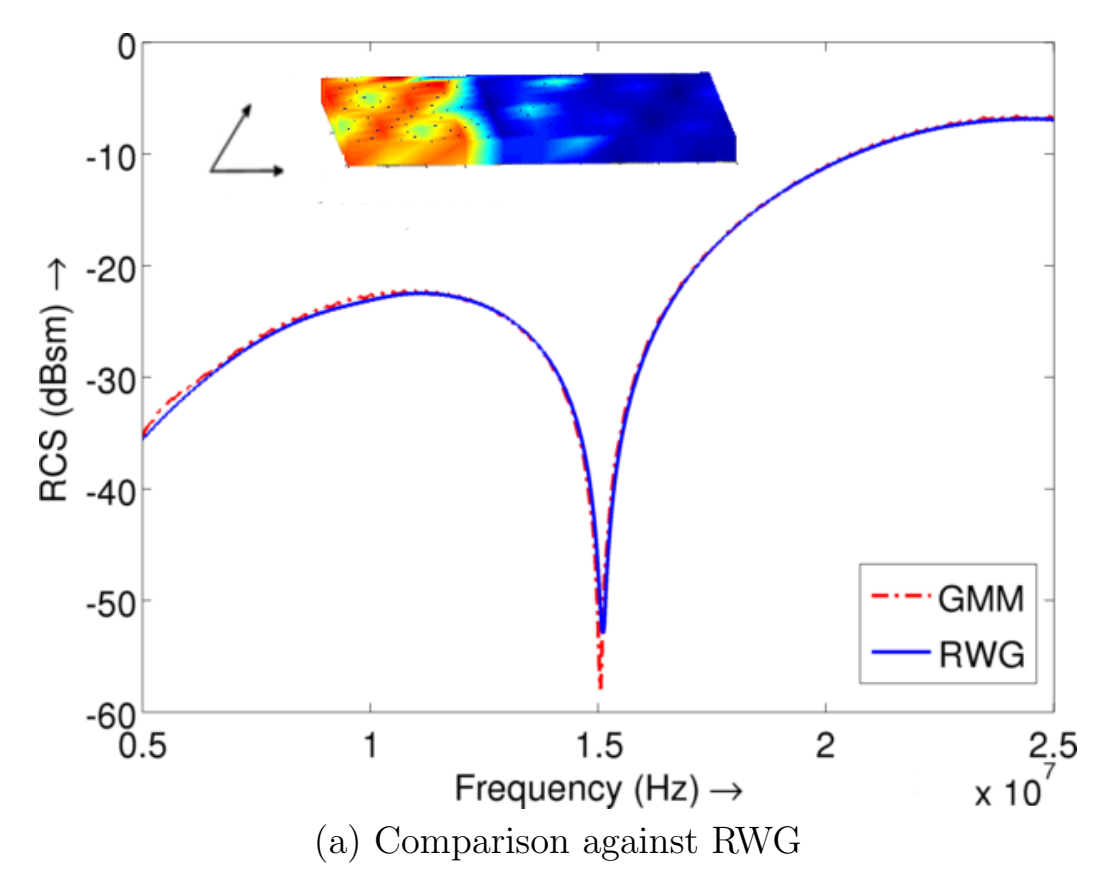


Figure 6.4: Backscatter RCS comparison for (a) a thin box of size $20m \times 1m \times 20m$ compared against RWG discretization and (b) a PEC cube of side 0.7m compared against both RWG and experimental result. The inset figures show snapshots of the magnitude of the current density on the scatterer.

from the frequency domain RCS at lower frequencies. While this needs to be further investigated for the EFIE, this nevertheless does point to the low frequency stability of the GMM discretization.

In figure 6.5b, we illustrate the utility of using a local surface Helmholtz decomposition. The use of a global Helmholtz decomposition, such as in the loop-star scheme [93], would preclude the application to multiply connected domains, such as the toroid shown inset in figure 6.5b. However, being based on a local surface Helmholtz decomposition, the GMM scheme is directly applicable to multiply connected domains. Figure 6.5b compares the backscatter RCS due to the scattering of a $-\hat{\mathbf{z}}$ directed plane wave polarized along $\hat{\mathbf{x}}$ from a PEC toroid of outer radius

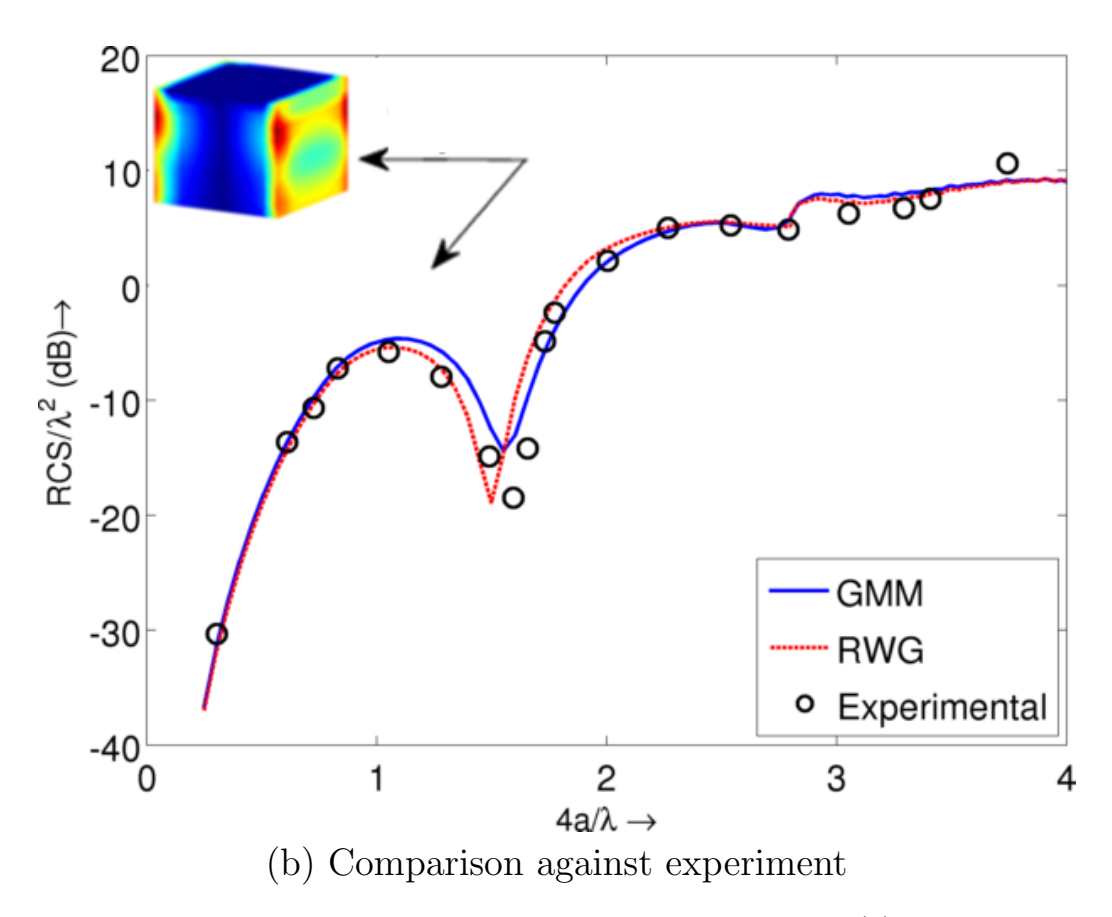


Figure 6.4 Continued: Backscatter RCS comparison for (a) a thin box of size $20m \times 1m \times 20m$ compared against RWG discretization and (b) a PEC cube of side 0.7m compared against both RWG and experimental result. The inset figures show snapshots of the magnitude of the current density on the scatterer.

0.75m and inner radius 0.5m, discretized using 1503 GMM and 3900 RWG unknowns respectively. The center frequency of the incident field $f_0 = 300MHz$ and the bandwidth is $f_{bw} = 150MHz$. The agreement of the RCS demonstrates the validity of using the GMM scheme for multiply connected domains.

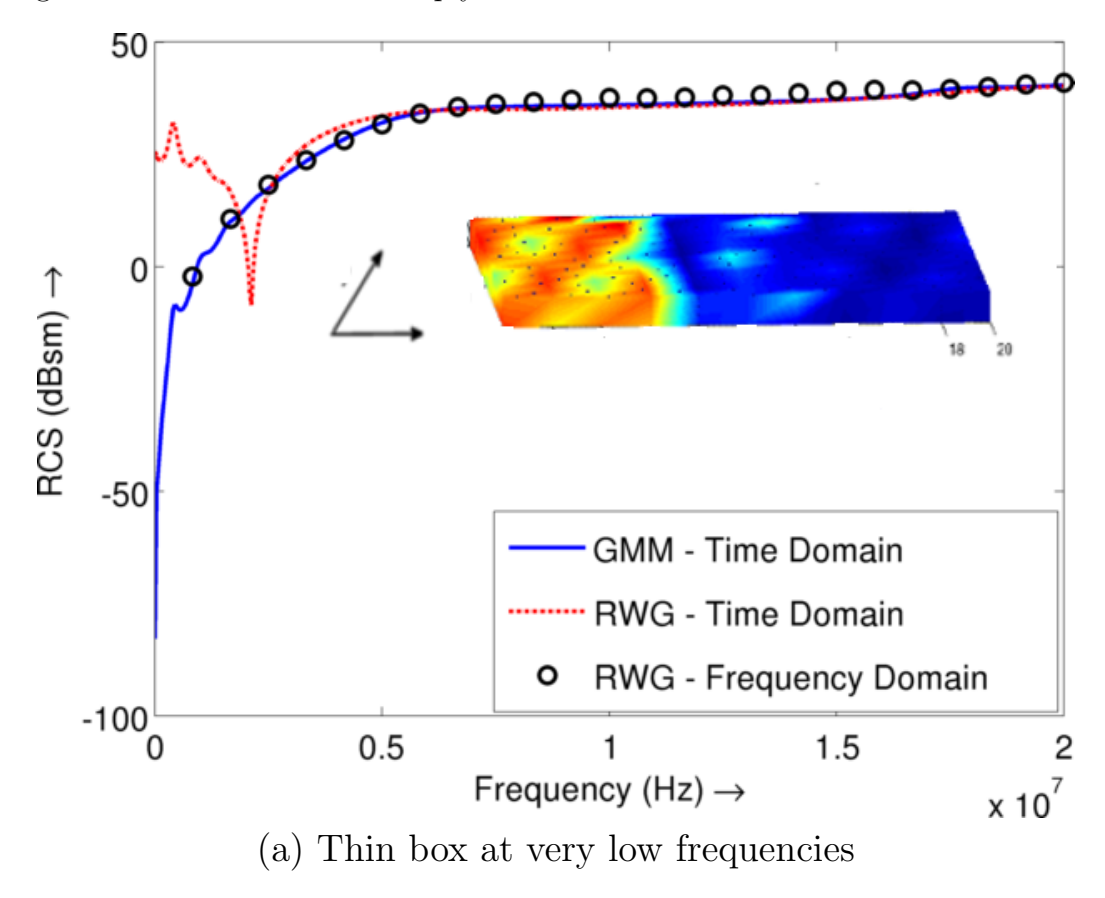


Figure 6.5: Backscatter RCS comparison for (a) thin box $(20m \times 1m \times 20m)$ and (b) a toroid (outer radius 0.75m and inner radius 0.5m). The inset figures show a snapshot of the magnitude of the current density and direction of propagation and incidence.

6.6.3 Mixtures of basis functions

Here, we present examples to illustrate the capability of the GMM scheme to mix basis functions in time domain. To this end, we first use the GMM discretization to generate the backscatter RCS due to scattering from a PEC box of dimensions $1.0m \times 4.0m \times 1.0m$ aligned with the long axis along $\hat{\mathbf{x}}$, discretized uniformly at

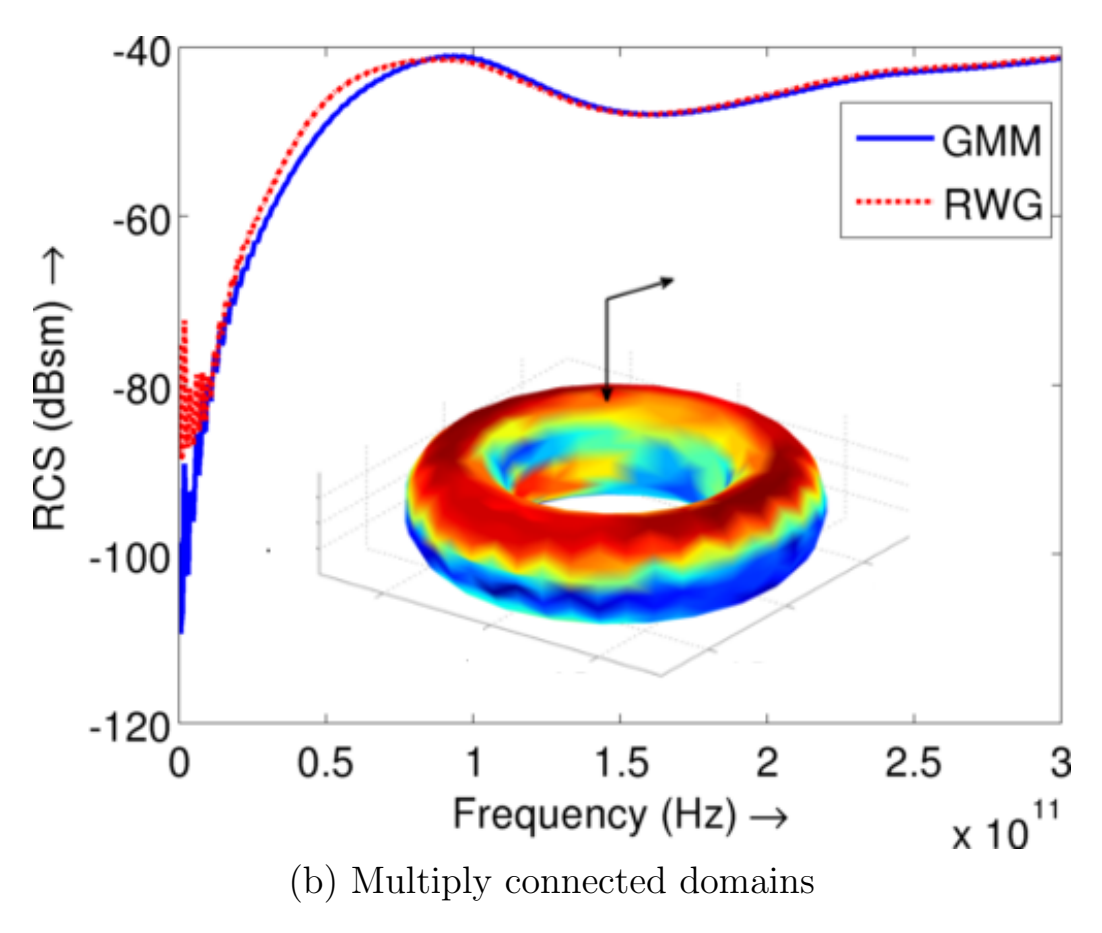


Figure 6.5 Continued: Backscatter RCS comparison for (a) thin box $(20m \times 1m \times 20m)$ and (b) a toroid (outer radius 0.75m and inner radius 0.5m). The inset figures show a snapshot of the magnitude of the current density and direction of propagation and incidence.

 $0.2\lambda_m$ at the highest frequency. Following this, the box is re-meshed with an average edge length of $0.2\lambda_m$, 0.2m from the two narrow ends, and $0.4\lambda_m$ elsewhere. Then the GMM discretization is applied to the new mesh using basis functions of order p=1 near the edge and p=2 elsewhere. Figure 6.6a shows the excellent agreement between the RCS obtained from these two cases. The $\hat{\mathbf{x}}$ polarized incident field is incident along $-\hat{\mathbf{z}}$ and $f_0=60MHz$ and $f_{bw}=30MHz$.

In figure 6.6b the backscatter RCS due to scattering of a $\hat{\mathbf{x}}$ polarized Gaussian modulated plane wave incident along $-\hat{\mathbf{z}}$ with center frequency 300MHz and bandwidth 299.9MHz on the above thin NASA almond $(0.3m \times 1.15m \times 3m)$ aligned along the $\hat{\mathbf{x}}$ axis. The almond is discretized with an average edge length of 0.1m. First the RCS is computed using GMM basis functions of order p=1 everywhere. Following this, GMM basis functions complete to order p=2 are used in all patches within 0.2m of the tip. Again, the RCS match each other very well.

Finally in figure 6.6c we mix three orders of basis functions. The inset in figure 6.6c shows a PEC box of dimension $3m \times 3m \times 6m$ aligned along the $\hat{\mathbf{x}}$ axis. An $\hat{\mathbf{x}}$ -polarized incident field of center frequency 200MHz and bandwidth 100MHz is incident on this box along $-\hat{\mathbf{z}}$. The backscatter RCS scattered by the box is computed using, first a uniform discretization of (average edge length) h = 0.1m everywhere and basis functions of order p = 1 everywhere. This is followed by discretizing the box using h = 0.1m near the corners, h = 0.2m near the edges and h = 0.25m elsewhere. The RCS is then computed using p = 1 in patches of size h = 0.1m, p = 2 where h = 0.2m and p = 3 where h = 0.25m. The two RCS are computed in figure 6.6c. The RCS, again, show excellent agreement.

The obvious advantage of this scheme is the ability to reduce the number of unknowns (the spatial unknown count dropped from 776 to 226 in the case of the box in figure 6.6a and from 11000 to 2800 in figure 6.6c). However, notwithstanding this gain in computational time, we would like to stress the ease of implementing the

mixture of orders of basis functions in the GMM scheme. Indeed, in the code, this change is effected simply by changing an input flag. This ability to trivially mix basis functions is unique to the GMM scheme.

6.6.4 Non conformal meshes

As before, one of the important advantages of disassociating the definition of the basis function from the underlying tessellation of the geometry is the ability to use non conformal meshes. This was investigated in some detail in earlier chapters. Here we consider scattering from a PEC box of dimensions $2.0m \times 0.2m \times 0.5m$. Two

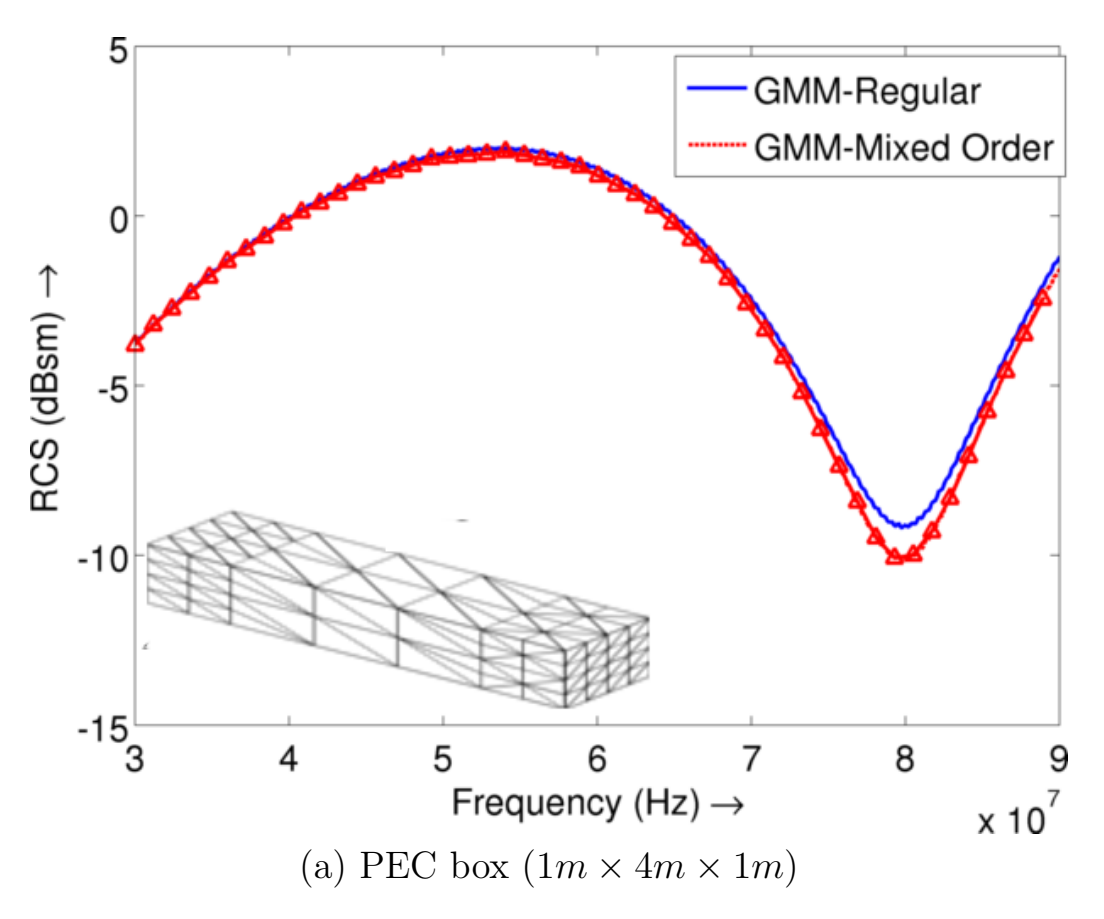


Figure 6.6: Backscatter RCS comparison of standard GMM vs. Mixed-order GMM (a) Box using p=1 near edges and p=2 in larger patches near center (b) NASA almond discretized with GMM basis functions complete to order p=2 near edges and p=1 elsewhere and (c) dielectric box using p=1 near edges, p=3 near the center and p=2 in the transition region.

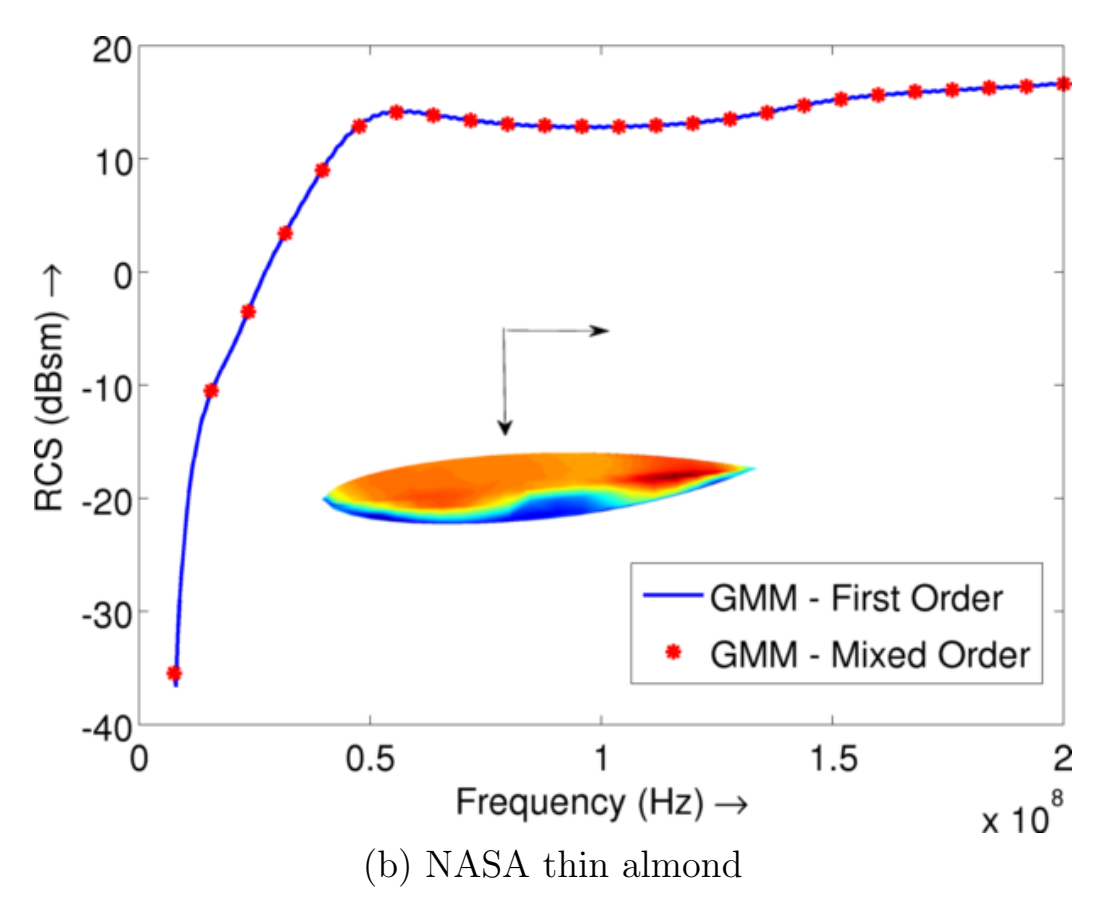


Figure 6.6 Continued: Backscatter RCS comparison of standard GMM vs. Mixed-order GMM (a) Box using p=1 near edges and p=2 in larger patches near center (b) NASA almond discretized with GMM basis functions complete to order p=2 near edges and p=1 elsewhere and (c) dielectric box using p=1 near edges, p=3 near the center and p=2 in the transition region.

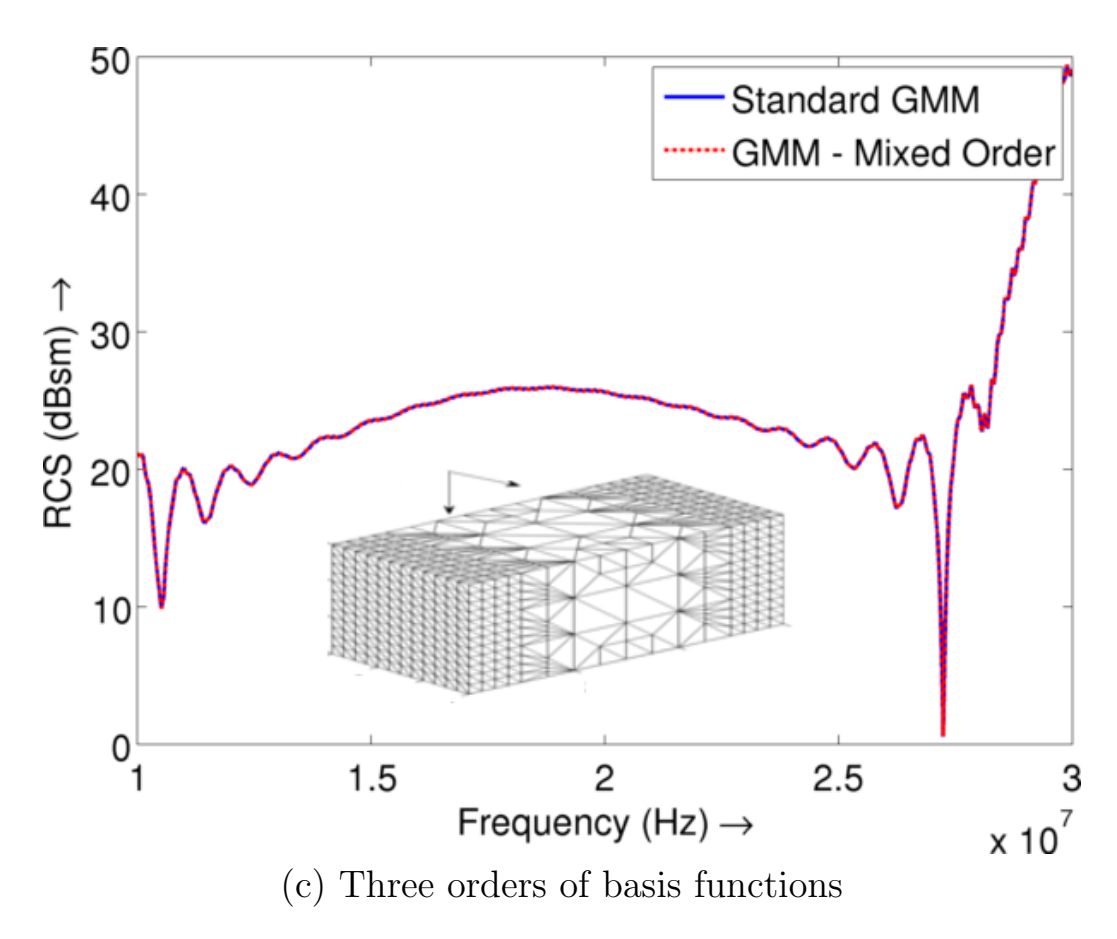
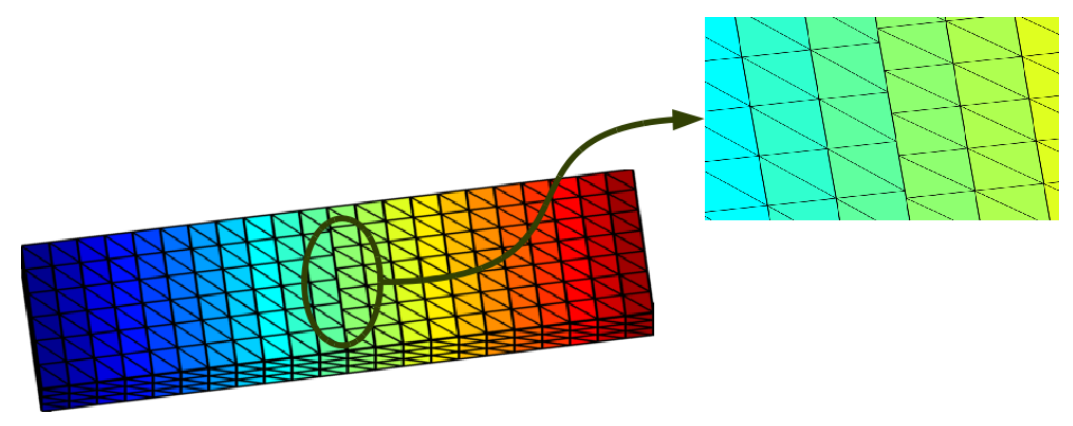


Figure 6.6 Continued: Backscatter RCS comparison of standard GMM vs. Mixed-order GMM (a) Box using p=1 near edges and p=2 in larger patches near center (b) NASA almond discretized with GMM basis functions complete to order p=2 near edges and p=1 elsewhere and (c) dielectric box using p=1 near edges, p=3 near the center and p=2 in the transition region.

halves of the box are meshed at slightly different discretization rates to obtain a non conformal mesh. The backscattered RCS is computed due to scattering of a $\hat{\mathbf{x}}$ polarized plane wave incident along $\hat{\mathbf{z}}$. The RCS obtained due to scattering from a discretization constructed on this non conformal mesh is compared against that is obtained by constructing a fully conformal mesh on the geometry. The agreement of the RCS shown in figure 6.7 demonstrates the ability of the GMM scheme to seamlessly handle non conformal meshes.



(a) Non conformal mesh for a box

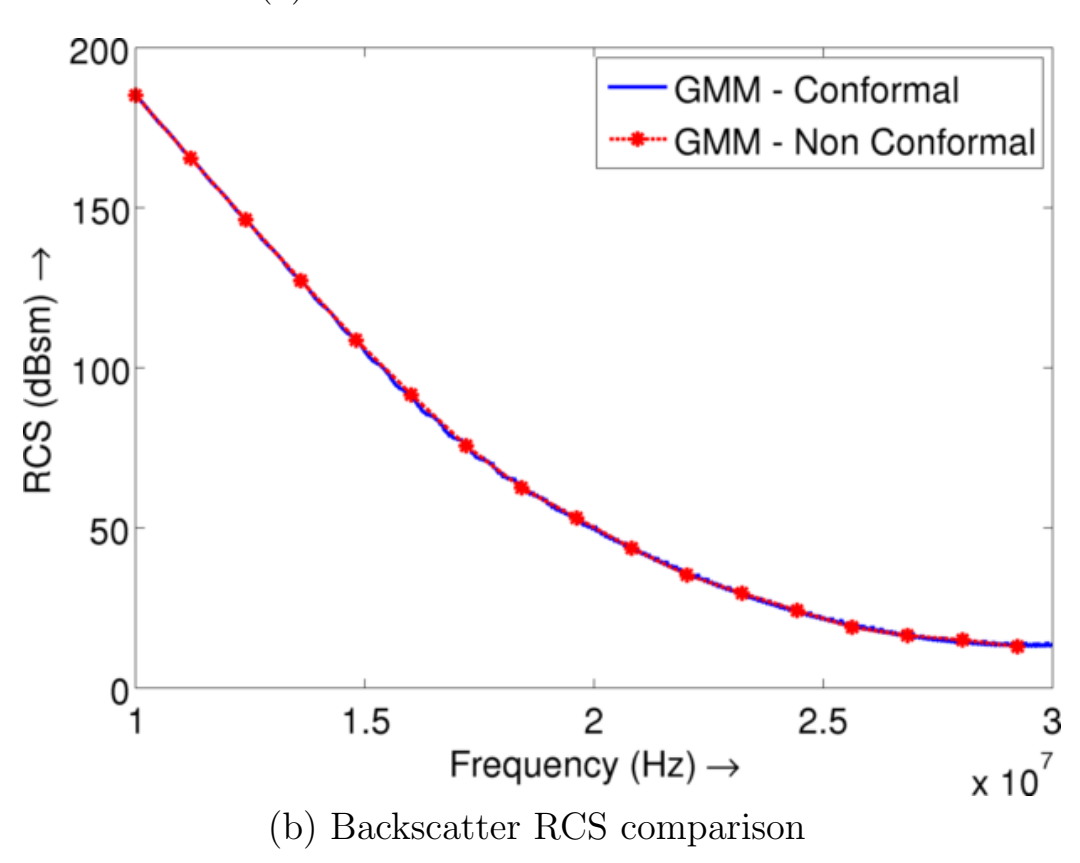


Figure 6.7: Backscatter RCS comparison for scattering from a non conformally meshed PEC box. RCS obtained by using the GMM discretization on a non conformal mesh (shown inset) compared against that obtained by discretizing on a (standard) conformal mesh for a thin box

Chapter 7

Conclusions and Future Work

This thesis introduces a novel umbrella framework for the solution of integral equations through the method of moments. The technique expands the basis function spaces that can be used to construct MoM solutions. The GMM framework encompasses a wide variety of schemes, such as meshless methods, Nystrom schemes, point cloud techniques as well as standard RWG based models. We have introduced a mechanism for the near complete decoupling of the basis function definition from the underlying tessellation, in stark contrast to the existing methods, where the basis function is usually designed to take advantage of an existing tessellation. The standard tessellation is replaced by an overlapping tessellation and a partition of unity function. The implicit continuity imposed by the partition of unity function allows for the above decoupling that then facilitates the use of a wide variety of approximation functions. The use of such functions in a traditional RWG scheme requires extremely careful manipulations.

In addition to the GMM framework, this thesis also proposes a *local* Helmhotlz decomposition based basis function scheme has resulted in a well conditioned system over a wide range of frequencies. This has important implications in the design of solution schemes for complex geometries involving a wide range of discretization

scales. Results have been presented that demonstrate the accuracy and advantages of the technique presented here.

The final two chapters of the thesis also describe the application of the GMM discretization scheme to the analysis of scattering from dielectric bodies and to time domain scattering. The advantages of the GMM technique are shown in terms of the well conditioned nature of the matrix systems in the discretization of the PM-CHWT system and the low frequency stability of the discretized time domain integral equations.

The chief contributions of this work are detailed below.

- An umbrella framework for the discretization of electromagnetic integral equations. A theoretical foundation has been laid for the development of Partition of Unity based basis functions and their error bounds have been rigorously derived for smooth geometries. A mechanism has been described for the possible decoupling of the geometry description and the basis function definition.
- A novel basis function design has been proposed which relies on a local Helmholtz decomposition and a mechanism has been described for its implementation using a variety of approximation functions.
- A detailed implementation structure has been provided for the GMM starting from commonly available meshes where a prescription has been provided for
 - The construction of patches
 - The definition of functions on these patches
 - Design of a partition of unity function
 - Design of approximation function
 - Removal of extra degrees of freedom and
 - Evaluation of the matrix elements.

- The technique has been applied to a wide variety of examples both validating the technique and demonstrating its prowess.
- An important consequence of the basis function definition in terms of well conditioned nature of the matrix system has been demonstrated for a very wide variety of geometries and formulations. Specifically, the system has been shown to result in (i) well conditioned matrix systems for PEC and dielectric objects over more than 6 decades of frequencies and (ii) low frequency stable discretizations in time domain.
- The technique has been extended to the discretization of the PMCHWT and Müller integral equations for the analysis of scattering from homogeneous dielectric bodies.
- The GMM has been applied to the analysis of transient scattering from PEC objects and the ability of the technique to result in a stable system at very low frequencies where the standard discretization breaks down has been demonstrated through several examples.

7.1 Future Work

The work that has been reported in this thesis opens the door for a variety of future research directions. We identify some of them in the remainder of this chapter.

7.1.1 Mathematical proof for the well conditioned nature of the GMM

The GMM discretized integral equations have been shown to be well conditioned over an extensive range of geometries and frequency scales. In particular, it was

demonstrated that for both PEC and dielectric objects, the numerical system has a near-constant condition number over more than 6 decades of frequency (or correspondingly length scales). This has very important consequences in the analysis of multi-scale objects. In addition to well conditioned matrix systems, the ability to trivially integrate multiple basis functions in the basis space will also enable the analysis of realistic geometries. This well conditioned nature of the discretized equations have also been translated to time domain where the GMM discretization has been shown to result in low frequency stable systems. Again, this result has important and far reaching consequences in the analysis of transient scattering. The immediate future work in this direction is to develop a rigorous set of proofs for the low frequency stability of the GMM discretization and potential bounds on the condition number of the matrix system. This can start by examining the projections of the basis functions on the eigen values of canonical structures and estimating condition numbers. Further proofs of the well conditioned nature can be obtained by examining the function spaces spanned by the basis functions involved in the GMM. A study of this nature will provide solid footing on which to design basis functions for realistic and challenging problems involving very large scales of discretization.

7.1.2 Generalized higher order patch construction

The GMM technique developed here has been implemented for flat triangulations. However extension to smoother geometry descriptions is extremely straightforward and will form the first of future efforts. Higher order patches are typically defined on a tangent triangle using shifted Sylvester polynomials [74]. To extend the GMM to such patch definitions using the structure described in this thesis is relatively easy. The patches can be constructed starting from nodes, with the collection of "higher order" triangles sharing that node forming a patch. The rest of the implementation structure will remain essentially unchanged with the sole exception of the construction

of matrix elements. Numerical integration on the curved triangles will have to now account for the curvature. Similarly the analytical integration routines will need to be redesigned. However, interesting questions arise if higher order patches are not constructed using such a combination of triangles. Another possible design is to construct a surface such that it coincides with the original surface at a finite set of points but maintains a continuous surface normal. This has the advantage of both having a smooth surface description and, at the same time, allowing for continuity of the normal component and thereby avoiding the need for the evaluation of singular integrals on the line as described in 4. The use of higher order patches have been shown to lead to significant gains in accuracy.

7.1.3 Further development of the transient GMM

The application of the GMM basis functions described in this work to the discretization of the time domain integral equations leaves a lot of interesting issues to be resolved. The main among these are the convergence properties of the inverse of the time domain operator. Further, the well conditioned nature of the discretized frequency domain operator leads to the expectation that the GMM discretization of the time domain integral equation will lead to a stable discrete system. This has been shown in several numerical examples in this thesis and a rigorous mathematical proof is a natural follow-up. Finally, the advantages of using a GMM-type discretization based on a partition of unity framework from both a stability and accuracy point of view can be explored.

7.1.4 Application to multi-scale geometries

The well conditioned nature of the GMM at low frequencies motivates its application to multi-scale geometries. In addition to the use of the fast multipole method that has already been applied to the GMM, the accelerated Cartesian expansions can also be implemented trivially within a GMM framework making it an excellent choice for the solution of scattering problems from highly multi-scale geometries. Further, straightforward parallelization of the GMM framework will enable the analysis of extremely large and realistic structures.

7.1.5 Domain Decomposition

The ability to include arbitrary functions in the basis function space of the GMM scheme can be exploited in a domain decomposition framework. Domain decomposition techniques have existed in literature for a while now and involve separating the domain of interest into smaller regions each of which are analyzed separately. The idea of domain decomposition is popular in constructing differential equation based solvers, and has been present in integral equation solvers for a while although it has only recently been used for analyzing mixed scale problems. This technique can be extended to integral equations and can be very useful for solving highly multi scale problems. The GMM framework is excellently suited to domain decomposition problems. The freedom of choice of basis functions allows a flexibility to use basis functions best suited for each sub domain and the partition of unity framework provides a natural mechanism for the interaction of these domains.

7.1.6 Application to other integral equations

Finally, the GMM mechanism has been developed in this work for electromagnetic integral equations. Their extension to the solution of integral equation formulations of acoustic scattering problem is expected to be straightforward and will become an area of active future research.

BIBLIOGRAPHY

BIBLIOGRAPHY

- [1] R. Mittra, Ed., Computer Techniques for Electromagnetics. Oxford: Pergamon Press, 1973.
- [2] L. F. Richardson, "The approximate arithmetical solution by finite differences of physical problems involving differential equations, with an application to the stress in a masonary dam," *Philosophical Transactions of the Royal Society of London: Series A*, vol. 210, pp. 307–357, 1901.
- [3] R. Courant, K. O. Freidrichs, and L. H., "Uber die partiellen differenzengleichungen der mathematischen physik," *Annals of Mathematics*, vol. 100, pp. 32–74, 1928.
- [4] P. D. Lax, "Weak solutions of nonlinear hyperbolic equations and their numerical computation," *Communications of Pure and Applied Mathematics*, vol. 7, pp. 159–193, 1954.
- [5] P. D. Lax and B. Wendroff, "Systems of conservation laws," *Commun. Pure Appl. Math.*, vol. 13, pp. 217–237, 1960.
- [6] A. Taflove and S. Hagness, Computational Electrodynamics: The Finite Difference Time Domain Method. Boston: Artech House, 2000.
- [7] S. C. Brenner and L. R. Scott, *The Mathematical Theory of Finite Element Methods*. Springer, 2002.
- [8] J. M. Jin, The Finite Element Method in Electromagnetics. New York: Wiley, 2002.
- [9] I. Babuska, "Error Bounds for the Finite Element Methods," *Numerische Mathematik*, vol. 333, pp. 322–333, 1971.
- [10] —, "The finite element method with lagrange multipliers," Numerische Mathematik, pp. 179–192, 1973.

- [11] A. Bossavit and J.-C. Verite, "A mixed fem-biem method to solve 3-d eddy-current problems," *Magnetics, IEEE Transactions on*, vol. 18, no. 2, pp. 431–435, Mar 1982.
- [12] A. Bendali, "Numerical analysis of the exterior boundary value problem for the time- harmonic maxwell equations by a boundary finite element method part 1: The continuous problem," *Mathematics of Computation*, vol. 43, no. 167, pp. 29–46, jul 1984.
- [13] —, "Numerical analysis of the exterior boundary value problem for the time-harmonic maxwell equations by a boundary finite element method part 2: The discrete problem," *Mathematics of Computation*, vol. 43, no. 167, pp. 47–68, jul 1984.
- [14] M. L. Barton and Z. J. Cendes, "New vector finite elements for threedimensional magnetic field computation," *Journal of Applied Physics*, vol. 61, pp. 3919–3921, Apr. 1987.
- [15] R. Lee and A. C. Cangellaris, "A study of discretization error in the finite element approximation of wave solution," *IEEE Transactions on Antennas and Propagation*, vol. 40, pp. 542–549, 1992.
- [16] D. Botteldooren, "Acoustical finite-difference time-domain simulation in a quasi-cartesian grid," *Journal of the Acoustical Society of America*, vol. 95, no. 5, pp. 2313–2319, 1994.
- [17] —, "Finite-difference time-domain simulation of low-frequency room acoustic problems," *Journal of the Acoustical Society of America*, vol. 98, no. 6, pp. 3302–3308, 1995.
- [18] J.-M. Jin, "Finte element-boundary element methods for electromagnetic scattering," Ph.D. dissertation, The University of Michigan, 1989.
- [19] A. F. Peterson, Mapped Vector Basis Functions for Electromagnetic Integral Equations. Morgan & Claypool, 2006.
- [20] I. Perugia, D. Schötzau, and P. Monk, "Stabilized interior penalty methods for the time-harmonic maxwell equations," *Computer Methods in Applied Mechan*ics and Engineering, vol. 191, no. 41, pp. 4675–4697, September 2002.
- [21] C. Lu, J. Villa, B. Shanker, and L. Kempel, "Generalized finite element method for analyzing scattering from non-lipschitzian domains," in *Antennas and Propagation Society International Symposium 2006*, *IEEE*, 9-14 July 2006, pp. 1783–1786.
- [22] Y.-J. Li and J.-M. Jin, "A new dual-primal domain decomposition approach for finite element simulation of 3-d large-scale electromagnetic problems," Antennas and Propagation, IEEE Transactions on, vol. 55, no. 10, pp. 2803–2810, Oct. 2007.

- [23] R. F. Harrington, "Boundary integral formulations for homogeneous material bodies," *Journal of Electromagnetic Waves and Applications*, vol. 3, pp. 1–15, 1989.
- [24] —, Field Computation by Moment Method. MacMillan Publishing Company, 1968.
- [25] J. R. Mautz and R. F. Harrington, "H-field, e-field, and combined field solutions for conducting bodies of revolution," $AE\ddot{U}$, vol. 32, pp. 157–164, 1978.
- [26] —, "Electromagnetic scattering from a homogeneous body of revolution," $AE\ddot{U}$, vol. 33, pp. 71–80, 1979.
- [27] W. C. Chew, M. Tong, and B. Hu, *Integral Equation Methods for Electromagnetic and Elastic Waves*, C. A. Balanis, Ed. Morgan & Claypool, 2009.
- [28] R. Kress, Linear Integral Equations. Springer-Verlag, 1989.
- [29] A. J. Poggio and E. K. Miller, "Integral equation solutions of three-dimensional scattering problems," in *Computer Techniques for Electromagnetics*, R. Mittra, Ed. Oxford: Pergamon Press, 1973.
- [30] J.-C. Nedelec, Acoustic and Electromagnetic Equations: Integral Representations for Harmonic Problems. Springer, March 2001. [Online]. Available: http://www.amazon.ca/exec/obidos/redirect?tag=citeulike09-20&path=ASIN/0387951555
- [31] R. Adams, "Physical and analytical properties of a stabilized electric field integral equation," *IEEE T ANTENN PROPAG*, vol. 52, no. 2, pp. 362–372, 2004.
- [32] A. Buffa and S. H. Christiansen, "The electric Field integral equation on Lipschitz screens: definitions and numerical approximation," *Numerische Mathe*matik, vol. 94, pp. 229–267, 2003.
- [33] A. Buffa and R. Hiptmair, "A coercive combined field integral equation for electromagnetic scattering," *Society*, vol. 42, no. 2, pp. 621–640, 2004.
- [34] S. H. Christiansen, "Discrete fredholm properties and convergence estimates for the electric field integral equation," *Math. Comput.*, vol. 73, no. 245, pp. 143–167, 2004.
- [35] T. Ha-Duong, On retarded potential boundary integral equations and their discretisation in Topics in Computational Wave Propagation: Direct and Inverse Problems. Springer-Verlag,, 2003, p. 301336.
- [36] R. Hiptmair, "Higher order whitney forms," *Progress in Electromagnetics Research*, vol. 32, pp. 271–299, 1988.

- [37] G. Hsiao and R. Kleinman, "Mathematical foundations for error estimation in numerical solutions of integral equations in electromagnetics," *Antennas and Propagation*, *IEEE Transactions on*, vol. 45, no. 3, pp. 316–328, March 1997.
- [38] R. Coifman, V. Rokhlin, and S. Wandzura, "The fast multipole method for the wave equation: A pedestrian prescription," *IEEE Antennas Propagat. Mag.*, vol. 35, no. 3, pp. 7–12, 1993.
- [39] V. Rokhlin, "Diagonal forms of translation operators for the helmholtz equation in three dimensions," *Applied and Computational Harmonic Analysis*, vol. 1, pp. 82–93, 1993.
- [40] H. Huang and B. Shanker, "A \(\chi(n)\) procedure for evaluating the yukawa potential and the ewald summation for peroidic systems," Submited to J. Comp. Phys. (Technical Report Available at https://www.egr.msu.edu/ece/Technicalpapers/), 2007.
- [41] L. Greengard and W. D. Gropp, "A parallel version of the fast multipole method," *Computers and Mathematics with Applications*, vol. 20, pp. 63–71, 1990.
- [42] L. Greengard and V. Rokhlin, "A new version of the fast multipole method for the laplace equation in three dimensions," *Acta Numerica*, vol. 6, pp. 229–269, 1997.
- [43] —, "A fast algorithm for particle simulations," *Journal of Computational Physics*, vol. 20, pp. 63–71, 1987.
- [44] W. C. Chew, J. M. Jin, C. C. Lu, E. Michielssen, and J. M. Song, "Fast solution methods in electromagnetics," *IEEE Transactions on Antennas and Propaga*tion, vol. 45, pp. 533–543, 1997.
- [45] J. M. Song and W. C. Chew, "Multilevel fast-multipole algorithm for solving combined field integral equations of electromagnetic scattering," *Microwave and Optical Technology Letters*, vol. 10, no. 1, pp. 14–19, 1995.
- [46] J. M. Song, C. C. Lu, and W. C. Chew, "Mlfma for electromagnetic scattering by large complex objects," *IEEE Transactions on Antennas and Propagation*, vol. 45, pp. 1488–1493, 1997.
- [47] W. Chew, E. Michielssen, J. M. Song, and J. M. Jin, Eds., Fast and Efficient Algorithms in Computational Electromagnetics. Norwood, MA, USA: Artech House, Inc., 2001.
- [48] M. Vikram, H. Huang, B. Shanker, and T. Van, "A novel wideband fmm for fast integral equation solution of multiscale problems in electromagnetics," Antennas and Propagation, IEEE Transactions on, vol. 57, no. 7, pp. 2094–2104, July 2009.

- [49] A. Ergin, B. Shanker, and E. Michielssen, "The plane-wave time-domain algorithm for the fast analysis of transient wave phenomena," *Antennas and Propagation Magazine*, *IEEE*, vol. 41, no. 4, pp. 39–52, Aug. 1999.
- [50] A. A. Ergin, B. Shanker, and E. Michielssen, "Fast evaluation of three-dimensional transient wave fields using diagonal translation operators," *Journal of Computational Physics*, vol. 146, no. 1, pp. 157–180, 1998.
- [51] B. Shanker, A. A. Ergin, K. Ayg¨n, and E. Michielssen, "Analysis of transient electromagnetic scattering phenomena using a two-level lane wave time domain algorithm," *IEEE Trans. Antennas and Propagat.*, vol. 48, pp. 510–523, 2000.
- [52] B. Shanker, A. Ergin, M. Lu, and E. Michielssen, "Fast analysis of transient electromagnetic scattering phenomena using the multilevel plane wave time domain algorithm," *Antennas and Propagation, IEEE Transactions on*, vol. 51, no. 3, pp. 628–641, March 2003.
- [53] B. Shanker, A. A. Ergin, and E. Michielssen, "Analysis of transient scattering from penetrable bodies using using the multilevel plane wave time domain algorithm," *Journal of Optical Society of America*, vol. 19, pp. 716–726, 2002.
- [54] G. Kobidze, J. Gao, B. Shanker, and E. Michielssen, "A fast time domain integral equation based scheme for analyzing scattering from dispersive objects," Antennas and Propagation, IEEE Transactions on, vol. 53, no. 3, pp. 1215–1226, March 2005.
- [55] P. Jiang, K. Yegin, S. Li, B. Shanker, and E. Michielssen, "An improved plane wave time domain algorithm for dissipative media," in *Antennas and Propagation Society International Symposium*, 2003. IEEE, vol. 3, 22-27 June 2003, pp. 563–566vol.3.
- [56] G. Kobidze and B. Shanker, "Integral equation based analysis of scattering from 3d inhomogeneous anisotropic bodies," in *Antennas and Propagation Society International Symposium*, 2003. IEEE, vol. 1, 22-27 June 2003, pp. 633–636vol.1.
- [57] A. A. Ergin, B. Shanker, and E. Michielssen, "Analysis of transient wave scattering from rigid bodies using a burton-miller approach," *Journal of the Acoustical Society of America*, vol. 106, no. 5, pp. 2396–2404, 1999.
- [58] N.-W. Chen, B. Shanker, and E. Michielssen, "Integral-equation-based analysis of transient scattering from periodic perfectly conducting structures," in *Microwaves, Antennas and Propagation, IEE Proceedings* -, vol. 150, 10 April 2003, pp. 120–124.
- [59] J. H. Richmond, "A wire-grid model for scattering by conducting bodies," *IEEE Transactions on Antennas & Propagation*, vol. AP-14, pp. 782–786, 1966.

- [60] E. K. Miller and F. J. Deadrick, "Some computational aspects of thin-wire modeling," in *Numerical and Asymptotic Techniques in Electromagnetics*, R. Mittra, Ed. Springer-Verlag, 1975.
- [61] K. S. H. Lee, L. Marin, and J. P. Castillo, "Limitations of wire- grid modeling of a closed surface," *IEEE Transactions on Electromagnetic Compatability*, vol. EMC-18, pp. 123–129, 1976.
- [62] N. C. Albertsen, J. E. Hansen, and N. E. Jensen, "Computation of radiation from wire antennas on conducting bodies," *IEEE Transactions on An*, vol. AP-22, pp. 200–206, 1974.
- [63] D. L. Knepp and J. Goldhirsh, "Numerical analysis of electromagnetic radiation properties of smooth conducting bodies," *IEEE Transactions on Antennas & Propagation*, vol. AP-20, pp. 383–388, 1972.
- [64] N. N. Wang, J. H. Richmond, and M. C. Gilreath, "Sinusoidal reaction formulation for radiation and scattering from conducting surfaces," *IEEE Transactions* on Antennas & Propagation, vol. AP-23, pp. 376–382, 1975.
- [65] E. H. Newman and D. M. Pozar, "Electromagnetic modeling of composite wire and surface geometries," *IEEE Transactions on Antennas & Propagation*, vol. AP-26, pp. 784–789, 1978.
- [66] A. Sankar and T. Tong, "Current computation on complex structures by finite-element method," *Electronics Letters*, vol. 11, pp. 481–482, 1975.
- [67] J. J. H. Wang, "Numerical analysis of three-dimensional arbitrarily-shaped conducting scatters by trilateral surface cell modelling," *Radio Science*, vol. 13, pp. 947–952, 1978.
- [68] J. J. H. Wang and C. Papanicolopulos, "Surface patch modeling of scatterers of arbitrary shapes," in *The digest of the International Symposium of the Antennas and Propagation Society*, 1979.
- [69] G. Jeng and A. Wexler, "Finite element, boundary integral equation analysis of scattering problems," in *URSI Symposium on Electromagnetic Theory*, 1977.
- [70] A. W. Glisson and D. R. Wilton, "Simple and efficient numerical methods for problems of electromagnetic radiation and scattering from surface," *IEEE Transactions on Antennas and Propagation*, vol. 28, pp. 593–603, 1980.
- [71] S. M. Rao, D. R. Wilton, and A. W. Glisson, "Electromagnetic scattering by surfaces of arbitrary shape," *IEEE Transactions on Antennas and Propagation*, vol. 30, pp. 408–418, 1982.
- [72] J. Nedelec, "Mixed finite elements in \mathbb{R}^3 ," Numer. Math, pp. 93–315, 1980.

- [73] P.-A. Raviart and J. M. Thomas, *Mathematical aspects of finite element methods*. Springer, 1975, vol. 606, ch. A mixed finite element method for 2nd order elliptic problems, pp. 292–315.
- [74] R. D. Graglia, D. R. Wilton, and A. F. Peterson, "Higher order interpolatory vector bases for computational electromagnetics," *IEEE Transactions on An*tennas and Propagation, vol. 45, pp. 329–342, 1997.
- [75] W. Cai, T. Yu, H. Wang, and Y. Yu, "High-order mixed rwg basis functions for electromagnetic applications," *IEEE Transactions on Microwave Theory and Techniques*, vol. 49, no. 7, pp. 1295–1303, Jul 2001.
- [76] J. M. Melenk and I. Babuska, "The partition of unity finite element method
 : Basic theory and applications," Computer Methods in Applied Mechanical Engineering, vol. 139, pp. 289–314, 1996.
- [77] C. Lu and B. Shanker, "Generalized finite element method for vector electromagnetic problems," *IEEE Transactions on Antennas and Propagation*, vol. 55, no. 5, pp. 1369–1381, May 2007.
- [78] N. Nair and B. Shanker, "Generalized method of moments: A novel discretization scheme for integral equations," to appear in IEEE Transactions on Antennas and Propagation; technical report available at https://www.egr.msu.edu/ece/technical_papers, 2010.
- [79] D. Wilton and S. Govind, "Incorporation of edge conditions in moment method solutions," *IEEE Transactions on Antennas and Propagation*, vol. 25, no. 6, pp. 845–850, Nov 1977.
- [80] W. Brown and D. Wilton, "Singular basis functions and curvilinear triangles in the solution of the electric field integral equation," *Antennas and Propagation*, *IEEE Transactions on*, vol. 47, no. 2, pp. 347–353, Feb 1999.
- [81] R. Graglia and G. Lombardi, "Singular higher order complete vector bases for finite methods," *IEEE Transactions on Antennas and Propagation*, vol. 52, no. 7, pp. 1672–1685, July 2004.
- [82] A. F. Peterson and M. M. Bibby, "High-order numerical solutions of the mfie for the linear dipole," *IEEE Transactions on Antennas and Propagation*, vol. 52, pp. 2684–2691, 2004.
- [83] M. M. Bibby, A. F. Peterson, and C. M. Coldwell, "High order representations for singular currents at corners," *IEEE Transactions on Antennas and Propagation*, vol. 56, pp. 2277–2287, 2008.
- [84] N. Nair, C. Lu, and B. Shanker, "Differential and integral equation solvers based on generalized moments and partitions of unity," in *Electromagnetics in Advanced Applications*, 2007. ICEAA 2007. International Conference on, Sept. 2007, pp. 974–977.

- [85] W. C. Chew, Waves and Fields in Inhomogeneous Media. New York: Van Nostrand Reinhold, 1990.
- [86] A. F. Peterson, S. L. Ray, and R. Mittra, Computational Methods for Electromagnetics, 1st ed., ser. IEEE/OUP series on electromagnetic wave theory. New York: IEEE Press, 1998.
- [87] J. A. Stratton, Electromagnetic theory, ser. International series in physics. New York: McGraw-Hill, 1941.
- [88] A. W. Maue, "The formulation of a general diffraction problem by an integral equation," *Zeitschrift fur Physik A*, vol. 126, pp. 601–618, 1949.
- [89] L. N. Medgyesi-Mitschang, J. M. Putnam, and M. B. Gedera, "Generalized method of moments for three-dimensional penetrable scatteres," J. Opt. Soc. Am. A, vol. 11, pp. 1383–1398, 1994.
- [90] K. A. Michalski and D. Zheng, "Electromagnetic scattering and radiation by surfaces of arbitrary shape in layered media," *IEEE Transactions on Antennas* and Propagation, vol. 38, pp. 335–344, 1990.
- [91] —, "Electromagnetic scattering and radiation by surfaces of arbitrary shape in layered media. ii. implementation and results for contiguous half-spaces," *IEEE Transactions on Antennas and Propagation*, vol. 38, pp. 345–352, 1990.
- [92] S. Rao and D. Wilton, "Transient scattering by conducting surfaces of arbitrary shape," *IEEE Transactions on Antennas and Propagation*, vol. 39, no. 1, pp. 56–61, 1991. [Online]. Available: http://ieeexplore.ieee.org/lpdocs/epic03/wrapper.htm?arnumber=64435
- [93] G. Vecchi, "Loop-Star Decomposition of Basis Functions in the Discretization of the EFIE," *IEEE Transactions on Antennas and Propagation*, vol. 47, no. 2, pp. 339–346, 1999.
- [94] T. J. Cui and W. C. Chew, "Accurate Analysis of Wire Structures From Very-Low Frequency to Microwave Frequency," *IEEE Transactions on Antennas and Propagation*, vol. 50, no. 3, pp. 301–307, 2002.
- [95] F. Andriulli, K. Cools, H. Bagci, F. Olyslager, A. Buffa, S. Christiansen, and E. Michielssen, "A multiplicative calderon preconditioner for the electric field integral equation," *IEEE Transactions on Antennas and Propagation*, vol. 56, no. 8, pp. 2398–2412, Aug. 2008.
- [96] A. Bossavit, Computational Electromagnetism. Academic Press, 1998.
- [97] R. J. Adams, N. J. Champagne, and S. Member, "A Numerical Implementation of a Modified Form of the Electric Field Integral Equation," *IEEE Transactions on Antennas and Propagation*,

- vol. 52, no. 9, pp. 2262–2266, September 2004. [Online]. Available: http://ieeexplore.ieee.org/lpdocs/epic03/wrapper.htm?arnumber=1331612
- [98] O. Tuncer, C. Lu, N. Nair, B. Shanker, and L. C. Kempel, "Further development of the vector generalized finite element method and its hybridization with boundary integrals," accepted for publication in IEEE Transactions on Antennas and Propagation; technical report available at https://www.egr.msu.edu/ece/technical_papers, 2010.
- [99] I. Babuska and J. M. Melenek, "The partition of unity method," *International Journal for Numerical Methods in Engineering*, vol. 40, pp. 727–858, 1997.
- [100] R. Scharstein, "Helmholtz decomposition of surface electric current in electromagnetic scattering problems," System Theory, 1991. Proceedings., Twenty-Third Southeastern Symposium on, pp. 424–426, Mar 1991.
- [101] N. Nair and B. Shanker, "An extension of the generalized method of moments to higher order geometries," in *Proceedings of the 25th International Review of Progress in Applied Computational Electromagnetics*, 2009.
- [102] A. Buffa and S. H. Christiansen, "A dual finite element complex on the barycentric refinement," *Mathematics of Computation*, vol. 76, no. 260, pp. 1743–1769, 2007.
- [103] C. Delgado, E. Garcia, F. Catedra, and R. Mittra, "Generation of characteristic basis functions defined over large surfaces by using a multilevel approach," *IEEE Transactions on Antennas and Propagation*, vol. 57, no. 4, pp. 1299–1301, Apr. 2009.
- [104] M. Khayat and D. Wilton, "Numerical evaluation of singular and near-singular potential Integrals," *IEEE Transactions on Antennas and Propagation*, vol. 53, no. 10, pp. 3180–3190, October 2005. [Online]. Available: http://ieeexplore.ieee.org/lpdocs/epic03/wrapper.htm?arnumber=1514571
- [105] L. Knockaert, "A general gauss theorem for evaluating singular integrals over polyhedral domains," *Electromagnetics*, vol. vol, pp. 11pp269–280, 1991.
- [106] S. Jarvenpaa, M. Taskinen, and P. Ylä-oijala, "Singularity extraction technique for integral equation methods with higher order basis functions on plane triangles and tetrahedra," *International Journal for Numerical Methods in Engineering*, vol. 58, pp. 1149–1165, 2003.
- [107] L. F. Canino, J. J. Ottusch, M. A. Stalzer, J. L. Visher, and S. M. Wandzura, "Numerical solution of the helmholtz equation in 2d and 3d using a high-order nystrom discretization," *Journal of Computational Physics*, vol. 146, no. 2, pp. 627–663, 1998.

- [108] M. Vikram and B. Shanker, "An incomplete review of fast multipole methods from static to wideband as applied to problems in computational electromagnetics," *Applied Computational Electromagnetics Society Journal*, vol. 27, p. 79, 2009.
- [109] A. Chatterjee, J. Jin, and J. L. Volakis, "Edge-based finite elements and vector abc's applied to 3-d scattering," *IEEE Transactions on Antennas and Propagation*, vol. 41, pp. 221–226, 1993.
- [110] S.-C. Lee, M. N. Vouvakis, and J.-F. Lee, "A non-overlapping domain decomposition method with non-matching grids for modeling large finite antenna arrays," *J. Comput. Phys.*, vol. 203, no. 1, pp. 1–21, 2005.
- [111] C. Muller, Foundations of the Mathematical Theory of Electromagnetic Waves. Berlin: Springer Verlag, 1969.
- [112] P. Yla-Oijala and M. Taskinen, "Well-Conditioned Müller Formulation for Electromagnetic Scattering by Dielectric Objects," *October*, vol. 53, no. 10, pp. 3316–3323, 2005.
- [113] F. P. Andriulli, K. Cools, F. Olyslager, and E. Michielssen, "Time Domain CalderÓn Identities and Their Application to the Integral Equation Analysis of Scattering by PEC Objects Part II: Stability," *IEEE Transactions on Antennas and Propagation*, vol. 57, no. 8, pp. 2365–2375, August 2009. [Online]. Available: http://ieeexplore.ieee.org/lpdocs/epic03/wrapper.htm?arnumber=5067343
- [114] B. Shanker, A. A. Ergin, K. Agyün, and E. Michielssen, "Analysis of transient electromagnetic scattering from closed surfaces using a combined field integral equation," *IEEE Transactions on Antennas and Propagation*, vol. 48, pp. 1064–1074, 2000.
- [115] A. A. Ergin, B. Shanker, and E. Michielssen, "Transient analysis of acoustic scattering using marching-on-in-time with plane wave time domain algorithm," *J. Acoustical Soc. Am.*, vol. 106, pp. 2405–2416, 1999.
- [116] D. Weile, G. Pisharody, N.-W. Chen, B. Shanker, and E. Michielssen, "A novel scheme for the solution of the time-domain integral equations of electromagnetics," *Antennas and Propagation, IEEE Transactions on*, vol. 52, no. 1, pp. 283–295, Jan. 2004.
- [117] J. J. Knab, "Interpolation of bandlimited functions using the approximate prolate series," *IEEE Trans. Information Theory*, vol. 25, pp. 717–720, 1979.
- [118] A. Pray, N. V. Nair, and B. Shanker, "A generalized discretization scheme for transient integral equations," in to appear in Proceedings of the International Symposium on Antennas and Propagation, 2010.

[119] A. Pray, N. Nair, and B. Shanker, "Evaluation of retarded potential integrals using an approximation to the green's function," To be submitted to IEEE Transactions on Antennas and Propagation, 2010.